Methods and models to control and predict behavior of two dimensional paper networks for diagnostics

Gina Ella Fridley

A dissertation
submitted in partial fulfillment of the
requirements for the degree of

Doctor of Philosophy

University of Washington

2014

Reading Committee:

Paul Yager, Chair

Daniel Ratner

James Lai

Program Authorized to Offer Degree:

Bioengineering

University of Washington

Abstract

Methods and models to control and predict behavior of
two dimensional paper networks for diagnostics

Gina Ella Fridley

Chair of the Supervisory Committee:
Professor Paul Yager
Bioengineering

Medical care is dramatically more efficient when physicians can diagnose their patient's illness to guide appropriate treatment. Currently, there are two classes of diagnostic tests: high-performance gold standard laboratory-based tests that require complex and expensive infrastructure that is not available in clinics, homes, or rural areas; and inexpensive, easy-to-use, rapid lateral flow tests that often have poor sensitivity and specificity. Novel devices that achieve high sensitivity and specificity, while remaining accessible for point-of-care diagnosis in low-resource settings, would dramatically improve heath outcomes around the world.

Recent developments toward 2-dimensional paper network (2DPN) diagnostics that combine the sophistication of microfluidics with the simplicity and low cost of lateral flow tests are a promising solution for point-of-care diagnostics. Integration, automation and design of these 2DPN devices would be improved if device engineers could predict how their assays would behave without needing to iterate through dozens of experiments to optimize conditions. These improvements can be realized through the development of techniques to

predict and *control* the behavior of a variety of different components that are used in the assay design process.

This project has developed a set of methods and models that are a valuable step toward the goal of fully controlled and "engineerable" assays. First, the process of printing reagents onto nitrocellulose membranes has been characterized—examining and modeling the imbibition of liquids into membranes. Second, techniques were developed to study protein adsorption to nitrocellulose surfaces, and a model was developed to evaluate and compare different rates of this adsorption process. Third, methods were developed to pattern and dry reagents for storage directly within the nitrocellulose membranes, and subsequently rehydrate them in a variety of controlled spatial and temporal distributions in a device. Fourth, a multi-step malaria assay was implemented using solely patterned and dried reagents. Fifth, a computational model of transport and binding of reagents within a single pore was developed to provide insight into the various parameters governing assay signal. Finally, another computational model was built to illustrate the multitude of binding interactions that occur when multivalent analytes and antibodies are used in an assay system.

Table of Contents

Acknowledgements

This research was conducted at the University of Washington, advised by Dr. Paul Yager in the Department of Bioengineering, whose guidance was essential to the successful completion of this project. It would not have been possible, however, without the support and work of many other researchers. Dr. Elain Fu provided a significant amount of guidance throughout the project, as well as data and resources for the multivalent model described in Chapter 7. Carly Holstein was a valuable collaborator and sounding board throughout all of the research, with a particular emphasis on the protein adsorption methods described in Chapter 4. Huy Le performed many of the patterned reagents experiments in Chapter 5 and 6, and was instrumental in the development of those methods during his time as a capstone student and later as a research scientist. Much of the patterned dry reagents work was based on studies of dried reagent viability by Dean Stevens and Sujatha Ramachandran. Christiane Adcock refined the lateral flow depletion technique described in Chapter 4, and performed many of the associated experiments, while a high school student volunteer in the laboratory. Luke Allpress continued work with dried reagents. Data illustrating differential binding of premixed versus sequential assays in Chapter 7 was collected by Tinny Liang and Elain Fu, and their work with the malaria assay served as much of the foundation for the assay in Chapter 6. Several figures were adapted from the fantastic graphics designed by Dean Stevens. Cathryn Olsen and Vicki Watkins from GE Global research developed the spin-coating technique for nitrocellulose on SPR slides used in Chapter 4. Peter Kauffman built the fluorescence imaging set-ups used in Chapter 4 and 5, and was invaluable in all things optical, mechanical, and electronic. Chelsea Musick ensured that meetings were scheduled, that supplies were purchased, and that everything in the lab ran smoothly and efficiently.

The concepts and inspiration for much of this work came from discussions with all members of the Yager, Lutz, and Fu groups, particularly: Carly Holstein, Elain Fu, Barry Lutz, Jennifer Osborn, Rachana Shah, Dean Stevens, Peter Kauffman, Josh Buser, Samantha Byrnes, Tinny Liang, Mallory Monahan, Paula Ladd, Koji Abe, Nuttada Panpradist, Bhushan Toley, Srinath Rangarajan, Maxwell Wheeler, Lisa Lafleur, Josh Bishop, all of the collaborating partners of the Flu project team, and members of the Fu/Lutz/Yager Comsol Club.

I would also like to acknowledge my entire supervisory committee: Paul Yager, Dan Ratner, James Lai, Pat Stayton and Eve Riskin, for their support of this project and helpful suggestions throughout the process.

This work was supported by funding from the National Science Foundation Graduate Research Fellowship under Grant No. DGE – 0718124, the University of Washington Department of Bioengineering, and the following grants: NIH–NIBIB [ARRA] 1RC1EB010593 and NIH–NIAID 1 R01 AI 096184-01.

1 Introduction

1.1 Problem Description

Accurate medical diagnoses lead to more effective and efficient medical treatment. The current state of medicine worldwide is at a powerful crossroads: the quality of medicine is improving in developing countries—more and more medical treatments are becoming available, though in many instances accurate diagnostics lag the corresponding treatments, leading to mis-prescription and over-prescription [1, 2]. Meanwhile, in developed countries healthcare costs continue to skyrocket to larger and larger percentages of nations' gross domestic product [3], and policies are shifting toward proactive and primary care [4, 5]. In both of these cases, simpler medical tests are needed—tests than can be performed by a minimally skilled person: perhaps a field medical worker in a Peruvian jungle village, a medical assistant at a primary care clinic in Yakima, or a parent in a Seattle apartment.

Gold standard diagnostic tests have high sensitivity and specificity, but require resources such as reliable electricity, clean water, and skilled laboratory technicians, which are often not available in clinics or rural areas in developing countries. While clean water and electricity are readily available in the United States and other developed countries, primary care clinics typically do not have the financial or infrastructural resources to employ highly trained laboratory technicians. Because high-performance gold standard tests are not appropriate for this wide range of low-resource settings, simpler and cheaper tests must be used instead.

Lateral flow tests are the most commonly used simple diagnostic, since they are inexpensive, easy to use, and rely on capillary flow, so no external pumps are needed. Unfortunately, existing lateral flow tests have inadequate sensitivity and specificity to

diagnose many important diseases, from influenza to malaria [6-11]. Devices are needed to bridge this gap, and achieve high sensitivity and specificity while remaining accessible for point-of-care diagnosis in low-resource settings. Two-dimensional paper networks (2DPNs) are a novel type of point-of-care diagnostic test that are based on the same principles of basic lateral flow tests, but incorporate some of the sophisticated capabilities of laboratory scale gold standard tests [12-15]. These 2DPN devices offer a promising opportunity to improve the performance of point-of-care diagnostics, but the field is still in its infancy, and several technical problems still exist in the implementation of these devices for fully automated assays.

One broad challenge facing 2DPN engineers is that while these devices offer increased sophistication and performance capabilities, this added sophistication brings with it a level of increased design complexity. In a single device, the actions of many phenomena occur in concert to carry out a successful assay—if any one step fails, the result is invalid. The symphony of interactions includes players such as the sample liquid, buffers, and reagents, which must be introduced and combined in controlled ways, then flow through the assay membrane via capillary wicking, and react in the assay test zone in rapid, specific and predictable ways. Some aspects of the complex system of a 2DPN are individually well characterized—flow rates and flow profiles through porous materials, or the mechanism and kinetics of antibody-antigen binding—but the behavior of multiple phenomena occurring simultaneously has yet to be analyzed, or modeled in a predictive capacity.

Overall, these systems need two types of improvements: first, methods to enable device engineers to more tightly *control* these phenomena, and second, computational models to better *predict* the behavior that will result from varying different parameters in future designs.

1.2 Proposed Solution

This project has sought to facilitate the design and enhance the fundamental understanding of more sophisticated 2DPN assays through the development of methods to study and control behavior in 2DPN devices, and computational models to better predict how assay performance will respond to variations in parameters. The specific attributes of these methods and models are described below.

1.3 Summary of Thesis

This thesis is divided into eight chapters. Chapter 1 describes the problem and proposed solution. Chapter 2 provides key background information and a literature review of the current state of the art of a variety of methods and fundamental theory that form the basis for the novel work of this thesis. Chapters 3–7 describe the novel contributions, specific methods and major findings of this work.

Chapter 3 introduces a problem central to much of this work: the deposition of materials onto porous substrates via printing. This process of printing reagents onto nitrocellulose membranes was characterized to allow more precise control and understanding of the distribution of liquids as they are a deposited onto the surface of, and wick into a nitrocellulose membrane. After examining this imbibition of liquids into membranes, a computational model was developed to better understand the flow rates within the membrane as liquids are imbibed into the material.

Chapter 4 discusses the development of techniques to study protein adsorption to surfaces. Several different strategies were tried—to varying degrees of success—and finally a simple and high-throughput assay was designed, taking advantage of the predictable liquid deposition properties of precision printing on nitrocellulose, as described in Chapter 3. After

developing this technique, a model was built upon the basic printing model from Chapter 3 to evaluate and compare different rates of this adsorption process.

Chapter 5 describes another set of methods that take advantage of the well-controlled process of printing onto nitrocellulose: several techniques were developed to pattern reagents for dry storage directly within the nitrocellulose membranes. These techniques enabled the subsequent rehydration of dried reagent depots in a variety of tightly-controlled spatial and temporal distributions within a device. Again, to enhance the "engineerablity" of these techniques, a companion computational model was developed to simulate how different spatial and temporal distributions could be tuned.

Chapter 6 presents a multi-step high-sensitivity 2DPN immunoassay that was implemented using solely the patterned and dried reagents developed in Chapter 5. This assay is a meaningful example of the utility of patterning reagents directly onto assay devices, and could be use in other assays to incorporate reagents for controlled rehydration and combination. Furthermore, these patterning methods also have the potential to simplify device fabrication by reducing the number of components, and reduce user steps by facilitating automated operation.

Chapter 7 discusses the development of two separate computational models that begin to enhance our understanding of the complex interactions of the many phenomena that occur simultaneously within a 2DPN assay. The first model simplifies the entire assay system to a single pore, to facilitate the incorporation of convective and diffusive transport, along with surface binding events. With this model we sought to provide insight into the various parameters governing the assay response. The second model discussed here was built to illustrate the multitude of binding interactions that occur when multivalent analytes and

detection antibodies are used in an assay system. Depending on the relative concentrations of different species, very different complexes can be formed in the system, and the detectability of each type of complexes could be very different within a single 2DPN assay.

Finally, Chapter 8 discusses the overall conclusions and implications of this work, and suggests opportunities for future work in this area of research.

2 Background

2.1 Point-of-care diagnostics for low-resource settings

In the developing world

Infectious diseases are a major cause of morbidity and mortality globally; in 2002 the World Health Organization (WHO) estimated that the burden of disease due to infectious and parasitic diseases was over 23% of the total disability-adjusted-life-years (DALYs) that year. Of the 350 million DALYs attributable to infectious and parasitic diseases, 84.5 million were attributable to HIV/AIDS; 46.5 million were attributable to malaria; and 94.6 million were due to respiratory infections [16]. Medications for treatment and management of these diseases are increasingly available in low- and middle-income countries. In contrast, rapid and accurate diagnoses are often unavailable [1, 2]. Gold standard diagnostic tests, such as nucleic acid amplification and enzyme-linked immunosorbent assays (ELISAs), which have overall high sensitivity and specificity, are very expensive and require significant instrumentation and skilled technicians. Unfortunately, many areas do not have the healthcare resources or the basic infrastructure, such as electricity and running water, to operate medical testing laboratories. For that reason, high-performance assays are frequently inaccessible to patients in such settings [1, 2].

There has been a recent push toward rapid tests for point-of-care diagnosis of infection for use in both clinics and remote areas. To help further these goals, experts at the WHO have developed the "ASSURED" criteria for assessing POC diagnostics; viable rapid tests must be **A**ffordable, **S**ensitive, **S**pecific, **U**ser-friendly, **R**apid & **R**obust, **E**quipment-free, and **D**elivered to those who need them [17, 18].

In the developed world

Healthcare spending in developed countries is skyrocketing to unmanageable levels [3], leading to legislation and policies that attempt to emphasize primary preventive care and effective management of disease [19]. Because of these changes, there is a powerful shift in medical technology development toward devices and tests that can provide more *value* for their price, rather than simply designing for performance without any regard for cost as was previously the case [3, 5]. Furthermore, consumers have a growing enthusiasm for self-management of their own health, and the recent FDA approval of the OraSure OraQuick® HIV test for over-the-counter sale and at-home use has opened a door to broader use of home-based testing.

Though it may come as a surprise, consumers' homes or primary care clinics can be considered low-resource settings, even in countries like the U.S., where electricity and running water are readily available. Consumers are not trained to perform medical diagnostic tests, so automation and ease-of-use are essential test attributes. Primary care clinics do not have the infrastructure or human resources for most gold-standard laboratory tests. Both of these use cases require a rapid and easily-interpreted result, and an affordable price point that does not require thousands of tests per year to reach economies of scale.

The work in this thesis has sought to improve the performance of point-of-care assays in *all types of low-resource settings* by advancing the capabilities of paper-based diagnostic tests.

Current point-of-care diagnostics

Although some point-of-care tests are currently available on the market, most of them do not fully satisfy the ASSURED requirements. For example, assays with high sensitivity

and specificity, such as microfluidic devices, typically have higher cost, require more user steps and often need additional instrumentation. Conversely, inexpensive and equipment-free tests, such as lateral flow tests, make sacrifices in assay performance in favor of simplicity [2]. This section describes in detail attributes of current point-of-care diagnostic technologies.

Microfluidic diagnostics

Over the past decade several microfluidic diagnostics have been developed for POC applications, such as blood glucose monitors, the hand-held iSTAT device, and the Cepheid Gene Xpert. These devices have some characteristics that make them promising for POC use: they require low sample volumes, often have integrated reagents, include some forms of sample preparation, and in many cases perform automated sample-to-result processing. Paul Yager's laboratory at the University of Washington developed the DxBox, a microfluidic card-based, pneumatically driven, and multiplexed diagnostic system for use in the developing world. The DxBox is able to diagnose a panel of fever-causing pathogens through both immunoassays and nucleic acid amplification. Since all reagents, buffers and processing steps are contained on the microfluidic card, the device requires minimal user training [20, 21]. Though microfluidic-based systems address many of the needs of POC diagnostics in low-resource settings, they are non-ideal for settings outside of larger hospitals because they are often prohibitively expensive, need instrumentation, and may require maintenance in the field.

Lateral flow tests

Lateral flow tests (LFTs) have been used as POC diagnostics for several decades [22]. These easy-to-use devices are made from porous wicking materials, typically paper or paper-like membranes, such as nitrocellulose, and rely on capillary wicking to drive flow.

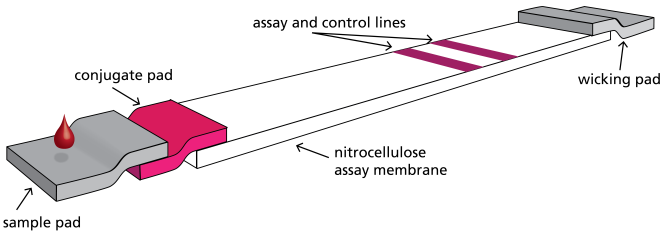

Figure 1: Lateral flow test. Sample is added to the sample pad, rehydrates conjugate and wicks through the nitrocellulose assay membrane to the assay and control lines, where signal is generated. An absorbent wicking pad drives flow.

These devices are well-suited for POC use because they are disposable, inexpensive, stable for long-term storage, need minimal operator steps, and require no external pumps or valves [17]. The most well known LFT is the home pregnancy test, but other applications include testing for drugs of abuse and rapid diagnosis of infectious diseases, like HIV, malaria, and influenza [6, 8, 23-29]. A schematic of an LFT is illustrated in Figure 1. In an LFT, the patient sample is applied to the sample pad and wicks to the conjugate pad where it rehydrates the detection reagent. The fluid then continues to wick down the strip to the test line where a line will appear if the sample contains the analyte of interest. Most LFTs also include a process control line just downstream from the test line to verify that all reagents were rehydrated and flow reached the test zone, which ensures that the test has been run correctly [22]. While these tests have been very widely used, their results are semi-quantitative at best, and many POC LFTs still show unacceptably low sensitivity and specificity [7, 22].

Two-dimensional paper networks for improved point-of-care diagnostics

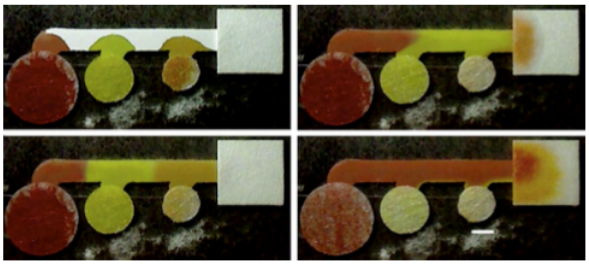

Figure 2: Timed sequential delivery of different liquids from 3 separate inlets. 2DPNs offer increased fluidic control compared to typical lateral flow tests. Figure from Fu et al. [12]

Recently, sophisticated paper-based technologies have been introduced that are driven by the same capillary flow mechanism used by simple LFTs [12-15, 30-39]. These new paper-based[1] tests have demonstrated a breadth of functionalities unavailable to previous LFTs. Many of these implementations include multiplexed analyte detection [37, 40], fluidic timing controls [13, 15, 39, 41-43], and on-strip chemical signal amplification [12, 14]. Because these paper devices rely on capillary flow, no external pumps or instrumentation is required. More generally, these devices maintain many of the benefits of LFTs, including greater ease-of-use and a lower price point relative to bench-top or microfluidic assays. In this thesis, we utilize a class of paper-based devices known as two-dimensional paper networks (2DPNs), in which devices are cut into more sophisticated geometry, rather than the single strip format of LFTs. For example, automated on-strip chemical signal amplification was demonstrated by Fu et al. using a 3-inlet 2DPN device to deliver multiple reagents in a timed sequence (Figure 2) [12]. In a subsequent publication, these authors used a similar device to implement a multi-step assay, using that signal enhancement chemistry to improve their limit of detection over unenhanced levels [44].

[1] The word "paper" is typically defined as a porous material compressed from cellulose pulp. In the context of this dissertation the word will be used to include other porous media such as nitrocellulose.

Areas for improvement in 2D paper networks

2DPNs have demonstrated many exciting improvements over existing lateral flow assays by expanding the fluidic capabilities available to paper devices; however, device integration and automation would be improved if the behavior of reagents and analytes within the device were more easily controlled and predicted.

The following sections discuss the major functions of 2D paper network assays relevant to this work, and illustrate the need for more sophisticated tools to predict and control these processes.

2.2 Immunoassays

Mechanisms of protein-based assays on solid substrates

In general, immunoassays are set of methods that use specific antibodies to facilitate detection of a particular analyte, often a disease antigen from a patient sample [45], other methods using non-antibody proteins for capture and detection are often still referred to as immunoassays, and will be considered as such for the purposes of this discussion. These protein-based assays are in contrast to nucleic acid-based detection methods such as nucleic acid amplification tests (NAATs), which will not be discussed here.

Lateral flow tests and protein-based 2DPN assays, as well as enzyme-linked immunosorbent assays (ELISAs) are examples of different varieties of immunoassays. ELISAs are a gold-standard method to assay for the presence of a particular analyte of interest, and are performed in laboratory settings using multiwall plates, micropipetted liquid volumes and precise timing of individual steps executed by a skilled laboratory technician [45, 46]. However, the same types of binding interactions used in ELISAs are the foundation for both lateral flow and 2DPN-format protein-based assays. There are three

categories of mechanisms used in these types of assays: direct, indirect, and competition immunoassays [46]. The differences in these mechanisms of detection are described briefly below and are illustrated in Figure 3.

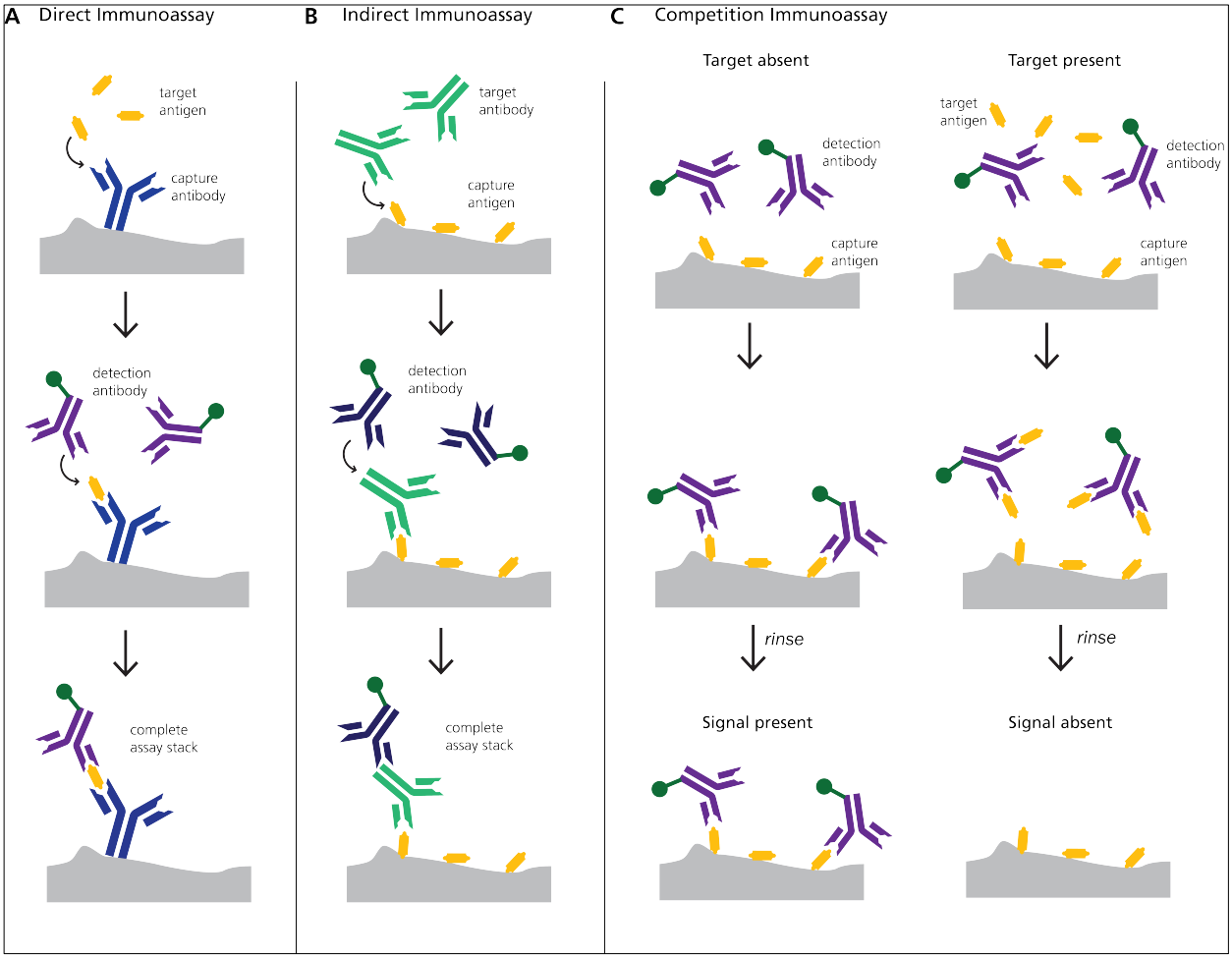

Figure 3: Comparison of the three types of immunoassays. A. Direct immunoassay: the target antigen is captured and then detected using a detection antibody. B. Indirect immunoassay: a patient's immune response to an antigen is measured by capturing the patient's antibody against a particular antigen, and then detected using an antibody targeted to the patient's antibody. C. Competition immunoassay: an antigen is detected via the absence of signal that occurs when the antigen present in a sample competes for binding with the detection antibody. This type of immunoassay is very different from the other two because the absence of signal indicates the presence of the target.

Direct immunoassay

In a direct immunoassay, the target of interest (e.g. a antigen from a particular pathogen) binds to a capture molecule is immobilized on the assay substrate, typically an antibody

specific to the target of interest. Then, the assay signal is measured based on a detection molecule that also binds to the target, forming a "sandwich," as shown in Figure 3A. The capture molecule in this case is an antibody that binds to the antigen of interest, and the detection molecule is a second, labeled antibody [45, 46].

Indirect immunoassay

Indirect immunoassays measure a patient's immune response to a particular antigen, by detecting the antibodies produced against a given antigen, but do not measure the antigen itself. This is achieved by immobilizing the pathogen antigen on the assay substrate, and using that to capture the antibodies generated in response to that particular pathogen. As with the direct immunoassay, the signal is generated by a labeled detection antibody, in this case, an antibody designed to bind to the antibodies that are detected from the patient (see Figure 3B) [45, 46].

Competition immunoassay

Competition immunoassays are typically used for analytes that are small molecules and are too small to be "sandwiched" in between a capture species and a detection antibody. This is because the mechanism of the competition immunoassay is significantly different from both direct and indirect assays, and no complete assay sandwich is needed. This assay measures the level of a particular analyte in a sample by measuring the competition for binding of a labeled detection molecule with analyte immobilized onto the assay surface. Because of this competition for binding, a competition immunoassay is the only case where signal readout is inverted: lower signal indicates higher concentration of analyte. To perform an assay, the detection molecule is mixed with the patient sample, allowing time for analyte in the sample to bind, then this mixture is introduce to the assay substrate. At high levels of analyte in the sample, there is no free detection molecule to bind to the surface, leading to

no signal in the assay. Conversely when no analyte is present in the sample, the detection antibody is free to bind to the capture molecule on the assay substrate, leading to the highest possible signal. See Figure 3C for an illustration of the competition assay [45, 46].

Immunoassay signal-generation mechanisms

In all of these immunoassay formats, the detection antibody must be tagged with some kind of detectable label (see Figure 4) [22, 47]. A variety of different detection methods can be used in these assays: blue polymer beads or gold nanoparticles are common colorimeteric signal-generating species in lateral flow tests [22]. These methods are particularly popular because the colored signal that appears on the white background can be interpreted visually by an untrained user. Conversely, in cases where an instrumented detector may be used, fluorescent dyes can also be covalently attached to detection antibodies, which can be very sensitive because the zero-analyte condition is total darkness and any additional analyte increases the signal above that low background [48]. Another high-sensitivity detection method is to covalently attach an enzyme (e.g. horseradish peroxidase) to the detection antibody. This enzyme can then catalyze the chemical transformation of a chromogenic substrate to a visible signal [49-52].

Enzyme-linked labels are typically used in ELISA (hence "enzyme-linked" beginning that method's name) [50-52], and can be used in lateral flow tests as well [49]. Two benefit to the use of enzymes for signal-generation are: (1) a single enzyme can generate many colored products, resulting in an amplified level of signal (see Figure 4A), and (2) the kinetics of enzymatic product generation can be measured, yielding quantitative assay results [52]. Unlike the case of enzymatic signal generation however, fluorescent labels, polymer beads, or gold nanoparticles are used, there is no inherent signal amplification, because each colored particle binds directly to a target analyte (see Figure 4B and C). There is a method

to enhance the signal generated by gold nanoparticles however, though it requires an extra assay step. When a gold or silver salt (e.g. silver lactate) and a reducing agent are together in the presence of a gold nanoparticle, the metal ions from the salt are reduced to gold or silver metal and are deposited onto the surface of the nanoparticle (see Figure 4D) [53-56]. As the nanoparticles increase in size, their light absorption profile changes, shifting the apparent color from reddish-pink to purplish-black, and increasing the visible signal for a given concentration of analyte [14, 44]. Typical lateral flow tests are not able to perform multi-step processes, but this kind of multi-step amplification is a perfect example of an added function that could be implemented in a 2DPN device.

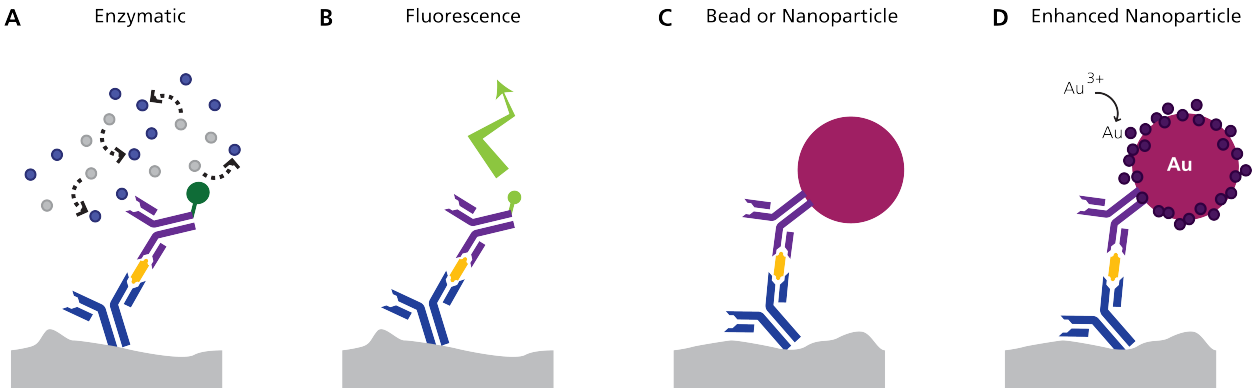

Figure 4: Detection mechanisms used in immunoassays. A. Enzymatic signal generation utilizes an enzyme, such as horseradish peroxidase, covalently attached to the detection antibody to generate a colorimetric signal. A major benefit of enzymatic signal generation is that each enzyme can catalyze many reactions, leading to built-in signal enhancement. B. Fluorescence detection utilizes fluorescent dyes covalently attached to the detection antibody. In the assay, a detector is used to measure fluorescence signal. This method can be very sensitive, due to low background signal, but it requires more instrumentation and cannot be detected by the naked eye. C. Gold nanoparticles or blue latex beads are commonly used for detection in many lateral flow tests. They are easily viewed by the naked eye, but sensitivity can be an issue. D. Signal enhancement chemistries can increase the visible signal generated from gold nanoparticle-based detection. These methods introduce extra steps: a gold salt is reduced to gold atoms on the surface of the nanoparticle, increasing its size and changing its light absorption spectrum from reddish-pink to purplish-black. (Schematics based on figures by Dean Stevens).

Binding reactions and kinetics

Antibody-antigen interactions are typically modeled using one-to-one first-order binding kinetics, which are described by the following rate equations:

$$\frac{d[AB]}{dt} = k_{on}[A][B] - k_{off}[AB]$$

$$\frac{d[B]}{dt} = -k_{on}[A][B] + k_{off}[AB]$$

$$\frac{d[A]}{dt} = -k_{on}[A][B] + k_{off}[AB]$$

Where A and B are the interacting species and AB is the complex that forms when they bind [57]. The affinity of these interactions is typically characterized by the dissociation constant, K_d:

$$K_d = \frac{k_{off}}{k_{on}}$$

For specific interactions, on-rates are typically on the order of 10^4–10^6 $M^{-1}s^{-1}$, and off rates are < 10^{-3} s^{-1}, resulting in K_d values of 10^{-7} M or below. High-affinity antibodies have K_ds in the high pM range, and the binding of biotin by Streptavidin has the strongest known K_d of 10^{-14} M [58]. These kinetic rates, along with protein concentrations, drive complex formation, and must be understood for viable immunoassay design.

A multitude of factors affect assay signal

In all types of immunoassays, several different variables affect the signal that is generated for a given concentration of target. The starting concentrations of detection reagents and surface-immobilized capture molecules will govern the equilibrium concentration of detectable signal; the kinetics of the interaction and the duration of time allowed for binding to occur will determine if the assay even reaches an equilibrium level of bound complexes [22, 45]. The problem becomes even more complicated in the context of automated microfluidic or paper-fluidic assays, because in those assays, built-in fluidic flow

rates control interaction times available for analyte binding; and in multi-step assays the timing of reagent delivery influences assay results [1, 2, 13, 44, 59]. Some of these factors are well understood and can be incorporated into novel assay design, however, when taken together the factors form a complex set of possibilities and near-endless combinations of conditions that need to be optimized in the development of any one assay.

2.3 Physics of flow

Understanding the physics of flow is essential before attempting to design methods to improve the function and capabilities of any kind of fluidic device, whether microfluidic or paper-fluidic. Before delving into the specifics of flow in porous materials, we will present a brief discussion of the simpler case of flow in channels, which forms the basis of many of the principles of flow in porous matrices as well.

Flow in channels

The Navier-Stokes equations are an application of Newton's second law (the conservation of momentum) to describe fluid motion in the most general case. These nonlinear partial differential equations can be used to describe a vast range of fluidic phenomena, from blood flow in a capillary to air flow around an airplane wing [60]. Fortunately for those of us who study liquids in microfluidics, there are several simplifications that can be made to the Navier-Stokes equations. First, liquids are generally considered incompressible, that is, regardless of the pressure applied, the density of that liquid will not change. Second, the viscosity of a given parcel of liquid does not change. Together, these assumptions simplify the Navier-Stokes equations to:

$$\rho\left(\frac{\partial \mathbf{v}}{\partial t} + \mathbf{v}\cdot\nabla\mathbf{v}\right) = -\nabla p + \mu\,\nabla^2\mathbf{v} + \mathbf{f} \qquad \text{Equation 1}$$

Where ρ is fluid density, $\mathbf{v}$ is the fluid's velocity field, ∇p is the pressure gradient, μ is fluid viscosity, and $\mathbf{f}$ represents all body forces acting on the fluid.

For an incompressible fluid, the continuity equation describing the conservation of mass can be simplified from:

$$\frac{D\rho}{Dt} + \rho(\nabla \cdot \mathbf{v}) = 0$$

to:

$$\nabla \cdot \mathbf{v} = 0$$

Another simplification that can usually be used in microfluidic channels is based on a non-dimensional number called the Reynolds number, a non-dimensional parameter that compares viscous forces to inertial forces on a fluid:

$$Re = \frac{inertial\ forces}{viscous\ forces} = \frac{\rho v l}{\mu} \qquad \text{Equation 2}$$

where ρ is fluid density, *v* is the fluid velocity, *l* is a characteristic dimension of the fluid channel and μ is fluid viscosity. At low Reynolds number (<10), flow is laminar, defined by flow streamlines moving parallel to the channel walls, and the only mixing that occurs between adjacent streams is through diffusion [61, 62]. Flows under these conditions lead to parabolic flow profiles (Figure 5), which is now commonly referred to as Hagen-Poiseuille flow, after Gotthilf Heinrich Ludwig Hagen and Jean Léonard Marie Poiseuille, who both independently derived an equation describing this phenomenon in a cylindrical pipe [63]:

$$Q = \frac{\pi R^4 \Delta P}{8 \mu L}$$ Equation 3

Where Q is the volumetric flow rate, R is the pipe radius, ΔP is the pressure drop across the length of the pipe, μ is the liquid viscosity and L is the length of the pipe. These types of flows are common in microfluidic systems, and experimental data are quite consistent with the behavior predicted by Equation 3.

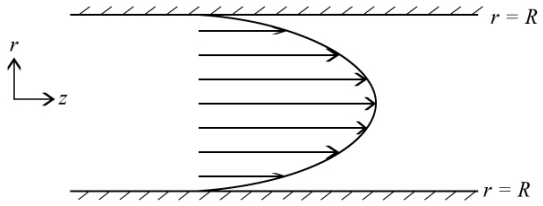

Figure 5: Poiseiulle flow in a pipe gives a characteristic parabolic shape, with v=0 at the walls and v_{max} at the center of the pipe. From Micro and Nanoscale Transport Phenomena by B. Kirby [64].

In the case of even lower Reynolds number flows (Re<1), viscous forces dominate over inertial forces, and the Navier-Stokes equations can be simplified even further, by neglecting the inertial and unsteady terms in the equations, commonly referred to as "Stokes Flow" [64]:

$$\nabla p = \mu \nabla^2 \mathbf{v}$$ Equation 4

These very-low Reynolds number flows are very unlike most macroscale phenomena that we encounter in our day-to-day lives—if a person wanted to swim in honey (μ=3000 cP) at Re~1, they would have to move slower than 1 *mm*/s [62]. However, flows in many microfluidic and paper-microfluidic (i.e. 2DPN) conditions result in Reynolds numbers much less than 1, so these simplifications apply when modeling these systems.

Solute transport in channels

There are typically solutes of various kinds (proteins, salts, dyes) in solution within fluids contained in devices relevant to this work, and in addition to being carried by the moving fluid, molecular diffusion can also play a significant role in the transport of these solutes.

Molecular diffusion is caused by the random Brownian motion of particles, and is more significant for smaller particles and at higher temperatures. The diffusivity, D, of a molecule can be approximate by the Stokes-Einstein equation:

$$D = \frac{k_B T}{6\pi\eta a}$$

Where k_B is Boltzmann's constant, T is temperature, a is the particle radius, and η is solution viscosity [64]. Fick's first law of diffusion describes the bulk flux of particles down their concentration gradient:

$$\boldsymbol{J} = -D\nabla C$$

Fick's second law relates how concentration changes over time, and is derived from Fick's first law together with conservations of mass:

$$\frac{\partial C}{\partial t} = D\nabla^2 C$$

Based on these equations governing diffusion, we can approximate the characteristic diffusion distance in a given time:

$$L = \sqrt{2Dt}$$

Therefore diffusion is proportional to the square root of time—it takes 4x as long to diffuse twice as far, which means that over longer distance scales, diffusion becomes less relevant than on shorter time scales. When diffusive transport is happening simultaneously with convective transport via flow velocity, we often want to understand which process is dominantly controlling transport. A non-dimensional number called the Péclet number compares the relative importance of convective versus diffusive transport:

$$Pe = \frac{UL}{D}$$

Where U is the flow velocity, D is diffusivity, and L is the relevant length scale (e.g. channel diameter). At low Péclet number, diffusion dominates transport, whereas at high Péclet number, convection dominates. An interesting high-Péclet phenomenon that can be observed in the parabolic flow profile of Poiseuille flow is the enhanced apparent diffusion caused by Taylor-Aris dispersion [64-66]. This phenomenon can be explained in two steps: first, assuming the complete absence of diffusion (Figure 64 part 2), the parabolic flow carries a bolus of solute a further distance near the center of the channel, compared to the edges, because of the higher velocity at the center. Then, when diffusion is considered, the solute diffuses down its concentration gradient at all locations, resulting in a much broader bolus in the axial direction (Figure 6 part 4).

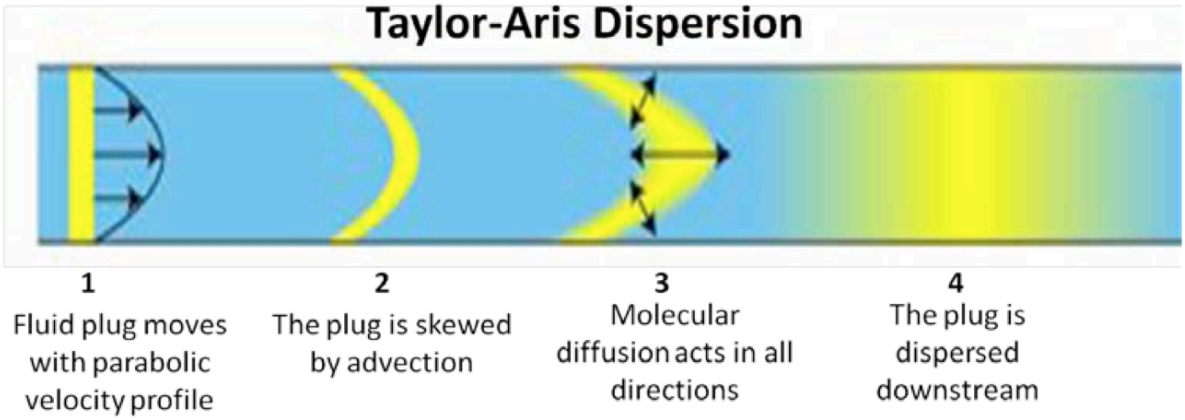

Figure 6: Schematic of Taylor-Aris dispersion in a channel. Figure courtesy of Dean Stevens.

Flow in porous materials

The equations and relations that describe flow in porous devices predate paper-based diagnostics by several decades and were originally developed for applications such as soil mechanics, pulp and paper development, and petroleum engineering [67-69]. Though these applications appear disparate, all of them require an understanding of flow in porous media, which can range from nitrocellulose membranes to rocks, soil, or wood fibers.

Capillary flow is affected by several characteristics of the porous media itself: pore size, pore distribution, and porosity; and also by characteristics of the fluid moving through the porous substrate: viscosity and surface tension; and finally by the interaction between the two: the contact angle of the fluid with the porous material [61, 67, 69].

Most porous media has some tortuosity—the "twistiness" that is defined by the ratio of the actual path length through a pore to the straight-line distance (Figure 7) [70]. Tortuosity can vary widely from material to material, and it is challenging to measure the tortuosity of a particular porous media directly. Experimentally, it is common to approximate tortuosity based on hindered-diffusion measurements in porous media using the equation:

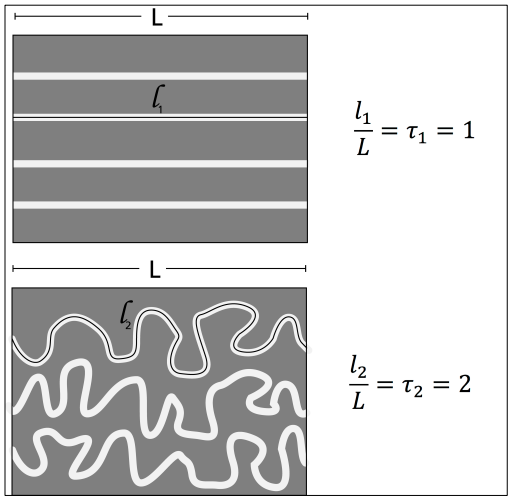

Figure 7: Tortuosity (τ) is the ratio of the actual pore path length to the straight line distance that the pore traverses. Perfectly straight pores (above) have τ = 1; twisting pores (below) have τ > 1.

$$\frac{D_e}{D_m} = \frac{\phi}{\tau^2} \qquad \text{Equation 5}$$

where D_e represents the effective diffusivity (absent any convection through the material), D_m is the molecular diffusivity as observed in a non-porous channel, ϕ is the porosity of the material, and τ is the tortuosity [70]. Using this equation, tortuosity can be approximated if porosity, molecular diffusivity and apparent diffusivity are known.

Measuring tortuosity directly is very challenging—Gommes et al. developed a method to compute an average tortuosity by making 3D computer reconstructions of tomography images [71], and then related the theoretical tortuosity calculated using Equation 5 to their measurements from reconstructed tomography images, and confirmed that these methods are consistent. Furthermore, they demonstrated that porosity and tortuosity are inversely related (Figure 8) so increasing porosity implies decreasing tortuosity. This inverse relationship between porosity and tortuosity is itself intuitive: in an open random porous network there will be more void space, pores will be more interconnected, allowing any individual path from the inlet to the outlet to be relatively straight. Conversely, in a low-porosity material, more of the space is occupied by solid matrix, and pores are more like individual random paths through the material, increasing the tortuosity. The paper materials used in 2DPNs typically have very high porosities (ε>0.7) [73, 74], which indicates a tortuosity of ~1.1 based on the correlations described by Gommes et al.

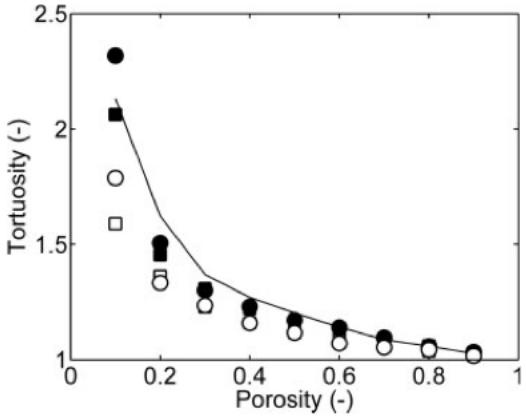

Figure 8: Inverse relationship between porosity and tortuosity of porous materials, from Gommes et al. Plotted points are tortuosity values calculated based on different models of their 3D reconstructions of tomographic images. Solid line shows data calculated based on Kim and Torquato's hindered diffusion measurements in a variety of different porous materials [71, 72].

Pore size values are approximated by membrane manufacturers, and are measured using two methods. First, the largest pore sizes are determined by forcing particles of increasing size through the membrane, and the point at which they no longer pass through is reported as the nominal pore size. That method is challenging to reproduce at large scale, so a more common method for pore size determination is via bubble point measurements. In these measurements air is forced through an unbacked wetted membrane, and the pressure at which air bubbles appear is the reported bubble point. Like particle-based measurements however, bubble point only provides information about the largest pores in the substrate, rather than a complete description of the pore size distribution. Another major drawback to the bubble point measurement is that the well-described inverse relationship between bubble point and pore diameter is only valid for pore sizes between 0.1–3 μm. Because of the unreliability of measurements on larger pore membranes, the pore diameter is typically reported as a "pore size rating" to approximate the diameter. The membranes used in nitrocellulose 2DPNs have pore size ratings on the order of 10 μm [74]. To better understand the inner pore structure of some of these membranes, we acquired scanning electron microscopy (SEM) images of these membranes, one of which is reproduced here in Figure 9.

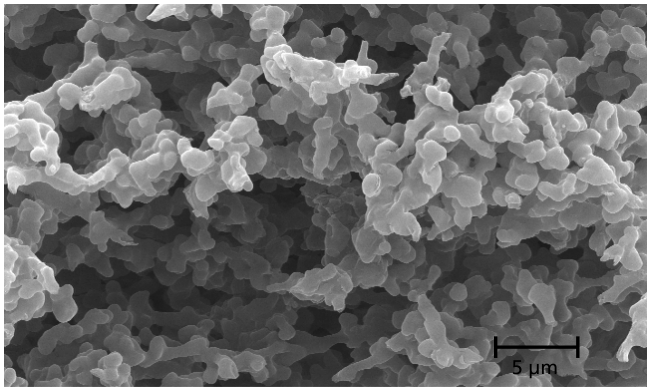

Figure 9: Scanning electron microscopy image of nitrocellulose membrane, with 5 μm scale bar shown at bottom right.

Porous media can be approximated as a bundle of straight pores, each one behaving as a very small pipe [75]. The flow in each of these pores approximates the parabolic profile predicted by Poiseuille, yet when they are bundled as a group, the bulk flow profile is the flat fluid front of plug flow (Figure 10). The straight-pore assumption is clearly a simplification, but it is a reasonable approximation for describing flow in paper materials given the low approximate tortuosity discussed above. This simplification allows us to use conventional fluidic principles, such as Poiseulle flow and the Reynolds number, to provide insight into the behavior of fluid in these pores. When the Reynolds number is calculated for paper membranes, which typically have pore diameters on the order of 1–10 μm, it is approximately 10^{-3}, when the fluid velocity is approximated as 0.1–1 mm/s. At this small scale, viscosity, diffusion and surface tension dominate over inertial effects.

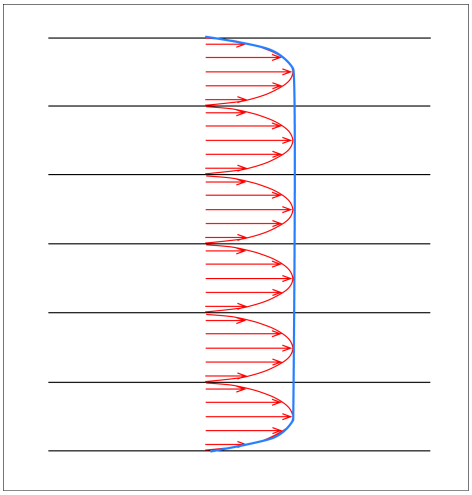

Figure 10: Approximating porous media as a bundle of small pipes. The flow in each small pipe follows the parabolic profile of Poiseiulle flow (red), but when taken together, the bulk flow is the flat shape of plug flow (blue line).

Because our systems fall within the low Reynolds number regime, there are well-characterized models to describe their flow behavior. As a dry porous membrane wicks fluid, the wet-out process is governed by the Lucas-Washburn equation [69, 76]:

$$L^2 = \frac{\gamma r_p \cos\theta \, t}{2\mu} \qquad \text{Equation 6}$$

where L is the length of the column of fluid in the porous material and is a function of the pore diameter, d_p, the surface tension of the fluid, γ, the fluid viscosity, μ, and the cosine of

the contact angle, θ. Taking the derivative of L with respect to t we find that the rate of wet-out is:

$$\frac{dL}{dt} = \frac{1}{2}\sqrt{\frac{\gamma r_p \cos\theta}{2\mu t}}$$

Replacing the $\sqrt{t}$ term in the denominator as a function of L, we can see that the rate of wet-out is actually inversely proportional to the length of the fluid column:

$$\frac{dL}{dt} = \frac{\gamma r_p \cos\theta}{4\mu L} \qquad \text{Equation 7}$$

This slowing is due to the balance between the capillary pressure driving flow and the viscous resistance of the fluid in the pore, as the fluid column grows longer:

$$\Delta P_{\text{capillary}} = \frac{2\gamma \cos\theta}{r_p} \qquad \text{Equation 8}$$

$$R_{viscous} = \frac{8\mu L}{\pi {r_p}^4} \qquad \text{Equation 9}$$

This viscous resistance applies specifically to the case of a *single* pipe—if the radius were half the size, the resistance would be 16 times more and the capillary pressure would be two times more. By using the electricity analogy of flow, where voltage (V) is analogous to the pressure differential (ΔP), current (I) is analogous to volumetric flow (Q), and electrical resistance (R) analogous to viscous resistance ($R_{viscous}$), we see that this results in a 8-fold decrease in volumetric flow:

$$I = \frac{V}{R} \qquad \sim \qquad Q = \frac{\Delta P}{R_{viscous}}$$

However, recall that a bulk porous material is approximated as a bundle of *several* pores: if the radius of a single pore were half the size, the resistance in an individual pore would be 16 times more, but there would be four times as many pores (given constant porosity and cross-sectional area), so the overall increase in resistance would be only four times in a bulk porous material. This leads us to the idea of the permeability (κ) of the porous material, which is a bulk property—essentially an inverse resistance—that can be measured experimentally, and is a composite parameter that depends on pore size ($\kappa \propto r^2$), tortuosity ($\kappa \propto 1/\tau$), porosity ($\kappa \propto \phi$), and empirical factors based on the nature of the porous material [70].

Henry Darcy used the permeability as a parameter in his famous equation modeling of flow in fully-wetted porous media (note that his equation also takes the form of the electrical analog) [67]:

$$Q = -\frac{\Delta P}{R} \text{ where } R = \frac{\mu l}{\kappa w h} \qquad \text{Equation 10}$$

where wh is the paper cross-sectional area of width w and height h, and ΔP is the pressure drop occurring over the a length l of the porous material. This equation assumes that flow is fed by an infinite source of fluid. It also assumes that as the wicking pad becomes wetted, the fluidic resistance does not increase; this is a false assumption, but it a sufficient approximation as long as the wicking pad has low resistance per unit distance, and the pad does not approach saturation.

It is also valuable to note that when l in Darcy's law is taken as a variable (i.e. wet-out flow), Darcy's law predicts the same $1/l$ velocity dependence as the Lucas-Washburn Equation (Equation 7).

These equations describe an approximation of flow in porous media, though it is neither comprehensive nor perfectly accurate. Entire dissertations and careers can be dedicated to developing more sophisticated models of these transport processes—for example, fractals have been used to model the chaotic and random nature of the porous media itself—however that is beyond the scope of what is needed for our goals of improving 2DPN devices. Readers who hope to explore those complexities are referred to one of the several books that introduce the subject [75, 77, 78].

Solute transport in porous media

Just as solutes in channels are transported via both convection and diffusion, solutes in channels also experience diffusive transport, however it is somewhat more complicated. As mentioned above, hindered diffusion experiments are used to approximate tortuosity by measuring the decrease in diffusivity of a solute observed in porous media (Equation 5) [70].

Once convection is introduced, however, diffusion is no longer hindered, but rather *enhanced* by mechanical dispersion. Jennifer Osborn studies these effects in her dissertation and observed that at higher radial Péclet numbers (using the pore radius as the characteristic length scale), the effective diffusivity of solutes was dramatically higher than reported molecular diffusivity values [79]. The same phenomenon has been observed in the geological context of porous media, and studies have shown a linear relationship between the diffusivity enhancement and the Péclet number for the flow:

$$\frac{D_{eff}}{D_m} \propto Pe = \frac{UL}{D_m}$$

Where D_m is the molecular diffusivity and D_{eff} is the effective observed diffusivity [80]. It is currently unclear exactly what causes this mechanical dispersion, though "streamline hopping" and tortuous flow paths have both been suggested to contribute [79, 80]. For more information on this topic, the reader is referred to the following publications [72, 75, 77-85].

2.4 Physics of printing on porous materials

Lateral flow immunoassays and two-dimensional paper network assays both require the incorporation of a variety of assay reagents, ranging from capture molecules immobilized at the test and control lines, to detection reagents stored dry upstream for later rehydration. Historically, only capture molecules have been deposited directly onto nitrocellulose assay membranes, but there are significant benefits to also including reagents for rehydration and downstream use directly on the assay membrane as well, and novel techniques to implement these tools will be described in detail in Chapter 5 of this thesis.

Printing is a very familiar—perhaps even mundane—task for most of us. However, there is a long history of research behind the apparently simple process. Many fundamental and groundbreaking discoveries remain trade secrets or proprietary knowledge, to help maintain the competitive advantages enjoyed by some manufacturers. Other aspects of this research have been made public through scientific publications, though, and this body of research will be discussed, with a particular focus on enhancing our understanding of printing on nitrocellulose for the purposes of 2DPN design and fabrication.

The physical phenomenon of printing is simply a specific instance of wicking—all of the fluid dynamics in porous media physics described above (Section 2.3) using Darcy's Law

(Equation 10) and the Lucas-Washburn equation (Equation 6) still apply. However, three additional processes must be considered as well: liquid delivery to the membrane, droplet spreading on the surface of the membrane prior to wicking, and evaporation of the liquid during and after wicking. These processes govern the liquid flow rates through the porous material during imbibition and the subsequent distribution of solutes (e.g. inks, proteins, salts) within the membrane after printing, and are therefore essential to understand in some detail when designing devices heavily dependent on printing reagents [86-88].

Several parameters influence the rates of all of these processes, and the printed results depend on the exact combination of parameters that describe a particular case. These parameters include: the surface tension of the liquid, the contact angle between the substrate and the liquid, the membrane pore size, the membrane pore size distribution, the capillary pressure of the porous material (which is actually just a function of other parameters, see Equation 8 in Section 2.3), the ambient relative humidity, the rate of liquid deposition and the volume of individual printed droplets [86-89].

Surface tension (γ) is a property, not of a liquid alone, but of the interfaces that liquid shares with other materials, and represents the amount of energy required to increase the surface area of that interface [90]. For example, water, which has strong molecular cohesion, will require the input of significant energy to increase the surface area of an air-water interface because that will reduce the energetically favorable water-water interactions, and create new less favorable water-air interaction at the newly created surface. Typically, γ without a specific subscript modifier represents the liquid-air surface tension, while the surface tension of a solid-liquid interface is reported in terms of the contact angle.

The contact angle between a liquid and solid is dependent on the three different surface tension measurements of the system: the solid-liquid surface tension, the liquid-gas surface tension, and the solid-gas surface tension, called Young's equation [90]:

$$\cos\theta = \frac{\gamma_{sg} - \gamma_{sl}}{\gamma_{lg}} \qquad \text{Equation 11}$$

The contact angle that a liquid forms with a solid is the physical result of the energetic optimization, minimizing unfavorable surfaces and maximizing favorable ones (Figure 11) [90]. Hydrophilic materials have energetically favorable interactions with water, and result in contact angles less than 90°—energetically, the surface would "rather" share an interface with water than with air. Conversely, hydrophobic materials have energetically unfavorable interactions with water, and result in contact angles greater than 90°, because the surface has a lower energy interface with air. A special case exists for super hydrophobic materials, where the liquid-solid surface tension is equal to the liquid-air surface tension and the contact angle is 180°, and a perfect spherical droplet is formed.

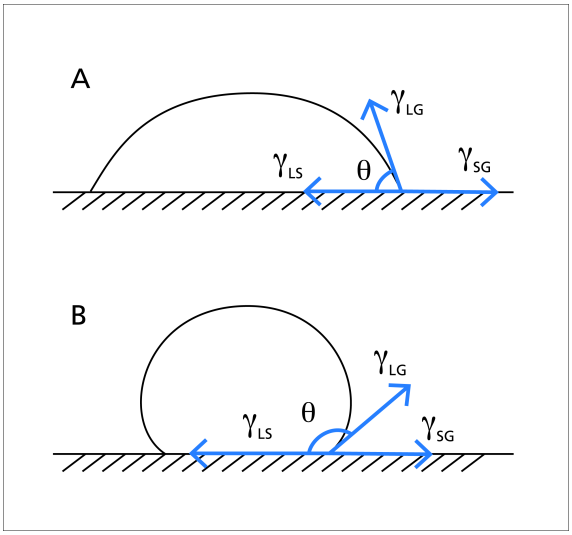

Figure 11: Contact angles are derived from surface tension values (γ_{LS}, γ_{LG}, γ_{SG}). A) Hydrophilic surfaces have favorable interactions with water, leading to a larger shared area and lower contact angle (θ). B) Hydrophobic surfaces have unfavorable interactions with water, and minimize their shared area with a larger contact angle.

The contact angle is important to wetting of porous materials because the capillary pressure is proportional to the cosine of the contact angle (Equation 8), so for contact angles greater than 90°, the capillary pressure is negative and liquid will not be pulled into the

membrane by capillary pressure alone. The contact angle also dictates the shape of the spherical cap of liquid formed on the membrane surface while the droplet is spreading on the membrane. While Equation 11 suggests a single contact angle value, in reality contact angles exhibit hysteresis—there is a maximum contact angle, which is observed when the droplet is advancing along a surface (or volume is being added), yielding the "advancing contact angle"; and a minimum contact angle, which is observed while the drop is receding (or losing volume), yielding the "receding contact angle" (see Figure 12) [86, 90]. Both of these measurements are commonly reported when discussing contact angles, and the equilibrium contact angle falls somewhere between the two. To further complicate the situation for porous materials, there are two relevant *types* of contact angle: the microscale contact angle, which describes the contact angle on a flat non-porous surface, and the macroscale contact angle, which is measured on a porous substrate, and is the relevant angle for approximating the spreading of a spherical cap of liquid deposited on a surface [91]. The micro- and macroscale contact angles are typically different because in the porous macroscale case, the liquid spherical cap is contacting a surface that is partially composed of open pores as well as the solid material, rather than an extended surface of pure substrate. For nitrocellulose membranes, reported water droplet contact angle measurements are reproduced in Table 1 [92].

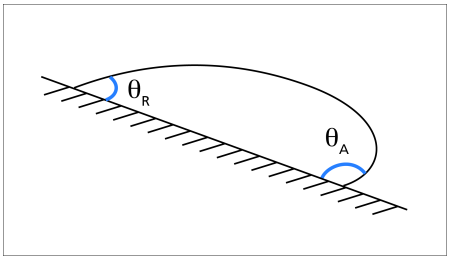

Figure 12: Contact angle hysteresis in a tilted droplet. The advancing contact angle (θ_A) is the maximum stable contact angle and the receding contact angle (θ_R) is the minimum. The equilibrium contact angle discussed above is between these two values.

Table 1: Various liquid contact angles on the surface of nitrocellulose membranes [92]

Membrane pore size (μm)	Advancing contact angle theta A	Receding contact angle theta R
Non-porous	67°	46°
0.22 μm	51°	7°
3.0 μm	46°	7°

Both the contact angle and the liquid-air surface tension are factors in the capillary pressure, and also, together with gravity and droplet size, dictate the shape that a droplet will form on a surface. Generally, a small liquid volume will form a spherical cap, whereas a larger volume will be pulled down by gravity to form a puddle on the membrane surface [93]. The scale over which this transition occurs can be approximated by the Bond number, which compares the relative importance of curvature (surface tension) versus gravity [94]:

$$Bo = \frac{\rho g a^2}{\gamma} \qquad \text{Equation 12}$$

Where ρ is the liquid density, g is acceleration due to gravity, a is the droplet radius, and γ is surface tension. For Bo ~1, the relative importance of gravity and curvature are comparable. For water, a droplet radius of ~2 mm, gives Bo ~1, and this length scale is referred to as the capillary length scale for the air-water interface [94]. When examining printing processes, we are typically not interested in large liquid volumes—the largest volume that we consider is a hand-pipetted 1 μL drop, which is equivalent to 1 mm^3; in these cases gravity does not play a major role in governing the shape of a liquid drop spreading on the membrane surface. The droplet volume and the rate of droplet delivery do have a significant effect on the characteristics of printing however, because large volumes,

or even small volumes added in very quick succession will lead to larger and larger liquid caps forming on the surface, which changes the dynamics of imbibition.

Membrane pore size is another key parameter in determining the rate of liquid imbibition into a membrane. While smaller pores can induce a larger capillary pressure (see Equation 8), the also have larger fluidic resistance (Equation 9), leading to the inverse relationship between pore size and wicking rate that is expressed in the Lucas-Washburn Equation (Equation 6). Therefore, larger pores dramatically increase the rate of droplet imbibition. As discussed in 2.3, due to the comparatively high force generated by capillary pressure relative to gravity, gravitational effects are neglected when considering capillary wicking over the distances relevant to printing and imbibition in 2DPNs.

Evaporation is an essential component of printing—as the liquid carrying the printed solute evaporates; it leaves behind the printed material. Excessively fast evaporation can result in no printing, if drops evaporate before they hit the surface; or surface-only printing, if drops evaporate before they are imbibed into the porous material. However, when printing in a humidified chamber, the timescale of evaporation is slow (~minutes) relative to the other processes (~ seconds), so it can be considered independently from droplet deposition, spreading and imbibition [95]. Another effect of evaporation that must be considered is that evaporation primarily from the edges of a printed area can drive outward flow of solutes, resulting in a "coffee stain effect", if they are not adsorbed to the substrate [95].

Many specific cases of printing have been modeled, but each relies on a different set of assumptions and emphasizes a different aspect of the physics. A few studies are generally relevant to the case of printing onto nitrocellulose membranes, and can provide insights into the relative timescales of droplet delivery, spreading and imbibition for 2DPNs.

Denesuk et al. developed a mathematical model of a single droplet imbibing into a porous substrate, approximating the porous surface consisting of a set of vertical, unconnected pores. In this work, they considered two possible droplet imbibition modes: constant drawing area (CDA), where, after forming a spherical cap on the surface, the droplet maintains a constant contact area with the surface (Figure 13B); or decreasing drawing area (DDA), where the droplet radius decreases, maintaining a constant contact angle (Figure 13A) [89].

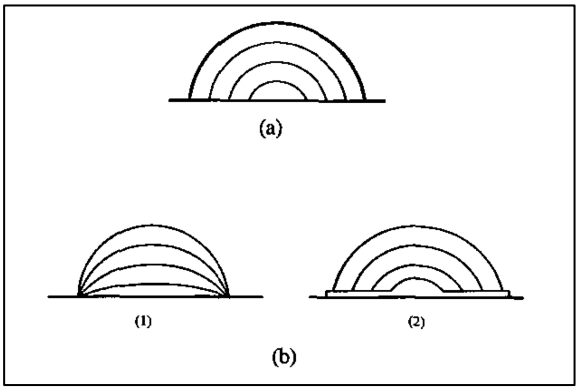

Figure 13: Denesuk et al. theorized two possible modes of droplet imbibition: A) Decreasing drawing area (DDA), where the droplet radius decreased, while maintaining a constant contact area, and B) Constant drawing area (CDA), where the contact area remained constant, either through (1) decreasing contact angle or (2) a thin film covering the porous surface, with a decreasing radius drop sitting atop the film. Figure from Denesuk et al. [89]

By their computation, the timescale of droplet imbibition in the constant drawing area case is:

$$\tau_{CDA} = \left(\frac{V_o}{r_d^2 \lambda}\right); \quad \text{where } \lambda \equiv \pi a_p \sqrt{\frac{\gamma \cos\theta R_p}{2\mu}} \qquad \text{Equation 13}$$

Where V_o is the initial droplet volume, r_d is the initial droplet radius, a_p is the area density of pores on the surface (approximately the porosity), γ is the liquid-air surface tension, θ is the liquid-solid contact angle, R_p is the pore radius, and μ is the liquid viscosity.

For the decreasing drawing area case, the timescale is simply:

$$\tau_{DDA} = 9\tau_{CDA} \qquad \text{Equation 14}$$

In this study, Denesuk et al. also extend their solution to an interconnected pore case, and show that interconnected pores simply decrease the droplet depletion time by a factor of 9 in both the CDA and DDA cases. When they compared this model to experimental results with a single liquid-membrane system, they observed that the droplet size decreased, and the timescale followed the DDA model. They theorized that other systems could exhibit CDA behavior, and it is challenging to predict *a priori* which will occur; however, the authors concluded that the CDA and DDA cases form an upper and a lower limit on the timescale of imbibition, which can be useful when approximating the timescale for other systems [89].

In their approximations, Denesuk et al. assumed that the droplet spreading process is much more rapid than imbibition, and therefore neglected spreading when calculating the approximate time for imbibition. Holman et al. followed up on the work by Denesuk et al. by arguing that droplet spreading and imbibition occur on similar time scales, and therefore added a droplet-spreading phase to their model. During the droplet-spreading phase the droplet shifts from a sphere sitting on the surface to a spherical cap while simultaneously imbibing into the porous material throughout the process. They observed that the pore size of the substrate material was a major factor in the rate of imbibition, and for larger pore sizes, the droplet fully absorbed into the substrate even before it had extended out to its equilibrium fully-spread diameter [87].

Building upon both Denesuk et al. and Holman et al., Hilpert and Ben-David developed a comprehensive model that includes droplet spreading, which they refer to as an "increasing drawing area" (IDA) phase; as well as the constant drawing area (CDA) and decreasing drawing area (DDA) phases (Figure 14), described by Denesuk et al. Hilpert and Ben-David argue that together these three phases can fully describe the spreading and imbibition processes, and one can approximate the stage at which imbibition begins, relative to spreading [86].

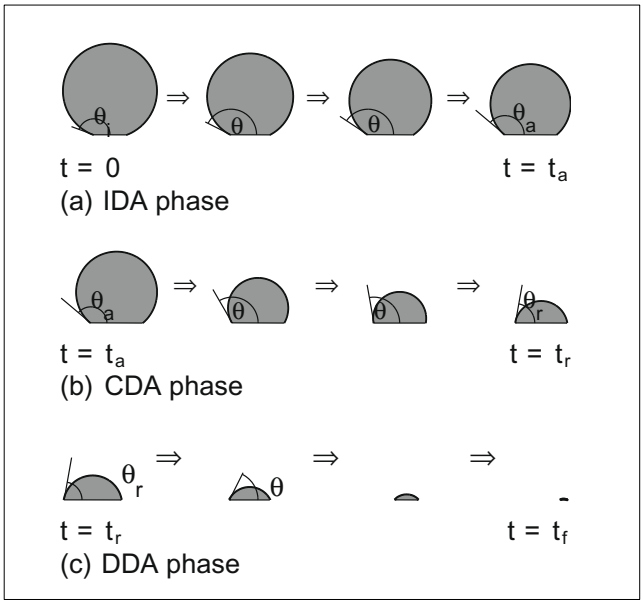

Figure 14: Phases of droplet imbibition into a porous medium. A) Increasing drawing area: as the droplet spreads on the membrane surface, the contact area between the droplet and surface increases, causing a corresponding decrease in the contact angle from the initial contact angle to the advancing contact angle. B) Constant drawing area: as the droplet is sucked into the membrane the contact area remains constant while the contact angle decreases from the advancing contact angle to the receding contact angle. C) Decreasing drawing area: as the droplet becomes very small, its contact area on the porous surface decreases to zero. This phase occurs once the contact angle has dropped below the receding contact angle. Figure from Hilpert and Ben-David [86].

Based on this review of the literature and comparing the rates of the different processes involved, we suggest 4 very simplified modes of printing, based on the relative rates of different processes (Figure 15). Rarely will one mode completely and accurately represent a real-life printing situation, but approximate characteristics of printing can be approximated by comparing the respective rates of liquid deposition, droplet spreading, imbibition, and evaporation. A specific application of these models to the phenomenon of printing on nitrocellulose membranes will be discussed in Chapter 3, in an effort to elucidate the details of that particular process which is relevant to 2DPN design.

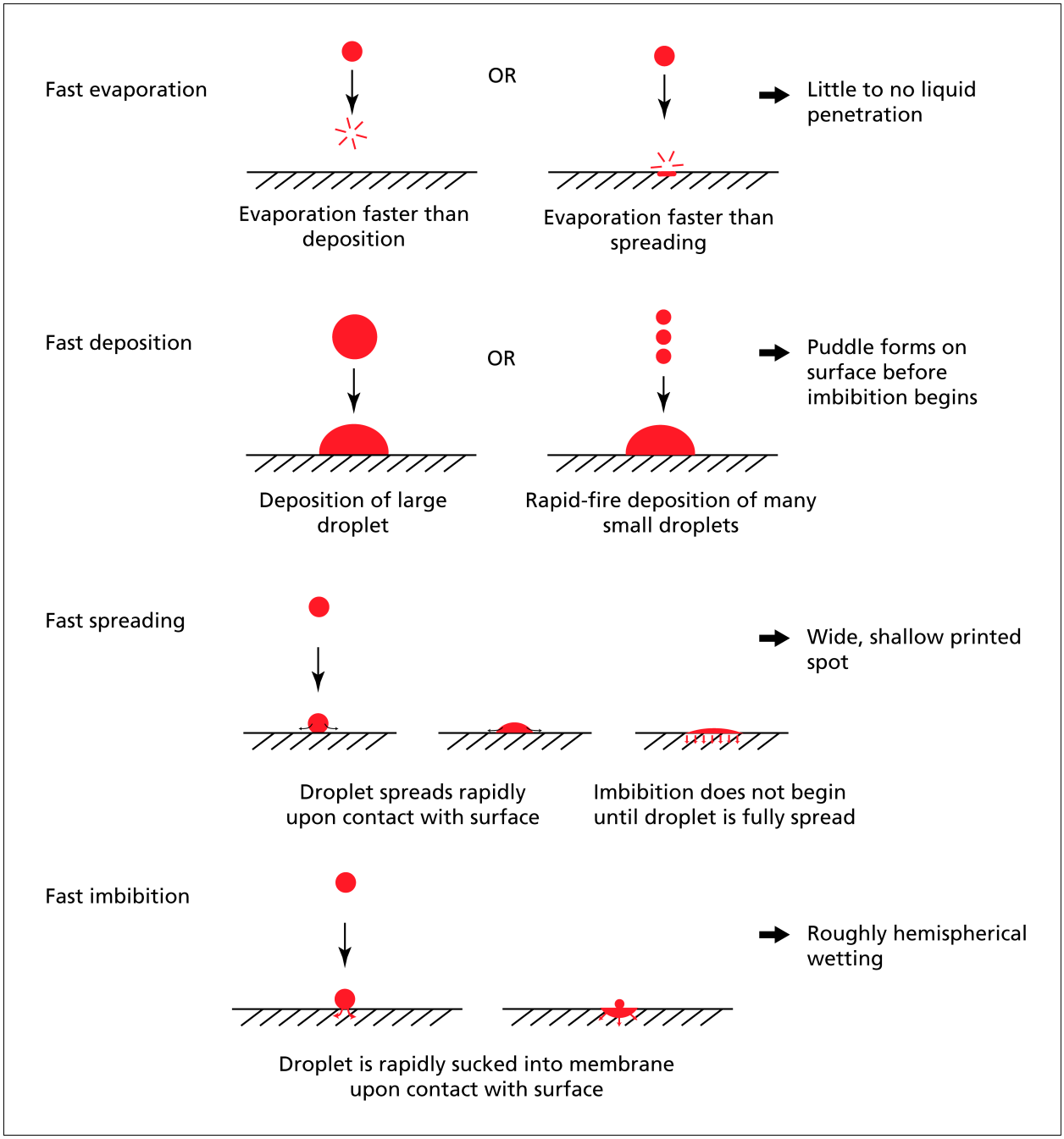

Figure 15: Simplified modes of printing, based on the relative rates of different aspects of the printing process. Any given real-life situation cannot be thoroughly described by just one of these simplified modes, however they can provide insight into approximate behavior.

For the reader who has an exceptional interest in printing models, the following references can provide more detail and nuance than is relevant to this dissertation [96-99].

Overall, the literature provides a foundation for understanding printing onto a porous substrate, though because all of the parameters describing a particular case are defined by that particular membrane-liquid interaction, each case must be evaluated to determine the flows and transport within that system. To understand reagent printing onto nitrocellulose for 2DPN design, we must investigate the particulars of that system, and develop a model of the flow and reagent transport during that process.

2.5 Reagent storage, rehydration, and patterning

A critical aspect of designing diagnostics for low-resource settings is to have all reagents included on the device in dry form. The use of dry reagents reduces user steps, removes the need for a cold chain, and facilitates device automation [44, 59, 100].

Generally, proteins lose function when they are exposed to high temperatures or dried in an uncontrolled process [101]. However, a wide body of research has demonstrated that trehalose (α-D-glucopyranosyl α-D-glucopyranoside) can be used to stabilize dried proteins for extended periods of time at elevated temperatures [101-105]. Sucrose (α-D-glucopyranosyl-(1→2)-ß-D-fructofuranoside) has also been used in some cases to store dried proteins [100, 101]. Because of the utility of these sugars for stabilizing proteins, the mechanism for this behavior has been thoroughly studied. It is believed that the high glass transition temperature of trehalose (106 ºC [106]) ensures this sugar remains in the glassy state with lower molecular mobility at elevated temperatures, thus protecting the protein against degradation and crystallization [101, 102, 105]. Furthermore, the hydroxyl groups of the sugar molecules substitute for the waters of hydration of the protein, which are lost upon drying, and act to preserve the protein's native conformation [101]. Sucrose and trehalose are both non-reducing disaccharides and are unable to undergo the Maillard reaction with amino acids, so they are suitable for long-term storage with proteins [107].

Because dried reagents are such an important consideration in the development of diagnostics for low-resource settings, several techniques have been developed for dry reagent storage and subsequent rehydration. Garcia and colleagues developed dry reagent storage cavities inset into the channel wall of a microfluidic device. Specifically, they demonstrated reconstitution of functional beta-galactosidase enzyme after 14 days of desiccated storage in these cavities, when dextran and trehalose were used as a carbohydrate matrix for preservation. Furthermore, they achieved spatial and temporal control of the rehydration of reagents by varying the shape and dimensions of the cavity, fluid flow rate, channel dimensions, and the chemical composition of the carbohydrate matrix [102]. Another method for the incorporation of dry reagents into microfluidic devices was demonstrated by Stevens et al., who stored gold-conjugated IgG antibodies on polyester conjugate pads enclosed in a microfluidic assay card. Upon rehydration the antibodies were used in an on-card flow-through immunoassay for malaria antigen. Different amounts of sucrose and trehalose were added to improve preservation, and they found that adding sucrose and trehalose at concentrations between 5%-10% retained 80-96% signal after 60 days of dry storage at 4°C, 20°C, and 40°C, with maximum signal preservation achieved when 5% of each sugar was used [100].

Conjugate pads have also been used to store detection reagents upstream of the capture line for later rehydration in lateral flow immunoassays [22] and they have been utilized more recently in 2DPNs [44]. However, the use of these separate pads has two significant disadvantages: it offers minimal control over the spatial and temporal release of rehydrated reagent, and it requires additional materials and components that add to manufacturing costs. Some recent developments have sought to address the latter of these concerns. Whatman, a subsidiary of GE Healthcare, has developed a porous substrate called Fusion 5

that is designed to function in all of the roles required in a lateral flow strip—conjugate pad, assay membrane and wicking pad [22]. Alternatively, Abe et al. have built upon past demonstrations in which locally patterned color-generating chemical reaction reagents on multiple outlet arms are used to detect small molecules such as protein, glucose, or sample pH [33, 37, 108, 109]. In particular, they have shown the ability to rehydrate and flow gold-anti-IgG antibody conjugate that had been hand-spotted and dried on blocked cellulose membranes and to use it downstream to detect IgG in PBS [110]. Their work is the first to use reagents rehydrated from cellulose, but still shows significant variability in the extent of conjugate rehydration, as well as relatively high background levels of nonspecific adsorption. Furthermore, these techniques for storing reagents directly on assay membranes do not offer control over the spatial and temporal profile of reagent rehydration. This is an area of research that still has potential to expand the capabilities and lower the costs of paper-based devices.

In addition to their work hand-spotting gold conjugate on cellulose, Abe and colleagues have demonstrated the utility of inkjet printing as a method for patterning channels and reagents in paper-based devices [109, 110]. The use of inkjet printers to apply reagents to biosensors has been a common method for functionalizing surfaces because it is rapid, uses low reagent volumes, can allow rapid parallel deposition of different reagents and does not risk damaging the surface through contact [111-113]. Specifically, piezoelectric inkjet printing is preferred over thermal inkjet printing for biological applications because the high temperatures (200-300°C) required by thermal printing can damage biomolecules [111]. However, Nishioka et al. observed decreased activity of the enzyme horseradish peroxidase when it was patterned using a piezoelectric printer due to the high compression forces exerted by the piezo crystal. The addition of glucose and trehalose protected the

enzyme through the formation of hydrogen bonding, resulted in negligible activity loss at lower compression rates [114]. Alternatively, in their study comparing ELISA well-printing methods, Lonini et al. observed no detectable difference in activity between enzymes pipetted by hand versus those printed using a piezoelectric printer [115]. These results are all consistent with piezoelectric inkjet patterning as a viable method for depositing reagents onto porous substrates for storage, particularly when sucrose and trehalose are added to reagents as stabilizers prior to patterning.

Inspired by the controlled rehydration techniques developed by Garcia et al. for microfluidics, and the high-precision afforded by piezoelectric printing methods, a portion of this thesis unites the existing technologies described here to develop a method for patterning reagents directly onto 2DPNs for storage and controlled rehydration.

2.6 Computational modeling of 2DPNs

As described above, mathematical and computational models are frequently used to predict behavior in traditional microfluidic devices and fluid dynamics in general [60, 64]. In the burgeoning field of paper microfluidics however, this type of modeling is only in the beginning stages. New models push the predictive capabilities available to paper microfluidic engineers, and enhance our conceptual understanding of how a variety of factors influence the behaviors of 2DPN devices.

Thus far, computational models of paper microfluidics have been built in Comsol Multiphysics (Comsol, Inc., Burlington, MA) using that software's built-in porous media package governed by Darcy's Law, characterized by a constant wetted region and constant volumetric flow rates (shown in Equation 7). Osborn et al. made significant advancements in the capabilities of paper networks by translated several fundamental microfluidic

applications to paper networks [15]. In the process, they developed a simple model clearly correlating fluidic resistance to volumetric flow rate, as predicted by Darcy's law [15]. This elegant match between mathematics and experimental measurement was a strong first step for effective computational modeling of paper devices.

By incorporating an iterative solver and a moving finite element mesh, Mendez et al. developed a model approximating the process of fluid wetting into paper devices, which is governed by the Lucas-Washburn Equation (Equation 6), rather than Darcy's Law. Furthermore, they demonstrated both experimentally and computationally that devices with widening geometries can yield quasi-steady linear flow velocity through in the main channel, even during the time-dependent Lucas-Washburn wet-out phase [116].

Another aspect of designing 2DPN devices is their sometimes-complicated geometry. To better understand flow profiles around corners of different types, Fu et al. modeled the transport of a dilute species within the porous material, and then compared the distribution predicted by the model to experiments tracking the position of a different-colored solute [39]. This model effectively predicted the flow and transport around a bend in a 2DPN and could be used in future device design—potentially reducing the number of experiments needing to be performed to optimize a particular geometry.

These three models are groundbreaking in the field of paper microfluidics because they bring a degree of predictive power to the engineering process for new paper-based assays. They are just a starting point however, in the broad range of modeling capabilities that could be used to understand the complicated systems that interact in paper microfluidic assays, and improve their "engineerability". Part of this thesis develops computational models of the transport of reagents and of binding interactions that occur in the assay

region of these devices. Other aspects of computational modeling are highlighted throughout this thesis—they are all instances where the development of a computational model of the system both improved our understanding and predictive power for future devices and experiments.

2.7 Conclusions

2DPNs offer many improvements in sensitivity and specificity of LFTs by integrating multiple assay steps and controlled fluidic handling. At the same time, the cost of materials, level of user training required and lack of external instrumentation all make 2DPNs more suitable for low-resource POC settings that existing microfluidic systems. These characteristics make 2DPNs a very promising platform for future POC diagnostic tests. However, the toolkit currently available to those wanting to integrate sophisticated 2DPN assays is lacking the predictive power of effective computational models, as well as tightly controlled reagent-deposition and rehydration techniques that could dramatically improve the versatility of these devices.

3 Characterization and modeling of printing onto nitrocellulose

3.1 Objectives and Motivation

Reagent deposition onto assay membranes is an essential step in 2DPN device fabrication, and this deposition process must be very well understood and tightly controlled to ensure that assays are sensitive, reproducible, and robust. As described in section 2.5, there are a variety of methods to deposit reagents onto assay membranes, and piezoelectric printing is particularly well suited for this purpose. There is a rich literature base with detailed information about printing onto porous media and the process of droplet imbibition into porous materials, which is reviewed in detail in Section 2.4. While that body of literature highlights many of the issues faced when printing reagents onto nitrocellulose materials and helps us to frame our understanding of the process of printing, it does not specifically describe the liquid and reagent transport that occurs during printing reagents onto nitrocellulose in our development of our 2DPN devices. Prior to implementing more sophisticated functions, it was necessary to formulate a basic understanding of printing onto our particular membranes. After characterizing the fundamentals of printing, a simple 3D computational model of fluid and reagent transport in porous media was developed using Comsol Multiphysics®.

This fundamental understanding and simple model were later used to develop a straightforward protein adsorption measurement technique (described in Chapter 4) and sophisticated methods to rehydrated reagents patterned and dried directly on nitrocellulose membranes (Chapters 5 and 6).

3.2 Description and characterization of droplet imbibition

Typically, multiple droplets are printed onto the same location, when printing capture lines in previous 2DPNs, to ensure that the liquid penetrated the entire depth of the membrane, and that protein solutions were distributed throughout the thickness. A common technique was to print 20-40 droplets per spot, with a line spacing of 250 μm between spots [44, 49]. To improve a variety of different aspects of printing, our objective was to better understand the flow of liquid and the distribution of solutes during that printing process. Later in this thesis, we will use that enhanced understanding to implement piezoelectric reagent printing in a more useful and targeted way in 2DPN design.

3.2.1 Experimental methods

Patterning and storage

To examine droplet imbibition into nitrocellulose membranes, multiple droplets were applied to the same location and the resulting spot was examined.

In order for the spotted area to be visible after drying, red food coloring (Safeway) was used as the spotting fluid, diluted 1:4 in deionized water and filtered through a 0.02 μm centrifugal filter. Previous work in our laboratory had shown that red food coloring does not adsorb to membranes, so it was believed to be a good marker for the total wetted area of liquid applied during printing. Food coloring was printed on a variety of nitrocellulose membranes using a Scienion S3 Flexarrayer (Berlin, Germany), with ambient humidity set to 50% relative humidity at room temperature (~68°F). Individual droplet volumes were approximately 450 pL, and were dispensed at 500 Hz. Each membrane was spotted with several different numbers of droplets arrayed across the membrane in triplicate.

The membranes used were: FF80HP, a backed membrane with 90 μm thickness and 0.77 porosity (GE Healthcare Life Sciences, Pittsburg, PA), and AE100, an unbacked membrane from the same manufacturer, who reports that similar manufacturing processes were used, except for the backing material, so similar parameters were assumed [117]. All membranes were placed directly onto the printing platform within the S3 enclosure. Additionally, because the Mylar backing material on backed membranes prevents evaporation from occurring from the backed surface, a comparable non-evaporative condition was desired from unbacked membranes. To achieve this non-evaporative condition, a piece of cellulose was saturated in water and placed on the printing platform, and then on top of this cellulose was placed a piece of window screen, and finally the unbacked membrane rested upon the window screen. The window screen separated the membrane slightly from the wet cellulose, allowing the underside of the membrane to experience near-100% relative humidity while not actually wetting the membrane and interfering with the printing process.

After spotting, all membranes were placed into Mylar envelopes for storage, and kept in a desiccator overnight before imaging, and then thereafter in the Mylar envelopes in ambient laboratory conditions.

Image acquisition and quantification

Spotted membranes were scanned using a flatbed scanner (Epson Perfection V700 Photo, Epson, Long Beach, CA) with image gamma set to 1. Scanned images were saved as 16-bit tiff files, with 600 pixels per inch. All membranes were scanned from both the top (printed) side and the bottom side, and the sizes of spots were compared to evaluate outward wicking during the spotting process.

Images were quantified in ImageJ (U.S. National Institutes of Health, Bethesda, MD [118]). The spot area quantification protocol proceeded as follows:

1. Color channels of each of the images were separated. The blue channel had been determined to have the highest contrast between spots and background, so for each image, it was saved as a separate file for evaluation.
2. All images were converted to 8-bit color.
3. The front side of the backed membrane was selected as the "standard", and it was used to determine the background threshold by quantifying the average pixel intensity of the blue channel image, then adding 3x the standard deviation of the pixel intensity. This threshold value was evaluated to be 181.
4. All images were thresholded to black and white using 181 as the threshold.
5. Spots were detected using the "Analyze Particles" function in ImageJ. Rarely, a piece of lint or dust was detected as a particle, but these falsely-detected spots were disregarded.
6. Spot areas were quantified in pixels and then converted to millimeters using 600 px/in, and 25.4 in/mm, resulting in a linear conversion of 23.6 px/mm, and 558 px^2/mm^2.

3.2.2 Results

Initial observations during printing confirmed that red food coloring does not adsorb to the membranes during imbibition and spotting, and therefore the resulting dry red spot illustrates the total wetted area of a given printed volume.

AE100

The size of spots visible on the front (printed) and back side of the AE100 unbacked membrane were compared (Figure 18). At very low volumes (1-5 drops) spots were only visible from the front of the membrane and not the back. This observation is not surprising: the droplets initially wet the membrane in a hemispherical shape, and at low volumes, the underside of the hemisphere has not yet reached the back side of the membrane (Figure 16A). At slightly higher volumes, the spots become visible from the back side but still are much smaller than when viewed from the front side. Again, this is not surprising: the hemispherical wetting area has transitioned to a truncated hemisphere (Figure 16B) that is smaller when viewed from below. Finally, at a later point in the wetting process (50 drops), we observe that the spot sizes become equal when viewed from the top and bottom. This occurs as the truncated hemisphere wetted region transitions to a cylinder-shaped wetted region when a large enough volume is applied that the surface tension and capillary pressure at the wet-dry boundary attempt to minimize the interfacial area (Figure 16C). The image of printed spots is shown in Figure 18.

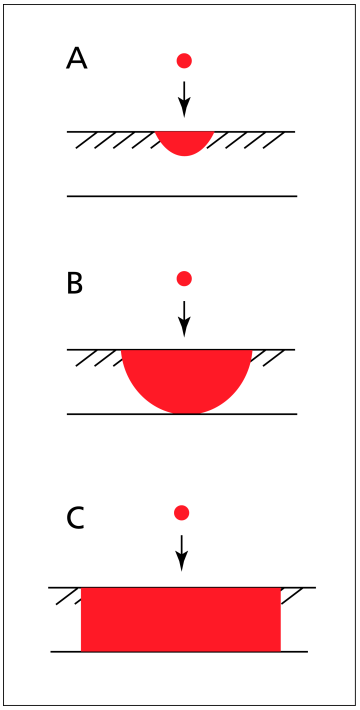

Figure 16: Side view schematic of droplet wicking through a porous material. A) Initially the droplet occupies a hemispherical volume in the membrane. B) Once the wetting front reaches the bottom side of the membrane, the wetted volume is a truncated hemisphere. C) Eventually the wetted area becomes a cylinder.

FF80HP

Quantifying the spot size on the backed FF80HP membrane was initially similar to the unbacked AE100. At small volumes, spots are not visible from the back side, and then as

spots become visible on the back side, they still remain smaller than the same spots when viewed from the front (Figure 18). However, with the FF80HP membrane, there is only a short range of volumes for which the spot sizes area equal when viewed from the top and bottom, where the wetted region is a cylinder-shape. For larger spot volumes (~20 drops, or roughly 8 nL) on the FF80HP membrane, spots begin to be *larger* when viewed from the underside (Figure 17). We hypothesized two possible explanations for this behavior: first, the lack of evaporation from the underside allows liquid to wick slightly further on the backed side of the membrane; and second, water at the interface between the nitrocellulose and the Mylar has a lower contact angle than at the air-nitrocellulose interface at the top of the membrane, allowing it to be energetically favorable for the liquid to redistribute and creep further along the backed side of the membrane.

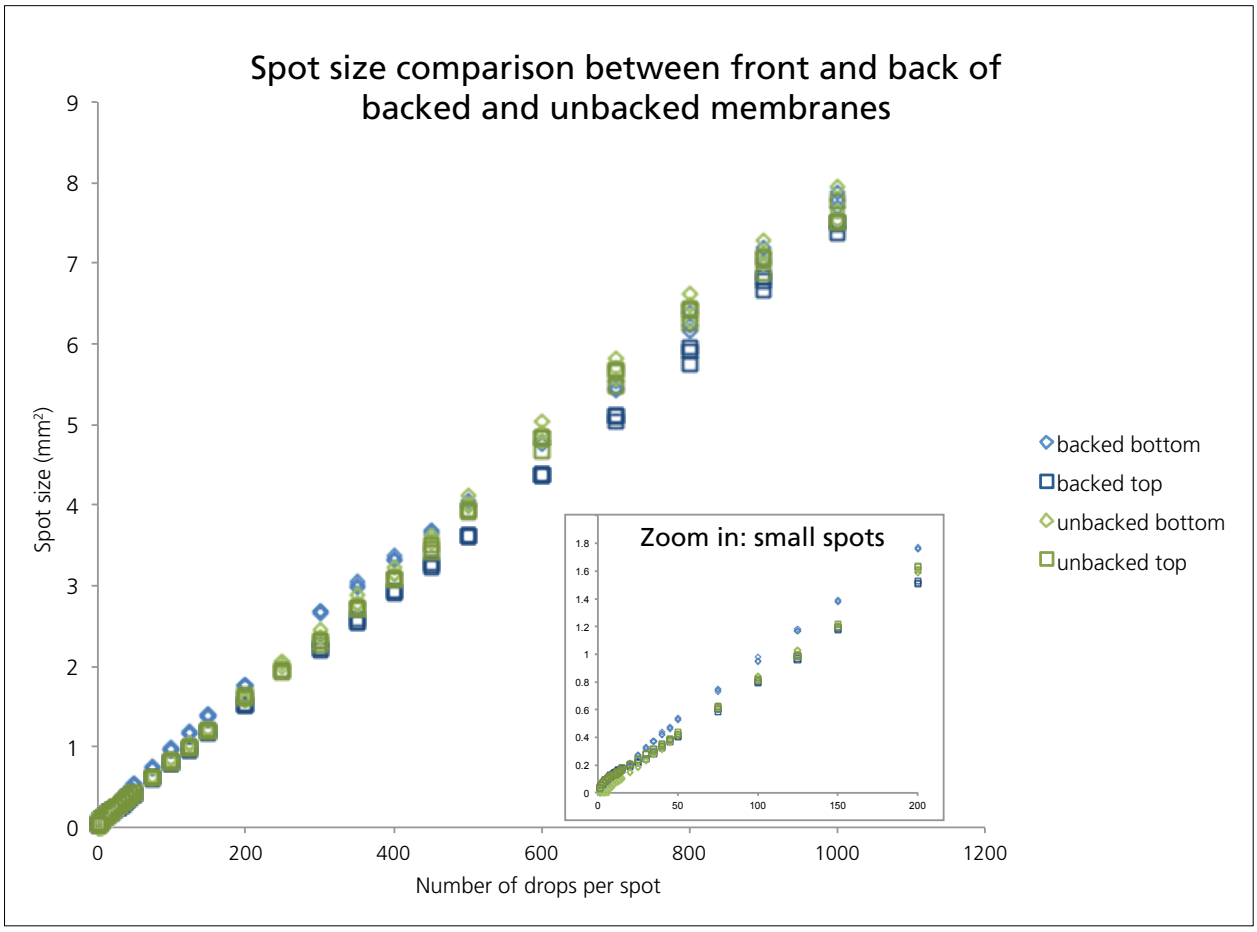

Figure 17: Quantification of spot sizes resulting from printing on backed (FF80HP) and unbacked (AE100) membranes. Inset shows a magnified view of spots ranging from 1-200 drops per spot. Oddly, the back side view of moderate-size spots on backed membranes are much larger than the top-side view. This phenomenon was explored further by humidifying the underside of unbacked membranes to generate a "non-evaporating" back side of the membrane, analogous to the non-evaporative condition on the back of a backed membrane.

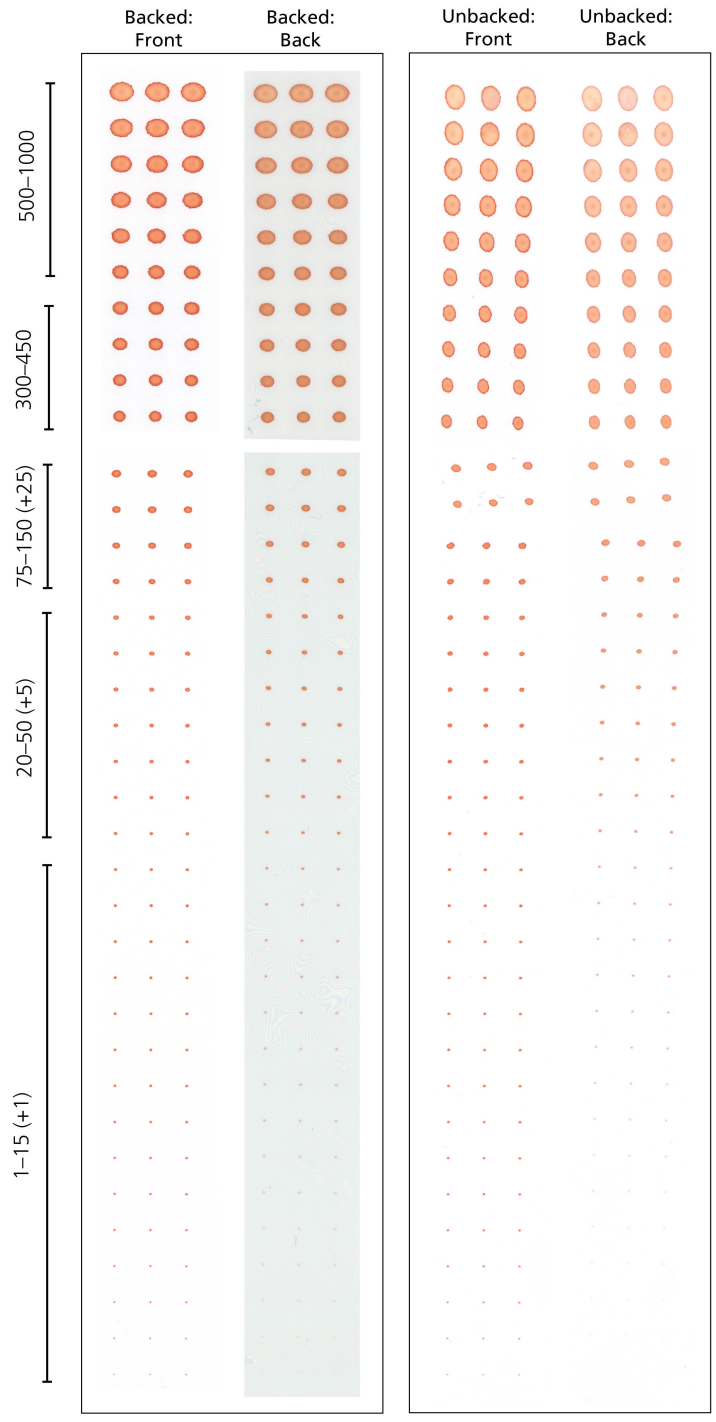

Figure 18: Red food coloring printing series. Comparison between front and back sides of backed (FF80HP) and unbacked (AE100) membranes. Number of droplets printed at each spot are indicated at left. When viewed from the top side, spots are visible (though faintly) down to a single droplet. However, from the bottom side, the spots are not visible until multiple droplets have been printed.

Non-evaporating AE100

The “non-evaporating” unbacked condition was devised to evaluate these two different explanations. If a lack of evaporation on the underside of the membrane were primarily responsible for larger wetted areas on the underside of the membrane, an unbacked membrane thoroughly humidified from the underside would also yield larger spots when viewed from the underside. In this non-evaporating unbacked case, spots were slightly larger when viewed from the underside, but not nearly as dramatically so as in the case of the backed membrane (Figure 19). This observation leads us to the conclusion that both humidity and the Mylar-nitrocellulose interface cause the enhanced wicking on the under side of the membrane.

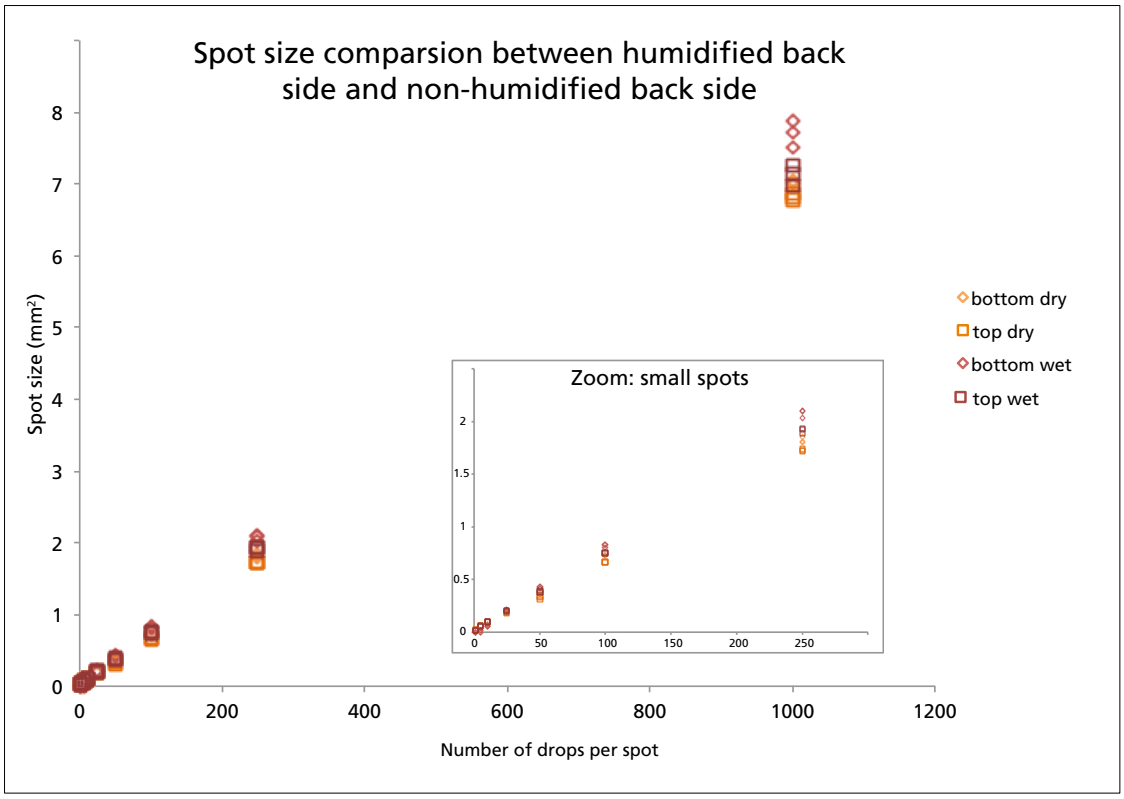

Figure 19: Quantification of spot sizes in the non-evaporating unbacked case, compared to an unbacked membrane without the underside humification. While the humidification does increase the back side spot size relative to a non-humidified case, the difference is not as pronounced as occurs on backed membranes.

3.3 Computational model of flow during printing

Building a computational model of printing onto our nitrocellulose membranes served two purposes: first, we hoped to simplify the complex printing process in such a way that we could represent the flow profile of liquid wicking into the membrane during printing. The second goal was to use our understanding of the flow during printing to later model protein adsorption during printing, which will be discussed in Chapter 4.

The first step in characterizing piezoelectric printing of our solutions onto nitrocellulose was to compare the approximate rates of the four sub-processes of printing: droplet delivery, spreading, imbibition, and evaporation.

Droplet delivery

The S3 piezoelectric printer was set to dispense droplets at 500 Hz, with droplet volumes of roughly 500 pL. These values imply a liquid delivery rate of 250 nL/sec, and 2 ms between droplets. If droplet imbibition into the paper is slower than 2 ms, liquid will build up on the surface; if imbibition is faster than 2 ms, no liquid will build up.

Spreading

There is an entire literature based on droplet spreading phenomena, which will not be discussed here. However, Radke et al. have written an excellent textbook on the subject [92], which points to several other references on that subject.

For the purposes of estimating the rate of droplet spreading during printing on nitrocellulose, we will simplify by calculating the rate of a single printed droplet spreading to a spherical cap on a non-porous substrate. The fully-spread radius of the spherical cap will be approximated by the equilibrium contact angle, estimated as 30°, based on the data from Table 1. Using a droplet volume of 500 pL, the spherical cap radius will be 210 μm.

To calculate the time required for a droplet to spread to this spherical cap shape, we use the solution presented in Chapter 3 of Radke et al. regarding the kinetics of droplet spreading, for droplet radius as a function of time [119]:

$$R(t) = 0.65\lambda_c \left(\frac{\gamma V^3}{\mu}\right)^{0.1} (t + t_{in})^{0.1} \qquad \text{Equation 15}$$

Where $R(t)$ is the droplet spreading radius as a function of time, λ_c is a characteristic constant that is ~1 [119], V is the droplet volume, and t_{in} refers to the duration of the rapid inertial phase of spreading in which the droplet hits the surface, which is very small

relative to the time of viscous spreading. Based on this calculation, we estimate the time required for complete droplet spreading to be 1.2 seconds. It is important to note however, that due to the R^{10} dependence of this function, early spreading is very rapid—the time to spread to R=100 μm is 0.0007 seconds, and the time to reach a hemispherical cap with R=60 μm is only 4.4×10^{-6} seconds.

Imbibition

To estimate the timescale of droplet imbibition only (neglecting spreading effects), we use the expression developed by Denesuk et al. (discussed in Section 2.4) for droplet imbibition time. However, since the extent of droplet spreading significantly impacts droplet imbibition time, we have calculated a few different imbibition times, which represent approximate bounds on the rate of imbibition. Recalling Figure 15—if imbibition is rapid relative to spreading, the imbibition contact area will be small, whereas the case of complete spreading prior to imbibition will lead to a larger imbibition contact area. Additionally, Denesuk et al. present two modes of imbibition: constant drawing area (CDA) and decreasing drawing area (DDA) to describe the shape of the droplet as it retracts and is drawn into the paper (recall Figure 13), so approximate imbibition times were calculated for both of these regimes. These calculations are presented in Table 2, along with the corresponding times to spread to a given radius as described in the previous section (refer to Equation 13 and Equation 14).

Table 2: Comparison of the timescales of droplet spreading and imbibition

Radius of contact area	τ_{CDA}	τ_{DDA}	$\tau_{spreading}$
40 μm (< hemisphere)	$8.8x10^{-5}$ s	$7.9x10^{-4}$ s	7.7×10^{-8} s
60 μm (hemisphere)	$1.7x10^{-5}$ s	$1.6x10^{-4}$ s	4.4×10^{-6} s
100 μm	$2.3x10^{-6}$ s	$2.0x10^{-5}$ s	$7.3 x10^{-4}$ s
210 μm (full spreading)	$1.2x10^{-7}$ s	$1.0x10^{-6}$ s	1.2 s

Comparing these imbibition times with the droplet spreading times, it is clear that imbibition is slower than spreading initially, but because the spreading process slows dramatically, imbibition because much more rapid when R~100 μm. Both spreading and imbibition occur simultaneously until the droplet is full absorbed into the membrane, but as a simplification, we approximate that the first few droplets arriving at the membrane will spread to roughly 100 μm and then absorb into the membrane at that wetted radius, forming a near-hemispherical wetted area.

This imbibition analysis is specifically considering early droplets getting sucked into the membrane, and it is apparent that both droplet spreading and imbibition are much more rapid that droplet delivery by the piezoelectric printing nozzle. However, as more and more droplets are deposited in a single location, the wetted area expands (Figure 16), increasing the fluidic resistance to capillary flow (as expressed in Darcy's Law, Equation 9). By integrating the resistance imposed by a given wetted area, we can determine the volumetric flow predicted by Darcy's law, to approximate the change in imbibition rate with the increase in wetted area, and thereby compare the decreasing imbibition flow rate with the rate of droplet deposition.

Initially, we approximate the wetted area is a hemispherical shape (Figure 16A), with an increasing radius of wetting r_w. The fluidic resistance of this expanding hemisphere can be calculated based on Equation 9 with the integral:

$$R_{visc} = \frac{\mu}{2\pi\kappa}\int_{r_0}^{r_w}\frac{dr}{r^2}$$

Where r_0 is the initially wetted radius (approximated as 60 µm because that is the hemispherical radius for a 500 pL droplet), and r_w is the variable wetted front. The initial wetted radius is needed because resistance is undefined for $r = 0$. Dividing the capillary pressure by this resistance yields the volumetric flow rate for hemispherical wetting drawn by capillary pressure:

$$Q = \frac{\Delta P_{cap}}{R_{visc}} = \frac{4\pi\gamma\cos\theta\,\kappa}{r_{pore}\mu}\left(\frac{r_0 r_w}{r_w - r_0}\right) \qquad \text{Equation 16}$$

This flow rate applies until the wetting front reaches the bottom side of the membrane, when r_w is equal to the membrane thickness, or approximately 100 µm, at which point the wetting shape transition to a truncated hemisphere (Figure 16B). For simplicity however, we will assume that the wetted area shape skips the spherical section phase and goes directly to a cylindrical wetting area (Figure 16C). The fluidic resistance of a wetting cylinder is described by the following integral:

$$R_{visc} = \frac{\mu}{2\pi\kappa h}\int_{r_0}^{r_w}\frac{dr}{r}$$

The capillary pressure divided by this resistance yields the volumetric flow for an outwardly wetting cylinder:

$$Q = \frac{\Delta P_{cap}}{R_{visc}} = \frac{2\pi\gamma \cos\theta\, \kappa h}{r_{pore}\mu}\left(\frac{1}{\ln\left(\frac{r_w}{r_0}\right)}\right) \qquad \text{Equation 17}$$

We can define the overall volumetric flow rate as a piecewise function described by Equation 16 for 60µm < r_w<100 µm; and Equation 17 for r_w >100 µm. Using approximate values for our nitrocellulose materials that were determined experimentally by Joshua Buser in our laboratory, this volumetric flow rate can be plotted for the range of wetted radii applicable to our droplet printing experiments, and then compared to the rate of droplet deposition by the piezoelectric printer (~250 nL/s), to determine if liquid pools on the surface at any point in our printing process. As shown in Figure 20, the capillary-driven

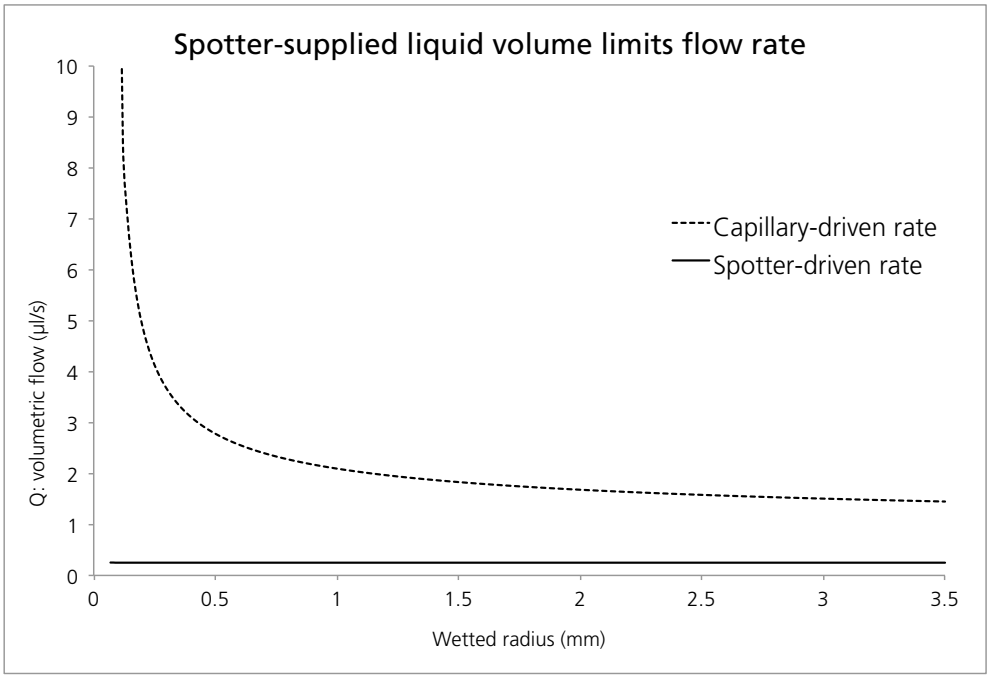

Figure 20: Comparison of the capillary-pressure-driven volumetric flow rate and the spotter-driven rate of liquid deposition (250 nL/s). It is clear from this graph that as the wetted area expands radially outward, liquid flow rate is limited by the volume supplied by printing, not by capillary flow.

volumetric flow rate (dashed line) is much larger than the rate of droplet delivery to the membrane (solid line), which implies that droplets do not pool on the membrane surface and that the flow rate within the membrane is actually limited by the rate of droplet deposition rather than capillary flow.

Evaporation

Using the built-in droplet camera with time-controlled strobe illumination, drops can be visualized at different points as they are dispensed from the nozzle. When the strobe is set to 200 μs delay, droplets are observed 450 μm from the nozzle tip, leading to a droplet velocity of 2.25 m/s. The paper substrate is typically 1 mm or less from the nozzle tip during printing, so the time required for a droplet to hit the surface is 0.4 ms. As with other aspects of droplet studies, droplet evaporation rates have been studied in great detail. We will use the droplet evaporation calculations presented by H.J. Holterman [120], in *Kinetics and evaporation of droplets in air*. Their Equation 54 approximates the lifetime of a small droplet. Based on 50% humidity, ambient temperature of 20°C, and an initial droplet diameter of 95 μm, the droplet lifetime is 16 seconds, much, much longer than the time required for the droplet to hit the surface and be completely absorbed. For these reasons, we have determined that it is acceptable to neglect evaporation for this analysis.

3.3.1 Model components and parameters

Physics

This computation model of printing uses the Darcy Flow module in Comsol Multiphysics (Comsol, Inc., Burlington, MA), governed by Darcy's equation for flow in porous media (refer to section 2.3, Equation 11). However, because the flow of liquid during printing is limited by the supply of droplets to the surface (as described above), the capillary pressure of the membrane does not control the flow rate throughout the membrane. Instead, the

total volumetric flow rate is constant, and equal to the printing rate, in our case, approximated to 500 pL at 500 Hz, or 250 nL/second. It is important to note here that the Darcy flow module in Comsol does not include a mathematical description of the air-water interface that occurs during wetting, however, because the flow rate is constant in time, the liquid-air front does not need to be tracked mathematically. Instead, the Transport of Dilute Species module was used to simulate the transport of a solute (e.g. food coloring) that is introduced to the model membrane at that constant flow rate supplied by the printer. Then, these model-generated spot sizes were compared to experimental results.

Geometry

The model geometry is shown in Figure 21. A 2D axisymmetric geometry was chosen to represent the radially spreading droplets. The height of the model rectangle, h, represents the thickness of the membrane. The length of the inlet line (dashed line with Q = 250 nL) represents the radius of the zone where the droplet contacts and imbibes into the membrane (as described in 3.3. above).

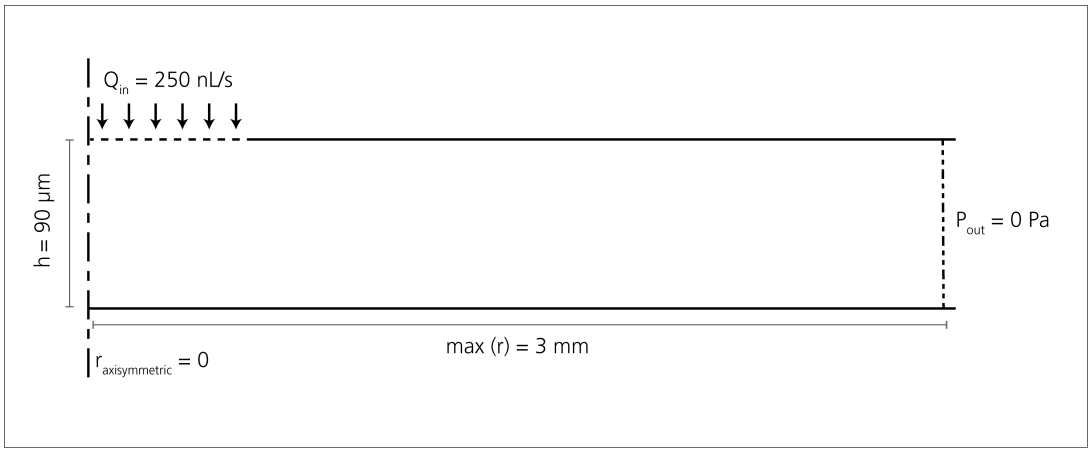

Figure 21: Schematic of model geometry

Parameters

Several parameters that govern wicking and printing are used in this model. These key parameters are listed in Table 3.

Table 3: Input parameters used in printing model

Parameter name	Parameter symbol	Input value*
Membrane thickness	h	90 µm
Porosity	ε	0.77
Droplet volume	V_d	500 pL
Spotting rate	f_d	500 Hz
Droplet inlet radius	r_{inlet}	100 µm

* input values of membrane parameters were based on experiments performed by Joshua Buser; input values of spotting parameters were determined based on spotter settings; droplet inlet radius was approximated as described above

Parameters describing the membrane itself, such as the porosity (ε) and membrane thickness (h), control the size of the resulting spots for a given set of spotting parameters. Membrane parameters that do not impact the void volume of the membrane, and instead govern capillary flow rates within the membrane, such as permeability and capillary pressure, do not actually impact this model, because flow is completely limited by the printed supply of liquid. Parameters of the printing process, such as the droplet volume and droplet-printing rate, govern the rate at which the spot expands over time on a particular membrane. One very important note however, is that this model only applies in situations in which flow is limited by the supply of liquid via printing; in cases where liquid is supplied more rapidly than capillary flow can wick it away, liquid droplets build up on the surface of the membrane resulting in imbibition that is not as simply defined and can not be described with this computational model.

3.3.2 Comparison of model to experimental results

Though this model makes mathematical and physical sense, it would be strengthened by a comparison to experimental data. Other researchers in our laboratory have developed methods to characterize membrane parameters, such as porosity, thickness, capillary pressure and permeability [73], so these parameters were used as model inputs. The resulting model results were then compared with the experimental results from the red food coloring spotting experiments, by evaluating the model-predicted spot areas with the observed spot areas. This comparison is illustrated in Figure 22, which clearly demonstrates a very close match between the experimental data and model predictions.

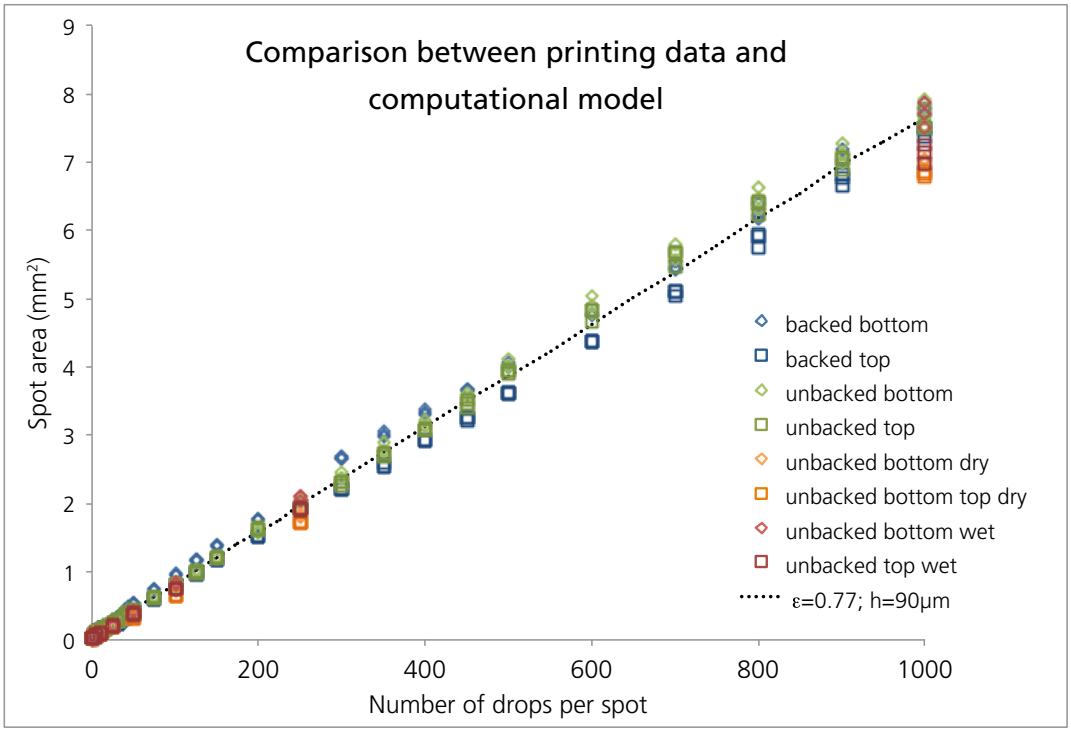

Figure 22: Plot of experimentally determined printing spot area (colored markers) compared to computational model (black dashed line). The computational model was run using experimentally determined membrane parameters for the backed FF80HP: porosity (ε) of 0.77 and thickness (h) of 90 μm. As mentioned previously, the unbacked membrane (AE100) is reported to be fabricated using similar processes and formulations, so it should not be surprising that the behavior is similar. The orange and red markers are data points from the humidified/non-humidified unbacked membrane experiments, and are reproduced here for a complete comparison.

Given the close match between experiment and model predictions, we can begin to use the model to better understand behavior in the printing system. One useful output of this model is the velocity field through the wetted space, which is shown in Figure 23.

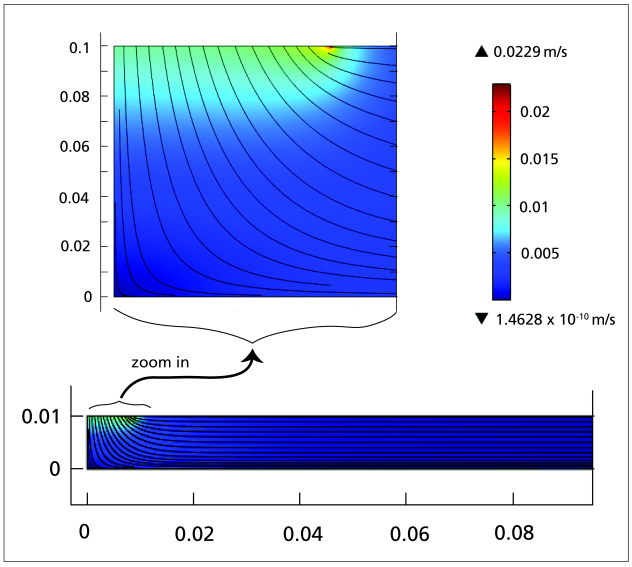

Figure 23: Comsol-predicted radial velocity field through the membrane given constant volumetric flow of 350 nL/s at the inlet.

3.3.3 Probing model parameter space

One useful function of this simple model is to examine how spot size varies as different model parameters are varied, to determine the effect that different membrane parameters have on the resulting spot sizes during printing.

The two membrane parameters that dramatically impact the spot area occupied by a given spotted volume are the porosity and thickness of a membrane. Intuitively, it is clear that a lower porosity membrane will result in larger apparent spots because the porous matrix has less void volume and therefore the same volume of liquid would spread out further. Similarly, a thinner membrane will result in larger spots for the same liquid volume, because there is simply less void space in a thinner membrane. An interesting and useful

feature of the spotting model, however, is that it allows us to explore how changing these two parameters simultaneously will affect spot size. Figure 24 illustrates the resulting differences in spot size when the porosity and thickness of the model membrane are varied across the range typically observed in the nitrocellulose assay membranes that our group uses.

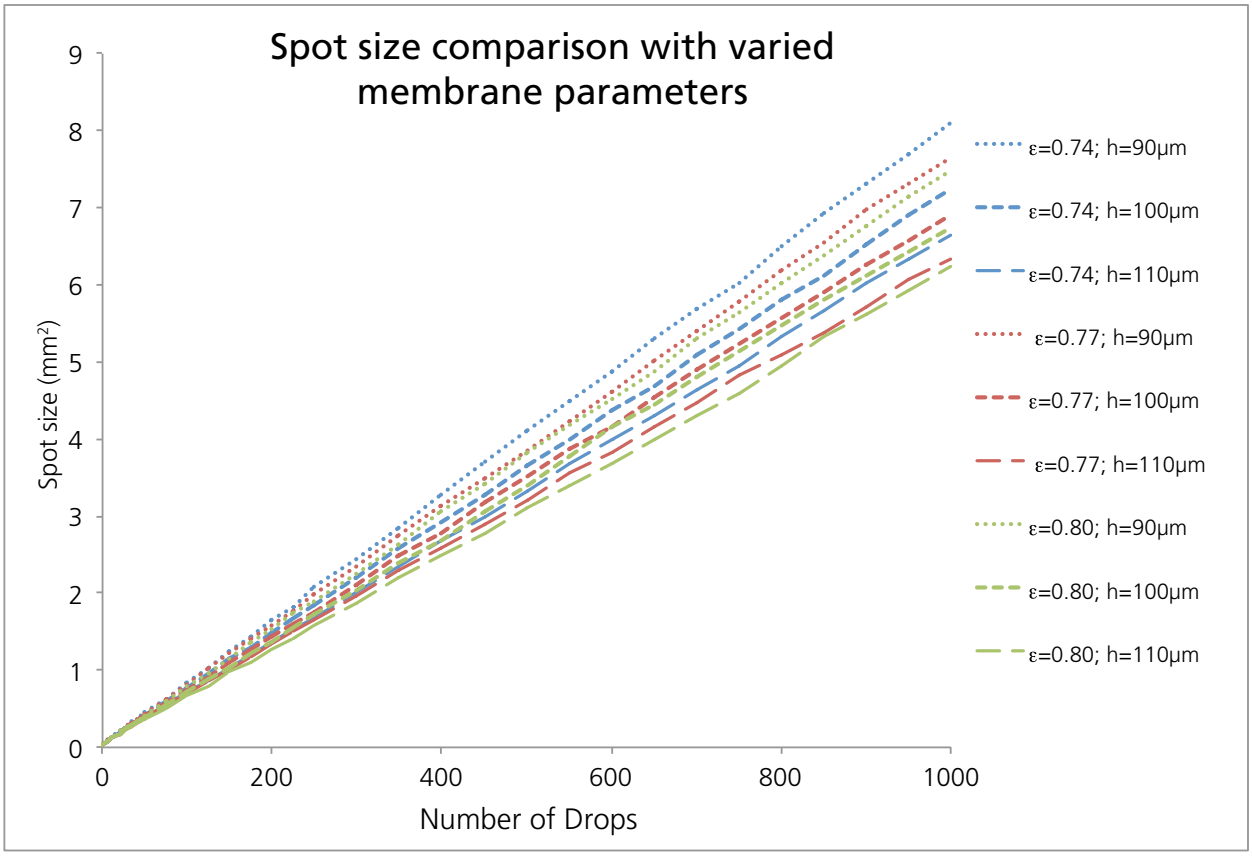

Figure 24: Model-generated spot areas, based on different membrane input parameters. Unsurprisingly, thinner membranes lead to larger spots, as do lower porosity membranes, due to the decrease in void volume available for liquid to occupy.

3.4 Conclusions

Chapter 3 has presented a thorough quantitative analysis of printing in nitrocellulose membrane materials, a computational fluid dynamics simulation of flow during printing, and experimental data that support the computational model. Though printing red food

coloring is not used in our devices, these experiments and models have deepened our understanding of printing on that materials used for designing 2DPNs. The understanding gained in the work was essential for the development of subsequent methods, and the model was later expanded to the more sophisticated model described in Chapter 4. Overall, the work presented in Chapter 3 is the foundation upon which Chapters 4, 5 and 6 are built.

4 Quantification and modeling of protein adsorption to nitrocellulose

4.1 Objectives and motivation

Nitrocellulose has long been known for its capacity for biomolecules to adsorb to its porous surface [121-123]. This well-known characteristic later led to nitrocellulose membranes becoming the fundamental substrate for lateral flow immunoassays [22], ranging from pregnancy tests to rapid diagnostics for infectious disease. Despite this common application in protein assays, the protein-binding capacity of nitrocellulose is not well understood, nor has it been characterized in a meaningful or quantitative way. We have sought to develop a set of simple and quantitative methods to probe and evaluate a wide variety of protein-nitrocellulose interactions. The path to a straightforward protein adsorption assay was not straight or simple, however, and a wide variety of strategies were approached in this process. These unsuccessful methods will be discussed briefly, to help future graduate students avoid dead ends or wasted time, and to better illustrate the rationale and necessity of the methods that, in the end, proved quite effective for the purposes of quantifying protein adsorption in the context of assay design.

4.2 Early attempts to quantify protein adsorption to nitrocellulose

Surface plasmon resonance of proteins adsorbing nitrocellulose films

Surface plasmon resonance (SPR), a well-established technique commonly employed to quantify binding interactions, was investigated in an initial attempt to yield quantitative on- and off-rates of protein adsorption to nitrocellulose films. In brief, the fundamental principle of SPR is that a gold film absorbs light of a very precise wavelength (the *resonance* wavelength) creating an electromagnetic *plasmon* of electrons that extends roughly 100-500 nanometers beyond the edge of that gold film [124, 125]. The particular wavelength that is absorbed is dependent on the index of refraction of the material

neighboring the gold film. When the index of refraction of that nearby material changes a tiny fraction, the resonance wavelength that is absorbed by the gold film also changes. (As an aside, some SPR instruments vary the angle of incidence of the light, and measure differences in the resonance *angle*, but this is based on the same principle). This change can be detected and measured [124, 125]. For binding assays, this technique is so sensitive that one can quantify the on- and off-rates of binding of an antibody to a protein immobilized on the gold surface, and has been thoroughly characterized and is now commonly used for on- and off-rate measurements [57, 125-127].

Because it is so frequently used to measure binding interactions, we believed that SPR could yield similarly quantitative data about protein adsorption to nitrocellulose surfaces. However, the nitrocellulose membranes used in our lateral flow 2D paper network assays are approximately 100 μm thick—close to 1000x the relevant thickness of the gold surface plasmon. To overcome this problem, our collaborators, Cathryn Olson and Vicki Watkins, at GE Global Research (Niskayuna, NY), developed a protocol to spin-coat a dense (non-porous) film of nitrocellulose onto the gold slides used in SPR. These films were characterized thoroughly using ellipsometry, atomic force microscopy, and x-ray photoelectron spectroscopy, they were determined to be 10 nm thick (+/- 1 nm), sufficiently thin for effective SPR.

SPR experiments were performed in a Biacore T100 (GE Healthcare, Pittsburg, PA). Nitrocellulose-coated SPR slides were equilibrated with pH 7 HEPES buffered saline (HBS) for 2 hours prior to exposing them to any protein, to ensure than no false signal would be observed as the film swelled or shrank in the new buffer solution. Afterward, IgG (ChromPure whole mouse IgG, Jackson Immunoresearch, West Grove, PA) was introduced to the chip; a different concentration was flowed through each of the four separate channels

of the instrument. Unfortunately no signal was observed, even at the highest concentration (1 μM). To troubleshoot this lack of binding, a varying-pH series of binding assays were performed at 87 nM in a series of acetate buffers (see Figure 25A). Varying the flow buffer pH resulted in some binding observed at pH values of 5 and below. One set of SPR experiments at varying concentrations of IgG was performed at pH 5 in acetate buffer and three concentrations of IgG (10 nM, 100 nM and 1 μM, plus a no-IgG control).

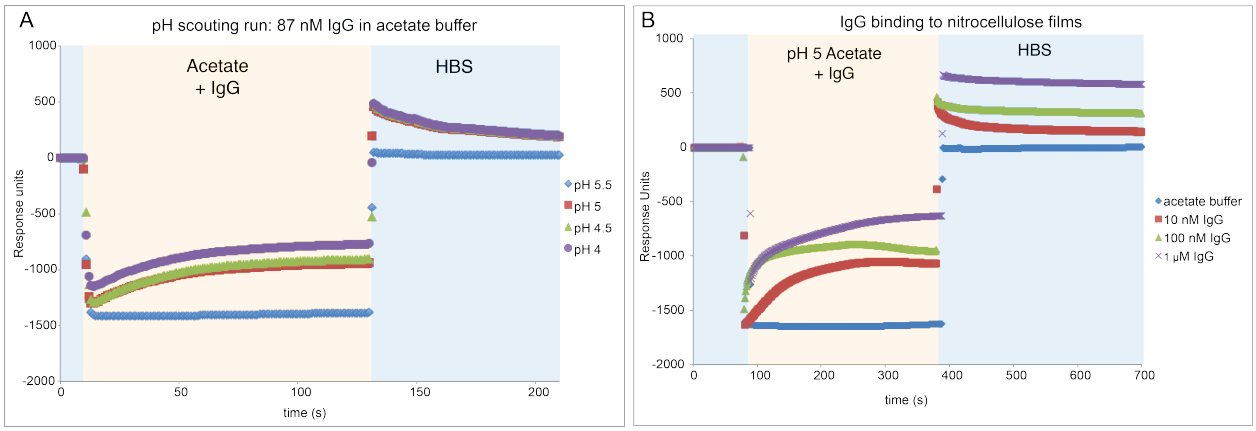

Figure 25: SPR results illustrating pH-dependent IgG adsorption on nitrocellulose dense films. Films were spin-coated on SPR slides to 10 nm thickness by collaborators at GE Global Research. HBS buffer was used as the SPR system fluid, and because HBS has a different refractive index from acetate buffer the signal jumps between two baselines when the buffers are switched. To facilitate interpretation, the background of the graphs has been shaded according to the buffer that was in the system at that time: orange indicates acetate and blue indicates HBS. A. A pH-scouting run was performed because initial adsorption experiments at pH 7 yielded no observable adsorption. This pH-scouting run showed that at pH 5 and below, IgG adsorbed to the nitrocellulose film, but at pH 5.5, no adsorption was observed. B. Because of the pH-dependence, the next set of experiments were performed in acetate buffer at pH 5. This set of experiments showed some concentration-dependence of adsorption, but before continuing with further SPR, we decided to curtail that line of experimentation because it did not accurately reflect the porous system that we were most interested in examining.

These experiments indeed showed concentration-dependent adsorption (Figure 25B), but because lateral flow assay experiments with nitrocellulose membranes consistently showed strong adsorption of IgG to membranes at neutral pH, we critically re-examined the utility of SPR for measuring adsorption in the context of membranes. Specifically, three major factors motivated us to discontinue further exploration of SPR as a method to quantify protein adsorption to nitrocellulose. First, the major discrepancy between SPR experiments

on thin nitrocellulose films compared to the more relevant experiments on porous nitrocellulose was a clear indicator that the two systems were not as analogous as we had hoped. Second we had some theoretical concerns about the significant differences in relevant diffusion distances and surface area available for protein binding in the dense SPR films vs. the open porous network of a nitrocellulose membrane. Finally, we had serious questions about possible differences in the molecular surfaces in porous vs. dense film nitrocellulose, and follow up surface analysis studies using time-of-flight secondary ion mass spectrometry did not yield conclusive results, and caused further doubts that the two materials were truly comparable.

Solution depletion of protein onto nitrocellulose membranes

Another unsuccessful method to quantify adsorption was based on analyzing protein concentrations in liquid solution. This method was inspired by work by Hou et al. [128, 129], who examined the adsorption of gold nanoparticles onto lipid bilayers by quantifying the amount of nanoparticles depleted from solution at varying time points, and fit the results to the Langmuir adsorption isotherm, yielding approximate adsorption constants [129]. To summarize our modification of this solution depletion, technique varying concentrations of fluorescent protein solutions were prepared, quantified using a fluorescence plate reader (Tecan, Männendorf, Switzerland) and then aliquoted into Eppendorf tubes. Circular pieces (r=2.5 mm) of unbacked nitrocellulose were cut on a CO_2 laser (see cutting protocol detailed in 4.3.1), and then one piece was submerged in each protein solution tube. At different time points, the nitrocellulose was removed, and the protein concentration in the tube was quantified using the fluorescence plate reader.

Practically, these experiments had serious problems with reproducibility, feasibility, and expense of reagents. Each round of protein depletion experiments used several milligrams

of protein and included up to 96 separate 1 mL Eppendorf tubes (because of time points and replicates). Even a small piece of nitrocellulose has a very large internal surface area—the surface area ratio of these membranes is typically ~100x, so the 20 mm^2 piece would have 2000 mm^2 available internal surface area for binding; therefore, very large quantities of protein were needed to ensure sufficient protein was present to reach theoretical saturation.

Furthermore, there were theoretical concerns about the viability of these experiments. Unlike in a well-mixed solution, the pores of a fully-wetted nitrocellulose membrane are very diffusion-limited: even if the tubes in which the membranes are held are placed on a shaker, there is no flow through the pores in a fully saturated membrane, so all replenishment of depleted intra-pore solutions is driven only by diffusion. This problem is actually two-fold—the intra-pore solution does not get replenished via flow, likely causing the surface protein coverage within pores to be below saturation levels; and furthermore, there is less depletion of the bulk solution due to ineffective transport, causing the measured solution protein concentration to be minimally depleted.

After experimenting with a variety of proteins, the solution protein depletion experiments were discontinued because of these practical and theoretical concerns.

4.3 Protein depletion in lateral flow

Because traditional techniques to quantify adsorption had not yielded useful data, we sought to explore novel methods to quantify the protein adsorption onto nitrocellulose membranes. Inspired by the idea of using protein depletion from solution, but recognizing that inefficient intra-pore transport in the absence of convection was a major limitation to the earlier protein depletion experiments, we designed a method to deplete protein from solution during lateral flow.

In this novel method, varying concentrations of protein solution were applied to a bare nitrocellulose membrane and allowed to wick through the length of the membrane via lateral flow. When the protein solution is exposed to a bare nitrocellulose surface, some fraction of the protein adsorbs to the membrane and is depleted from solution, leaving a slightly lower concentration moving forward down the strip. As protein adsorbs to the membrane, it is depleted from solution, eventually depleting all of the protein and leaving a characteristic distribution of adsorbed protein (see Figure 26 for schematic). Our goal with

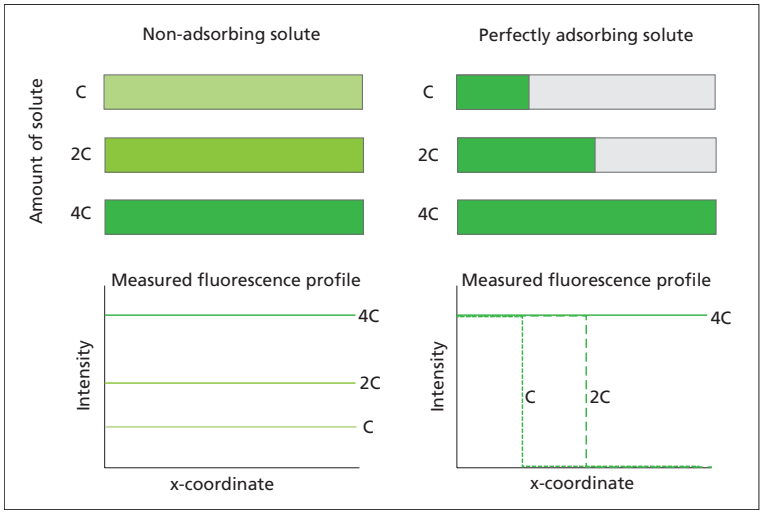

Figure 26: Comparison of distribution profiles of a solute on a membrane after flow for two theoretical solutes. First, a non-adsorbing solute (left), which is distributed evenly in solution after the liquid has fully wicked into the membrane. Therefore, if the concentration of solute is doubled, the color intensity will also double. The second case is a perfectly-adsorbing solute (right) will adsorb to the first bare area of nitrocellulose to which it is exposed. In this case, doubling the concentration of solute with double the length of the area with protein adsorbed, until the amount of protein added is equal to the amount necessary to saturate the membrane with protein (in this case "4C"). While some real solutes are non-adsorbing (red food coloring for instance), no solutes are perfectly-adsorbing. However, these two extremes can inform our analysis of protein adsorption during lateral flow.

this work was to compare these distributions across different proteins and concentrations to approximate the relative rates of protein adsorption.

All of this work was done in close collaboration with Christiane Adcock, an exceptional high school student volunteer in the lab, who contributed significantly to the development of these methods.

4.3.1 Experimental methods

Device fabrication and solution preparation

All nitrocellulose devices and cellulose wicking pads were designed in Autocad (Autodesk, San Rafael, CA), and were cut using a CO_2 laser (Universal Laser Systems, Scottsdale, AZ), as described previously [130]. Strips were cut to 24 mm long 8-leg combs (see Figure 27) for endpoint analysis. Tor time-course analysis, four-legged combs were used, at three different lengths: "short" (36 mm), "medium" (42 mm), and "long" (48 mm), to achieve three different flow rates through the devices.

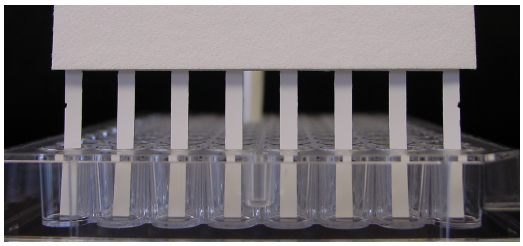

Figure 27: 8-leg nitrocellulose device wicking liquid from row 1 of a 96-well plate. (Image courtesy of Carly Holstein).

Three fluorescently labeled proteins were used in end-point experiments: FITC-labeled IgG (ChromPure whole mouse IgG, Jackson Immunoresearch, West Grove, PA), FITC-labeled IgG Fc fragment (ChromPure mouse IgG Fc fragment, Jackson Immunoresearch, West Grove, PA), and streptavidin (AlexaFluor 488-labeled Streptavidin, Invitrogen, Carlsbad, CA). Fluorescently labeled proteins were diluted in phosphate buffered saline (pH 7.4). All proteins were purchased having been commercially fluorescently labeled with either FITC, or AlexaFluor-488 a green fluorescent dye analogous to FITC but with improved resistance

to photobleaching. The ChromPure Mouse IgG from Jackson ImmunoResearch was provided by the supplier containing 15 mg/ml bovine serum albumin (BSA) in addition to the IgG. Before this IgG could be used, it was purified using a Protein A/G IgG purification column (Thermo Scientific, Waltham, MA), following the instructions provided in the package. The concentration of all stock solutions was measured using a NanoDrop spectrophotometer (Thermo Scientific, Waltham, MA). Only the whole IgG was used in the time-course experiments.

Protein depletion in lateral flow protocol

Initially, experiments were performed by loading a 96-well plate with: 20 µl PBS in all row 1 wells, and 20 µl sample in row 2 wells. 8-leg nitrocellulose combs were set into row 1 until all of the PBS had been completely wicked into the legs, and then moved on to row 2 (see Figure 27). Four different solutions were loaded into the eight "row 2" wells: 0.02 mg/ml protein, 0.1 mg/ml protein, 0.05 mg/ml protein, and PBS with no protein as a negative control, resulting in each concentration being run in duplicate on each comb. Two combs of each protein were used, providing four replicates for each protein at each concentration.

Later, a poly(methyl methacrylate) jig was designed to hold glass capillary tubes for reagents delivery to the device, which enabled video acquisition of the entire experiment. The jig was also designed in Autocad and cut on the laser cutter. In those experiments, 4-leg nitrocellulose comb devices were placed into the plastic jig for stabilization and for reproducible fluid application. All fluids were added using glass capillary tubes held vertically touching the nitrocellulose device, similar to methods developed by Dharmaraja et al. [131] which ensured reproducible and rapid switching between different solutions (see Figure 28), and facilitated a post-protein wash step. These experiments were performed with four-leg combs of the three lengths described above. Only one replicate for each

concentration and leg length was performed, and unfortunately due to a mis-alignment between the capillaries and the membranes, the long-leg combs did not run properly. The volume of PBS pre- and post-wash that were used were dependent on the device leg length and were selected by determining the volume that fully wet a single leg: 9 µl for short legs, 11 µl for medium legs, and 14 µl for long legs. The same volume of protein solution was used for all devices: 20 µl.

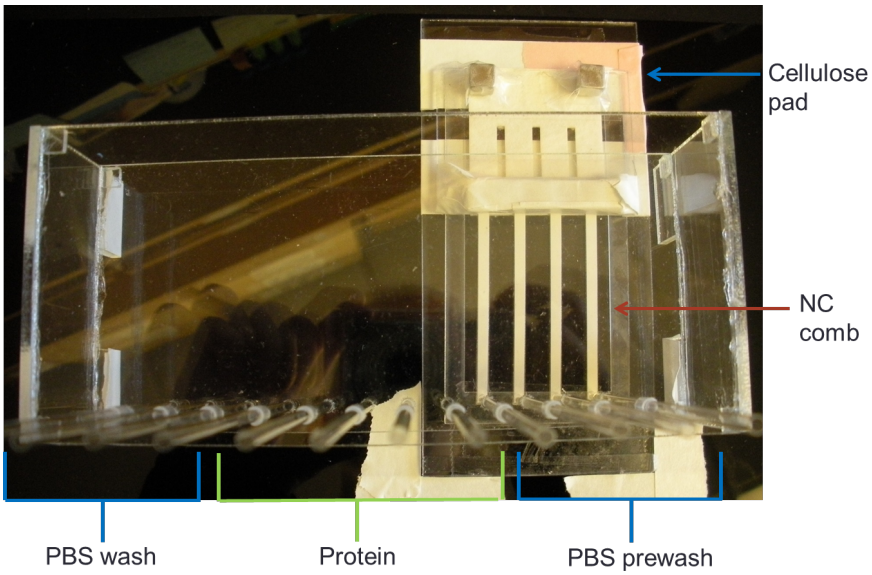

Figure 28: Plastic jig with capillary tubes for liquid application onto nitrocellulose (NC) comb. 12 capillary tubes were used to apply 3 different solutions to each of the 4 legs of the nitrocellulose comb; these tubes are labeled "PBS wash, "protein" and "PBS prewash" accordingly. After each set of capillaries empties its fluid load onto the nitrocellulose comb, the entire plastic jig is shifted to the right, allowing the next set of liquids to load onto the nitrocellulose, while continuously acquiring video.

In both experimental set-ups, all legs of the device were first wetted out with PBS buffer. This initial wet-out step was used to ensure that flow in all device legs had transitioned to the constant flow rate of Darcy Flow, rather than the time-dependent flow that occurs during wet-out, governed by the Lucas-Washburn Equation (see 2.3 for a discussion of Darcy vs. Lucas-Washburn flow).

Imaging and quantitation

Experiments using the 96-well plate format for solution loading were only analyzed at the end point of the experiment. Experiments were performed in a light-tight box without any illumination to minimize photobleaching. After running protein solutions, the strips were imaged in the same light-tight box illuminated by a pair of blue LEDs positioned to minimize reflections. A single image for analysis was acquired with a web camera (Logitech, Fremont, CA) fitted with a 550 nm high-pass filter (FEL0550, Thor labs, Newton, NJ).

Experiments using the plastic jig and capillary tubes for protein loading were suitable for continuous video acquisition, which enabled time-course analysis. The entire experiment was conducted in the same light-tight box described above, with the same video acquisition set-up. Videos were captured at 1 frame per 30 seconds for 10 minutes. To minimize photobleaching, the LEDs were connected to a timed circuit that enabled 1-second illumination only during image acquisition, but complete darkness for the remaining 29 seconds.

To normalize for lighting variations, a sheet of fluorescent PMMA was imaged in the same light-tight box, with the same acquisition settings. All protein adsorption data files were normalized by dividing the original image or video by this fluorescent flood field. After normalization, images were analyzed in ImageJ (NIH, Bethesda, MD [118]) by drawing a region of interest (ROI) rectangle within each leg of each device, and quantifying the average fluorescence intensity at all positions down the strip. Line profile analysis of a single image is built in to ImageJ, so that was used for the endpoint measurements. For time-course measurements from several-frame videos, the ImageJ macro "StackProfileData" was used [132].

4.3.2 Results

Endpoint analysis

The endpoint adsorption profiles of three different proteins: IgG, IgG Fc fragment, and streptavidin, each at three concentrations, were compared, with four replicates of each condition. These three proteins were chosen because of their relevance to 2DPN assay design: IgG is typically used as a capture species in lateral flow immunoassays, including some 2DPNs and streptavidin has been used as a membrane-binding anchor for a biotinylated capture species that may not stick strongly to the membrane itself. While the IgG Fc fragment is not itself a capture molecule (the Fc fragment does not actually have any antigen-binding region, see Figure 29), we hoped to understand the orientation of IgG adsorption. When assay engineers use IgG as a capture species, the hope is that all of the IgGs on the surface are oriented "right-side up", with both antigen-binding domains facing outward, though it is generally acknowledged that a more reasonable assumption is of randomly oriented IgGs (Figure 29B). We sought to understand if there is a difference in adsorption rates of different regions of the IgG molecule, leading to non-random orientation of IgGs on the membrane surface.

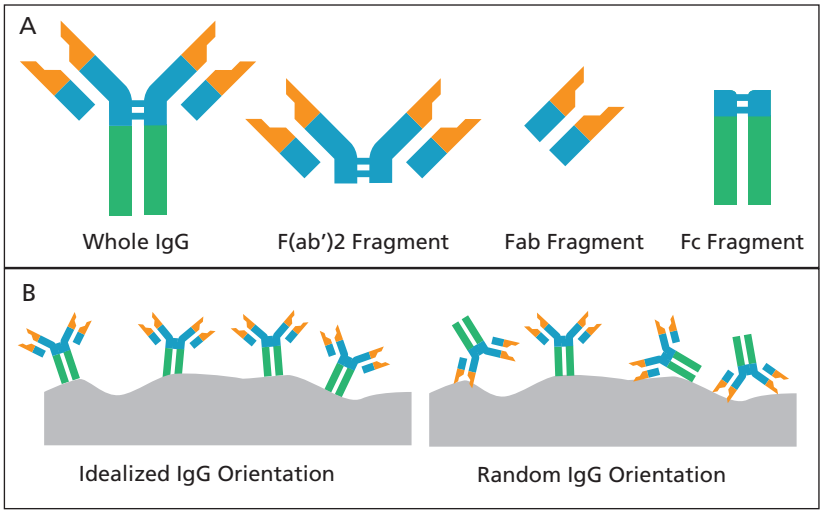

Figure 29: A. Schematic representation of IgG fragments. B. Idealized IgG adsorption to a membrane with all IgGs positioned antigen-binding-domain side-up, compared to a more realistic random orientation of IgGs. [Schematic based on figures created by Dr. Dean Stevens]

As can be seen in Figure 30, the distribution of adsorbed protein along the length of the strips is distinct for each protein, and reflects the rate of that protein's adsorption to the membrane. Recall that a *constant volume* of each protein solution is added to each strip, and that volume is more than the total volume to wick through the strip, so in the extreme case of a solute that exhibits no adsorption, all strips would be uniformly fluorescent along their length, and a strip with protein added at half the concentration would be half as bright. Conversely, in the case of perfect adsorption, the membrane would be fully saturated from the beginning until the point of complete protein depletion, at which point the fluorescence intensity would drop to zero, and a strip with protein added at half the concentration would halve the *length* of fluorescence intensity (Figure 26).

Using those theoretical extremes in adsorption behavior, we can interpret the results observed with different real proteins on nitrocellulose. A shallow, faint gradient, as seen in the case of streptavidin adsorption (Figure 30A and B), indicates a slowly adsorbing protein—as the protein is wicked through the strip, the rate of adsorption is slower than the rate of wicking, resulting in minimal depletion and a more uniform distribution. The sharp peak seen at the beginning of the strips seems inconsistent with that explanation, however we hypothesize that this is due to the comb being set in a 96-well plate, so the first ~3 mm of the strips are fully submerged in the protein solution and have a much longer time available for adsorption. The IgG Fc fragment yields an adsorption profile that peaks initially and then drops off downstream, which suggests a mid-range adsorption rate: the protein is depleted from solution by the time the fluid front reaches the downstream end of the strip, but as the concentration decreases, less protein adsorbs to the membrane. Finally, whole IgG appears to exhibit the most rapid adsorption to the membrane, with more protein adsorbed to the membrane overall, and a much steeper gradient as protein is fully

depleted from solution (this is especially apparent in the 0.05 mg/ml case, where a very short zone with significant protein adsorption is visible at the beginning end of the strip, and depletes to zero very suddenly around x = 15 mm).

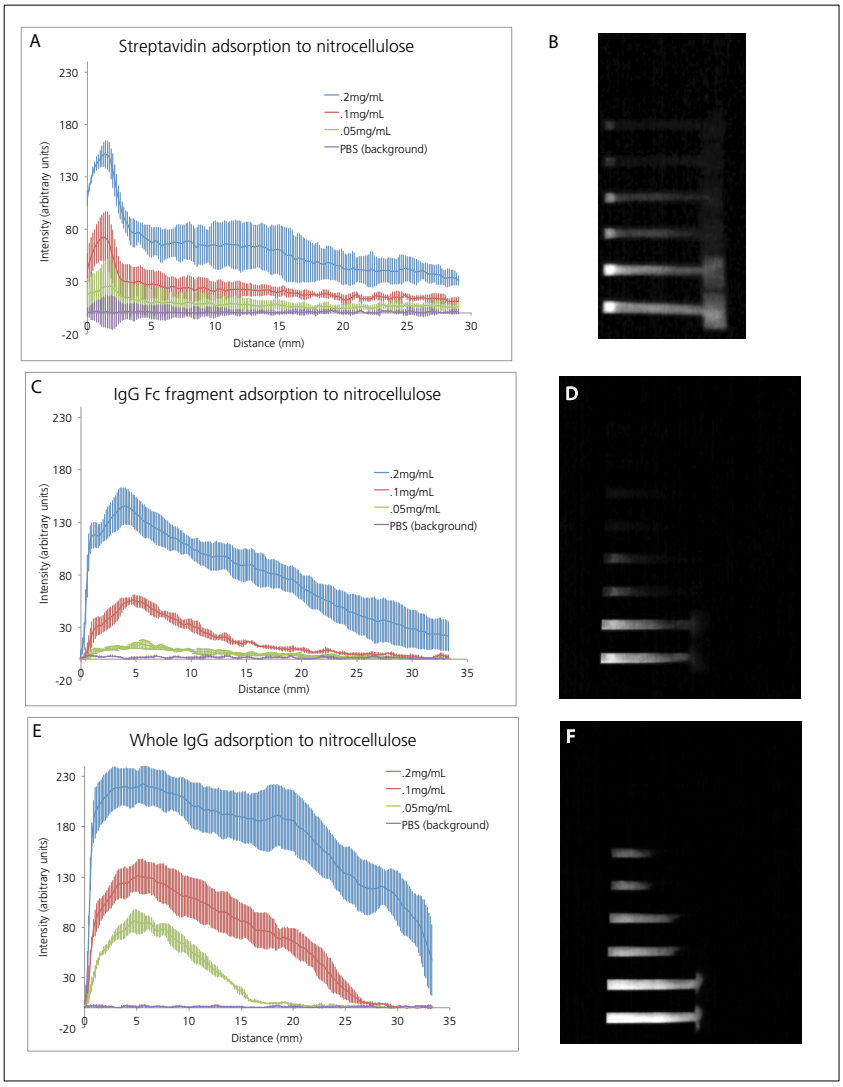

Figure 30: Line profiles of endpoint protein adsorption measurements, along with sample images of strips after adsorption. The low-intensity and relatively uniform profile of streptavidin adsorption (A and B) suggests that streptavidin adsorbs more slowly than either IgG Fc fragment (C and D) or whole IgG (E and F). The adsorption profile of the Fc fragment is in the middle: there is clearly more of a gradient along the strip, indicating that the protein is depleted as the liquid is wicking along the length, however the gradient has a shallower slope that that observed with whole IgG. Which yields the most abrupt depletion profiles. The bright florescence upstream reveals that a large amount of IgG adsorbs quite rapidly, and the sharp decline indicates that protein is depleted from solution before it reaches the downstream end. While not the clean step function profile exhibited by the theoretical "perfectly-adsorbing" protein, the rapid adsorption of IgG is clearly the closest of these three proteins to that theoretical extreme. (N=4 strips for each protein and concentration condition.)

Time-course analysis

Because the concentration of protein in solution and the amount of protein adsorbed to the membrane are depending on each other, and are both functions of time as well as position down the membrane, we hoped to gain a more complete understanding of these variables using a time-course analysis of protein adsorption by recording videos of adsorption. We also added a PBS buffer wash step after the protein addition, to ensure that all fluorescence visible on the membrane was due to protein adsorbed to the surface, rather than protein in solution within the pores. To do these measurements, we built the PMMA jig described above, and use capillary tubes to deliver fluid to the membranes. Only whole IgG adsorption was examined, and only one replicate of these experiments was performed, because after the first set of time-course experiments, it was clear that this method required a significant amount of time for each replicate, and was very reagent intensive. Furthermore, due to a mistake in setting the contact between the capillaries and the long-legged device, this device did not run properly, and therefore there are no results from that variation. The results that we did observe, however, are consistent with the endpoint analysis described above, and are shown in Figure 31.

4.3.3 Discussion

Because of the significant time and reagents required for each experiments, this method for examining protein adsorption did not fit the design requirements of being a simple, straightforward and high-throughput technique, so these lateral flow adsorption experiments were curtailed. The next section describes a method that is similar in principle, but mitigates the downsides, via precision spotting of proteins.

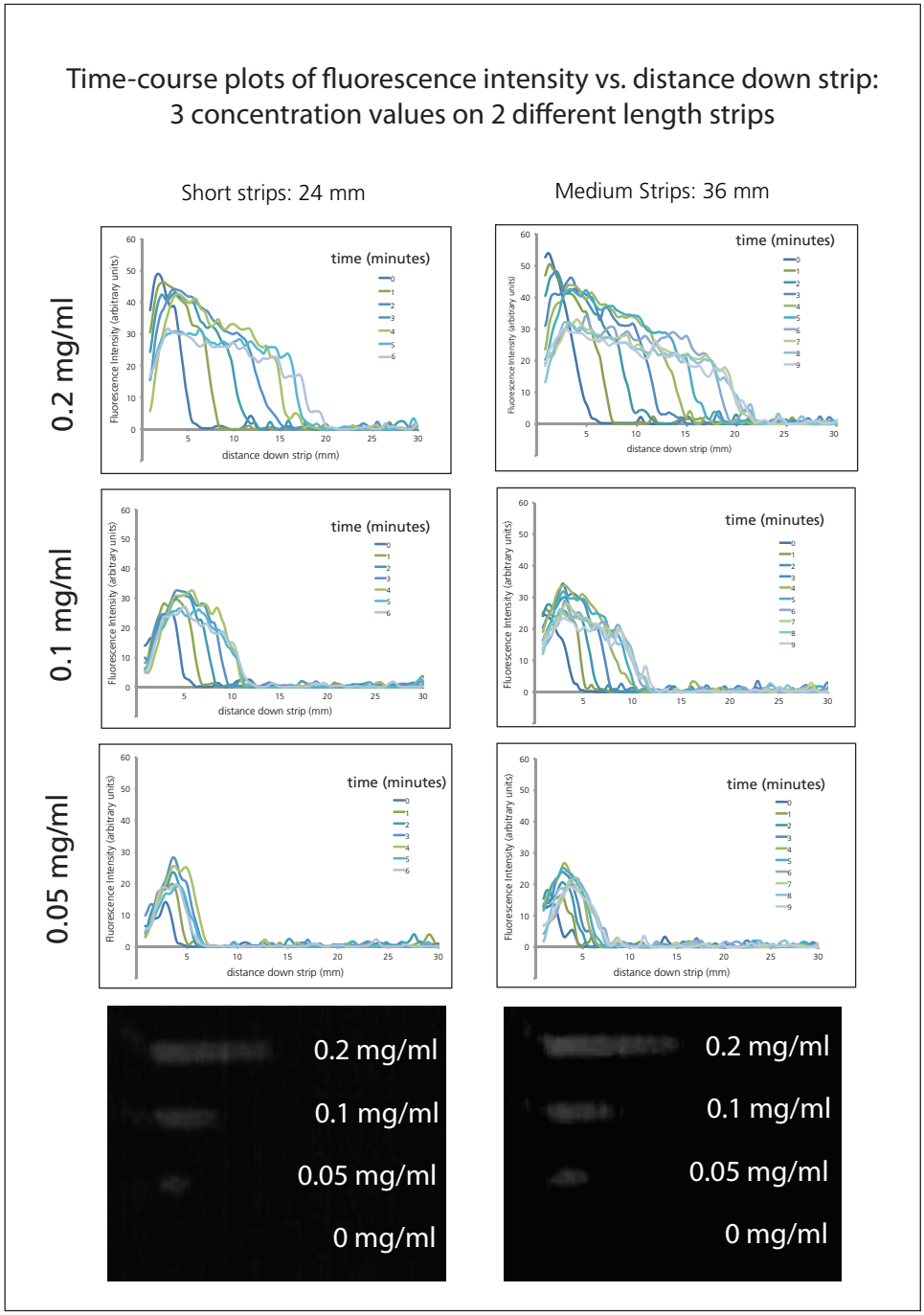

Figure 31: Time course measurements of whole IgG adsorption during flow. Line plots represent the measured fluorescence intensity along the length of the strips at different time points. Measurements from short-legged strips (24 mm) are shown on the left, measurements from medium-legged strips (36 mm) are shown on the right. There was a mistake in setting up the inlet capillaries for the long-legged device, so that one did not run properly. At the bottom of each column is an image of the final fluorescence profile of each of the experiments. Recalling Figure 30 and Figure 31, these results suggest that IgG adsorbs rapidly to the membrane surface.

4.4 Precision spotting of proteins to assess adsorption

The lateral flow depletion experiments described in 4.3 demonstrated that different proteins adsorbed at different rates during lateral flow, and that method was a vast improvement over both SPR and solution-depletion measurements, a major drawback to was the use of relatively large quantities of reagents, and the significant time required for each experiment. To reduce the amount of time and reagents needed, while maintaining the underlying benefits of depleting protein from solution during flow, we implemented the protein depletion technique in the small scale of individual printed spots of protein. Based on our in-depth analysis of printing on nitrocellulose, described in Chapter 3, we understood the flow occurring within a spreading spot, and so hypothesized that a similar depletion-in-flow experiment could be performed by simply spotting proteins onto membranes. Furthermore, we realized that printing is the typical method of applying proteins to nitrocellulose for assays, and so the adsorption of proteins to membranes during this process is inherently valuable for assay design.

Because of the small volume of droplets delivered in the piezoelectric printing process (1000 drops at 500pL per drop), liquid enters the membrane and flows outward radially, creating a near-circular spot (spots are not perfectly circular due to anisotropies in flow characteristics of this membrane, FF80HP). As the liquid flows outward, protein adsorbs to the membrane surface and is depleted from solution. As with lateral flow depletion experiments, more rapidly adsorbing proteins are depleted more quickly than they flow outward, leading to smaller spots (as compared to lateral flow depletion, where more rapid adsorption leads to shorter bands of adsorbed protein). At higher concentrations the membrane surface can become saturated at smaller spot diameters, resulting in larger spots. See Figure 32 for a schematic of this depletion process.

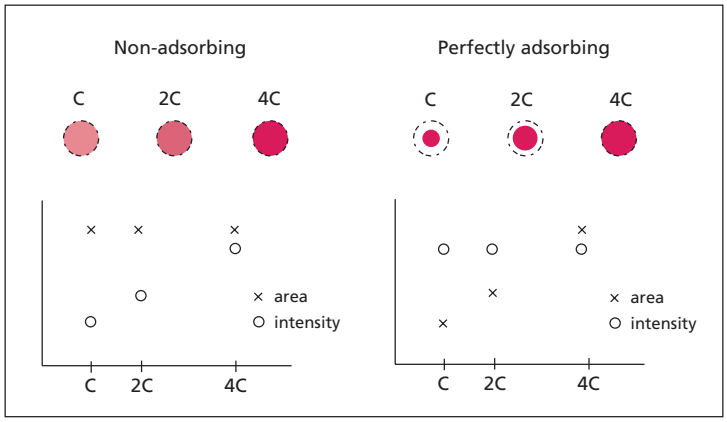

Figure 32: Schematic of protein adsorption during printing.

This method was developed in collaboration with another graduate student, Carly Holstein, and involves additional techniques that assess the robustness of protein adsorption to nitrocellulose using a variety of stringent washes. Those "lateral flow challenge" techniques are vitally important to 2DPN assay development, but are more closely related to work described by C. Holstein, and therefore will not be discussed here.

4.4.1 Experimental methods

Device fabrication and spotting

All porous devices consisted of backed nitrocellulose membranes (Millipore Hi Flow Plus 135, Millipore, Billerica, MA and GE Healthcare FF80HP, Pittsburg, PA) cut using a CO_2 laser (Universal Laser Systems, Scottsdale, AZ) as described previously [130]. Devices designs were drawn in AutoCAD (Autodesk, San Rafael, CA). Polycloncal mouse IgG and its fragments were purchased already commercially digested and purified as "ChromPure" proteins from Jackson Immunoresearch. Protein G was purchased from Thermo Scientific and solid dried BSA was purchased from Sigma-Aldrich.

Strips were printed with proteins using the S3 piezoelectric printer (Scienion AG, Berlin, Germany) described above. Proteins were spotted at concentrations between 0.5 mg/ml and 5.6 mg/ml, in phosphate buffered saline pH 7.4. Proteins must be filtered to remove particulates before introducing them to the S3, however a small amount of protein is often lost to adsorption to filter membranes, so instead of filtering, each protein sample was centrifuged at 8000 rpm for 5 minutes. Except as described otherwise, all printed spots consisted of 1000 droplets at 450-500 pL, printed at 500 Hz in a closed chamber at 50% relative humidity and ~68°F ambient temperature. See Chapter 3 for a thorough discussion of printing.

In "real-time rinsing experiments, the S3 printer was set up with two nozzles concurrently. One nozzle was loaded with protein solution, the other contained only water; the print run was designed such that different solutions could be spotted in the same location with minimal time delay between them (~10-20 seconds). Four different conditions were compared: 500 nL protein only (no rinse), 500 nL protein + 1 µL water, 1µL water + 500 nL protein, and 1 µl water + 500 nL protein + 1 µl water.

After spotting, strips were stored overnight in a desiccator before staining.

Protein staining

All membranes were stained in Ponceau S stain (Sigma Aldrich) for visualization of protein spots. Early experiments were stained using Ponceau S straight from the bottle, but experiments performed by Karen Keniston, an undergraduate in the lab, showed that the addition of 40% methanol improves the uniformity of protein spot staining.

Ponceau S stain is a negatively charged pinkish red dye used for staining of protein gels and blots on nitrocellulose and other membranes. The negative charge of the dye binds to

positively charged amino groups within proteins, and also interacts non-covalently with non-polar protein regions [133, 134]. Because these interactions are not one-to-one by weight or moles, it is virtually impossible to quantitatively compare the staining of two different proteins, and the stain intensity is only semi-quantitative: a darker stain indicates the presence of more protein, but 2x intensity does not indicate 2x the protein amount [135]. Comparing the stain intensity of different spots of a single large protein (Ponceau has been reported to be less sensitive staining proteins <15 kDa [135]) or a consistent mix of proteins (e.g. polyclonal IgG) is more reliable, though still not nearly as quantitative as specific quantification with a labeled antibody [135].

Protein-spotted nitrocellulose strips were soaked in petri dishes filled with Ponceau S (+ 40% methanol, where used) for 5 minutes, then removed and gently dabbed on Kimwipes (Kimberly-Clark) to remove excess stain, and then rinsed by soaking in petri dishes filled with water for 2 minutes. Later we discovered that re-rinsing by soaking in clean water for about 10 seconds dramatically reduced pink background staining of the membrane. After removing strips from the final water rinse, they were dabbed on clean Kimwipes to remove excess water, and then set on another Kimwipe to dry.

Imaging and interpretation

All strips were dried overnight in ambient laboratory conditions after staining, and then scanned on a flatbed scanner (Epson Perfection V700 Photo, Epson, Long Beach, CA) in 16-bit color, with gamma set to 1.

Protein adsorption data from these strips was interpreted in two ways: first, spot sizes and intensities were compared qualitatively. Second, the area occupied by each protein spot was

quantified using ImageJ. A similar analysis protocol was used to quantify the spot area as was described in section 3.2 to determine the area of red food coloring spots:

1. Color channels of each of the images were separated. The green channel had been determined to have the highest contrast between spots and background, so for each image, it was saved as a separate file for evaluation.
2. All images were converted to 8-bit color.
3. All images were thresholded to black and white using a threshold dependent on the average signal of the image.
4. Spots were detected using the "Analyze Particles" function in ImageJ. The limits for "Analyze Particles" were:
    a. Area: 500–50000 px^2
    b. Circularity: 0.3–1
5. Regions of interest generated by "Analyze Particles" were saved as an ROI file, and then re-opened in a non-thresholded image to quantify the average intensity of each spot.
6. Spot areas were also quantified using the ROIs generated by "Analyze Particles". The output was measured in pixels and then converted to millimeters using 600 px/in, and 25.4 in/mm, resulting in a linear conversion of 23.6 px/mm, and 558 px^2/mm^2.

For IgG fragment analysis, the background threshold was determined to be 221, and for real-time rinsing analysis of non-washed spots, the threshold was determined to be 232. In both cases the threshold was determined using a non-inverted, 8-bit image, taking the average minus three times the standard deviation of the background.

The BSA spots generated in the real-time rinsing experiments had very faint outer rings (see Figure 37, in the results section) that were not detected by the automated "Analyze particles" function, so these spots were analyzed by hand-drawing a ROI around those

spots. This method is not as reproducible, but we did not want to under-represent the spot size for those spots.

4.4.2 Results

IgG fragments

The primary goal in developing a method to quantify protein adsorption to nitrocellulose was to provide a tool that would be generally applicable for assessing the adsorption of a protein to nitrocellulose, particularly for use in 2DPN assays. As discussed in Section 4.3, one use of this method is to compare relative adsorption rates of different IgG fragments to better approximate the orientation of capture-IgGs on the nitrocellulose surface. In Section 4.3 we showed that whole IgG adsorbed more rapidly than the Fc fragment, but we discontinued those experiments before examining other IgG fragments, so we turned to those experiments as an interesting and useful test of the method to assess protein adsorption during printing.

Whole IgG and three fragments (Fc, Fab and F(ab')2) were compared at a range of concentrations. Proteins were spotted at 0.5 mg/ml, 2.3 mg/ml, and the stock solution concentration (which for Fc was 2.3 mg/ml, so it was only spotted at two concentrations). Red food coloring was spotted to illustrate the total wetted area. Two characteristics can be assessed through rough visual inspection. First, the size of spots resulting from printing the same protein at different concentrations can be compared. As shown in Figure 32, this allows us to determine whether the protein adsorbs to the membrane at all: a non-adsorbing protein at a lower concentration will result in the same spot size with lower intensity when compared to a high-concentration spot, whereas a perfectly adsorbing protein will result in spot areas that are proportional to the relative protein concentrations. All four proteins compared here result in varying spot sizes across the range of

concentrations to some degree, so it is clear that all of them adsorb to the membrane to some degree (Figure 33).

Secondly, protein spots containing different proteins at the same concentration can be compared to approximate their relative rates of adsorption (this is only relevant when comparing low concentrations for which there is no saturation). Here, at 0.5 mg/ml the different fragments result in different spot sizes, implying variation in their rates of adsorption to the membrane (Figure 33).

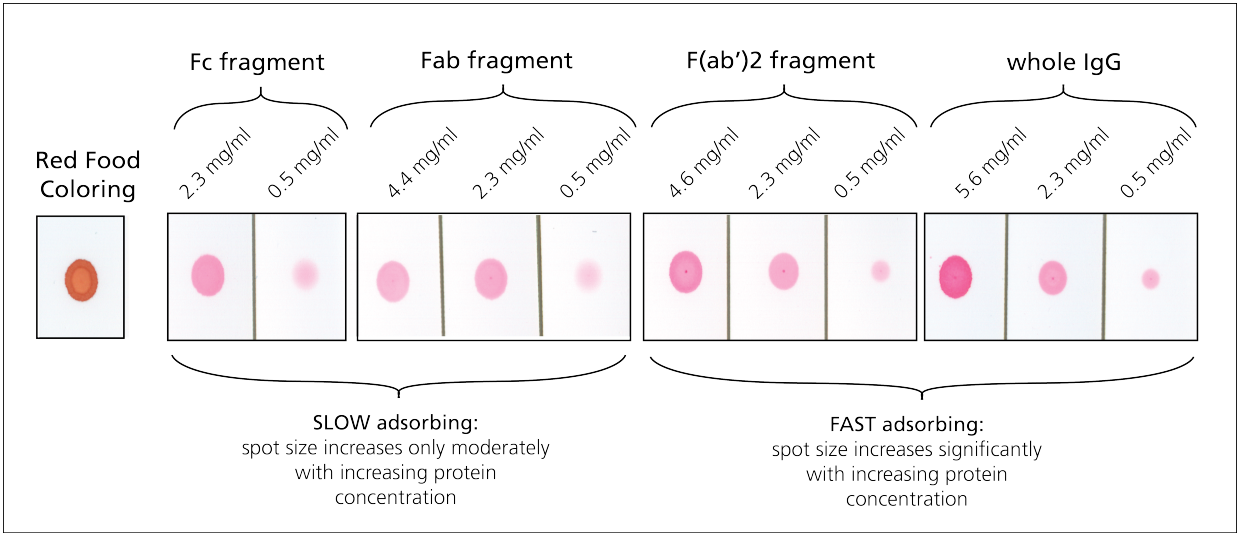

Figure 33: Ponceau S stained images of IgG fragments adsorbed to nitrocellulose during printing. All spots were printed with the *same volume* of protein solution (500nL), at different concentrations. The red food coloring spot (at left) illustrates the area fully wetted by that volume of liquid. Because of the small volume of droplets delivered in the piezoelectric printing process (1000 drops at 500pL per drop), liquid enters the membrane and flows outward radially, creating a near-circular spot (spots are not perfectly circular due to anisotropies in flow characteristics of this membrane, FF80HP). As the liquid flows outward, protein adsorbs to the membrane surface and is depleted from solution. More rapidly adsorbing proteins are depleted more quickly than they flow outward, leading to smaller spots. At higher concentrations, the membrane saturates with protein at smaller diameters, resulting in larger spots. See Figure 32 for a schematic of this depletion process, and Chapter 3 for a thorough discussion of flow during printing.

After making a rough visual assessment, protein spot size can be compared quantitatively (Figure 34). The quantitative measurements of spot area yield much of the same conclusions as could be observed visually—all four proteins form spots that are significantly smaller than the wetted area at the lowest concentration spotted, confirming that all of

these proteins do adsorb to the membrane. However, at this low concentration, the Fc and Fab fragments yield larger spots than the F(ab')2 fragment and whole IgG, indicating that F(ab')2 and IgG adsorb more rapidly. At higher concentrations, all protein spots approach the size of the wetted area because there is sufficient protein that it is not entirely depleted from solution, though it is adsorbing to the surface (Figure 34A).

By comparing protein spot sizes to the total wetted area (as approximated by red food coloring) using a two-tailed heteroscedactic Student's t-test, the size of several protein spots ($Fc_{2.3\ mg/ml}$, $Fab_{2.3\ mg/ml}$, $F(ab')2_{4.6\ mg/ml}$, and $IgG_{5.6\ mg/ml}$) were *not* statistically different than that of the wetted area ($p>0.05$), which leads us to hypothesize that in those cases, the protein was not fully depleted in flow and instead reaches the edges of the fully wetted area. A notable exception from this list is the $Fab_{4.4\ mg/ml}$ spot ($p=0.05$). However, since the lower-concentration $Fab_{2.3\ mg/ml}$ spot is not statistically smaller than the fully wetted area as represented by the red food coloring, and there is no logical explanation that at a greater concentration protein would be depleted more completely, we hypothesize that the protein in the $Fab_{4.4\ mg/ml}$ spot *does* actually reach the extent of the wetted area, but for that protein, the total wetted area is anomalously small. This disparity in the total wetted areas is likely due to the higher Fab concentration causing droplet instabilities during printing, resulting in smaller volume droplets and thus a smaller total wetted area, which is consistent with prior printing observations.

Comparing the average spot intensity can give a rough comparison of the amount of protein present per area for each protein. Recall, however, that because Ponceau S stain does not bind to proteins at a constant proportion (by either weight or moles), only semi-quantitative analysis of spot intensity is possible. At the lowest concentration, 0.5 mg/ml, IgG results in the darkest spot, and though we cannot quantify the relative amounts of protein per area,

this does suggest that IgG adsorbs more densely than the other proteins tested (Figure 34B). Additionally, there is a general trend towards darker spots at higher concentrations, consistent with both Langmuir's adsorption model and protein-ligand binding models that predict increased adsorption/binding rates with higher solute concentrations [136-138]. The $Fab_{4.4\ mg/ml}$ spot seems to break this pattern however, as the average intensity appears less intense than the $Fab_{2.3\ mg/ml}$ spot. However, a two-tailed, heteroscedactic Student's t-test comparing the average spot intensities for the 2.3 and 4.4 mg/ml spots reveals that the difference in intensities is not statistically significant (p=0.11), and as mentioned previously, the measured intensity using the Ponceau S stain is not quantitative, so no conclusions can be drawn about the relative levels of adsorption between those samples.

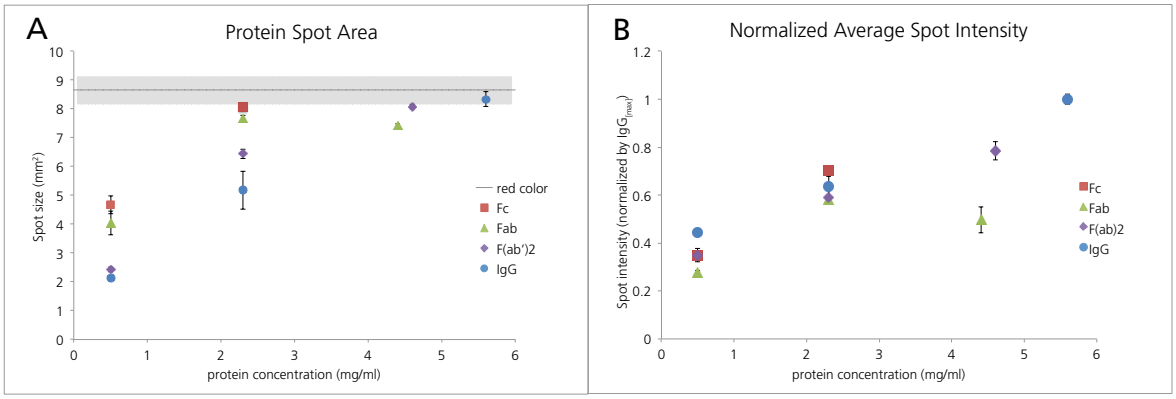

Figure 34: Quantitative comparison of IgG fragments. A. Comparison of protein spot areas. The size of the red food coloring spots is represented by a constant line to illustrate the total wetted area. The gray shading around the line represents the standard deviation of the size of the red food coloring spots. At the lower concentration, 0.5 mg/ml, all four proteins form spots significantly smaller than the wetted area, confirming that all of these proteins do adsorb to the membrane. However, the Fc and Fab fragments yield larger spots than the F(ab')2 fragment and whole IgG, indicating that F(ab')2 and IgG adsorb more rapidly. At higher concentrations, all protein spots approach the size of the wetted area because there is sufficient protein present that some adsorbs to the surface as it flows, but it is not entirely depleted from solution. B. Average spot intensity, normalized by the average intensity of the darkest protein spot—IgG at 5.6 mg/ml. This measurement is only semi-quantitative, because Ponceau S does not stain proteins at a constant ratio, however it can give a rough comparison of the amount of protein present per area for each protein. For example, at the lowest concentration, 0.5 mg/ml, IgG results in the darkest spot, and though we cannot quantify the relative amounts of protein per area, this does suggest that IgG adsorbs more densely than the other proteins tested, which is also supported by the spot area measurements that show that IgG spots are the smallest for all common concentrations tested.

Returning to our earlier question that sought to determine the likely orientation of IgG the membrane surface—we hoped that the relative rates of adsorption of the different IgG fragments would provide insight into this question. Because the results described here illustrate that both IgG and F(ab')2 adsorb more rapidly to the membrane than the Fc region, this suggests that a region of the antigen-binding domain mediates the rapid adsorption. Therefore, when IgG is printed on a nitrocellulose membrane, it is likely that a larger fraction of the spotted IgG is oriented with the antigen-binding domain downwards, adsorbed to the membrane. We hypothesize that the Fab fragment—which also contains an antigen-binding domain—does not absorb as rapidly as the whole IgG or the F(ab')2 because the Fab fragment only contains one antigen-binding domain, whereas both F(ab')2 and whole IgG contain two antigen-binding domains. This assessment is only a very rough approximation, and if a future student were particularly interested in this problem, a possible experiment that could shed more light on the subject would be a competitive adsorption study using two different fluorescent labels on different fragments (e.g. TRITC-Fc and FITC-F(ab')2), which could potentially provide more detailed information about their relative rates of adsorption when they are simultaneously exposed to a surface. That experiment is a more accurate representation of IgG adsorbing, since as IgG rotates its Fc region and F(ab')2 region are essentially competing for their interactions with the membrane surface, however it is outside the scope of this work.

More generally, using this method to quantify the adsorption of an arbitrary protein to nitrocellulose is confounded by some quantity of protein present in solution (*not* adsorbed to the membrane) that dries in place when the liquid evaporates away. The evaporation of a drop of liquid from a porous material is a very complicated process that is beyond the scope of this thesis. To simplify, however, evaporation is most rapid at the edges, causing some

liquid redistribution outwards, resulting in the "coffee-ring" effect—a darker band around the outside of a spot—for non-adsorbing solutes or when there is a significant excess of solute. For examples of the coffee-ring effect see the red food coloring spot in Figure 33, or the protein spots containing an excess of protein, such as the 4.6 mg/ml F(ab')2 spot. The very slight evaporation-generated flow outward is not sufficient to pull all of the excess solute to the edges of the spot, however; imagine the very last droplet applied to the spot: it soaks into the membrane rapidly (see Chapter 3), but because *every* droplet has passed through that area on its way outward, that surface is the most saturated with protein, leaving little available surface to adsorb protein. (As an aside, this is likely why most of the stained spots are exceptionally dark at the very center—this is the droplet entry point, and it is always exposed to the highest possible protein concentration.) The protein in solution in this last droplet is left behind when the liquid evaporates. In reality, it is not only the very last droplet that still contains non-adsorbed protein when the liquid evaporates. This phenomenon results in two possible effects: first, it may result in an artificial increase of the signal intensity of a spot, because excess protein remains in place after the liquid has evaporated; alternatively, if that excess protein does not stick well on top of the adsorbed protein layer, it may wash off the surface during staining, resulting in diminished total signal. To reduce the confounding effect of non-adsorbed protein, we added a "real-time rinsing" step to the experiment, which will be described in the next section.

Real-time rinsing: BSA, IgG, and Protein G

Three proteins were compared in the real-time rinsing experiments: BSA, which is known from others' experiments in the laboratory to adsorb slowly to nitrocellulose; Protein G, which has been immobilized on nitrocellulose for IgG capture; and whole IgG, which adsorbs very rapidly (as shown in previous experiments described here). An individual real-

time rinsing experiment contains a great deal of information. At the simplest level of analysis, the no-rinsing condition can be compared to approximate relative adsorption rates, as we did with the IgG fragments in the last section. This analysis supports the finding that BSA indeed adsorbs slowly—the 0.5 mg/ml BSA spot is significantly larger than either the Protein G or the IgG spots at the same concentration ($p<0.05$, by a two-tailed heteroscedactic t-test). Also, comparing spots within a single protein type, it is clear that with increasing concentration, the BSA spots do not show the steep increase in size that occurs with the Protein G or the IgG spots, further supporting the slow adsorption (Figure 35).

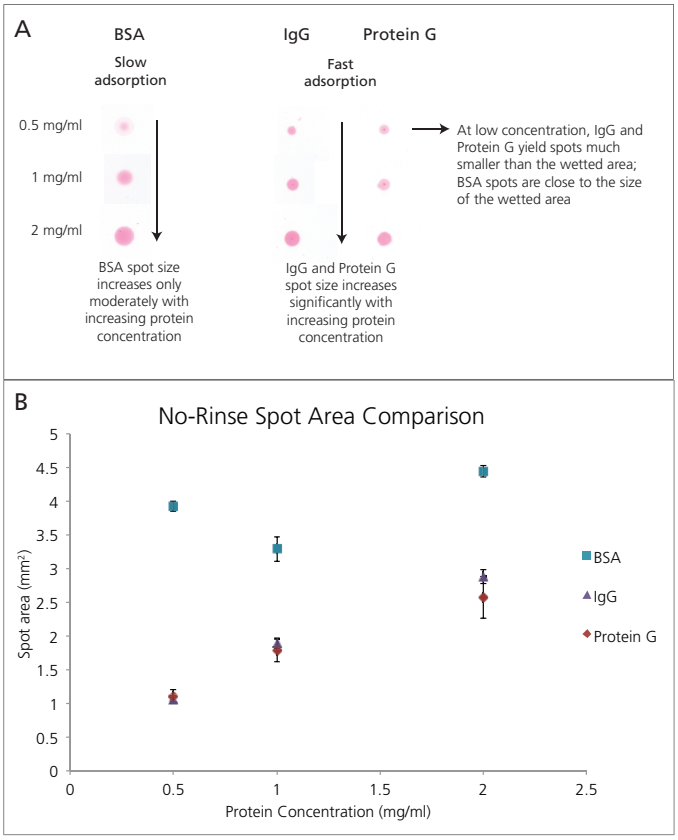

Figure 35: No rinse comparison of BSA, IgG and Protein G. A. When comparing the sizes of the low-concentration spots, it is clear that the IgG and Protein G spots are significantly smaller than the wetted area ($p<0.05$), indicating that the protein was depleted from solution before reaching the furthest wetted edge, whereas the BSA spot is closer in size to the total wetted area (roughly the size of the 2mg/ml BSA spot), suggesting that BSA adsorbs much more slowly. Similarly, when comparing the sizes of the sequence of spots for a single protein, spots that increase in size with increasing concentration (as both IgG and Protein G do here) indicate more rapid adsorption (recall Figure 32), because at higher concentrations there is more protein available to cover more of the surface before being depleted. Conversely, a slow adsorbing protein, like BSA, spreads more during printing before being adsorbed, even at low concentrations, so the spot sizes do not increase as substantially with increasing protein concentration. B. Quantified spot areas for the no-rinse condition. (N=4, error bars indicate standard deviation).

Next, we can examine differences between different "real-time rinses." The 1µl water rinse printed directly onto the protein spot immediately following protein printing significantly increased the area of the resulting protein spot area ($p<0.05$) for every protein and concentration set, except the 0.5 mg/ml Protein G spots, which did not show a significant increase in size ($p>0.05$). This observation is consistent with our hypothesis that during the protein printing process, there is an area near the center of the spot where a fraction of the protein remains in solution because there is not sufficient free membrane area for complete adsorption. The addition of a 1 µl printed water rinse pushes that protein outward, to an area of the membrane that has not yet saturated (Figure 36 columns 1 vs. 2).

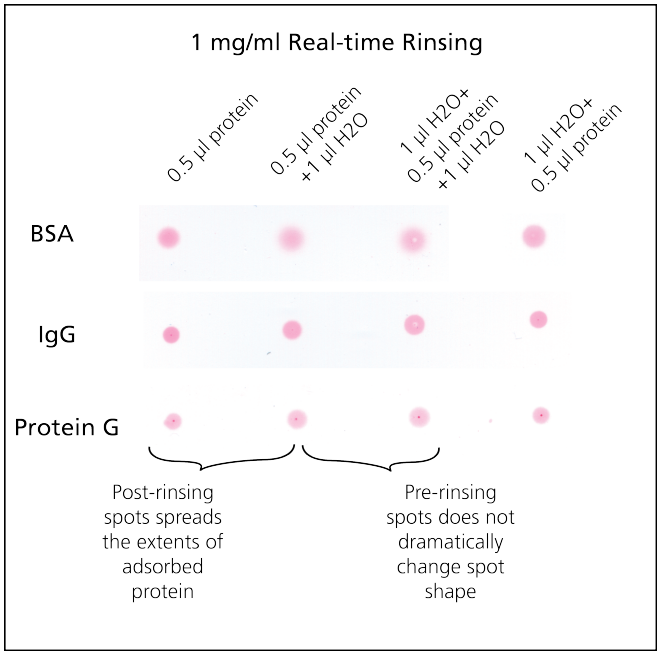

Figure 36: Real-time rinsing comparison between BSA, IgG, and Protein G, all at 1 mg/ml. Comparing non-rinsed and post-rinsed spots (columns 1 and 2) shows that for all of the proteins printed in this experiment, rinsing with water extends the area of the protein spot because non-adsorbed protein in solution is pushed outward by the water rinse, and adsorbs to non-saturated areas of the membrane. Comparing pre-rinsed spots with their corresponding non-pre-rinsed spots, there is minimal apparent difference in spot size (columns 2 vs 3, and 1 vs 4).

Conversely, the 1µl water pre-rinse does not have as clear of an effect. Visual inspection reveals that a pre-rinse together with a post-rinse yields a spot that is very similar to spots with a post-rinse only (Figure 36 column 2 vs. 3), with the most noticeable difference being a faint white zone near the center of pre-rinsed spots, the origins of which future experiments could examine. Comparing the non-rinsed spots (Figure 36 column 1) with the pre-rinsed only spots (column 4), it appears that there is only a very small difference in spot size. Quantifying these spot sizes does not completely resolve the issue. In most cases, the pre-rinse does not significantly change the spot size (pre-rinse with post-rinse: $BSA_{1\ mg/ml}$, $IgG_{0.5\ mg/ml}$, $IgG_{1\ mg/ml}$, all Protein G spots; without post-rinse: $BSA_{0.5\ mg/ml}$, $BSA_{1\ mg/ml}$, $IgG_{1\ mg/ml}$, $IgG_{2\ mg/ml}$ $p>0.05$), but in the others there is a significant, though small, difference ($p<0.05$). It is likely that this small difference could be explained by diffusion of protein from the leading edge of the protein solution into the adjacent water-wetted area, though further experiments would be needed to confirm this hypothesis.

The 0.5 mg/ml and 2 mg/ml BSA spots have a "halo" of signal at the furthest edge of the spot, which is especially apparent in the post-rinse-only spot (column 2, Figure 37). This halo resembles the hallmark coffee-ring effect. This is likely due to the very slow adsorption of BSA to the membrane allowing some protein to be drawn all the way out to the edges of the wetted area during rinsing. However, the halo is absent almost completely in the 1 mg/ml spots, suggesting that there is some difference between the protein preparations, despite them being serial dilutions. Future studies of BSA spotted on membranes could examine this behavior in more depth, however for the purposes of developing a method for examining protein adsorption to membranes, the behavior of BSA compared to IgG is an interesting example of differences in adsorption between different proteins.

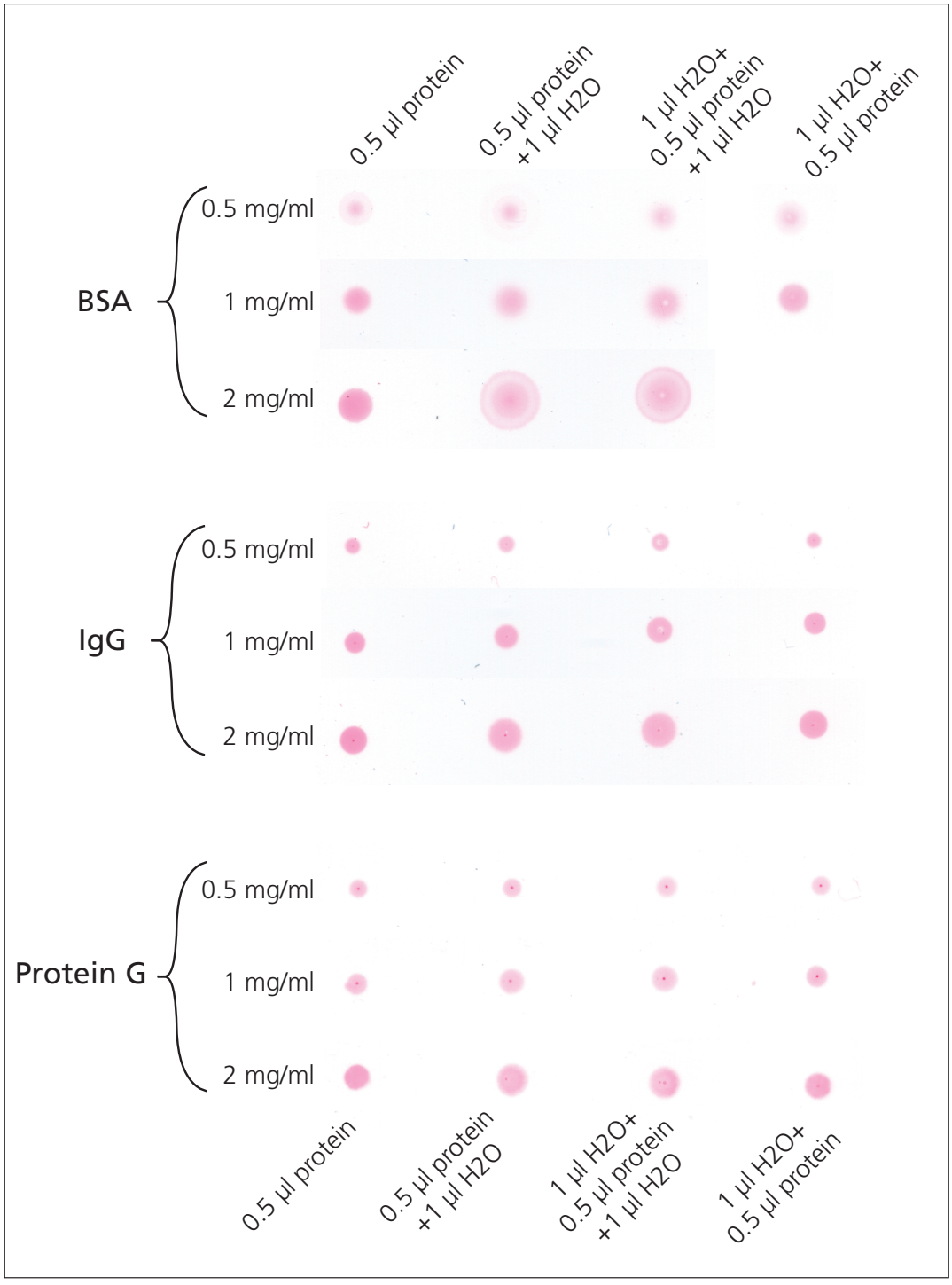

Figure 37: All real-time rinsing spots compared. Generally, post-rinsed spots are larger than non-post-rinsed spots because the 1 µl water rinse pushes protein outward to care membrane where it is able to adsorb. Pre-rinsing does not appear to have a major impact on spot size, though spots may be slightly larger due to diffusion between the protein solution and the water pre-rinse. (There was a printing misfire in the BSA 2 mg/ml pre-rinsed experiment, so it is not shown.)

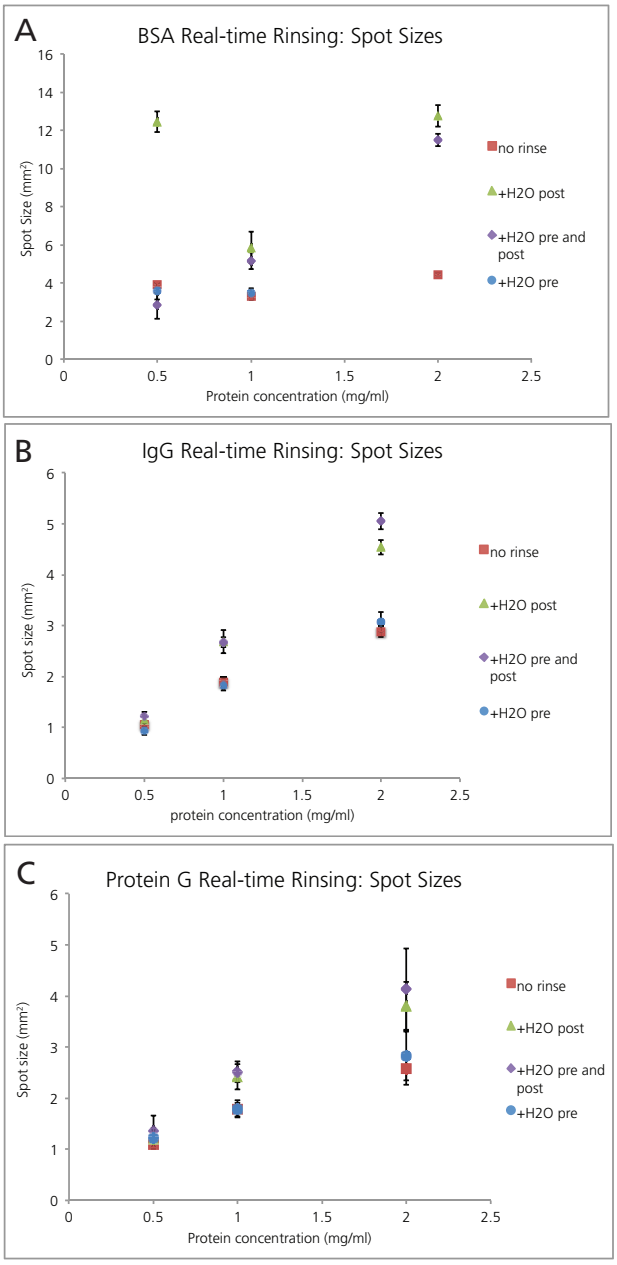

Figure 38: Graphs depicting protein spot sizes for a variety of protein concentrations and real-time rinse conditions. A. Spot size measurements from BSA spots. The exceptionally large size of the H_2O post-rinsed BSA spots is due to a "halo" of signal at the far edge of the spot. (See image in Figure 37). B. IgG spots sizes in a variety of real-time rinsing conditions. C. Protein G spots in real-time rinsing conditions. Generally, spot sizes increase with post-rinses due to non-adsorbed protein being pushed outward by the rinse. Some spots increase in size with pre-rinses, which we hypothesize is due to diffusion of protein between the protein solution and the water pre-rinse.

Even when quantitatively analyzing these spot images however, it is challenging to extract truly meaningful quantitative comparisons based on these spots because there are so many variables involved. Though these spots look incredibly simple, they are just the endpoint of a complex process: liquid is deposited and flows outward (as described in Chapter 3), meanwhile, at every location within that moving fluid there is some quantity of protein that is in solution and some quantity that is adsorbed to the surface. The local rate of adsorption is dependent on the solution concentration, the amount of available space for adsorption, and some (unknown) rate constant of adsorption. However, unlike a well-mixed tube, this flowing, dynamic system has a different local concentration at each location, leading to different adsorption rates everywhere.

4.4.3 Discussion

This technique to approximate protein adsorption rate via printing has achieved our initial goal to develop a method to better understand and compare protein adsorption to nitrocellulose. The process involved is analogous to protein printing for immobilization in 2DPN assays, and so the information provided can be applied directly to protein adsorption in assay development. Furthermore, this method is much more simple, streamlined, and high-throughput than the lateral flow depletion protocol described in section 4.3. However, assessing protein adsorption to membranes by comparing the printed spot sizes is still only a qualitative comparison of adsorption rate and strength, because the underlying system is much more complex than our analysis allows us to examine. We can quantitatively compare the sizes of spots, but do not yet have a way to translate that information into quantitative differences in adsorption. To begin to delve into those complexities, we have developed a computational model of adsorption, based on the printing model described in Chapter 3, which is described in the next section.

4.5 Computational model of protein adsorption during spotting

One of our primary objectives in the development of methods to study protein adsorption to nitrocellulose was to create a mechanism to quantitatively compare the underlying behavior of different proteins. While quantifying protein spot sizes as described in 4.4 yields *qualitative* differences in protein adsorption, a computational model could be used to provide relative adsorption rates, based on the quantitative spot area data.

4.5.1 Model components and parameters

Physics

This model is based on the printing model described in Chapter 3. The Darcy Flow parameters are unchanged from that initial model. However, because of the way that Comsol handles transport and binding in porous media, we can not define surface reactions at the microscope membrane surface—to Comsol, those surfaces don't exist, the porous network is only defined mathematically to the extent that it affects fluid velocity and transport. Therefore, to incorporate protein adsorption to the surface, we have added additional species: sites of nitrocellulose available to adsorb protein (N), and nitrocellulose-adsorbed-protein (A), and within the Comsol model settings we have disabled any kind of convective transport to ensure that these species are immobile. On the other hand, the protein of interest (P) is introduced with the printed liquid at the model inlet, and is carried by the convective flow within the membrane.

Throughout the model membrane space the following reaction is applied:

$$N + P \underset{k_{off}}{\overset{k_{on}}{\rightleftharpoons}} A$$

For conservation of species, the reaction rate of each is described by:

$$\frac{dN}{dt} = k_{off}[A] - k_{on}[N][P]$$

$$\frac{dP}{dt} = k_{off}[A] - k_{on}[N][P]$$

$$\frac{dA}{dt} = -k_{off}[A] + k_{on}[N][P]$$

Parameters

The parameters used within the model are essential to the model's ability to yield meaningful results that describe the physical conditions in real experiments. For that reason, all parameters were determined based on reasonable theoretical calculations and experiments, with the exception of the on- and off-rates, which we were seeking to approximate. The rate parameters were varied across a range of values, but their initial values were approximated based on literature values of antibody binding interactions (k_{on}~10^4–10^6 $M^{-1}s^{-1}$) [139, 140]. All of the flow parameters were described in Chapter 3. One minor modification however, was for this model the membrane thickness was adjusted to 120 μm, because a slightly thicker membrane (Millipore HF135, Billerica, MA) was used for the real-time rinsing experiments. The parameters added to describe protein adsorption are listed in Table 4.

Table 4: Adsorption model parameters

Parameters	Meaning	Value
D_P	Diffusivity of the protein	1 x10^{-10} [m^2/s]
N_0	Initial concentration of adsorption sites	*IgG*: 1.5 x 10^{-5} M *BSA & PG*: 3 x 10^{-5} M
k_{on}	On-rate of adsorption	Varied between 10^4–10^6 [$M^{-1}s^{-1}$]
k_{off}	Off-rate of desorption	10^{-3} [s^{-1}]
C_{in}	Inlet concentration of protein (0.5, 1, 2 mg/ml converted to M)	*IgG*: 3.3 μM, 6.7 μM, 13.3 μM *BSA & PG*: 7.7 μM, 15.4 μM, 30.8 μM

The diffusivity of the protein, D_P, was chosen based on previous experiments by Jennifer Osborn, that showed that the apparent diffusivity of proteins in nitrocellulose membranes was enhanced by mechanical dispersion due to the presence of the pores within the membrane [79].

The initial concentration of available sites for protein adsorption was approximated using two methods: first, we calculated a number based on known values, and second we estimated the saturation level, based on IgG spotting experiments. To calculate the value, we approximated IgG as a 10 nm sphere and calculated how many IgGs could fit in one square meter: 1.7 x 10^{-8} moles IgG. To convert this to a concentration of adsorption sites in moles/L, we need to calculate the total surface area in a liter volume of nitrocellulose. Assuming a membrane surface area ratio of 100 (internal surface area: frontal surface area), we approximate one square meter of frontal area to have an internal area of 100 m^2, which means that 1.7 x 10^{-6} moles of IgG can adsorb within one square meter of nitrocellulose membrane. Next, a membrane thickness of roughly 100 μm yields a volume of

0.1 L per frontal meter squared of nitrocellulose, so the "concentration" of adsorption sites is 1.7 x 10^{-5} M.

Using our second method, we used the rinsed printed IgG spots at 2 mg/ml, which appeared to be close to saturation, to approximate the amount of IgG required to saturate a volume of nitrocellulose. The spot area was 4.5 mm^2; with a thickness of 100µm, the spot volume is 0.45 µl. Printing 500 nL of IgG at 2 mg/ml yields 1 µg IgG. That mass of IgG in a volume of 0.27 µl gives a concentration of 1.5 x 10^{-5} M, which is remarkably close to our prior estimate. For the purposes of the model, we used 1.5 x 10^{-5} M as the N_{sites} parameter that described the initial number of sites available for adsorption.

BSA and Protein G are smaller than IgG. Both have a molecular weight of roughly 65 kDa, and the published dimensions of BSA are 4x4x14 nm [141].Performing a calculation analogous to the first approximation above, assuming square packing of BSA, with all proteins flat on the membrane in the 14x4 nm dimension, we approximated the maximum surface coverage to be 1.8x as many sites as when IgG is adsorbed. If the protein is approximated as a sphere with a 7 nm diameter, this ratio is 1.96x. For the purposes of the model, 2x the IgG value, or 3 x 10^{-5} M was used as the approximate number of available sites.

The initial concentration of adsorbed protein was set to zero everywhere in the model; the initial concentration of protein, C, was set to zero within the model membrane space and to C_{in} at the inlet. Additionally, to model the real-time rinsing condition, the inlet concentration was set to a step function: for $0<t<2$ seconds, C_{in} was set to a variety of values, but for $2<t<6$ seconds, $C_{in}= 0$ to simulate the 1 µl of water used as a rinse.

Initially the off-rate parameter was varied from 10^{-4}–10^{-2} s^{-1}, however we observed that even at the lowest relevant protein concentration, at the lowest on-rate that we tested, the effects of varying the off-rate were minimal (see Figure 39). Therefore, we set the off-rate to 10^{-3} s^{-1} for the remainder of the simulations to decrease the required number of varied parameters and therefore computation time. This lack of variation makes logical sense, as the timescale of the experiments was <5 seconds, much shorter than the relevant timescale of those off-rates.

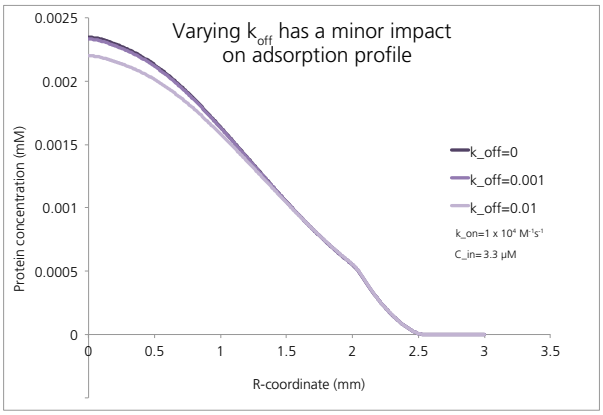

Figure 39: Distribution of protein adsorbed to the membrane, with varying k_off. Even when k_off is relatively rapid, at 0.01 s^{-1}, there is a minimal impact on the distribution of adsorbed protein, therefore this parameter was set to 0.001 s^{-1} for the remainder of the simulations.

4.5.2 Comparison between model and experimental results

Quantification of spot line profiles

Comsol model results were compared to radial line plots measured from the experimental "real time rinsing" data described in 4.4.

Line profiles for each spot were quantified in the following manner:

1. Two linear regions of interest were drawn across each spot in ImageJ: one horizontal and one vertical, taking care to center them at the center of each spot.
2. The line plot profile was acquired for each ROI, and the values were copied into Excel.
3. Membrane background levels were quantified using similar line profiles
    a. Backgrounds were averaged for each set of printing experiments to yield a single background value (i.e for each protein at each concentration)
    b. The standard deviation ($\sigma_{background}$) of all background values was calculated, and normalized by 255.

4. All values were inverted by subtracting the value from the background, and then normalized by 255.
5. All line profiles were plotted to ensure line profiles were aligned (not offset slightly) and could be averaged
6. Re-aligned profiles were averaged, resulting in an overall overage line profile.
    a. The standard deviation (σ_{signal}) was calculated at each position along the line profile
7. All values less than 5% of the maximum value for a given plot were set to zero for that line plot.
8. Lines were plotted with error bars indicating the overall normalized standard deviation ($\sigma_{signal} + \sigma_{background}$)

Model Quantification

Protein concentration data for all r-positions at the top (z=120μm) surface of the membrane were exported from Comsol and plotted in Excel. Two different concentrations are interesting for this analysis: the amount adsorbed to the membrane, "A", and the free protein "P". The sum of these two numbers represents the overall amount of protein at any given location. We chose to examine this "A+P" variable, because as described above in 4.4, we hypothesized that in non-rinsed spots, a portion of protein near the center of the spots does not adsorb to the membrane in the initial liquid deposition, but then as the liquid evaporates it either (a) adsorbs within that original wetted area, or (b) it dries in place, but is not adsorbed and therefore rinses away once the membrane is wetted (e.g. during staining), or (c) some combination of (a) and (b). If we monitored only the adsorbed protein in the simulation, that assumption would completely neglect any adsorption during the evaporation process. Therefore, we will discuss the model-predicted distribution of both "A" and "A+P", and note the instances where those numbers differ.

IgG model and experimental comparison

The simulation was performed using the parameters described above for IgG, sweeping through six k_{on} values: $1x10^4\ M^{-1}s^{-1}$, $2x10^4\ M^{-1}s^{-1}$, $5x10^4\ M^{-1}s^{-1}$, $10x10^4\ M^{-1}s^{-1}$, $25x10^4\ M^{-1}s^{-1}$, $100x10^4\ M^{-1}s^{-1}$. The resulting protein concentration distributions for the lowest IgG concentration (0.5 mg/ml) are shown in Figure 40.

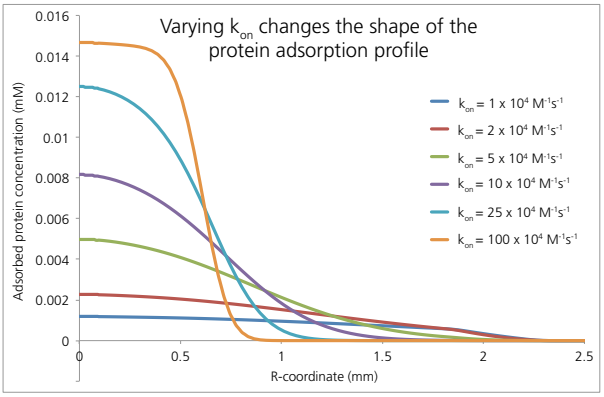

Figure 40: Varying the k_{on} parameter changes the shape of the protein adsorption curve: higher k_{on} values increase the rate of adsorption and allow the protein to saturate the membrane (orange curve) whereas with lower k_{on} values, the protein flows outward more rapidly than it can saturate the surface.

The best match to the IgG adsorption data is $k_{on} = 25x10^4\ M^{-1}s^{-1}$, based on the data features such as surface saturation of the 1 mg/ml spots from r=0 to roughly r=0.8, and the 2 mg/ml spots from r=0 to roughly r=1 (Figure 41). Also, the 0.5 mg/ml spots do not completely saturate to the same level that the 1 mg/ml and 2 mg/ml spots do, which is clearly shown in the model simulation (Figure 41B). In this case, where the model represents the rapid adsorption of IgG, the concentration of free protein is negligible (A≈A+P, as can be seen when comparing the solid and dashed lines in Figure 41B). This supports our hypothesis that the real-time rinse pushes the protein outward to areas of the membrane that are not yet saturated, where it adsorbs to the membrane as it flows outward.

The most obvious difference between the model and the experiment is the approximate spot radii predicted by the model versus those observed experimentally. In the experimental data, the radii are r~0.7 mm, 1mm, and 1.3mm, whereas the model predicts radii of roughly

1 mm, 1.2 mm and 1.5 mm. We hypothesize that this discrepancy is due to underestimating the N_{sites} parameter. This parameter has a significant impact on the eventual spot radius, which will be discussed later in this chapter.

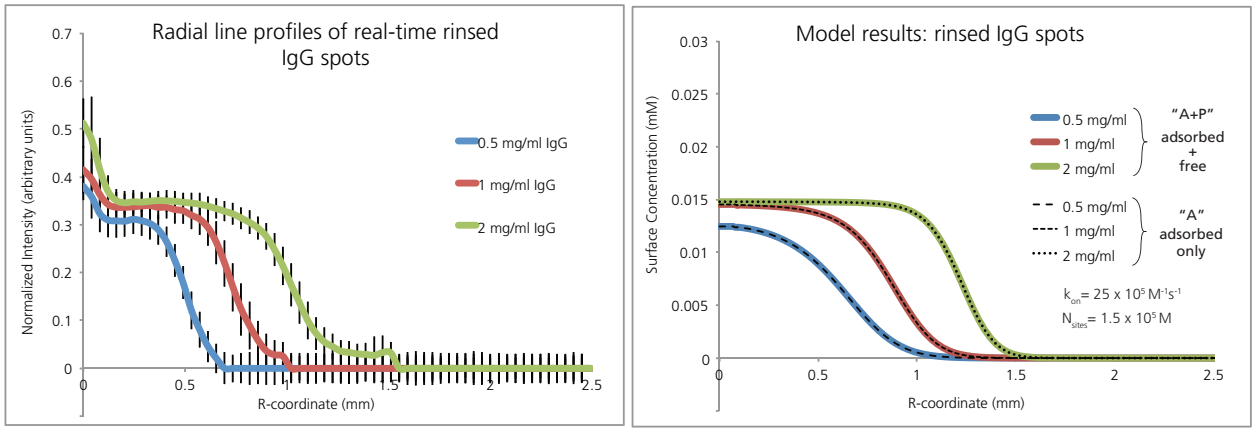

Figure 41: Experimental data from Ponceau S stained "real-time rinsed" IgG spots (A) compared with a Comsol Multiphysics computational simulation of protein adsorption in a porous membrane (B). In (A), the error bars indicate standard deviation over 4 spots, measured both vertically and horizontally, resulting in eight measurements for each concentration. In (B) both the adsorbed+free and adsorbed-only are plotted together (solid vs. dashed lines), which are equal in this simulation. Overall, the shapes of the curves are very similar between the experimental case and the simulated case: both the 1 mg/ml and 2 mg/ml samples saturate the membrane, but the 0.5 mg/ml sample does not. One notable difference between the model and the experiment is the point at which it appears that the concentration drops to zero—in the experimental data, the 0.5 mg/ml sample appears to drop to zero at r~0.7, whereas the same sample in the simulation does not drop to zero until nearly r~1, similarly, the 1 mg/ml and 2 mg/ml samples also appear to extend outward further in the simulation. We hypothesize that this discrepancy is due to underestimating the N_{sites} parameter. This parameter has a significant impact on the eventual spot radius, which will be discussed later in this chapter. All of the experimentally observed spots have a small spike of intensity at the very center (which can be seen visibly, see Figure 37), which does not appear in the simulations. We hypothesize that the spike is due to the very first droplet imbibing into a bare, dry membrane and adsorbing exceptionally rapidly and densely.

To further delve into the hypothesis that a spot has a significant amount of non-adsorbed protein near its center prior to a real-time rinsing step, we compared our experimental plot profiles of non-rinsed and rinsed spots with simulations. As can be seen in Figure 42, the "No Rinse" experiment is slightly darker and smaller than the "Rinsed" experiment at the same protein concentration, suggesting that some of the free protein in that initially wetted area does adsorb during drying, despite not adsorbing during the initial wetting flow (as evidenced by the lower level of protein in the "Rinsed" experiment: in that case the free

protein is pushed outward by the rinse). The simulated line profiles in Figure 42B are consistent with the experiment: the non-rinsed spot (dark green) is slightly smaller and has a higher concentration of protein than the rinsed spot (light green). Furthermore, the level of adsorbed-only protein in the no-rinse case (dashed line) has saturated the surface, and is lower than the total amount of adsorbed+free protein (dark green), while in the rinsed case, all of the protein has adsorbed to the surface (dotted and light green lines).

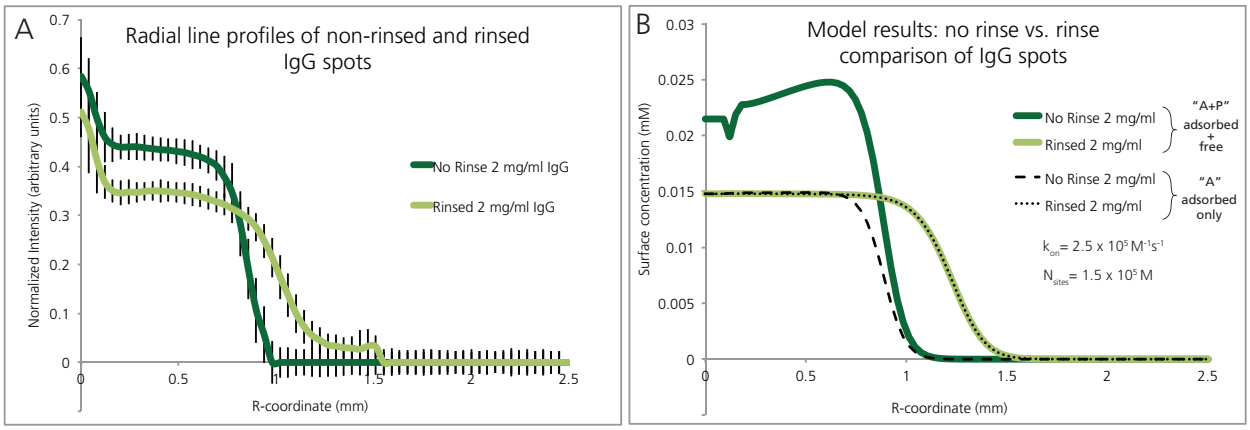

Figure 42: Comparison of non-rinsed (dark green) vs. rinsed (light green) 2 mg/ml IgG spots experimental data (A) and simulated results (B). Error bars in (A) represent standard deviation of eight measurements. In both sets of results, the rinsed spot is larger in size than the non-rinsed spot, and the non-rinsed spot has higher signal intensity. Dashed and dotted lines in (B) indicate the adsorbed-only fraction, and the solid lines indicate the total protein, adsorbed+free. Note that the adsorbed-only fraction is equal to total protein in the case of rinsed spots (light green and dotted lines), whereas in the non-rinsed case, the amount adsorbed (dashed line) has saturated the surface while free protein is also present within the spot. The higher intensity of the non-rinsed spots in the experimental data illustrates that some of this free protein sticks in place during drying and is not displaced upon staining. However, the difference in the relative intensities of the non-rinsed and rinsed spots in the experimental results compared to the simulated case suggests that a portion of the free protein is washed away during staining.

One discrepancy between the simulation and experiment is the large difference in the amount of protein between the simulated "No Rinse" and the simulated "Rinsed" case, when compared to experimental data. This difference could possibly be explained by the imprecise protein staining of Ponceau S not accurately reflecting the relative levels of protein, but the relative levels appear more significant than the imprecision of Ponceau S, which suggests

that not all of the non-adsorbed protein adsorbs during drying and some fraction of non-adsorbed IgG is washed away during staining.

BSA model and experimental comparison

The BSA protein adsorption spots were compared with a model just as described above for IgG. As mentioned in the "Parameters" section, above, because BSA is smaller than IgG, we adjusted the concentration of available sites (N_{sites}) and the inlet concentration (C_{in}) accordingly. As with IgG, the simulation was performed with six different k_{on} values, and the shapes of the plot profiles were compared visually to approximate the relevant k_{on}. Figure 43 shows the comparison between model results and experimental data using $K_{on} = 2 \times 10^4\ M^{-1}s^{-1}$.

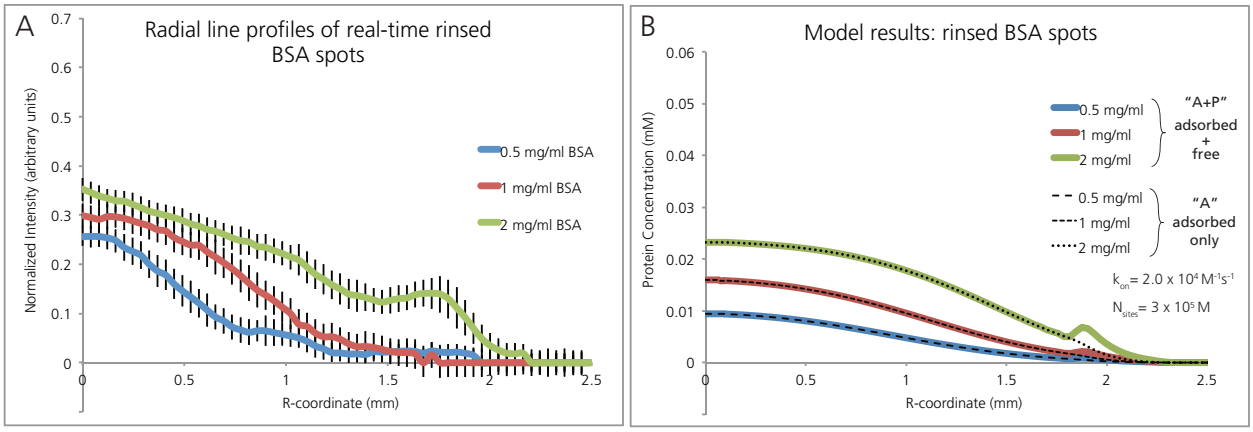

Figure 43: Experimental data from Ponceau S stained "real-time rinsed" BSA spots (A), compared with a Comsol Multiphysics computational simulation of protein adsorption in a porous membrane (B). In (A), the error bars indicate standard deviation over four spots, measured both vertically and horizontally, resulting in eight measurements for each concentration. In (B) both the adsorbed+free and adsorbed-only are plotted together (solid vs. dashed lines), and are almost equal, except for the slight bump at the outermost edge of the spot (particularly the 2 mg/ml spot, light green line), which is composed of free protein in the simulation. This bump is very consistent with the experimentally observed line profile in (A), suggesting that the fraction of free protein at the edge adsorbs during evaporation.

The most notable aspect of this comparison is the slight bump at the outermost edge of both the simulated and experimental 2 mg/ml spots. In the simulation, this bump consists of non-adsorbed protein that was pushed outward by the real-time rinse—evidenced by the

comparison between the total adsorbed+free protein (solid line) and the adsorbed-only fraction (dotted line)—which is again very consistent with our theory that not all of the protein in the center of a spot adsorbs during printing, and that a significant amount adsorbs during drying. This is particularly true for a slow-adsorbing protein like BSA, which does not approach saturating the surface during the short time span of printing, as illustrated in Figure 44. As with the IgG spots, the non-rinsed spot (dark green line) is smaller and darker than the rinsed spot (light green line) in both the experimental and simulated results. Again, the simulated non-rinsed spot contains a significant amount of free protein (comparing the dark green line with the dashed line in Figure 44). Some of this free protein adsorbs during evaporation, leading to the darker non-rinsed spots, but a portion also is likely washed away during staining, which is suggested by the smaller difference between the experimentally measured spot intensities versus the simulation.

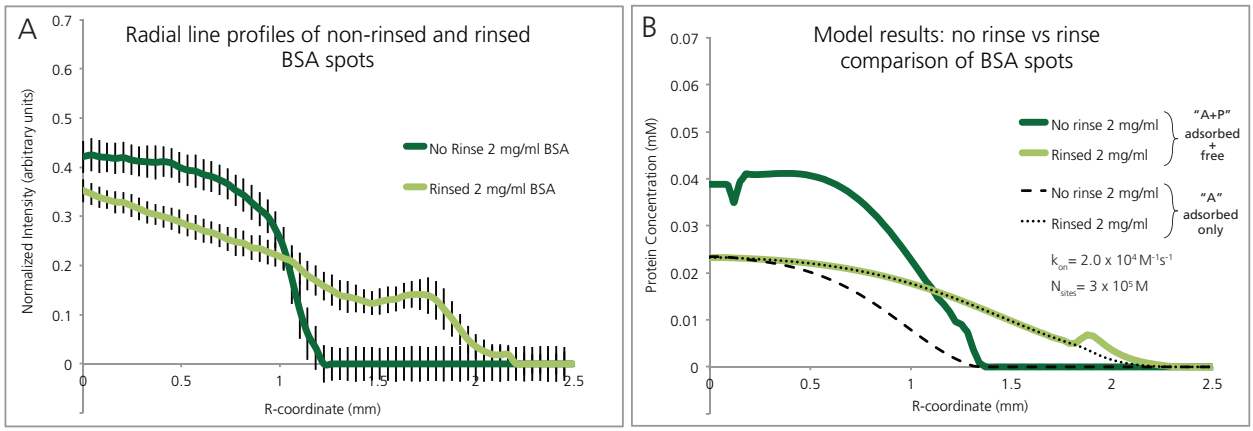

Figure 44: Comparison of non-rinsed (dark green) vs. rinsed (light green) 2 mg/ml BSA spots experimental data (A) and simulated results (B). Error bars in (A) represent standard deviation of eight measurements. In both sets of results, the rinsed spot is larger in size than the non-rinsed spot, and the non-rinsed spot has higher signal intensity. Dashed and dotted lines in (B) indicate the adsorbed-only fraction, and the solid lines indicate the total protein, adsorbed+free. Note that the adsorbed-only fraction is nearly equal to total protein in the case of rinsed spots (light green and dotted lines), except for the small bump of free protein toward the edge, which appears to adsorb in place during drying. Conversely in the non-rinsed case, the amount adsorbed (dashed line) has saturated the surface while free protein is also present within the spot. The higher intensity of the non-rinsed spots in the experimental data illustrates that some of this free protein sticks in place during drying and is not displaced upon staining. However, the difference in the relative intensities of the non-rinsed and rinsed spots in the experimental results compared to the simulated case suggests that a portion of the free protein is washed away during staining.

Protein G model and experimental comparison

Protein G is comparable in size to BSA, so the same concentration of available sites (N_{sites}) and the inlet concentration (C_{in}) were used for the Protein G simulation as were used for BSA. As with IgG and BSA, the simulation was performed with six different k_{on} values, and the shapes of the plot profiles were compared visually to approximate the relevant k_{on}. The comparison between model results and experimental data using $k_{on} = 10 \times 10^4\ M^{-1}s^{-1}$ is shown in Figure 45.

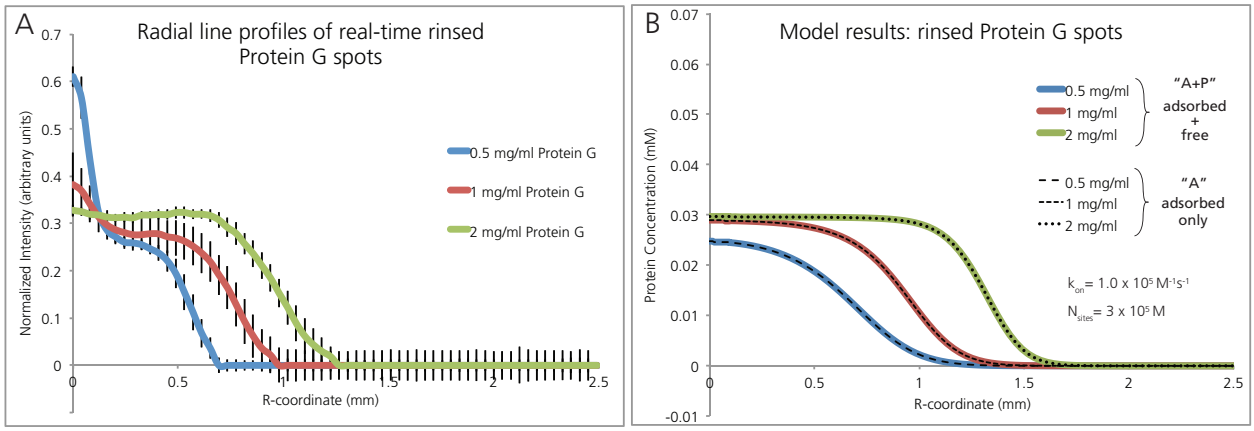

Figure 45: Experimental data from Ponceau S stained "real-time rinsed" Protein G spots (A), compared with a Comsol Multiphysics computational simulation of protein adsorption in a porous membrane (B). In (A), the error bars indicate standard deviation over four spots, measured both vertically and horizontally, resulting in eight measurements for each concentration. In (B) the adsorbed+free and adsorbed-only protein concentrations are equal, and are plotted together (solid vs. dashed lines). Generally, the simulated line profiles exhibit the same shape characteristics as the experimentally observed profiles, however, as observed in the IgG model-experiment comparison, the simulated spot sizes for Protein G are somewhat larger than the experimentally observed spots (simulated spot radii ~1 mm, 1.2 mm, and 1.5 mm, whereas experimentally observed radii ~0.7 mm, 1 mm, 1.3 mm), which we hypothesize is due to an underestimation of the number of available sites on the membrane surface. Figure 47 illustrates the impact of the N_{sites} parameter on the resulting spot sizes. As with the IgG spots, there is a sharp spike in intensity at the center of some of the Protein G spots, which we hypothesize is due to the first droplet striking a bare, dry membrane and adsorbing in a multilayer very rapidly, however, further experiments would be needed to confirm that theory, and examine why some spots do not exhibit this spike.

Generally, the simulated line profiles exhibit the same shape characteristics as the experimentally observed profiles. However, as observed in the IgG model-experiment comparison, the simulated spot sizes for Protein G are somewhat larger than the experimentally observed spots (simulated spot radii ~1 mm, 1.2 mm, and 1.5 mm, whereas experimentally observed radii ~0.7 mm, 1 mm, 1.3 mm), which we hypothesize is due to an underestimation of the number of available sites on the membrane surface, which will be discussed further later in this chapter.

Next, we compared the non-rinsed and rinsed Protein G spots with the corresponding simulations (Figure 46). This comparison is very similar to the comparison in the case of IgG rinsed and non-rinsed spots: both the experimental and simulated non-rinsed spots are

slightly darker and smaller than the rinsed spots at the same protein concentration. In the simulation, all of the protein in the rinsed spot has adsorbed to the surface (dotted and light green lines), but the level of adsorbed-only protein in the no-rinse case (dashed line) has saturated the surface and is lower than the total amount of adsorbed+free protein (dark green). The higher intensity of the non-rinsed experimental spot suggests that some of the free protein in that initially wetted area does adsorb during drying, despite not adsorbing during the initial wetting flow, however the differences in the relative intensity of the rinsed and non-rinsed spots in the experimental versus simulated cases suggests that some fraction of the free protein is washed away during staining (as was also hypothesized with the IgG and BSA results).

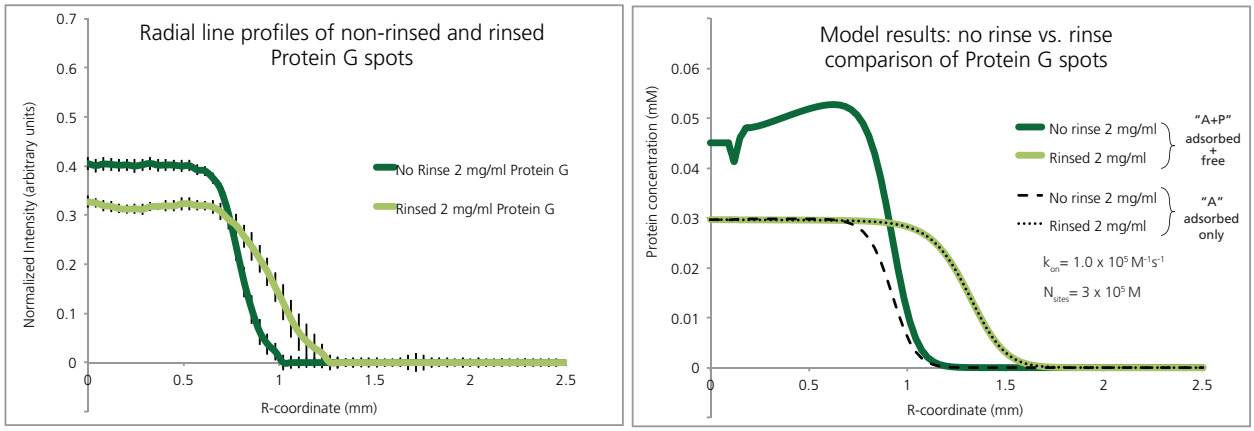

Figure 46: Comparison of non-rinsed (dark green) vs. rinsed (light green) 2 mg/ml Protein spots experimental data (A) and simulated results (B). Error bars in (A) represent standard deviation of eight measurements. In both sets of results, the rinsed spot is larger in size than the non-rinsed spot, and the non-rinsed spot has higher signal intensity. Dashed and dotted lines in (B) indicate the adsorbed-only fraction, and the solid lines indicate the total protein, adsorbed+free. Note that the adsorbed-only fraction is equal to total protein in the case of rinsed spots (light green and dotted lines), whereas in the non-rinsed case, the amount adsorbed (dashed line) has saturated the surface while free protein is also present within the spot, resulting in a higher level of total protein (dark green line). The higher intensity of the non-rinsed spots in the experimental data illustrates that some of this free protein sticks in place during drying and is not displaced upon staining. However, the difference in the relative intensities of the non-rinsed and rinsed spots in the experimental results compared to the simulated case suggests that a portion of the free protein is washed away during staining.

4.5.3 Insights from model

Some general observations arise from the comparisons between the simulated protein adsorption model and the experimental data. Overall, the model reproduces the experimental data quite well based on our approximated input parameters, such as N_{sites}, C_{in}, and the initial range of k_{on} values.

There were some obvious discrepancies between the model results and experimental data, however. Simulated non-rinsed spots showed higher relative amount of total protein versus the rinsed spots, when compared to the relative intensities of experimentally measured spots. This difference further supports our theory that experimentally, some of the free protein present within the non-rinsed spot is washed away during staining while another fraction of the free protein sticks in place during drying, leaving less protein in the non-rinsed spots than predicted by the simulation.

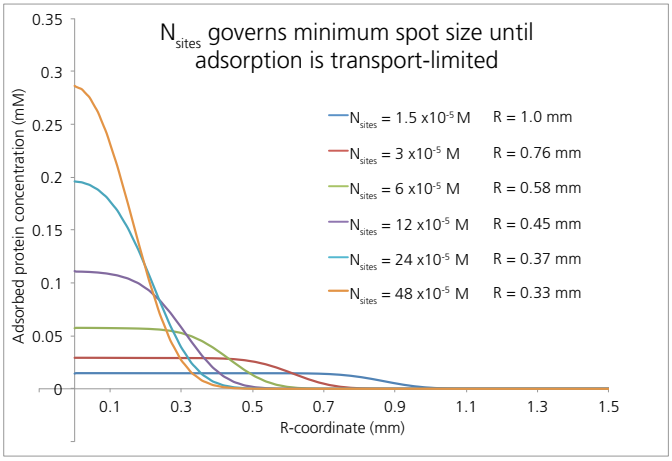

Figure 47: Simulated line profiles of rinsed spots for varying N_{sites} values. For values below 24 x 10^{-5} M, N_{sites} limits the minimum possible spot radius, due to protein saturation of the surface. However, when N_{sites} is 24 x 10^{-5} M or larger, protein adsorption is transport-limited, and increasing the N_{sites} parameters has a diminishing effect on the minimum spot size. The balance between transport-limited and saturation-limited is dependent on the inlet concentration though, and a very high inlet concentration would remain saturation-limited at a higher N_{sites} value. Here C_{in} was 6.7 μM and k_{on} was 250 $M^{-1}s^{-1}$.

The most notable difference between the model and the experimental results however, is the predicted size of spots, especially in the IgG and Protein G sets. In the model-experiment comparisons of rinsed spots above (Figure 41 and Figure 45), the model consistently predicts larger spots than were observed experimentally. We attribute this discrepancy to an underestimation of the number of available sites (N_{sites}), because this

parameter defines the maximum concentration of protein possible on the surface, which governs the minimum possible size of spots, particularly at higher on-rates where the membrane is quickly saturated. The relationship between N_{sites} and spot radius is illustrated in Figure 47, which demonstrates the inverse relationship between N_{sites} and minimum spot radius by showing adsorbed protein profiles of simulated rinsed spots at a variety of N_{sites} values, with constant k_{on} (25×10^4 $M^{-1}s^{-1}$) and C_{in} (6.7 µM, or 1 mg/ml IgG). These profiles have a similar shape: a saturated plateau at the N_{sites} value, and then a steep decline to zero once the protein is depleted from solution. The line profiles of the highest N_{sites} parameters (24×10^{-5} M and 48×10^{-5} M) are an exception to this pattern: in those cases, the protein does not quite saturate the surface because the protein adsorption is transport-limited. Once transport limits the rate of adsorption, saturation and N_{sites} no longer governs the minimum spot radius, however the N_{sites} values at which this occurs are much, much larger than those relevant for the adsorption questions we are discussing here.

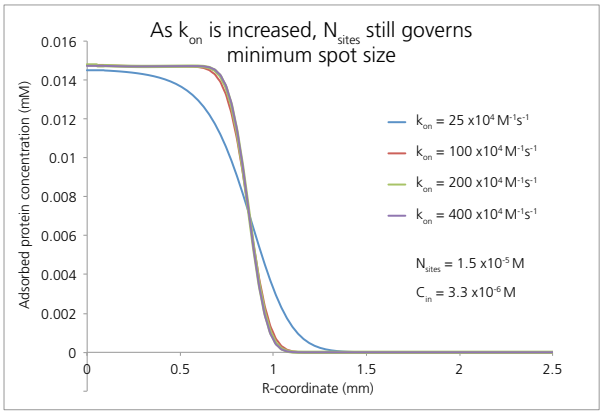

Figure 48: Increasing k_{on} does not result in smaller spots once the membrane has saturated. Here, protein adsorption profiles for rinsed spots at C_{in} = 3.3. µM and N_{sites} = 1.5×10^{-5} M, are plotted for increasingly rapid k_{on} values, and the spot size does not decrease, due to the protein fully saturating the membrane.

Conversely, the k_{on} value alters the shape of the adsorption profile and, in doing so, affects the spot radius value, which was shown earlier in Figure 40. In those simulated spots however, the *steepness* of the adsorbed protein line profile changes, rather than the saturation point. There, only the highest k_{on} value (100×10^4 $M^{-1}s^{-1}$) approached membrane

saturation, and the lower k_{on} values resulted in less and less fractional surface coverage, and therefore larger spots. The smallest possible spot is still limited by the number of sites available—as k_{on} is increased further, the spot size does not decrease indefinitely (shown in Figure 48, with C_{in}= 3.3 μM and N_{sites}=1.5 x 10^{-5} M), rather the steepness of the depletion increases, coming closer and closer to the "perfectly adsorbing protein" example illustrated in Figure 32. This further illustrates why it is likely that underestimating N_{sites} (rather than underestimating k_{on}) is the root cause of the too-large predicted spots within the simulation.

The system parameters that were estimated based on literature values, measured quantities and experimental results, yielded a model that fits reasonably well to our experimental results and this computational simulation provides useful insights into the transport and adsorption processes occurring as a protein adsorbs to nitrocellulose during printing. However, a very interesting future step for this work would be to use the Matlab-Comsol LiveLink package to sweep across a range of possible N_{sites} and k_{on} values, while running a non-linear fitting algorithm with experimentally observed data for each protein across all concentrations used in the experiments, to optimize more precisely determine approximate values for both parameters.

4.6 Conclusions

In this chapter we have developed a set of simple and quantitative methods to probe and evaluate a wide variety of protein-nitrocellulose interactions: printing protein solutions onto nitrocellulose membranes, and measuring the distribution of protein that adsorbs to the membrane during the printing process. This method is simple to perform and relatively high-throughput—several proteins at several concentrations can be printed in a single afternoon. It is not inherently quantitative, however, because even quantitative

comparisons between spot sizes only reflect a qualitative comparison of the underlying adsorption phenomena. Introducing a computational model of the system provides quantitative insight into the meaning behind spot sizes and radial protein distribution by approximating the on-rate of adsorption. The model described here is just a first step towards fully quantitative interpretations of protein-printing data; with improved parameter fitting and better estimates of surface capacity, these tools could be used have across many facets of assay design. As our collaborators design better analyte capture species, these methods can be used to evaluate the surface adsorption properties of novel proteins; or, these methods can be used to probe a wide range of protein adsorption interactions, to better understand what attributes enhance or reduce the rate of adsorption. These techniques could even be used to probe *specific* binding interactions, such as antibody-antigen binding, in nitrocellulose, since it is likely that SPR measurements do not accurately reflect the complex system of a porous matrix.

5 Spatial and temporal control of the rehydration of dried reagents patterned on porous devices

5.1 Objectives and Motivation

A critical aspect of designing diagnostics for low-resource settings is to have all reagents included on the device in dry form. The use of dry reagents reduces user steps, removes the need for a cold chain, and facilitates device automation. Traditionally, reagents have been stored dry within separate pad material that is placed in line with the fluidic pathways for rehydration at the time of use. For example, antibodies conjugated to gold particle labels have been stored dry in polyester pads in both conventional microfluidic [100] and lateral flow [22, 44] devices. However, the use of these separate pads has two significant disadvantages: it offers minimal control over the spatial and temporal release of rehydrated reagent, and it requires additional materials and components that add to manufacturing costs.

Alternative techniques for storing dried reagents could expand the capabilities and lower the costs of paper-based devices. Piezoelectric inkjet printing has previously been used in the manufacture of a variety of biosensors [111, 113], and offers flexibility in the location and number of reagents deposited on devices. In Chapter 5, we develop methods to print reagents directly onto porous materials for controlled rehydration and use in on-paper assays. Specifically, the feasibility of patterning reagents directly onto nitrocellulose for later rehydration has been evaluated and confirmed; methods have been demonstrated that control the spatial and temporal rehydration of patterned reagent; a Comsol Multiphysics® (Comsol, Inc., Burlington, MA) model that predicts rehydration has been developed; the rehydration profiles of patterned sugar depots were characterized; and finally, incompatible reagents were patterned separately and then recombined via rehydration.

5.2 Evaluating the feasibility of patterning reagents directly onto nitrocellulose for later rehydration

5.2.1 Introduction

Before developing methods to vary and control the rehydration of reagents patterned directly onto porous devices, we needed to determine if it would even be possible to achieve consistent and reproducible rehydration of patterned reagents. Evaluating this possibility was fundamental to the success of the entire aim, and was unprecedented—the efficient non-specific binding of proteins by nitrocellulose, which has been used by immunoassay developers to immobilize capture antibodies [22], was an obstacle that needed to be overcome in order for us to store reagents directly on-strip for later rehydration and use in downstream applications.

We identified three sub-goals that together would enable us to determine the overall feasibility of dry reagent storage via patterning directly onto porous devices. First, we examined the process of patterning reagents, to better understand the deposition and subsequent spread of reagents on nitrocellulose.

Second, as previously described, the literature suggests that drying reagents with sugars, particularly sucrose and trehalose, can improve long-term viability and storage [100-102]. Additionally, we hypothesized that the inclusion of bovine serum albumin (BSA) with the patterned reagent would help minimize non-specific binding of reagent at the patterned spots. For these reasons, we characterized the impact of adding sucrose, trehalose and BSA to reagents prior to patterning to improve the uniformity and reproducibility of rehydration.

Third, because nitrocellulose membranes exhibit such extensive non-specific binding, we needed to determine appropriate membrane blocking conditions to prevent patterned reagents from sticking irreversibly to the initially patterned spot, or sticking to downstream regions after rehydration.

5.2.2 Methods

Device patterning and construction

All porous devices consisted of backed 8 μm pore diameter nitrocellulose membranes (Millipore Hi Flow Plus 135, Billerica, MA) cut using a CO_2 laser (Universal Laser Systems, Scottsdale, AZ) to either 5mm x 50mm or 10mm x 50mm, as described previously [130]. Devices designs were drawn in AutoCAD (Autodesk, San Rafael, CA). The blocking protocol varied extensively; strips were blocked in 1% BSA+ 0.05% Tween in one of the following solutions: 1x phosphate buffered saline (PBS), 0.5x PBS, 0.1x PBS or DI water. Then strips were either dried, or rinsed in either DI water or DI water + 0.05% Tween, and then dried. Drying conditions were also varied: 37°C oven for 1 hour, 2 hours, or 24 hours, or not dried in the oven, but instead placed directly into a desiccator at room temperature. Alternatively, some strips were not blocked in advance, but rather "dynamically blocked" using a 10 μl bolus of fetal bovine serum (FBS) introduced immediately prior to wet-out with PBS buffer.

Alexafluor-488-labeled streptavidin (488SA) (Invitrogen, Carlsbad, CA) was used as a model protein, and was patterned onto strips using a piezoelectric noncontact printer (SciFLEXARRAYER S3, Scienion AG, Berlin, Germany). Typical droplet volumes were approximately 350–400 pl, though 40–100 droplets were usually patterned into a single spot, leading to spot volumes of 14-35 nl. After printing, strips were wrapped in foil to protect them from light, and then dried in a desiccator overnight and stored until use.

Rehydration of patterned spots and image collection

To set up experiments, nitrocellulose strips were affixed to a black poly(methylmethacrylate) (PMMA) substrate using double-sided tape (3M, St. Paul, MN). An untreated cellulose pad (Millipore, Billerica, MA; Whatman, Maidstone, Kent, UK), cut using the CO_2 laser, was placed at the downstream end of each strip as an "infinite" sink to drive continuous wicking. In experiments in which dynamic blocking was used, a polyester pad (Ahlstrom, Helsinki, Finland), also cut using the CO_2 laser, was placed at the upstream end of each strip. The polyester was pretreated with a solution composed of 0.25% Brij®, 0.5% BSA, and 100 mMTris, adjusted to a pH of 8.2, then dried for 2 h at 37 ºC and stored in a desiccator until use.

Cellulose strips were used to connect the device to a well containing PBS, which provided continuous flow. Small blocks of PMMA were placed over the cellulose strips to ensure consistent contact with the device. In traditionally blocked experiments, this cellulose strip was contacted directly to the nitrocellulose; in dynamically blocked experiments, 10 μl FBS was applied to the polyester pad, and then the cellulose strip was immediately contacted to the polyester pad, thereby starting flow through the device.

Experiments were conducted in a light-tight box, illuminated by a pair of blue LEDs positioned to minimize reflections. Uncompressed videos for analysis were acquired with a web camera (Logitech, Fremont, CA) fitted with a 550 nm high-pass filter (FEL0550, Thor labs, Newton, NJ).

Image analysis

The fluorescence of the 488SA was used as a visual marker of the protein's location after rehydration from its printed location. Uncompressed .avi files were analyzed with ImageJ

(NIH, Bethesda, MD [118]). When individual spots were analyzed, spot size was calculated using the "analyze particles" tool in ImageJ, selecting particles with circularity 0.5–1.0, and size 200–6000 px^2. Prior to analyzing particles, images were converted to black and white, using the dark background preset in ImageJ, with a minimum threshold of 55.

5.2.3 Results and Discussion

Characterization of rehydration of lines patterned onto nitrocellulose

One major consideration in the patterning of reagents for dry storage is the problem of achieving sufficient quantities of reagent to perform the assay in question. For that reason, initially we tried patterning a line of fluorescein across the strip, perpendicular to flow, to maximize the amount of reagent deposited in a given area. This pattern resulted in very non-uniform rehydration however, because the line of fluorescein disturbed flow across the strip then broke through randomly, like cracks in a dam (Figure 49). Therefore, later patterns focused on small spots of reagent, to minimize the disruption to the wet-out front caused by the dried reagent depots.

Figure 49: Fluorescein patterned across the width of a strip blocks wet-out,

Characterization of patterned protein spots

Patterning many droplets of protein solution in rapid succession resulted in larger volume spots with increasing size (Figure 50A and B). We hypothesized that the protein did not bind immediately to the nitrocellulose upon printing, but rather wicked outward with the liquid. For this reason, we believed that patterning smaller volumes at a time and then re-patterning the same location after the initial spots had dried would enable us to maintain small spot size, while still patterning increased volumes. Figure 50C shows four spots, all

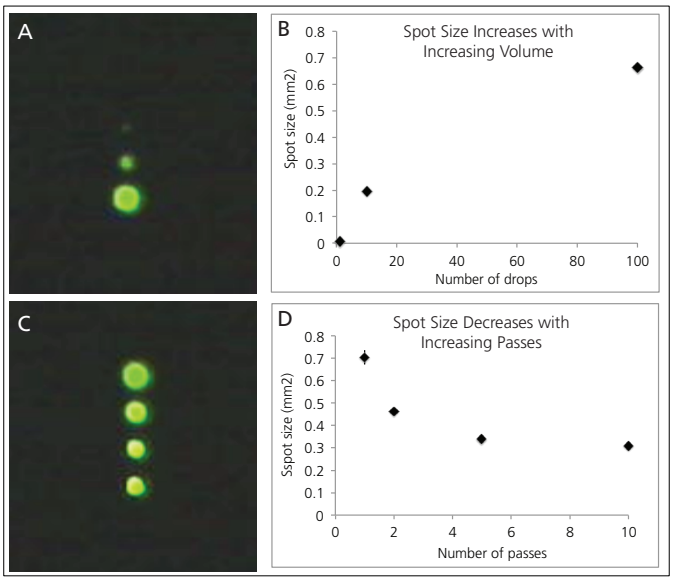

Figure 50:Patterning spots on nitrocellulose. A&B) Increasing the volume of liquid patterned at once clearly increases spot size. C&D) By patterning spots with decreasing the number of droplets deposited at once, but the same total volume spread over multiple passes, we decreased the overall spot size with increasing passes.

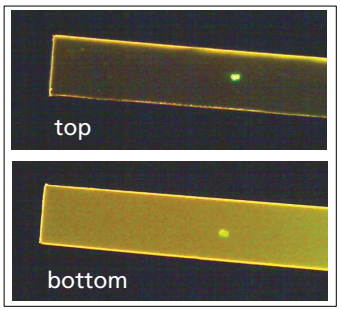

Figure 51: 488SA deposited on nitrocellulose spreads through the thickness of the membrane. The fluorescent spot is visible from both the top and the bottom. The increased fluorescence of the bottom image is due to the autofluorescence of the Mylar backing material.

containing 100 droplets total. Each spot was patterned with varying numbers of droplets at a time—the top spot was 100 droplets at once; the second, two passes of 50 droplets each, spaced one minute apart; the third, five passes of 20 droplets each, spaced one minute apart; the fourth, ten passes of ten droplets each, also spaced one minute apart. The graph shown in Figure 50d illustrates the decrease in spot area with increasing number of passes.

After determining the spread of patterned proteins across the top surface of the nitrocellulose, we determined that the printed 488SA permeated throughout the membrane by imaging both the front and back surfaces (Figure 51). The dramatically increased overall fluorescence of the back of the membrane relative to the front is due to the Mylar backing material, which exhibits significant autofluorescence.

Characterization of additives mixed with protein prior to patterning

To mitigate non-specific binding, we experimented with varying additives, such as sugars and non-specific proteins, mixed with our model protein prior to printing. By including sugars in the dried reagent mixture, the viscosity of the rehydrated reagent solution is increased, and this increase in viscosity has been used to provide control over the dissolution time of reagents dried in storage cavities in polydimethylsiloxane (PDMS) devices [102]. In addition to imparting control over the dissolution of dried reagents, the sugars sucrose and trehalose have been used to stabilize dried proteins [100-102]. The hydroxyl groups of the sugar molecules substitute for the waters of hydration of the protein which are lost upon drying, and act to preserve the protein's native conformation [101]. Additionally, the high glass transition temperature of trehalose (106 ºC) ensures that at elevated temperatures trehalose remains in the glassy state with lower molecular mobility, and thus protects the protein against degradation and crystallization [101, 102].

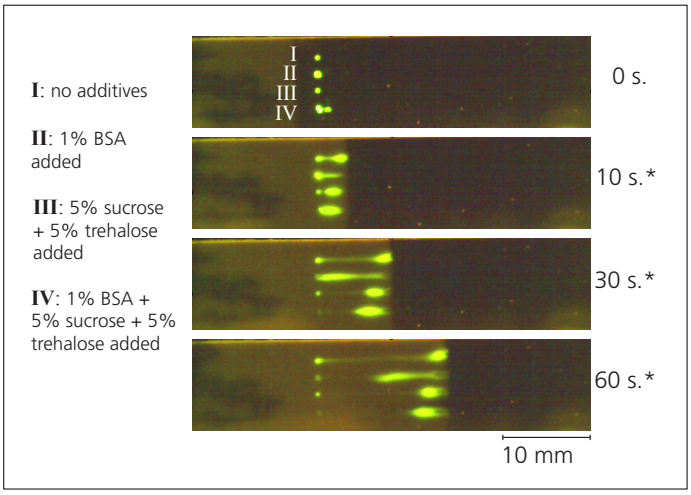

Figure 52: Mixing protein with different additives prior to printing yields dramatically different rehydration profiles. The combination of 5% sucrose, 5% trehalose and 1% BSA minimizes nonspecific binding at the site of printing, while also facilitating rapid rehydration into the wetting front. *time since wetting edge reached the spot.

The final additive mixture included 5% sucrose, 5% trehalose and 1% BSA. Figure 52 shows the different rehydration characteristics imparted by the additives, on a dynamically blocked device. Without any additives, a significant amount of the printed 488SA remains

non-specifically bound to the initial printed location, and the portion that does rehydrate into the fluid front leaves a long streak as it flows. The addition of 1% BSA reduces the amount of non-specifically bound 488SA, but causes a lag in the rehydration of the bulk. Adding only 5% sucrose and 5% trehalose appears to have the opposite effect—the 488SA is dissolved almost immediately into the fluid front, but more remains bound to the nitrocellulose than was with the inclusion of BSA. By adding all three components, a combination of the most desirable characteristics is observed; very little 488SA remains non-specifically bound, while the bulk of the rehydration occurs immediately at the wetting front.

Membrane blocking for rehydration

The blocking protocol used for rehydration needed significant optimization to achieve reproducible and uniform rehydration of printed protein. The initial blocking protocol consisted of blocking for 1 hr in a solution of 1% BSA + 0.05% Tween in 1x PBS, then drying for 1 hour in a 37°C oven. This resulted in non-uniform, highly irreproducible distribution of protein upon rehydration, which was partially due to the uneven wet-out front exhibited by membranes blocked in that manner. We were concerned that drying PBS solutions onto membranes left significant salt residues, which were disrupting wet-out. For that reason, variations to the blocking protocol were explored: we made blocker solutions containing lower concentrations of PBS, we examined the effects of rinsing membranes immediately after blocking, and we

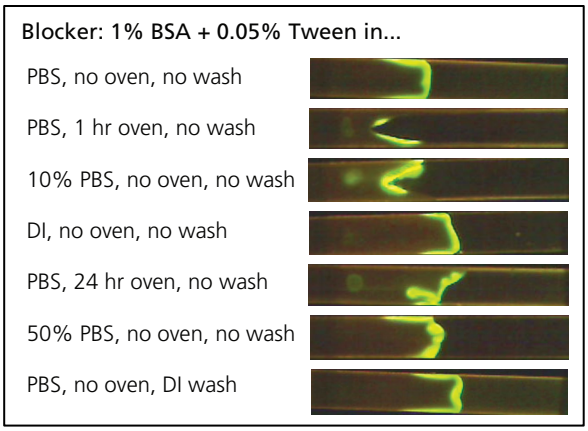

Figure 53: Various blocking protocols lead to uneven rehydration and flow.

varied the amount of time membranes were dried in the oven. Some of the resulting rehydration profiles are illustrated in Figure 53, and it is clear that none of these modifications improved the uniformity of wet-out. For that reason we switched to a dynamic blocking protocol, in which reagents were spotted on unblocked membranes and a 15 µl FBS bolus was applied to the upstream polyester pad at the beginning of the rehydration experiment.

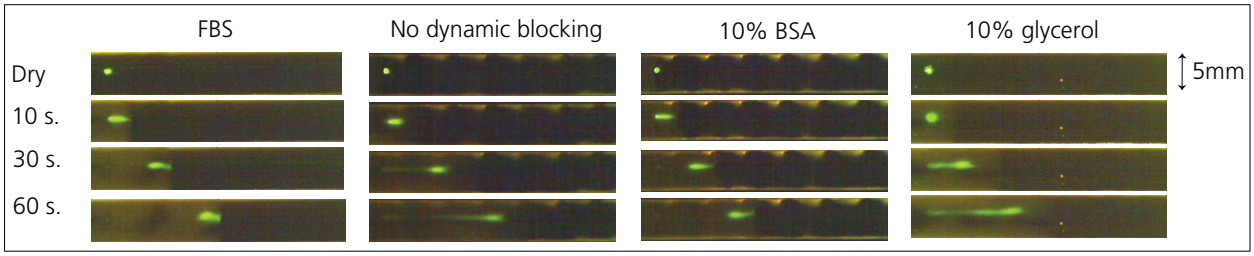

Figure 54: Dynamic blocking using 15 µl FBS before continuous flow of PBS improves wet-out uniformity and consistency of reagent rehydration. No dynamic blocking causes reagent spot to streak as it rehydrates. A pulse of 10% BSA also dynamically blocks the membrane, but 10% glycerol does not. This supports the hypothesis that the dynamic blocking effect is due to proteins in serum and 10% BSA nonspecifically coating the membrane, not the slower wet-out out due to higher viscosity.

The dynamic blocking protocol dramatically improved the uniformity and reproducibility of rehydration. We hypothesized that the dynamic blocking effect was due to the high concentration of proteins present in serum (approximately 6-8.5%, predominantly albumins [142]) non-specifically binding to the nitrocellulose during wet-out, thereby blocking the surface to minimize non-specific binding of the 488SA upon rehydration. To test this hypothesis, we compared 488SA rehydration profiles in unblocked strips, FBS dynamically blocked strips and strips dynamically blocked with 15 µl 10% BSA. Both FBS and 10% BSA dynamically blocked strips showed rapid and uniform rehydration, whereas unblocked strips showed significant streaking and non-specific binding of the 488SA (Figure 54), supporting the hypothesis that the presence of proteins in the dynamic blocker prevents non-specific binding of rehydrated protein. However, both FBS and 10% BSA have higher

viscosity than PBS: serum viscosity is 1.27 +/- 0.06 mPa•s at 37°C [143], 10% BSA viscosity is approximately 1.37 mPa•s [144], whereas the viscosity PBS is approximately that of tap water, (roughly 1 mPa•s at room temperature [145]). Therefore, an alternative hypothesis for the dynamic blocking effect was that the slow wet-out of FBS allowed more efficient dissolution of the dried protein into the wetting front. We tested this hypothesis by using 15 µl of 10% glycerol solution (viscosity = 1.31 mPa•s at 20°C [146]) applied as a dynamic blocker, and compared the results with the FBS and BSA dynamically blocked strips. Glycerol is not an effective dynamic blocking agent, and results in streaking and non-specific binding of 488SA, which further supports our initial hypothesis that the proteins contained in serum are responsible for blocking.

5.3 Development of methods to control the spatial and temporal rehydration of patterned reagents

5.3.1 Introduction

After successfully identifying conditions for reproducibly and uniformly patterning 488SA and rehydrating it directly from nitrocellulose membranes, we became interested in expanding that capability to increase the utility of our patterned reagent storage technique, so that it could be applicable to a variety of different paper-based assay devices.

Specifically, we developed four methods that together constitute a multi-functional tool kit to achieve sophisticated control of the spatial and temporal concentration gradients that are created as the reagent dissolves during capillary flow. First, we demonstrate the creation of uniform reagent pulses from patterned arrays of dried reagent. Second, we show that reagents stored dry in separate regions of the porous matrix can be combined upon rehydration for immediate use in the device. Third, we demonstrate that reagents can be reconstituted sequentially from dry storage depots with tunable delivery times. And fourth,

we show that the total time for dissolution can be varied to achieve a range of reagent delivery times to a downstream region. This work is published in Fridley et al. Lab on a Chip, 2012 [147].

5.3.2 Methods

Device patterning and construction

All porous devices were designed and cut as described above in 5.2.2. Reagents were patterned onto strips using a piezoelectric noncontact printer. After printing, strips were wrapped in foil to protect them from light, and then dried in a desiccator overnight and stored until use.

Spatial and temporal control of reagent dissolution experiments

For the experiments demonstrating the spatial and temporal control of rehydration, the dimensions of strips were either 5mm x 50mm or 10mm x 50mm, and Alexafluor-488-labeled streptavidin (488SA) (Invitrogen, Carlsbad, CA) was used as a model protein. Unless otherwise noted, the 488SA was printed at 0.5 mg/ml, in a solution also containing 1% BSA, 5% sucrose and 5% trehalose. Individual droplet volumes were 350–400pL, and spots were typically patterned with 5–10 drops per spot, with 10 repeat passes spaced one minute apart. This led to printed volumes between 17.5–35 nL. For delayed and extended pulses, 20% sucrose solution was patterned in barriers around spots or directly atop dried spots, to achieve the varying sucrose content described below. Sucrose droplet volumes were roughly 450 pL each. To achieve extremely extended rehydration, 488SA was patterned in 5 spots of 160 nL each, sequentially in the direction of flow. After these spots were dried, 200 nL of 20% sucrose was patterned directly atop each 488SA spot.

To set up experiments, nitrocellulose strips were affixed to a black poly(methylmethacrylate) (PMMA) substrate using double-sided tape (3M, St. Paul, MN). An untreated cellulose pads (Millipore, Billerica, MA; Whatman, Maidstone, Kent, UK), cut using the CO_2 laser, was placed at the downstream end of each strip as an "infinite" sink to drive continuous wicking. A polyester pad (Ahlstrom, Helsinki, Finland), also cut using the CO_2 laser, was placed at the upstream end of each strip. The polyester was pretreated with a solution composed of 0.25% Brij®, 0.5% BSA, and 100 mM Tris, adjusted to a pH of 8.2, then dried for 2 h at 37 ºC and stored in a desiccator until use.

At the start of an experiment, 15 µl fetal bovine serum (FBS) was applied to the polyester pad as a dynamic blocker to prevent non-specific adsorption of reagents to nitrocellulose. Immediately following the addition of FBS, cellulose strips were used to connect the polyester pads to a well containing phosphate buffered saline (PBS), which provided continuous flow through the device. Small blocks of PMMA were placed over the cellulose strips to ensure consistent contact with the device.

Experiments were conducted in a light-tight box, illuminated by a pair of blue LEDs positioned to minimize reflections. Uncompressed videos for analysis were acquired with a web camera (Logitech, Fremont, CA) fitted with a 550 nm high-pass filter (FEL0550, Thor labs, Newton, NJ).

Image analysis

The fluorescence of the 488SA was used as a visual marker of the protein's location after rehydration from its printed location. Uncompressed .avi files were analyzed with ImageJ (U.S. National Institutes of Health [118]) and Matlab (Mathworks, Natick, MA). The green channel of each video was extracted and corrected for (i) background fluorescence by

subtracting an image of the blank membrane, and (ii) non-uniformities caused by lighting or filter transmittance by normalizing with an image of fluorescein-flooded nitrocellulose.

The fluorescence profiles resulting from the combination of rehydrated spots were measured 2.5 cm downstream from the initial spot locations, to allow complete combination to occur. Delay times were determined by subtracting the time at which the control spot reached maximum fluorescence intensity from the time at which the delayed spot reached maximum intensity, at a distance of 1 mm downstream from the initial spot location. The duration of elongated spots was also measured at 1 mm downstream of the initial spot location. The maximum value of the background intensity was quantified, and then doubled to yield a minimum signal threshold; then the time during which the fluorescence signal remained over this threshold was considered the duration of the elongated pulse.

5.3.3 Results and Discussion

Spatially uniform pulses

First, spatially uniform pulses of reagent were created. Pulses such as these must be used in devices to ensure consistency of reagent delivery to downstream locations such as a capture zone. Uniform pulses can be achieved by patterning protein across the nitrocellulose strip, i.e. 90° to the direction of flow. Here, 10 spots were patterned across a strip, at 5 printing passes of 10 drops per spot each. The solution was 0.4 mg/ml 488SA + 5% sucrose + 5% trehalose +1% BSA. As the fluid front reaches these protein spots, the protein is dissolved with the liquid to yield a consistent, near-uniform pulse to a downstream region (Figure 55). By varying the amount of reagent printed in each spot and the number of spots arrayed across the strip, the amount of reagent delivered by the pulse can be tuned to suit the needs of a particular assay. It is important to note that the initial pattern of spots does not affect the resulting pulse: all spots rehydrate into the wetting

front, and diffuse together as long as the y-separation of spots is small, here 0.5 mm. This distance between spots, as well as the amount of reagent printed within each storage spot will affect the uniformity of the resulting pulse.

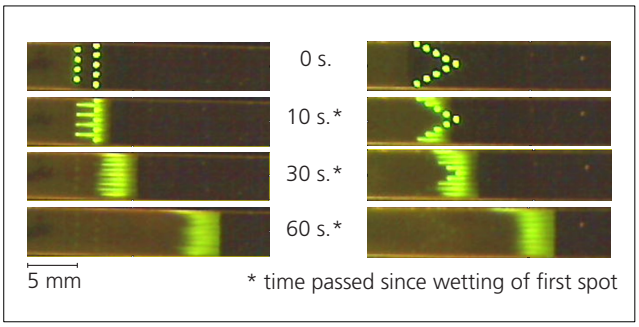

Figure 55: Uniform pulse of rehydrated reagents. Protein patterned perpendicular to the direction of flow rehydrates to form a spatially uniform pulse. The initial pattern does not influence the shape of the resulting pulse, however transverse spot spacing, number of spots and total protein contained in each spot controls the uniformity of the pulse.

Controlled combination upon rehydration

Second, we demonstrated the controlled combination of reagents from separate regions of a device. Printing reagents separately and later combining them facilitates the storage of reagents that must not interact until they are mixed immediately before use in an assay. We accomplished this by patterning protein spots sequentially along a nitrocellulose strip. Ten passes of the 488SA solution were patterned in alternating lines of 2 sequential "combined" spots of 5 drops per spot, and "single" spots of 10 drops per spot (a magnified image of the spots is shown at the top of Figure 56a). This led to combined spots each containing ~9 ng 488SA and single spots containing ~18 ng 488SA. A single strip contained an experiment in triplicate, alternating "combined spots" that mix to form a uniform spot, with "single spots". A y-separation of 1 mm is sufficient enough to prevent transverse inter-diffusion and results in several distinct streaks downstream. We observed that sequentially pattered spots mix by diffusion with previously dissolved spots to form a single pulse of

mixed reagents (Figure 56a), and the combination of spots yields a pulse that is indistinguishable from a pulse that results from a single dissolved spot (Figure 56b).

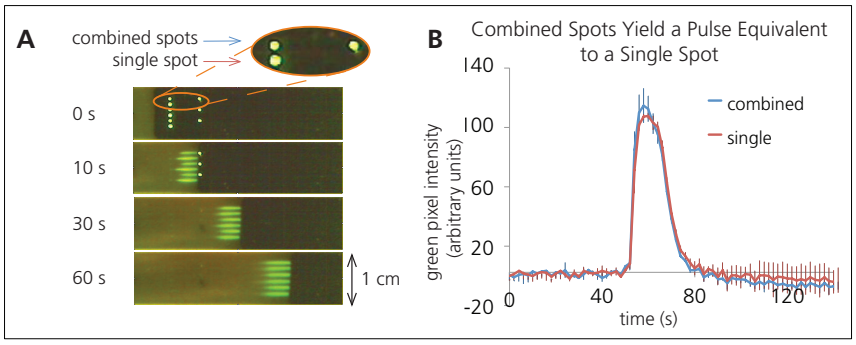

Figure 56: Combination of separately rehydrated reagents. Reagents can be printed separately and combined upon rehydration by patterning sequential spots along the direction of flow. A) Time lapse images illustrating the combination of 2 sequential rehydrated 9 ng 488SA spots, alongside rehydration of a single 18 ng 488SA spot. B) Plot of average fluorescence intensity vs. time at 2.5 cm downstream from the initial spot location, illustrating that separately printed spots combine to form a pulse equivalent to that created by a single rehydrated spot. (n = 3)

Delayed rehydration to enable sequential release

Third, the timing of rehydration was manipulated to enable sequential release of dried reagents patterned on porous membranes. This delay in rehydration was achieved using barriers of sucrose surrounding individual spots, similar to methods previously developed in our group. [13] These barriers were created by printing varying 20% sucrose solutions directly around the dried protein spot, which provided a time lag as the sucrose dissolved before the reagent could be released (Figure 57). 488SA was patterned of 10 passes of 10 drops per spot, and was dried for 10 minutes prior to patterning the sucrose solutions. Dramatically different delays, from 19 sec to 12 minutes, were achieved by printing hexagon-shaped sucrose barriers containing different amounts of total sucrose. Mid-delay sucrose barriers had the highest variability in delay times (Figure 57b), likely because

these barriers are the most sensitive to slight variations in the printing of sucrose barriers that lead to anomalous weak points in the barrier.

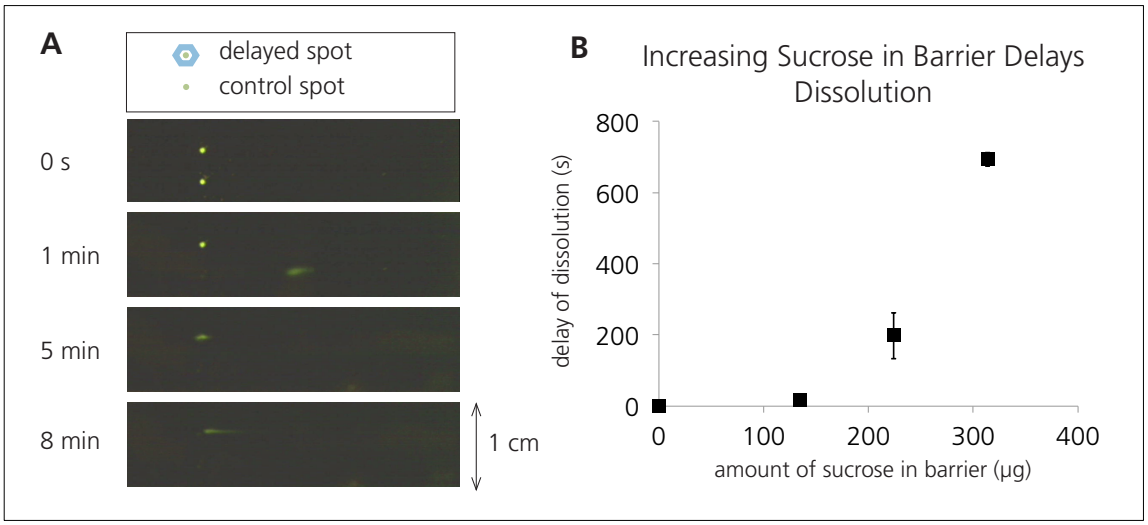

Figure 57: Delays of rehydration. Rehydration of a printed reagent can be delayed by patterning a sugar barrier encircling the reagent spot. A) Schematic of sugar barrier patterning and time-lapse images of delayed rehydration enabled by a sugar barrier. B) Plot showing the variable delay times achieved by varying the sugar content within the sugar barrier. (n=3)

Extended rehydration for longer pulses

Fourth, the time span over which a reagent dissolves from a dried reagent depot can be extended to yield longer time pulses of protein. Extended pulses allow for increased interaction times between a reagent pulse and a downstream capture or reaction zone, and could improve assay performance. We found that by printing sucrose solutions directly on top of dried protein spots, the duration of the dissolution time can be lengthened from less than 2 seconds in the control case, to over 50 seconds with 63 µg of extra sucrose added (Figure 4). Including different amounts of sucrose directly on top of dried reagent spots can tune the duration of the reagent pulse; however, high amounts of sucrose leads to large variability (Figure 58b and c). Additionally, Huy Le, an undergraduate capstone student, demonstrated methods for increasing the duration of rehydration yielded a technique for

extremely extended pulses, over which a dried reagent depot could deliver a nearly consistent stream for close to 4 minutes (Figure 58d).

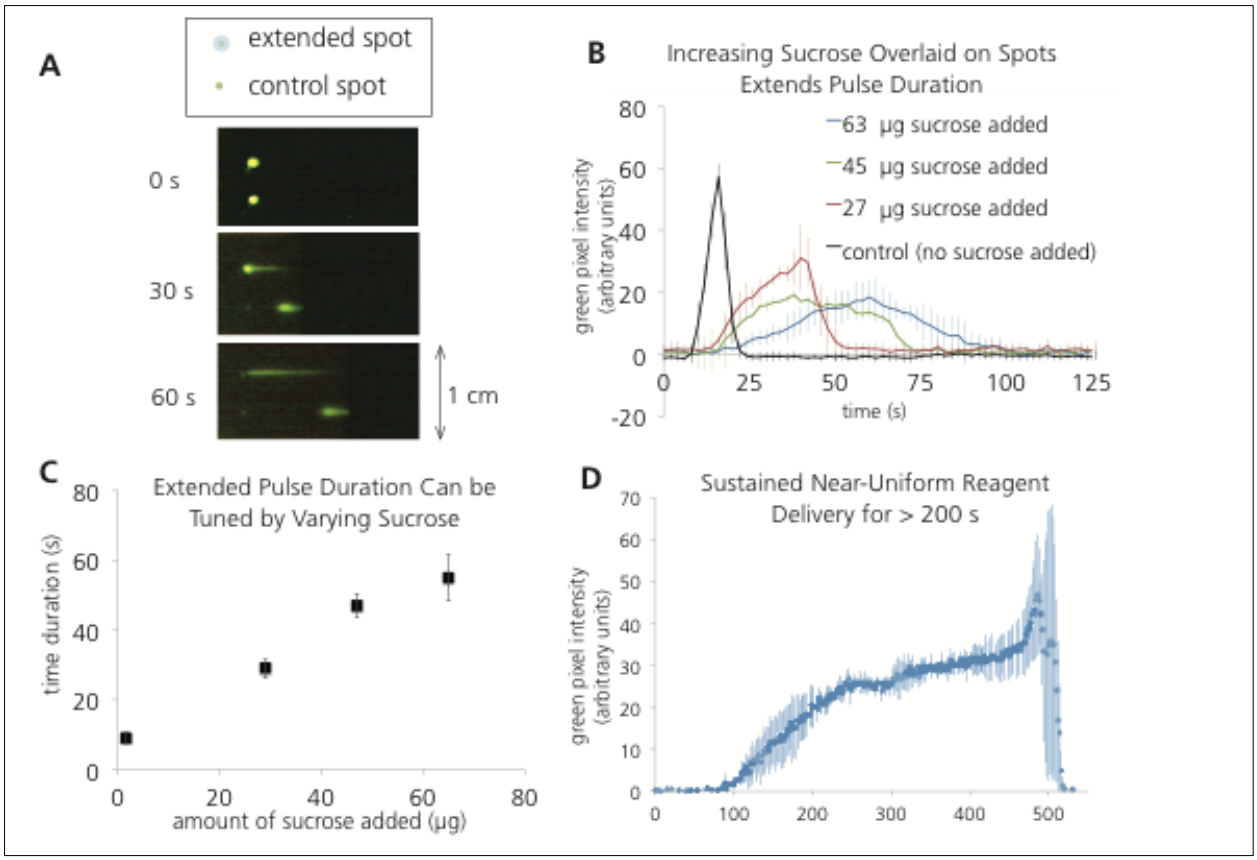

Figure 58: Extending rehydration of a patterned spot. Extended rehydration times can be achieved by patterning sucrose directly on top of a reagent spot. A) Schematic and time-lapse images illustrating extended rehydration times compared to a control. B) Plot of fluorescence intensity vs time of varying extended reagent pulses (n=3). C) Plot illustrating the tunability of pulse duration using varying amounts of sucrose (n=3). D) Plot of fluorescence intensity vs time for an extremely extended pulse, using larger volumes of 488SA and sucrose (n=3). The control spot contained no *additional* sucrose beyond the 5% sucrose, 5% trehalose and 1% BSA mixture that was always included with the spotted protein for rehydration.

5.4 Characterize rehydration of sugar from depots

5.4.1 Introduction

In the development of spatial and temporal controls for the rehydration of dried reagents, relatively large quantities of sucrose were used to both extend and delay the rehydration of patterned reagents, yet we did not fully understand the rehydration and downstream

profile of the sugar component of the system. The third goal of this chapter seeks to describe the rehydration of the sugar-based features that are used to control reagent rehydration.

Two sub-goals were developed to achieve this goal. First, we used methods developed for thin-layer chromatography of sugars to determine if fluorescein spiked into sugar solutions co-localized with the sugars upon rehydration. Second, fluorescein was used as a tracer to determine the rehydration profiles of sugar-based barriers.

5.4.2 Experimental Methods

Device construction

All porous devices were designed and cut as described above. For experiments comparing the rehydration and flow of different sugars versus fluorescein, strips were cut into "combs" containing 12 strips, each 1 cm wide by 10 cm long, to allow a long period of lateral flow. For future experiments that will evaluate the downstream distribution of sugars, and characterize the downstream effect that sugar barriers have on flow profiles, strips will be 1 cm wide x 5 cm long, which was the typical size used in 5.3 for spatial and temporal controls of rehydration.

Sugar and fluorescein chromatography

Diphenylamine-aniline-phosphoric acid (DAPA) reagent was prepared as described previously by Buchan et al [148]: A 4% solution of diphenylamine (w/w) (Sigma Aldrich, St Louis, MO) in ethanol (Sigma Aldrich, St Louis, MO), and a 4% solution of aniline (Sigma Aldrich, MO) in ethanol (w/w) were prepared. Then 50 mL of each were gently swirled together, and and 10 mL of 80% (w/v) phosphoric acid (Sigma Aldrich, St Louis, MO) was

added, and again swirled gently. A small chromatography sprayer was filled with 5 mL of the DAPA solution and placed in the hood for later use.

Five solutions were prepared to compare rehydration of sugars and fluorescein: 45% sucrose, 45% trehalose, 0.1 mg/ml fluorescein, 45% sucrose + 0.1 mg/ml fluorescein and 45% trehalose+0.1 mg/ml fluorescein. These solutions were hand-spotted in 1.6 µl spots on all 12 nitrocellulose strips on a comb, ~1.5 cm from the free end of the strips. A 2 cm x 14 cm cellulose pad was soaked in PBS and placed in contact with the nitrocellulose comb as a fluid source. Video of wet out and rehydration was acquired as detailed in 5.3.2. After strips wicked approximately 8 cm, the cellulose source pad was removed. The comb was immediately transferred to an 80°C hot plate in the hood to heat for 10 minutes (as detailed by Buchan et al [148]). After heating, the comb was taped to a large piece of paper, which was then taped on the back wall of the hood. Roughly 3 mL DAPA reagent was sprayed in a fine mist over the surface of the nitrocellulose. After drying for 10 minutes, the comb device was scanned (Epson Perfection V700 Photo, Epson, Long Beach, CA).

The final image of the fluorescence video acquired during wet-out was saved as a tiff file, and compared with the scanned image acquired after DAPA spraying, to evaluate the relative locations of sucrose, trehalose and fluorescein after rehydration.

Tracking rehydration of sugar barriers using fluorescein

Fluorescein was used to track the downstream distribution of sucrose after rehydration. Fluorescein was spiked into 20% sucrose solutions at 0.1 mg/ml, which were patterned into sucrose spots using a piezoelectric inkjet spotter as described in 5.3.2. After patterning, these devices were wrapped in foil and dried in a desiccator overnight, and stored until use. Experiments were performed exactly as described in 5.3.2, with the same experimental set-

up, except no 488SA was used; instead the location of the fluorescein was used to track the location of the sucrose contained in the sucrose barriers. Videos were analyzed to determine the consistency of sugar rehydration from strip-to-strip, as well as the downstream distribution of sugar upon rehydration.

5.4.3 Results and Discussion

To better understand the downstream distribution of sugar rehydrated from sugar barriers, we hoped to use fluorescein dye spiked into sugar barriers to track the location of sugar after rehydration. Because sucrose, trehalose and fluorescein are all small molecules with similar molecular weights and diffusivities, and fluorescein had been used previously as a tracer for rehydration [102], we anticipated that this method would be feasible. However, we needed to be certain that fluorescein spiked into sugar solutions would not separate chromatographically during flow through the porous substrate. In our experiments to determine whether sucrose and trehalose separate chromatographically from fluorescein after rehydration, we were unable are to use any of the common sugar-detection tests: Tollens' test, Benedict's test, or iodine, because both sucrose and trehalose are non-reducing disaccharides and do not react with any of those reagents. Instead, we used the diphenylamine-aniline-phosphoric acid (DAPA) reagent, which has been used extensively for detecting a wide variety of mono- and oligosaccharides on paper for thin layer chromatography [148-151].

Using the DAPA reagent [148], we compared the transport of sucrose, trehalose, fluorescein, sucrose + fluorescein, and trehalose + fluorescein from spots upon rehydration from nitrocellulose. Figure 59 shows our results; the location of fluorescein can be seen in the fluorescence image in A; the black streaks in B show the location of the sugars on the

same strips. It is clear from these images that when fluorescein is mixed with sugars prior to spotting, it localizes with the sugars during rehydration.

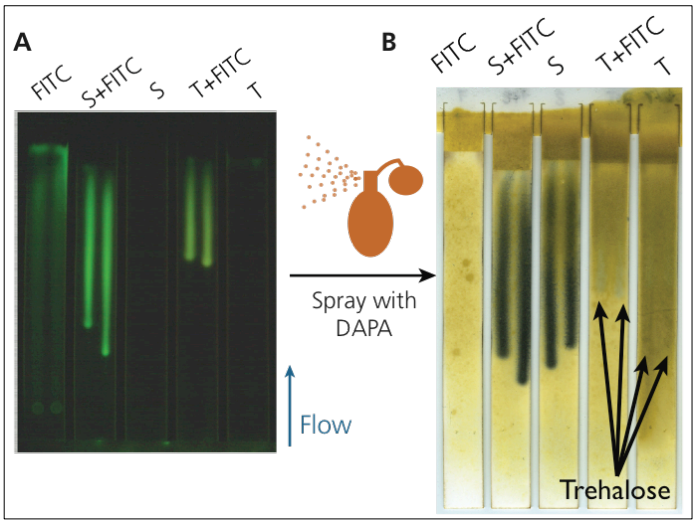

Figure 59: Tracking rehydration of fluorescein (FITC) and sugars. A) Fluorescence image of the strips after flow had progressed 8 cm. The location of FITC is clear from the green fluorescence. S=sucrose, T=trehalose. B) The same strips after being sprayed with the DAPA reagent. The black lines show where sucrose was present on the second two strips to the left. Arrows are pointing out the gray lines where trehalose was present. No black is present on the FITC-only strip. Taking both images together, it is clear that when FITC is mixed with either sucrose or trehalose, the fluorescence tracks with the location of the sugars.

Because fluorescein spiked into sucrose prior to spotting remains co-localized with the sucrose after rehydration, we tracked the downstream distribution of rehydrated sugar using a small amount of fluorescein mixed into sugar solutions prior to spotting. These experiments illustrated the transport of sucrose from the sugar barriers pattered around individual protein depots. As shown in Figure 60, there is some variability in the rehydration of sugar barriers, and it is clear that there are inconsistent weak points within the sugar barrier, as we suggested was the source of variation in the mid-range sugar barriers described above. We hypothesize that this is due to uneven sugar redistribution as the sugar rings are spotted and as the excess water evaporates. These issues need further exploration if sugar delays such as those described here will be used in more sophisticated

devices, however the proof-of-principle development of these rehydration controls still represents an exciting step in the creation of more finely-tuned techniques for high-performance 2DPNs. Another important observation gained from these sucrose wall rehydration experiments is the flow of wicking fluid *around* the sugar barriers, rather than through them—the center region is not permeated by liquid until the sugar wall breaks. This leads us to believe that the sugar wall makes that region of the membrane relatively impermeable to flow for a period of time as the sugar dissolves. This discovery is central to the next section, which describes a computational model of reagent rehydration.

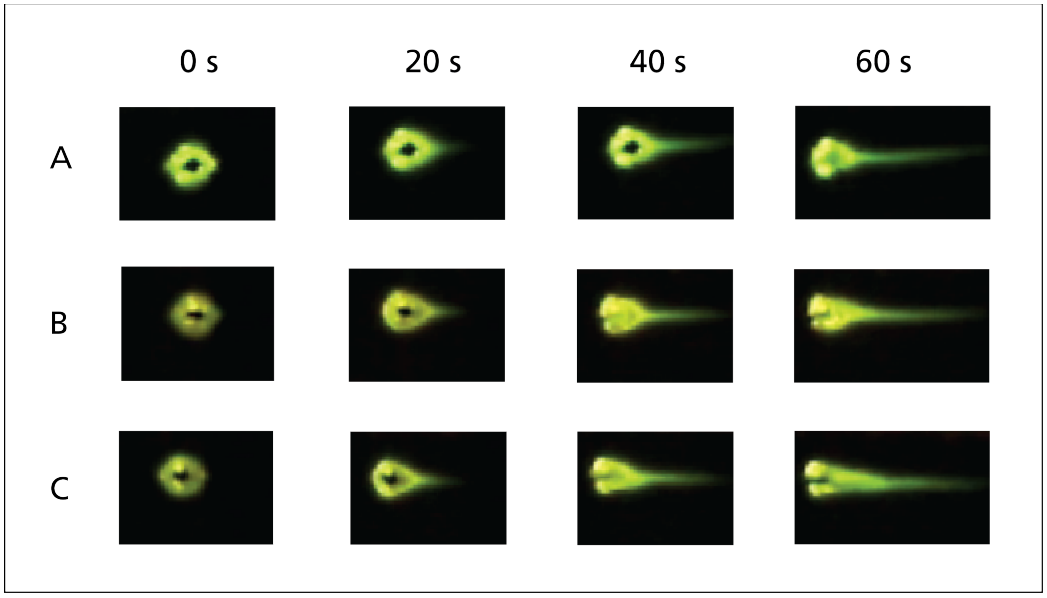

Figure 60: Rehydration of sugar barriers for delayed reagent rehydration. A 20% sucrose solution (like was used in section 5.3 to create barriers for delayed reagent rehydration) was spiked with fluorescein, to enable tracking of the sucrose upon rehydration. Three replicates (A, B, and C) are shown, and the variation in the timing and specific breakthrough point of sugar walls supports our hypothesis that very small variations in the sucrose distribution after spotting and during drying has a major effect on the sugar wall breakthrough profile. Despite the variations, however, it is clear that the fluid flow in all of these devices occurs *around* these barriers, and it is not until a weak point in the barrier breaks that flow is able to pass through the center region. This suggests that the sugar barrier does not only increase the local viscosity, but actually makes that region impermeable to flow for some period of time.

5.5 Development of a computational model of reagent rehydration

In the preceding sections we have described methods to pattern reagents on-device for controlled spatial and temporal distribution upon rehydration. Here we discuss a companion computational model that simulates the behavior of rehydrating reagents by implementing sucrose-concentration-dependent permeability in the Darcy's Law equation that describes flow in these porous devices, as suggested by our examination of the rehydration of sucrose barriers above. This model enhances our capability to model possible assays designs incorporating rehydration of dry reagents.

5.5.1 Model physics and parameters

Physics

A simple rectangular geometry was used, 9 mm wide by 30 mm long, similar to the strips used experimentally. The Darcy flow module was used to model flow through the porous material, though this was a simplification of the actual experiment—in the experiments, flow was wetting out the membrane so the velocity was actually predicted by the wet-out-length-dependent function of Washburn's equation, rather than the constant flow predicted by Darcy's law. Future iterations of the model could explore mechanisms to input variable flow rates, but for the proof-of-principle implementation described here, we were simply seeking to replicate rehydration behavior similar to that observed experimentally, and the variations in flow

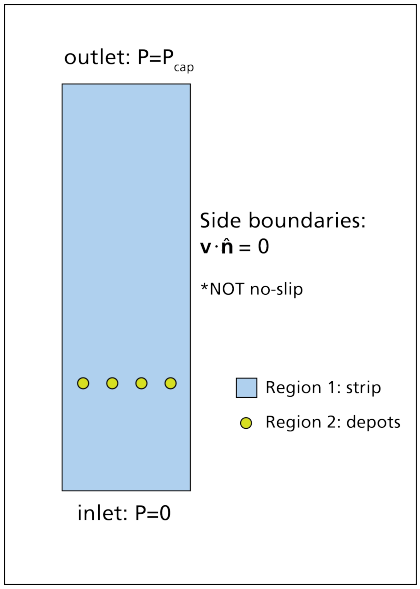

Figure 61: Schematic of reagent rehydration model geometry and boundary conditions. The blue region is the main strip area where no reagents are located initially, whereas the green spots are the storage depots that initially contain reagents.

rate were minimal compared to other attributes of reagent rehydration. Boundary conditions are shown in the model schematic in Figure 61.

Circular "reagent depots" were located at the upstream end of the model strip, as in experiments. To compare several cases in one model, we placed three models depots in line with each other. Each reagent depot was a circle 0.6 mm in diameter (approximately the diameter of actual printed depots). Two solutes were defined within these depots: sucrose and protein, and their initial concentrations were set to approximately the initial concentrations within actual experimental devices (see parameters below). The initial concentrations of both of these solutes were set to zero elsewhere in the model.

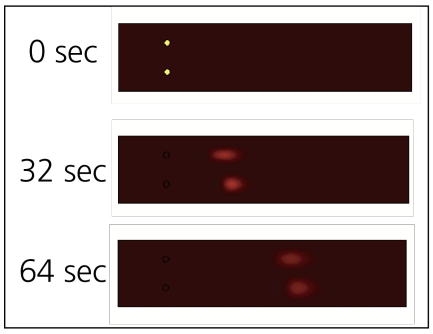

Figure 62: Computational simulation of rehydration with a sucrose-dependent viscosity function. This does *not* yield rehydration profiles similar to those observed in experiments. Previous work in the literature showed that this method was effective for modeling rehydration from cavities in the side of microfluidic channels [152], so it was the parameter were initially thought would recreate rehydration computationally. We turned our attention to membrane permeability, however, because experiments showed that reagent depots actually impeded flow, and reagents were sloughed off the sides of depots, while the center remained initially impermeable to flow, until the depot was sloughed away (see the assessment of sugar wall rehydration in section 5.3).

Previous work describing the rehydration of dried reagents from storage depots in the context of microfluidic devices successfully modeled the reagent rehydration profile by implementing a sucrose-depending solution viscosity [102, 152]. In that model, the viscosity-dependence yielded concentration gradients that were very consistent with their experimental results. However, when we tried a similar concentration-dependent viscosity in our model of reagent rehydration in porous media, the model representation was not representative of experimental results (see Figure 62). Instead, we turned to our observations of the rehydration process of patterned reagent spots, and particularly the experiments

examining the rehydration profiles of sugar barriers. From both of these sets of experiments we noticed that the spot takes some time to dissolve, and it initially appears that flow goes *around* reagent depots and sucrose features. Based on this, we concluded that membrane *permeability* is the fluid dynamics parameter of the system that is most impacted by the presence of sucrose and protein within the membrane. However, since high sucrose concentrations are known to increase solution viscosity, we also included sucrose-dependent viscosity in the model, to account for high-viscosity streams in the downstream flow.

Parameters

The parameters required in this model are included in Table 5. Refer to Figure 61 for a schematic of the different model zones and boundary conditions. Table 6 shows the initial concentrations of sucrose and protein in different areas of the model geometry.

Table 5: Input parameters for rehydration simulation

Parameter	Value	Units	Description
P_{cap}	-10800	Pa	Membrane capillary pressure
ρ	1000	kg/m^3	Water density
porosity	0.77	1	Percent void space in membrane
μ_1	$8.9x10^{-4}$ • visc_factor	Pa•s	Solution viscosity in region 1 of model
μ_2	$8.9x10^{-4}$	Pa•s	Solution viscosity in region 2 of model
κ_1	$5.5x10^{-13}$	m^2	Membrane permeability in region 1 of model
κ_2	$5.5x10^{-13}$ * perm_factor	m^2	Membrane permeability in region 2 of model
visc_factor	$2.3714\ c_{suc}^2 - 0.1168\ c_{suc} + 1.0756$	1	Sucrose-dependent solution viscosity factor in region 1
perm_factor	$\begin{cases} 1 \text{ for } c_{suc} < 0.1\ M \\ 0.1 \text{ for } c_{suc} > 0.1\ M \end{cases}$	1	Sucrose-dependent permeability of dried spots in region 2
D	$1x10^{-10}$	m^2/s	Solute diffusivity
D_factor	1/visc_factor	1	Based on the Stokes-Einstein equation, diffusivity is inversely related to viscosity

Table 6: Initial concentrations for model

Initial Condition	Value	Location
$C_{protein}$	16.4 μM	All depots (region 2)
$C_{protein}$ & $C_{sucrose}$	0 M	Region 1
$C_{sucrose}$	0.5 M	Depot #4 (control)
$C_{sucrose}$	3.6 M	Depot #3
$C_{sucrose}$	6 M	Depot #2
$C_{sucrose}$	8.4 M	Depot #1

Sucrose concentration-viscosity data from Iscotables 7th ed. [153] for sucrose concentrations from 0 to 1.2 M in water was fit to a parabolic function in excel to generate the sucrose-dependent viscosity factor. Though some initial reagent depot concentrations had much higher concentrations of sucrose than 1.2 M, because of the gradual rehydration of those depots, the local *rehydrated* sucrose concentration outside the depots did not exceed 1.2 M.

The sucrose-dependent viscosity function was not included in the viscosity of the reagent depot regions because doing so effectively "double-counted" the effects of sucrose in that region—for the purposes of the model, all sucrose within the depot was not yet rehydrated and thus decreased the local membrane permeability, whereas outside of the depot it was considered rehydrated, and there increased the liquid solution viscosity.

The capillary pressure, porosity and baseline permeability used in the model were based on calculations and experiments performed by Joshua Buser [73]. Parameters of the wicking liquid were set to literature values for water (except for the sucrose-dependent viscosity adjustment).

Initial concentration values were calculated based on known mass quantities of protein and sugar added to reagent depots in experiments, then divided by the volume of the depots.

5.5.2 Comparison of model to experiment

Section 5.3 discussed several methods for creating spatially and temporally controlled reagent rehydration profiles, including extended dissolution of reagents from spotted depots on a porous membrane when sucrose was patterned directly atop reagent spots. This computational simulation was designed to reproduce those experiments, which is does remarkably well. Figure 63 shows still frames from a simulation video side-by-side with still frames taken from a video recorded of a rehydration experiment, and it is clear that the profiles of rehydration are quite similar. As noted above, we ran a single simulation that included four different reagent depots: from top to bottom, 8.4 M sucrose, 6 M sucrose, 4.6 M sucrose, and 0.5 M sucrose (the control spot, which only includes the sucrose that is part of the rehydration mix that is mixed with the protein prior to spotting). In experiments, each different extended rehydration condition was printed on its own strip, along with a control spot,

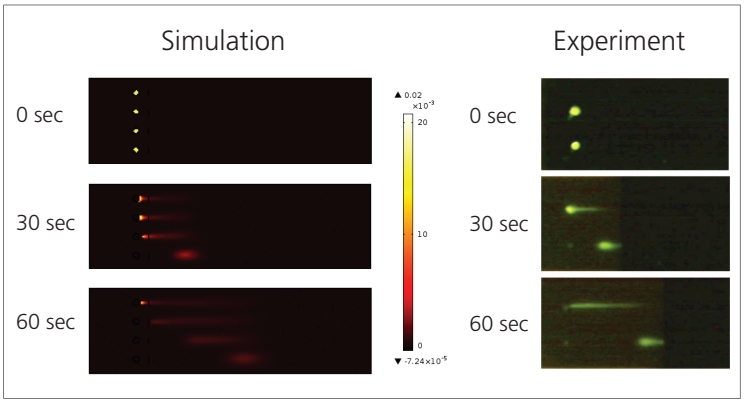

Figure 63: Still frames from computational simulation of extended reagent rehydration (left) compared to actual experimental images (right). This model represents the extended dissolution profiles as described in section 5.3. Accurate computational extended rehydration was achieved by implementing sucrose-dependent membrane permeability within the dry reagent depot regions, based on our observations that fluid flow initially goes *around* reagent depots, rather than through them, leading to the theory that dried sugar and reagents fills the pore space in a such a way that those dried materials locally reduce membrane permeability.

which is why only two spots are seen on the experimental images, whereas four spots are seen on the simulated images.

Both experimental and simulated rehydration was quantified over time, by measuring the amount of protein immediately downstream of the storage depot. As with the qualitative comparison shown above, the quantitative time-dependent rehydration profile generated by the simulation was consistent with our experimental results, as illustrated in Figure 64.

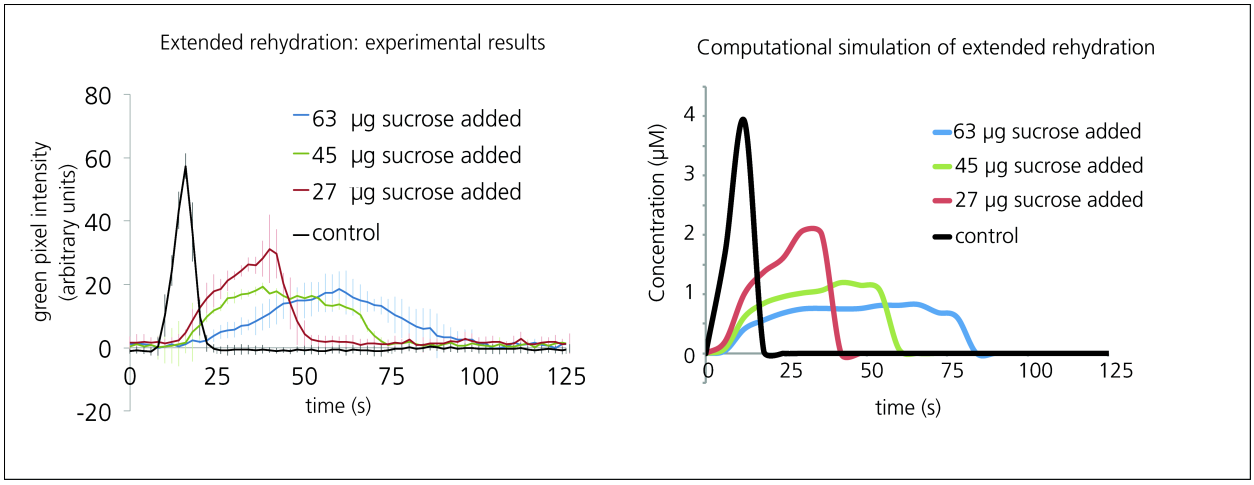

Figure 64: Comparison between experimentally observed extended reagent dissolution profiles (left) and computational simulation of rehydration (right). There is a roughly 10 second offset between the two graphs, because in the experiments spots did not begin to rehydrate until they were wet by the liquid wicking through the membrane in wet-out flow; in the simulation, however, the flow was governed by Darcy's law, which introduced constant-velocity flow everywhere in the model at t=0. Aside from this 10-second offset, there is remarkably good agreement between the simulation and experiment.

5.6 Reassembling separately patterned incompatible reagents via rehydration

In section 5.3 we demonstrated two separated spots of patterned 488SA combining upon rehydration to create a uniform pulse indiscernible from the pulse resulting from the rehydration of a single, larger spot; however, those experiments did not evaluate whether two different reagents patterned sequentially would actually mix upon rehydration to

enable separate storage of incompatible reagents that require mixing prior to use in an assay. Our fourth goal was to show the utility and feasibility of storing reagents separately and then combining them immediately prior to use.

A good example of this type of situation is the gold enhancement system that our laboratory currently uses to improve the limit of detection in several of our assays. This multi-component gold enhancement system requires that the components are stored separately and only mixed together immediately before use. Specifically, these components lose functionality if they are dried for storage after they have been mixed. Thus, they must be stored dry in separate regions and recombined on device for delivery to downstream regions of the assay. Previous work has shown effective rehydration and combination of these gold enhancement components from storage on glass fiber pads, to enhance a malaria PfHRP2 assay [44]. However, gold enhancement is just one example of a system in which these methods could be used.

Because our focus in these experiments was on combining the gold enhancement reagents, we used a simplified system in which a line of gold-labeled streptavidin was printed across the strip, and enhancement was quantified using patterned gold enhancement reagents.

5.6.1 Experimental Methods

Device patterning and construction

All porous devices were designed and cut as described above in 5.2.2 above. For gold enhancement experiments, all reagents were patterned onto strips using a piezoelectric noncontact printer (SciFLEXARRAYER S3, Scienion AG, Berlin, Germany). After printing, strips were wrapped in foil to protect them from light, and then dried in a desiccator overnight and stored until use. Nitrocellulose strips were initially cut to 0.5 cm x 5 cm

rectangles, and later the design was changed to a bottle-shaped silhouette—1 cm wide at the upstream end and 3 mm wide at the downstream end, with the taper halfway down the strip (see Figure 66 below).

Reagents and rehydration experiments

In all experiments, nitrocellulose strips patterned with were affixed to a black poly(methylmethacrylate) (PMMA) substrate using double-sided tape (3M, St. Paul, MN). Red and yellow felt-tip pens were used in initial experiments to validate the combination of sequentially patterned reagents. A single dot of yellow was positioned 7 mm from one end, then a single dot of red ink and additional 7 mm down from that. A wet cellulose pad was placed at the end closest to the yellow dot to begin flow. The cellulose pad was removed before the wetting front reached the end of the strip. Strips were dried and scanned (Epson Perfection V700 Photo, Epson, Long Beach, CA).

In subsequent experiments, a 0.375 µl line of gold-labeled streptavidin (OD 5 unless otherwise noted, Arista Biologicals, Allentown, PA) was patterned at the downstream end of the strip. Any color change at this line was used to quantify the success of gold enhancement. The gold enhancement solutions were purchased from Nanoprobes (Yaphank, NY), and the “enhancer”, “activator”, and “reducer” solutions were used in a 1:1:1 ratio. When liquid enhancement reagents were used these three components were mixed together immediately before use. Previous work in our lab demonstrated that the buffer solution, “D”, did not improve the level of gold enhancement, so we did not include it, to minimize the total volume needed.

A glass fiber pad (Ahlstrom, Helsinki, Finland), also cut using the CO_2 laser, was placed at the upstream end of each strip. At the start of an experiment, 15 µl fetal bovine serum

(FBS) was applied to the glass fiber pad as a dynamic blocker to prevent non-specific adsorption of reagents to nitrocellulose. In some experiments, immediately following the addition of FBS, cellulose strips were used to connect the glass fiber pads to a well containing phosphate buffered saline (PBS), which provided continuous flow through the device. In other experiments, a specific volume of PBS was applied directly to the glass fiber pad. Small blocks of PMMA were placed over the cellulose strips and glass fiber pads to ensure consistent contact with the device.

5.6.2 Results and Discussion

Demonstration of effective combination of colored dyes using sequential patterning and rehydration

In 5.3.3 we demonstrated the combination of sequentially patterned spots of fluorescently labeled streptavidin, however that experiment was unable to differentiate whether the combined spots mixed or simply lined up in order as they flowed downstream. As a preliminary test to evaluate the level of mixing, we spotted different colors of dye sequentially along a nitrocellulose strip and rehydrated them in PBS. We observed that the two colors of dye mixed upon rehydration, which supported our earlier hypothesis that sequential spots combine upon rehydration, and led us to further experiments aiming to combine separately patterned gold enhancement reagents.

Determination of acceptable volumes for gold enhancement

Our earlier experiments showed that patterning reagents in arrays of single spots (as in 5.3.3) allowed minimal flow disruption, which led us to believe that we were limited to relatively small overall volumes of gold enhancement reagents, especially compared to the 18-60 µl that previous studies have used [44, 79]. Therefore, before patterning gold enhancement reagents for rehydration, we wanted to determine the minimum volume of

enhancement solution that could be used and still give effective gold enhancement using liquid gold enhancement reagents. Initially we used 1x5 cm rectangular strips with OD 1.25 streptavidin-gold patterned across the downstream end, but we quickly realized that by changing the device design to a bottle-like shape, the streptavidin-gold region would be smaller, leading to more overall enhancement with a given volume of enhancement reagents. We designed a bottle-like shape intentionally, rather than just narrowing the strip overall, because we wanted to maintain the wide upstream region because our later experiments would require space to pattern the gold enhancement reagents.

We compared the enhancement achieved when 3 µl, 6 µl, 9 µl, and 15 µl of total combined gold enhancement reagents were used, in triplicate (see Figure 65). We noticed that 3 µl total, or 1 µl of each component, led to very uneven enhancement, leaving the middle of the gold line unenhanced in 2 strips, and no apparent enhancement in the third strip. However, 6 µl total was sufficient for reliable signal enhancement, and chose to use those volumes for our next experiments using patterned gold enhancement reagents.

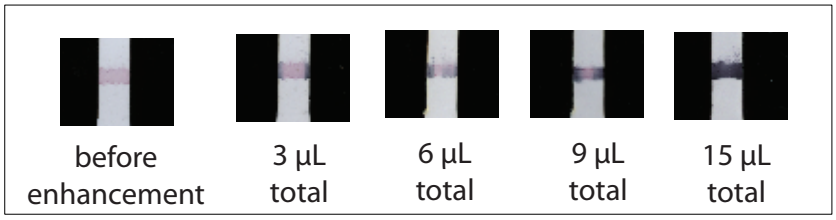

Figure 65: Determining acceptable volumes of gold enhancement solution. The far left image is a gold-streptavidin line at OD 1.25, before enhancement. The images on the right have increasing total gold enhancement solution (at a 1:1:1 ratio of enhancer:initiator:activator). We wanted the lowest volume that could give reproducible enhancement. 3 µl was insufficient, because enhancement only occurred at the edges, and was not reproducible.

Demonstrate effective combination of gold enhancement reagents using sequential patterning and rehydration

Our initial attempts to recombine separately patterned gold enhancement reagents were unsuccessful. Then, using 70 µl PBS, applied 10 µl at a time, over the course of 14 minutes, we observed some slight signal enhancement of 1.4 fold (+/- 0.2). This was promising, but this user-intensive buffer application protocol is not acceptable in a clinical point-of-care diagnostic, so we sought to simplify the required steps.

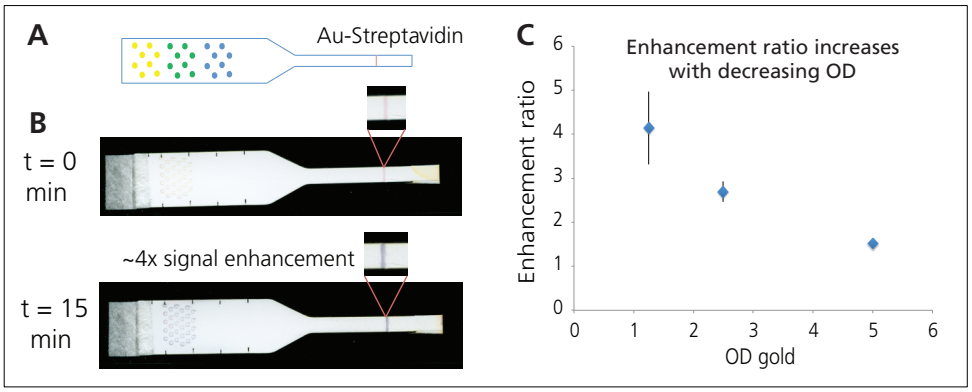

Figure 66: Combining gold enhancement reagents patterned on strip. A) Schematic of patterning. Yellow=enhancer, green=activator, blue=initiator. Spots were arrayed for minimal disruption to flow. B) Images of pre- and post-enhancement of a 1.25 OD gold-streptavidin line. After 15 minutes, enhancement was 4x the initial signal, using grayscale intensity. C) We observed increasing gold enhancement with decreasing OD gold striped across the membrane, however the variability was higher at the lower OD level.

We hypothesized that effective rehydration of the patterned reagents was improved by the slow flow rate achieved by multiple small buffer pulses. To test this hypothesis, we elongated the downstream end of the strip, beyond the streptavidin-gold patterned line, which yielded increasingly slowing flow rates in accordance with Washburn's equation [69], rather than the acceleration in flow rate that is observed when flow transitions from a nitrocellulose device to a cellulose wicking pad [154]. This modification resulted in reproducible gold enhancement, as shown in Figure 66. Furthermore, we observed increased enhancement of gold lines with decreasing optical density (Figure 66c).

5.7 Conclusions

The methods described in Chapter 5 enable the patterning of reagents onto porous devices for storage and subsequent rehydration and use in downstream assays, and to our knowledge, is the first example of such a technique. We have evaluated the patterning and rehydration of an example protein; designed techniques to enable spatial and temporal controls over the rehydration profiles of the protein; developed a computational model to predict the rehydration profiles of patterned reagent depots; and characterized the combination of separately patterned gold enhancement reagents. In developing this collection of methods we have leveraged our understanding of printing on nitrocellulose, described in Chapter 3, to enable much more sophisticated reagent rehydration mechanisms than existed previously. Next, in Chapter 6 we will describe how these controlled rehydration techniques can be implemented in the context of a 2DPN assay.

6 Development of a multi-step gold-enhanced assay using only patterned reagents

6.1 Objectives and Motivation

As described in Chapter 2, lateral flow tests (LFTs) have been widely accepted for a variety of applications, ranging from home pregnancy tests to rapid diagnostic tests for infectious diseases in low-resource settings. A major advantage of these devices over microfluidic point-of-care diagnostics (such as the Cepheid GeneXpert) is that the fluid flow in LFTs is driven entirely by capillary pressure, eliminating the need for any external pumps or vacuum sources. Furthermore, LFTs have widespread appeal because they satisfy many of the ASSURED criteria that were developed to describe ideal characteristics of point-of-care tests: **A**ffordable, **S**ensitive, **S**pecific, **U**ser-friendly, **R**apid & **R**obust, **E**quipment-free, and **D**elivered to those in need [17]. LFTs are low-cost, rapid, easy to use, and require little to no instrumentation to interpret results, however, most are still severely lacking in sensitivity [7].

There has been a recent push in the point-of-care diagnostics community to develop paper-based diagnostic tests that incorporate sophisticated functions into otherwise simple devices, stretching their capabilities while maintaining the core benefits of LFTs. These advancements include 2D and 3D paper devices that are capable of tasks such as multiplexing [33, 37, 38], sample processing [155], and signal enhancement [14, 156]—sophisticated functions that have previously been reserved for laboratory-based or traditional microfluidic tests. Conversely, traditional LFTs are only capable of performing a single step, and cannot incorporate enhancement steps or any sample processing.

One key characteristic of most of these newer paper-based devices that remains consistent with early LFTs is the inclusion of dried reagents in the assay device. There are several benefits to including all of the essential reagents dried *in situ* within a device. First, the number and complexity of user steps are reduced: the user does not need to identify, measure and add assay reagents to the device, which is particularly important when incorporating more sophisticated processes in a point-of-care test. Second, dried reagents are more resistant to damage at ambient temperatures, particularly when stabilizing additives, such as sucrose and trehalose [100, 101], are added. Third, reagents dried *in situ* can facilitate device automation because device geometry and reagent location within the device can be designed to automate multistep processes. Together these advantages have the potential to improve the robustness, affordability and ease-of-use of the device while decreasing the equipment needs. These four traits are crucial for designing devices appropriate for point-of-care diagnosis in low-resource settings [2, 18].

Traditionally, conjugate pads have been used to store dry reagents in both lateral flow [22, 156] and conventional microfluidic devices [100]. However, there are two significant disadvantages to using these separate pads, particularly when designing high-performance 2DPNs: they offer limited control over the release of rehydrated reagents, and they require additional materials and components that add to manufacturing costs. The fabrication costs of including conjugate pads are particularly substantial when used in two-dimensional paper diagnostics because unlike LFTs, 2D devices cannot be fabricated by slicing dozens of strips from a single sheet (Figure 67A). Instead, conjugate pads must be added in a "pick-pick-and-place" process (Figure 67B).

Methods for dry reagent storage, other than conjugate pads, in microfluidic devices have achieved such storage directly within the channels of these devices, for later controlled

release. Some examples of these techniques include cavities in channel walls to control the reconstitution of dried proteins [102], and "reagent integrators" to store and subsequently release predetermined dilutions of reagents into microfluidic devices [157]. Chapter 5 of this document presented analogous methods for controlled release of reagents stored directly on paper microfluidic device [147]. Those novel methods for printing reagents on porous substrates enabled controlled spatial and temporal concentration gradients of reagents rehydrating during capillary flow within a porous device. Furthermore, patterning reagents into arrays of individual spots allows the storage of incompatible reagents, such as a multi-component gold enhancement system that we used here for signal amplification, which loses functionality if the components are mixed prior to drying (as described in Chapter 5). In addition to the improved automation and storage capabilities that are generally enabled by dry reagents, these reagent printing techniques have the potential to simplify device manufacturing to a streamlined roll-to-roll bulk process (see Figure 67C).

Though high-throughput and high-performance roll-to-roll protein printers are commercially available, the current work was performed using laboratory-scale cutting and printing equipment, and further process optimization would be required to scale up to mass-scale manufacturing, and long-term storage validation tests would be needed to ensure shelf-stability of patterned reagents.

The work presented in Chapter 6 expands upon the methods described in Chapter 5 to present an example application of controlled reagent rehydration in the context of a multi-step signal-enhanced immunoassay for the malaria antigen *Plasmodium falciparum* histidine-rich protein 2 (*Pf*HRP2) with a limit of detection comparable to reported laboratory ELISA values [158]. Future studies are needed to confirm clinical performance and long-term storage of these devices, but this work clearly demonstrates that reagents

patterned and stored on nitrocellulose membranes can be rehydrated in a controlled manner, and used effectively in a signal-enhanced assay with good sensitivity.

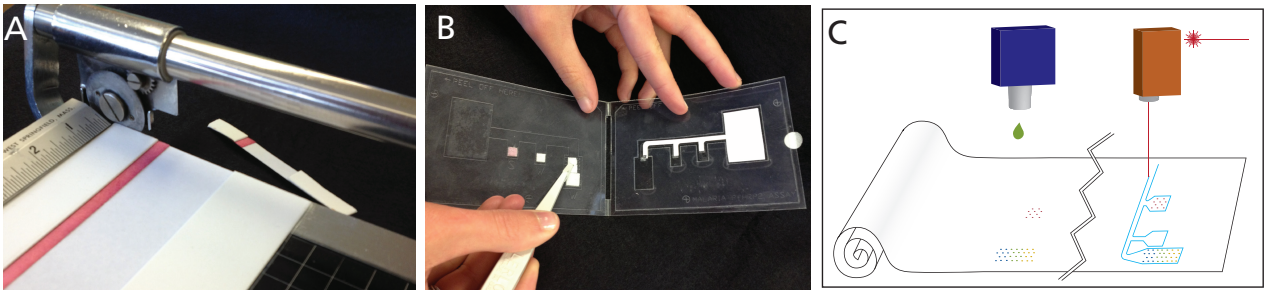

Figure 67: Fabrication schematics of different types of tests. (A) Slicing lateral flow tests apart is relatively simple and straightforward. However, (B) the "pick and place" process of laying down several pads containing a variety of dry reagents, which is required when conjugate pads are used in 2DPN devices, is inefficient and error-prone. Printing reagents directly onto the assay membrane, as described here, is a first step toward roll-to-roll fabrication (C), which is more high-throughput than pick-and-place methods.

Malaria is an interesting target for an inexpensive highly sensitive point-of-care diagnostic test, but perhaps for a surprising reason: malaria rates are dropping in many countries across the globe. The implementation of many targeted mosquito-control programs have dramatically reduced the malaria rates in many endemic areas, and several countries are actively seeking to eliminate endemic infections within their borders. A key part of this elimination effort requires rapid and extremely sensitive diagnostic tests to detect infections early, begin treatment, and implement further mosquito-control measures in the area in which the infection was acquired, and in many cases current malaria rapid diagnostic tests are insufficient for accurate diagnosis [9, 159].

Another example of a disease antigen used in currently poorly-performing rapid tests is the influenza nucleoprotein (NP), which is used to distinguish between influenza A and influenza B infection. Current influenza rapid tests for NP generally exhibit mediocre (10-70%) sensitivity [8, 160, 161], and would dramatically benefit from the increased

sophistication enabled by 2DPN devices. Future work in the laboratory will focus on this target, and the methods presented here could just as easily be extended beyond the application in a malaria assay to an influenza assay with improved sensitivity.

Previous work from our group has shown high-performance two-dimensional paper-based assays [12, 156] but the work presented here is particularly significant because all of the necessary reagents were patterned, dried, and stored on a single porous membrane, and rehydrated with the addition of sample and buffer upon the initiation of the assay. This method is a significant simplification of conventional methods that require storage in separate pads and subsequent placement in the device.

6.2 Introduction

Here we demonstrate an application of the reagent rehydration methods described in Chapter 5 in an on-strip assay for the malaria antigen *P. falciparum* Histidine-rich protein 2 (PfHRP2), to show that patterned reagents are sufficiently functional upon rehydration to function in a gold-enhanced PfHRP2 detection assay.

To succeed in this goal we had three major concerns to address. First, we confirmed that all assay reagents, including gold-labeled IgG detection antibody and all gold enhancement reagents, rehydrated sufficiently from their patterned locations. Second, we determined the appropriate device geometry so that input reagents would arrive sequentially at the detection zone. Third, we evaluated the limit of detection of these patterned-reagent devices and compared it with the limit of detection of other PfHRP2 assays.

6.3 Implementation of multi-step gold-enhanced PfHRP2 assay using only patterned reagents

6.3.1 Methods

Device patterning and construction

The initial assay blocking conditions, reagent quantities, and geometry were chosen to closely mimic the successful 3-inlet 2DPN assay for PfHRP2 demonstrated by Fu et al [44], which used only reagents dried onto glass fiber pads. 3-inlet 2DPN devices were cut from untreated backed 8 μm pore diameter nitrocellulose membranes as described above in 4.2.2. The antigen capture line (0.375 μl, 1 mg/ml mouse monoclonal anti-PfHRP2 IgM, from Immunology Consultants Lab, Portland, OR), and a process control (0.375 μl, 0.5 mg/ml ImmunoPure Antibody goat-anti-mouse IgG, Thermo Scientific) were immobilized at the downstream end of the common channel of the device. After patterning capture and control lines, we tried several different blocking conditions to achieve a successful assay; these different blocking conditions are described in 6.3.1.2.

After blocking, membranes were placed in a desiccated oven at 37°C for 2 hours, then transferred to a desiccator for storage. An antigen-capture line (0.375 μl, 1 mg/ml mouse monoclonal anti-*Pf*HRP2 IgM, Immunology Consultants Lab), and a process control (0.375 μl, 0.5 mg/ml ImmunoPure Antibody goat-anti-mouse IgG, Thermo Scientific) were immobilized at the downstream end of the common channel of the device via printing with a piezoelectric spotter (SciFLEXARRAYER S3, Scienion AG) (Figure 1). The non-specific adsorption of proteins to nitrocellulose in this way has long been used in the fabrication of LFTs[22].

The detection antibody (Immunogold conjugate mouse monoclonal anti-*Pf*HRP2, BBInternational), and gold enhancement solutions (GoldEnhance LM, Nanoprobes, Yaphank,

NY) were also printed onto the porous device using the piezoelectric printer, but these reagents were deposited in patterns to prevent non-specific immobilization, and facilitate controlled rehydration (see Figure 1 for a schematic of pattern and locations). To achieve this controlled rehydration, the detection antibody was mixed with 5% sucrose, 5% trehalose and 1% BSA prior to printing it onto the nitrocellulose surface. In our previous work we demonstrated that these additives improve the uniformity of rehydration of proteins after storage[162]. Then, a total of 2 μl of the detection antibody was patterned on the first inlet in a single array of 29 spots, spaced to at 1 mm from each other to prevent disruption of wet-out flow. Each of the three components of the gold enhancement reagent was patterned in a separate 2 μl, 29-spot array onto the third inlet. These three reagent arrays were sequenced in the order that the three solutions were required to mix: "enhancer" solution first must mix with "activator", and then that combined solution must mix with the "initiator". These components are proprietary so their exact composition is unknown to us, however, the basic process is as follows: the "enhancer" solution contains a gold salt that is chemically reduced to gold atoms by the combination of the "activator" and "initiator" in the reconstituted solution, in the presence of the gold conjugate. These gold atoms are deposited onto the surface of the gold conjugate nanoparticle, and this changes the light absorption of the conjugates captured at the detection region. The third inlet of the device was not pre-blocked, and no protein was added to the gold enhancement solutions because it was found to inhibit the enhancement activity of those reagents. After printing, strips were wrapped in foil to protect them from light, then dried in a desiccator and stored there until use (2–5 days).

Blocking variations

The first blocking protocol we used was "full blocking", in which devices blocked in PVP blocker (0.25% poly(vinyl pyrrolidone) (PVP)+ 0.25% BSA + 5% Sucrose + 15 mM NaN3 + 0.10% Tween-20) for 30 minutes, then dried overnight at 37°C and stored in a desiccator. Second, we tried "unblocked" devices, where the devices were not blocked at all. Third, we "partially blocked" some devices, by applying 14 µl PVP blocker to only the first inlet of each device, which was enough liquid to wick through the first inlet to the common channel, but not into the common channel; then devices were dried for 1 hr at 37°C, and stored in a desiccator.

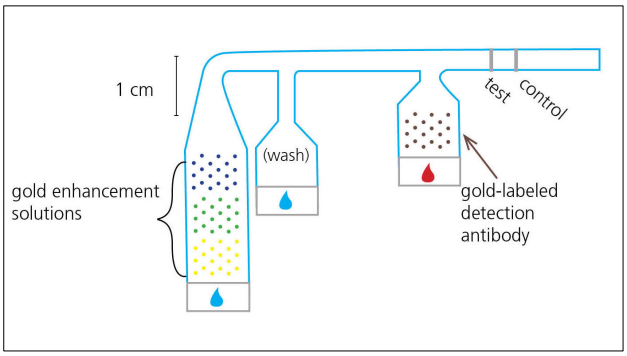

Figure 68: Schematic of patterned 2D paper network PfHRP2 assay indicating locations of patterned reagents. Mock sample is indicated by the red drop, buffer is indicated by the blue drops.

Protocol for running PfHRP2 assay using patterned reagents

Gold enhancement of an assay for the malaria antigen *P. falciparum* histidine-rich protein 2 (PfHRP2) (ImmunoDiagnostic, Inc., Woburn, MA) was used as a demonstration of a practical application of these techniques for printing and drying reagents directly on porous substrates.

To run an experiment, nitrocellulose devices were affixed to a PMMA substrate. An untreated glass fiber pad (Ahlstrom, Helsinki, Finland), cut using the CO_2 laser cutter, was placed at the upstream end of each inlet of the device. To begin the experiment, 30 µl of a mock sample consisting of PfHRP2 spiked at varying concentrations into FBS, was applied to the first inlet, 40 µl PBS was applied to the second inlet as a wash and 100 µl PBS was added to the final inlet. As the mock sample wicked into the first inlet, it rehydrated the

gold-labeled mouse-anti-PfHRP2 IgG. In all of the assay development experiments, a PfHRP2 concentration of 100 ng/ml was used; in limit-of-detection analysis, concentrations varied from 0–50 ng/ml, as detailed below. The PBS added to the third inlet rehydrated and combined the gold enhancement reagents. A time-lapse uncompressed .avi movie was taken 1 frame per 30 seconds for 60 minutes. Afterward, devices were dried in a desiccator for 30 minutes and imaged using a flatbed scanner (Epson Perfection V700 Photo, Epson, Long Beach, CA) with gamma set to 1. Scanned images were saved as 16-bit tiff files.

AVI video analysis

AVI videos of gold enhancement experiments were analyzed using ImageJ. Enhancement ratio was determined by comparing background-subtracted average signal intensity between the pre- and post-enhancement frames of the AVI movie. To define the signal line, we first subtracting the first frame of the AVI from the last frame, then thresholded the resulting image using the "dark background" threshold preset, and then used the "analyze particles" tool to determine a region of interest surrounding the signal line. The average signal intensity of this region was calculated for each frame of the AVI, then background-subtracted using a background region between the signal and control lines. Finally, the background-subtracted value was normalized, using the difference between the darkest value achieved in the control line and the whitest value seen in the background region. This background-subtracted normalized value was evaluated for every frame of the AVI. The factor of enhancement was quantified by dividing the final signal by the pre-enhancement signal.

6.3.2 Results and Discussion: Implementation of PfHRP2 detection using only patterned reagents

Achieving a functional PfHRP2 assay using gold enhancement of a gold-labeled detection antibody was an iterative process. By changing the blocking protocol, device geometry, and liquid volumes, we determined the set of conditions required to implement this assay. We used a PfHRP2 concentration of 100 ng/ml for these assay design experiments because previous work has shown that this concentration yields a strong pre-enhanced signal, which we used to troubleshoot assay development.

Our first PfHRP2 assay used fully blocked devices, cut in a similar geometry to that used by Fu et al [44] (the differences between the geometries are detailed above). Detection antibody and gold enhancement reagents were patterned after blocking. This initial assay design provided us with several key insights. First, the strong signal at the control line confirmed that the gold-labeled detection antibody was rehydrated from its storage site; furthermore, the lack of residual pink spots at the patterned storage site at the first inlet lead us to believe that *all* of the detection antibody was rehydrated.

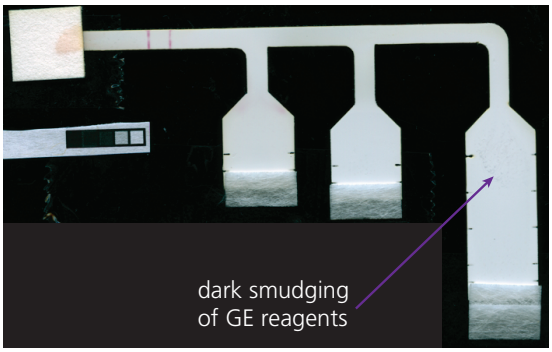

Figure 69: Successful PfHRP2 detection and unsuccessful gold enhancement, using patterned reagents on a blocked membrane. We hypothesize the gold enhancement reagents degraded when stored on a blocked membrane. The dark smudges at the top of the third inlet may be residual gold enhancement reagents.

Second, we observed successful detection of PfHRP2 at the test line, which confirmed that the antibody remains functional through printing, drying, and rehydration; additionally, it validates our initial estimate of the volume of printed detection antibody needed for signal

generation. Third, it was clear that no gold enhancement was visible on any of our devices. Earlier experiments validating the combination of patterned gold enhancement reagents (3.5) never used blocked membranes, so we hypothesized that the blocking interfered with gold enhancement. This hypothesis is supported by the dark colored smudges near the top of the third inlet in all of these devices (Figure 69)—it is possible that the gold enhancement chemistries autonucleate prematurely when stored on blocked devices.

The next assay iteration used unblocked devices, to address the issues observed with gold enhancement. In this case, partial gold enhancement of the control line occurred, but no signal was visible at the test line. Though the presence of the control line confirms that some detection antibody rehydrated, the residual pink spots on the first inlet show that much of the detection antibody was immobilized where it was printed, and was not able to rehydrate. We hypothesize that the lack of PfHRP2 signal is due to a significant portion of the PfHRP2 sample binding to this immobilized fraction of detection antibody, thereby depleting the amount PfHRP2 exposed to the downstream test line.

The third iteration assay used partially blocked membranes, wherein the first inlet was blocked with 14 μl PVP blocker, to facilitate rehydration of detection antibodies, and the rest of the device was not blocked, to maintain gold enhancement functionality. Another modification was the extension of the nitrocellulose "tail" downstream of the capture regions; this extended tail slowed the flow rate throughout the device, with the intention of providing and extended interaction time between the reagents and the capture lines. The third iteration devices yielded visible PfHRP2 signal, as well as partial gold enhancement of both capture and control lines. This uneven signal at the capture and control lines is a result of parallel, rather than sequential, delivery of inlet streams. While watching the flow profiles during the operation of the device, we observed that the blocked inlet exhibited

significantly slower wet-out than the unblocked inlets, which caused the two fluids to be delivered side-by-side through the common channel, rather than sequentially. This disruption of the timed delivery of sequential inlets prevented the top third of the test and control lines from being exposed to the antigen-detection antibody complex. Similarly, the buffer stream containing rehydrated gold enhancement chemistries arrived in the common channel before the wash buffer had ceased, causing those two stream to flow side-by-side over the test and control lines. In this case, the gold enhancement chemistries occupied only the top portion of the common channel, enhancing only a small part of the signal line.

The fourth iteration device addressed the issue of sequential delivery of the inlet fluids across the capture and control lines through two simultaneous modifications. First, diluting the PVP blocker in 0.1% Tween prior to blocking the first inlet slightly increased the flow rate through the first inlet. Second, changing the geometry to increase the time spacing between the first and second inlets allowed more time for the first inlet to empty before the arrival of the fluid from the second inlet. In this iteration we demonstrated a functional PfHRP2 assay, with 3.2 (+/- 0.2) fold gold signal enhancement (n=4) after 60 minutes (Figure 70 and Figure 71). Though the enhancement ratio here is modest, it is a clear demonstration of the viability of patterning and drying reagents onto a

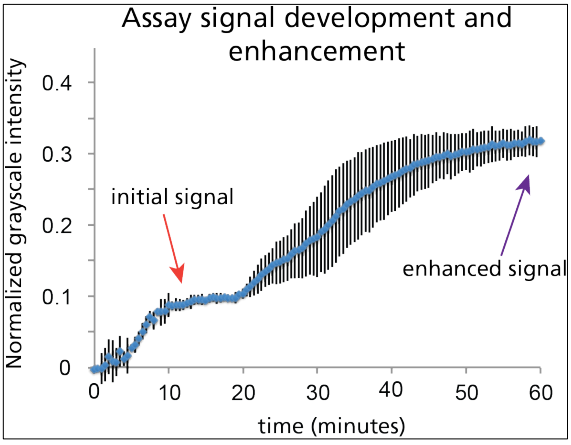

Figure 70: Assay signal vs. time. Time-lapse uncompressed avi files were acquired (1 frame per 30 sec.), and were analyzed using ImageJ (n=4, error bars = s.d.). The large error bars between 25 minutes and 50 minutes are due to variability in the time at which enhancement began, rather than the rate of enhancement. Over 3-fold enhancement is achieved through the use of the gold enhancement system.

paper device as a method for dry reagent storage in paper-based assays.

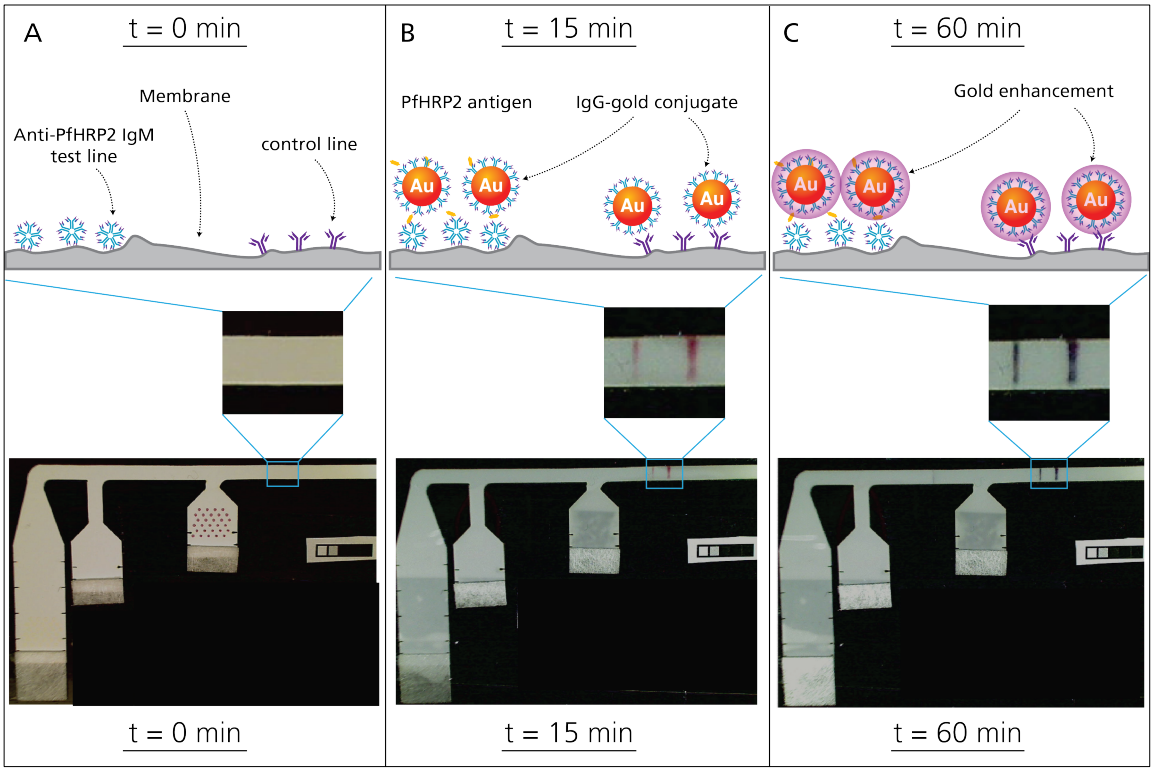

Figure 71: Time series of schematics and images illustrating gold signal development and enhancement. A) Device prior to fluid addition. Anti-PfHRP2 IgM was immobilized as a capture line, while goat-anti-mouse IgG was used as a control line. 30 µl of a mock sample consisting of PfHRP2 spiked at 100 ng/ml into FBS was applied to the right-most inlet, where Anti-PfHRP2 IgG-gold conjugate was patterned for rehydration. Immediately afterward, 40 µl and 100 µl PBS were applied to the middle and left inlets, respectively. B) The initial gold signal appears 15 minutes after fluid addition. At the test line the capture IgM, PfHRP2 antigen, and gold conjugate form a "sandwich", while the control line consists of goat-anti-mouse IgG binding to the mouse IgGs of the gold conjugate. C) Finally, the three gold enhancement solutions patterned on the left-most leg recombine upon rehydration and deposit more gold ions onto the surface of the gold nanoparticles, shifting the absorbance and turning the lines a dark black color. By 60 minutes, the gold enhancement has increased the signal to 3.2 (s.d. 0.2) times the unenhanced intensity. [Schematic based on figures by Dr. Dean Stevens]

6.4 Quantification of assay limit of detection

6.4.1 Methods

Device patterning and construction

All devices were patterned using the methods described in 6.3.1, using the "partial blocking" protocol described in 6.3.1. Rather than running assays taped to a PMMA support, assays were performed in Melinex enclosures to limit evaporation and improve

reproducibility. Assay device enclosures were cut from adhesive-coated Melinex sheets (Fralock, San Carlos, CA) using the CO_2 laser cutter (See Fu et al. Anal. Chem. 2012 for a full description of the development of analogous enclosures [156].)

Protocol for running PfHRP2 assay

As described in 6.3.1, a 30 µl "mock sample" consisting of known concentrations of stock *Pf*HRP2 antigen spiked into fetal bovine serum (FBS, Certified, One Shot™, US Origin, Gibco ®, 16000-077, Invitrogen, Carlsbad, CA) was applied to the first inlet, while 40 µl and 100 µl phosphate buffered saline (PBS) were applied to the second and third inlets, respectively. After addition of fluid, the Melinex enclosure was folded closed and sealed shut to limit evaporation. Mock samples were generated by diluting PfHRP2 antigen (ImmunoDx, Woburn, MA) in fetal bovine serum to 0 ng/ml, 5 ng/ml, 10 ng/ml, 25 ng/ml, 50 ng/ml on the same day that the assays were performed. All assays for limit of detection calculation were performed on the same day.

Image acquisition and analysis

All assay replicates were imaged at 15 minutes (before enhancement) and 60 minutes (after enhancement). Each full enclosure device was scanned to an uncompressed image file with a flatbed scanner (Epson Perfection V700 Photo, Epson, Long Beach, CA) with gamma set to 1. Four replicates were performed at each concentration (resulting in 20 devices overall), but two devices were designated as "enhancement failures" because the control line did not fully enhance, and these are not included in the graphical representation of results or LOD analysis.

Limit of detection quantification

To quantify signal for varying concentrations of *Pf*HRP2 scanned images were quantified using Matlab (MathWorks, Natick, MA), using a script that auto-detected the location and intensity of the test lines based on the location of the control line. The grayscale intensity of the test line was measured, and then the background value was subtracted. The limit of detection (LOD) of the assay was calculated as follows: $LOD = (LOB+1.645\sigma_t)/m$, where LOB = limit of blank (to be explained below), σ_t = the standard deviation of the lowest antigen test, and m is the slope of the signal response curve between zero and the lowest antigen test. The limit of blank is defined as: $LOB = average_{blank} + \sigma_b$, where σ_b = standard deviation of the blank (no antigen control), and signifies the highest concentration that statistically could still be a blank test [163].

6.4.2 Results and discussion

Clear visible signal was observed in all enhanced assay containing non-zero *Pf*HRP2 levels. The unenhanced signal generated by the 10 ng/ml assay was detectable by eye, however the signal from the 5 ng/ml test was not visible. For quantitative analysis, the pre- and post-enhanced assay signal was determined from scanned images using the Matlab script mentioned above. This quantification confirmed reproducible signal at all concentrations for the enhanced assay and as low as 10 ng/ml for the unenhanced assay. Both pre- and post-enhancement images had very low background signal in the negative controls, though the post-enhancement negatives did exhibit slightly darker and noisier negatives, which led to a slightly higher "limit of blank" for the enhanced assay (Figure 72). The intermediate wash step is used for two purposes: first, to rinse over the detection region to reduce false positive signal, and second, to prevent the gold conjugate from contacting the reconstituted gold enhancement system, which would also lead to higher false positives.

The wash and enhancement steps lead to an increase in signal observed in the enhanced assay that is significantly more than the increase in the limit of blank, which yields a 2.75-fold improvement in the overall limit of detection in the enhanced case. The limit of detection of the unenhanced assay was 9.9 ng/ml, whereas the enhanced assay resulted in a limit of detection of 3.6 ng/ml (Figure 72).

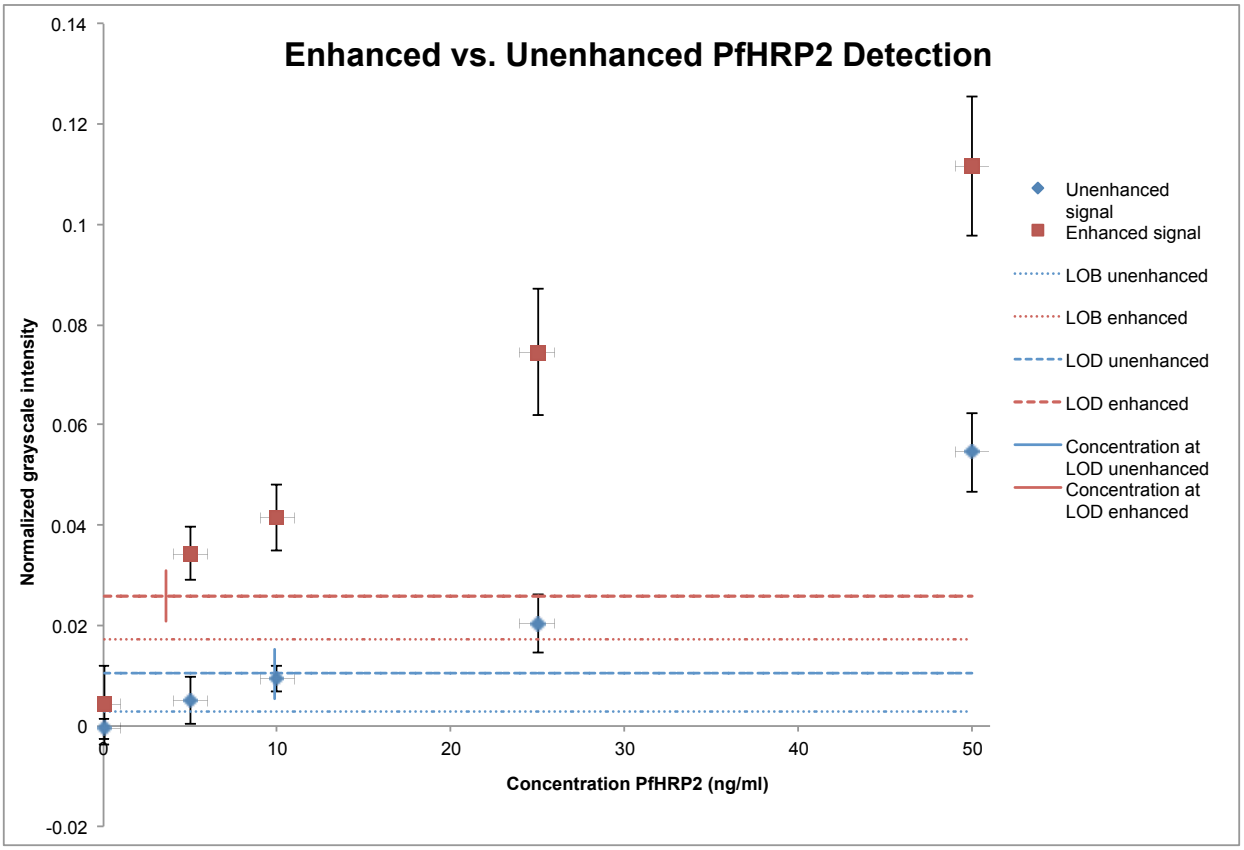

Figure 72: Unenhanced (blue) and enhanced (red) assay results for varying concentrations of *Pf*HRP2 antigen. Four replicates of each concentration were performed, and assay devices were imaged at 15 minutes to quantify unenhanced signal, and then again at 60 minutes to quantify the enhanced signal. The average signal for each concentration of antigen is plotted here (N=4, error bars = s.d.* N=2 for the enhanced 10 ng/ml data due to two tests failing to enhance fully.) Dashed lines indicate the limit of detection signal intensity for both enhanced (red) and unenhanced (blue) assays, and the short vertical lines intersecting those dashed lines indicate the *Pf*HRP2 concentration corresponding to that signal (at 3.6 ng/ml and 9.9 ng/ml respectively). The dotted lines indicate the limit of blank for both enhanced (red) and unenhanced (blue) assays.

Though this is just an initial proof-of-concept demonstration of the viability of patterning reagents for dry storage and subsequent rehydration, it is useful to compare these values with published limits of detection for a variety of malaria diagnostics (Table 7) to benchmark whether this sensitivity is even within a relevant clinical range. Based on limits of detection published in the literature, the analytical limit of detection for our assay is much lower than detection by microscopy, lower than observed LODs for commercially available RDTs, and is comparable to the upper end of reported ELISA detection LOD (see references included in table). Even at this early stage of development, this technique of patterning and later rehydrating reagents from dry storage within the membrane achieves a limit of detection within the clinical range, and the addition of a signal enhancement step significantly improves the limit of detection achieved by this device.

Table 7:Reported limits of detection for various malaria diagnostics

Method	Reported limit of detection	Converted limit of detection (parasites/μL ⇔ ng/mL)[a]	Source
Microscopy	20–50 parasites/μL	18 ng/mL–44 ng/mL	Moody et al.[25] and Guerin et al.[164]
ELISA	0.1–4 ng/ml	Roughly 0.1–4.5 parasites/μL	Butterworth et al.[165], Dondorp et al.[166], Kifude et al.[158]
In-lab RDTs (FirstSign™–ParaView; SD BIOLINE; Carestart™; ICT Malaria Combo Cassette)	6.94–27.75 ng/ml	8–30 parasites/μL[a]	Marquart et al. [167]
RDTs in the field	Varies widely; ~100 parasites/μL	~90 ng/mL	Moody et al.[25], Hendriksen et al.[168]

[a]Based on the model developed by Marquart et al. correlating PfHRP2 concentration to parasite levels, using their maximum circulating approximation: 6.94 ng/ml ~ 7.8 parasites/μL [167]

The current device described here could benefit from several process improvements that could potentially lower the limit of detection even further. The second leg of the device (Figure 68) is a wash step that prevents the gold conjugate from coming into direct contact with the gold enhancement solution, and rinses the detection region to reduce non-specific binding of conjugate. A more rigorous wash step may be able to further reduce this non-specifically bound gold conjugate. Additionally, an improved assay quantification algorithm could be designed to differentiate between stray marks and true signal (for example, one negative test had a dark smudge at the upper edge, which was included in the quantitation

method of the current algorithm, but was clearly not spanning the width of the strip). Another feature of this device that needs some improvement is the reproducibility of enhancement: out of the 20 devices that were tested, 2 failed to enhance fully. Based on the detection algorithm and the measured limit of detection, both of these tests would be correctly designated positive results, though if the level of antigen were quantified, it would be underestimated due to the incomplete enhancement. We hypothesize that the incomplete enhancement is due to a defect in timing that caused the enhancement and wash fluid streams to pass over the detection line simultaneously, with the enhancement stream at the top edge of the strip and the wash stream at the lower edge of the strip. Improvements in device actuation, such as the implementation of inlet capillaries as shown by Dharmaraja et al.[131] could mitigate this problem.

In the devices described here, all reagents were patterned onto the paper membranes and allowed to dry at room temperature for between 2–5 days before use in the assay. This demonstration of reagent drying within the porous nitrocellulose matrix, successful rehydration, and subsequent viability in the sample assay is a valuable first step towards incorporating these techniques in clinically relevant assays. These methods are very well suited for roll-to-roll manufacturing techniques, which are much more efficient for mass-scale device fabrication than the pick-and-place methods that would be required to fabricate an analogous 2DPN with many different dried reagent pads (see comparison in Figure 67). This is a proof-of-concept study to demonstrate the feasibility of patterned reagents in the context of paper-based assays however, and even after improving the details of device operation described above, several important next steps are needed before this assay device could be used in a clinical setting: (1) future studies designed to determine longer-term shelf stability and resistance to damage at extreme temperatures, (2) clinical sample

validation, using blinded samples both positive and negative for *P. falciparum* malaria at a wide range of parasitemia levels, and (3) manufacturing optimization to implement these fabrication methods within a roll-to-roll process. Another area of future work that is currently being actively pursued in the laboratory is implementing similar methods in other assay systems. The gold enhancement chemistry is effective for any gold-conjugate-based detection, so for another immunoassay, the only part of the assay that needs to be replaced is the specific detection antibodies both at the capture region and those conjugated to the gold nanoparticle for detection.

6.5 Conclusions

The work described in Chapter 6 has presented a simple and effective demonstration of the feasibility and utility of patterning multiple reagents sequentially on a porous device; it is just one example of the potential applications enabled by printing reagents directly on porous devices for controlled rehydration and use in assays. Generally, two-dimensional paper network assays offer a significant improvement over traditional lateral flow rapid tests by incorporating additional assays steps to dramatically improve assay sensitivity—our methods to pattern reagents for storage and rehydration take these advancements a step further by reducing the amount of reagents required to achieve the same level of performance, and also greatly simplifying device manufacturing. These methods are very well suited for roll-to-roll manufacturing techniques, which are much more efficient for mass-scale device fabrication than the pick-and-place methods that would be required to fabricate an analogous 2DPN with many different dried reagent pads. Though we are not at the stage of implementing mass-scale manufacturing of these devices, these considerations are absolutely essential for engineers who are seeking to develop technologies that will have the ability to make a real impact on point-of-care diagnostic medicine; technologies

that cannot be manufactured efficiently will never achieve the low cost and robustness that are required to make them deliverable to the patients and health centers that most desperately need them.

7 Develop computational models of transport and binding to improve assay "engineerability"

7.1 Objectives and motivation

Overall, this project has sought to facilitate the design and enhance the fundamental understanding of more sophisticated 2DPN assays. In other chapters of this thesis we have developed computational models that build a level of mathematical analysis upon experimental methods designed to control behavior of 2DPN devices. This chapter is somewhat of a departure from that strategy; instead of modeling specific methods, we built two simplified theoretical computational models, which could be used to begin to explore how binding interactions in 2DPNs respond to variations in different parameters, and examine the underlying physics of a 2DPN system.

The first model described in this chapter simplifies the porous network of a 2DPN device to a single 10 μm diameter pore. This simplification allows us to probe the effects of transport and binding parameters on the *surface* interactions within a pore. Whereas a bulk porous media reaction model (like in Chapter 4) simplifies the complex porous network by neglecting all internal surfaces, this model explicitly defines the surface, but neglects the complex structure of the porous medium. Both types of models simplify the random porous network, but in opposite ways, so they can be complementary when seeking to understand the processes of transport and surface reactions within a porous device.

The second model described here uses a zero-dimensional reaction model to predict the approximate relative frequency of different antigen-antibody species present in solution of multivalent analytes and binding molecules; in this case, gold conjugate and the malaria antigen *Pf*HRP2. The zero-dimensional model calculates the relative concentrations over

time, while assuming perfect mixing without regard to spatial dimensions. We have hypothesized that different complexes have different avidities for the surface-bound capture species, which could lead to different signal profiles in 2DPNs. Elain Fu and Tinny Liang have incorporated this simplified model in a bulk porous media model of pre-mixing versus sequential delivery of gold conjugate and PfHRP2, to represent the different distributions of binding species.

With both models, we hope to develop tools that can provide a conceptual understanding of the system, by simulating how variations in different parameters affect the performance of the system.

7.2 Develop a single-pore model of protein binding and adsorption in nitrocellulose

This model of transport and binding in a single pore of nitrocellulose was built from the ground up, starting with fluid flow in a pipe, adding in diffusive species transport, and finally including reactions. Each stage was designed based on the physics of the system and carefully assessed assumptions. Some of these assumptions are clearly simplifications (nitrocellulose is a very complex network, not at all like a simple tube), but by starting with the underlying physics, we were able to carefully control all assumptions and explicitly examine the micro-scale pore-sized view of transport and binding, which complements Comsol's built in bulk view "reactions in porous media" module that simplifies the complex porous matrix by neglecting internal surfaces.

7.2.1 Model components and parameters

Physics

Unlike the models described previously in this document, this model does not use the porous media physics built in to Comsol Multiphysics (Comsol, Inc., Burlington, MA) ; instead, it is built on the laminar flow module for flow in a pipe, with a geometry that approximates a single pore within the nitrocellulose membrane. This "single pore" is a 2-dimensional axisymmetric cylinder with a diameter of 10 μm (analogous to the approximate 10 μm membrane pore diameter) and a length of 4 mm (Figure 73), with a binding zone of 3 mm. This model geometry is clearly a simplification of the complex inner structure of a porous membrane—recall the SEM image from Chapter 2 (Figure 9); however, it is consistent with previous flow models representing porous media as a bundle of small tubes (Figure 10).

The benefit of this single pore model of nitrocellulose membranes, with an extremely extended aspect ratio, is it allows us to study the *microscale* interactions of solutes with the membrane surface over the *macroscale* length of an extended binding patch. Solutes and surface-binding interactions in the model are incorporated using the transport of dilute species modules, along with the surface reasons module. The solute, C, is introduced at the inlet and flows through the pipe in the laminar flow velocity field calculated based on the boundary conditions described for flow. The surface reactions are similar to those described in Chapter 4, except that here, the surface is explicitly a *surface*, rather than mathematically-defined immobile molecules perfectly distributed throughout the macroscale porous medium. Capture molecules on the membrane surface are represented by "S", and bound molecules are represented by "B".

At the surface the following reaction is applied:

$$S + C \underset{k_{off}}{\overset{k_{on}}{\rightleftharpoons}} B$$

For conservation of species, the reaction rate of each is described by:

$$\frac{dS}{dt} = k_{off}[B] - k_{on}[S][C]$$

$$\frac{dC}{dt} = k_{off}[B] - k_{on}[S][C]$$

$$\frac{dB}{dt} = -k_{off}[B] + k_{on}[S][C]$$

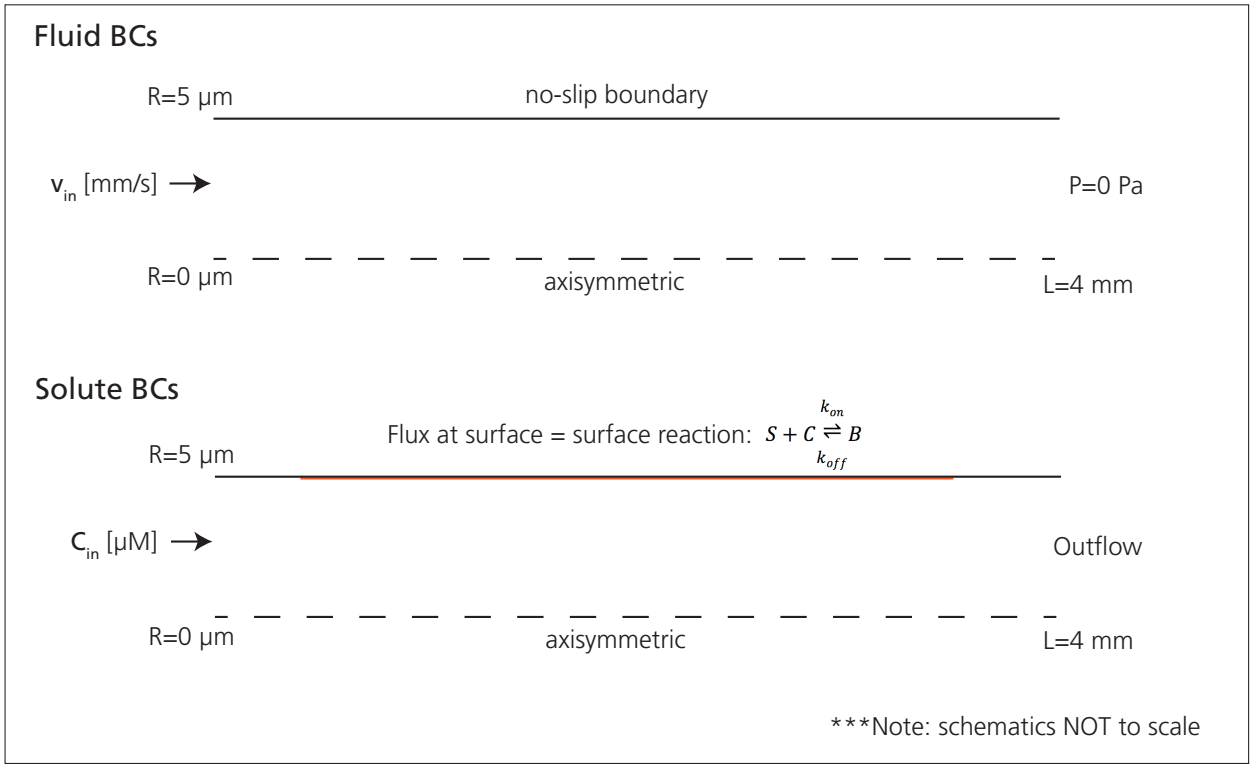

Figure 73: Schematics of the fluid and solute boundary conditions used in the single pore model.

Parameters

This model was built based on the physics of the system and carefully assessed assumptions to allow the simplification from a complex porous matrix to a single pore.

Parameter	Description	Value	Justification
C_{in}	Inlet concentration	5–40 nM	Measured
S_0	Density of surface sites	1 x 10^{-8} mol/m^2	Approximated
V_{in}	Inlet velocity	0.3 mm/s	Measured by Jeff Yang
R_p	Pore radius	5 µm	Manufacturer reported
D_{eff}	Diffusivity of solute	2 x 10^{-10} m^2/s	Measured by Jennifer Osborn, also approximated
k_{on}	On-rate of binding	1 x 10^4–10^6 $M^{-1}s^{-1}$	Literature values [139, 140, 169, 170]
k_{off}	Off-rate of binding	1 x 10^{-3}–10^{-4} s^{-1}	Literature values [139, 140, 169, 170]
t_{sample}	Time duration of solute pulse	230 s	Calculated
w_{strip}	Strip width	3 mm	Measured
vol_{sample}	Sample volume	20 µl	Measured

The inlet concentration was set to experimental values based on the concentrations used in experiments. These inlet values were measured using a NanoDrop Spectrometer (Thermo Scientific) to determine the stock protein concentration, and dilutions were adjusted accordingly.

The surface site density was calculated in the same ways that surface adsorption sites were determined in Chapter 4. First, we approximated IgG as a 10 nm sphere and calculated

how many IgGs could fit in one square meter: 1.7×10^{-8} moles IgG per m^2. Second, we used the rinsed printed IgG spots at 2 mg/ml, which appeared to be close to saturation, to approximate the amount of IgG required to saturate a given surface area of membrane. The spot area measured from the top of the membrane was 4.5 mm^2; with these membranes' surface area ratio of approximately 100, that gives a total internal surface area of 450 mm^2. Printing 500 nL of IgG at 2 mg/ml yields 1 μg or 6.7×10^{-12} moles IgG, yielding a surface concentration of 1.5×10^{-8} moles IgG per m^2. As mentioned in Chapter 4, these two estimates are remarkably similar, suggesting that the value is a reasonable estimate. However, because the experiment corresponding to this simulation was performed with a specific interaction (Protein G–IgG) we wanted to compensate for the random orientation of the surface-bound capture species, so we chose to round down to 1×10^{-8} moles/m^2 as the input surface site density.

Inlet velocity, v_{in}, was set to 0.3 mm/s, based on flow visualization experiments and calculations performed by Jeff Yang, an undergraduate in the lab.

Reported literature values for bulk molecular diffusivity (D_m) of a solute are inaccurate in porous media when Pe>>1, as described in Chapter 2. Therefore, we needed to approximate the effective solute diffusivity D_{eff} to use in the simulation. This approximation was performed in two ways. First, we used apparent diffusivity values from Jennifer Osborn's PhD thesis; wherein she described her observations of dramatically enhanced transverse transport in nitrocellulose membranes due to mechanical dispersion of solutes in flow through the porous medium, for radial Péclet numbers >>1 [79]. In those experiments, using membranes similar to those that we used in our experiments, she observed effective diffusivity values of roughly 2×10^{-10} m^2/s for IgG. Second, the literature describing transport

in porous media in the context of soils and rocks includes a discussion of enhanced transverse transport in porous media, where:

$$\frac{D_{eff}}{D_m} \propto Pe = \frac{vL}{D_m}$$

D_{eff} is the effective, observed diffusivity, D_m is the reported molecular diffusivity of the solute and Pe is the Péclet number [80]. Based on this approximation, and J. Osborn's experimental conditions with R_p = 4.5 μm and v = 0.1 mm/s, D_{eff} can be approximated as ~$4.5x10^{-10}$ m^2/s which is very close to her fitted D_{eff} value.

On- and off-rates for solute binding to surface species were based on reported literature values for Protein G–IgG binding [169, 170], and IgG–antigen binding [139, 140]. A discussion of the effects of different on- and off-rates on binding of solutes to the membrane is included later in this chapter.

The sample time parameter, t_{sample}, represents the amount of time it takes for a sample to completely empty through the simulated pore. Because in reality a single pore does not exist outside of the porous network, and the entire sample volume does not need to pass through a single pore, we calculate the sample time based on several other parameters of the experimental system: it is a function of the sample volume, the void volume per millimeter of membrane, and the flow velocity. For this simulation, the corresponding experiment was performed in nitrocellulose strips that were 3 mm wide, 120 μm thick, and had a porosity of 0.8, leading to a void volume of 0.288 μL per linear millimeter. The sample volume was 20 μL, which occupies 69.4 linear mm in a strip with the aforementioned characteristics. A flow velocity of 0.3 mm/s, leads to a t_{sample} of 231 s.

7.2.2 Building the model

To confirm that this simplified computational model predicted behavior consistent with the well-understood physics of transport in pipes, we checked the behavior of the model at each stage of its construction.

Diffusion only

The simplest implementation of the model is the no-flow, diffusion-only case, in which the velocity field is set to zero, but the solute is allowed to diffuse outward down the pipe from the inlet. In the no-flow case, Comsol simply calculates the concentration by solving Fick's Second Law:

$$\frac{dC}{dt} = D\nabla^2 C$$

We can approximate the characteristic diffusion distance at a given time as:

$$L = \sqrt{D_{eff} t}$$

Therefore, after 4x the time has passed, the characteristic diffusion distance is only 2x as far. When we compare the diffusion-only solute distribution for a range of diffusivity values at two different times, we can confirm that the model predicts the expected diffusion profiles.

Flow only

Second, we examined the velocity field predicted by the simulation, given the input inlet velocity, v_{in}. As described in Chapter 2, flow in a pipe has been thoroughly characterized, and can be described by Poiseuille's law, yielding a parabolic velocity field, with v = 0 at the walls of the pipe and a maximum velocity of 2x the average velocity at r = 0. The model-

predicted velocity field versus the r-coordinate of the pipe yields the expected parabolic velocity field, confirming that the appropriate boundary conditions were used for flow.

Taylor dispersion

Third, we confirmed that the model-predicted non-diffusion Taylor-Aris skewing of a solute bolus (Figure 6 part 2) when diffusion was set close to zero ($D=10^{-13}$ m^2/s, because D=0 results in a computational singularity). When a short plug of solute with negligible diffusivity was introduced to the model pore, it generated the appropriate parabolic-shaped solute distribution, and when diffusion was re-introduced, the model generated the predicted enhanced radial distribution (Figure 6 part 4).

Surface Reaction

Once the fluid flow and solute transport components of the model were confirmed to behave as expected, we integrated all of the flow and diffusion properties (D_{eff} = 2 x 10^{-10} m^2/s ; v_{in} = 0.3 mm/s) and introduced the surface reaction flux at the reaction zone indicated in Figure 73. This outward flux of solute C is balanced with a reaction generating B on the surface, as described above.

7.2.3 Varying parameters

Diffusivity: D_{eff}

To better understand the effect of diffusion in our system, we varied D_{eff} over a range of values from 2 x 10^{-11}–2 x 10^{-9} m^2/s, and found that diffusion does not dramatically affect quantity and distribution of surface-bound analyte (Figure 74). This is not to say that it has no impact, but rather, other parameters, such as analyte concentration, on-rate, or binding site density play a more significant role. A quick calculation can rationalize this model prediction. The characteristic diffusion time over a distance L is equal to: $t = L^2/D$, so we

can approximate the diffusion time given three possible D_{eff} values: 2 x 10^{-11} m^2/s (approximately the diffusivity of IgG in water [171]), 2 x 10^{-10} m^2/s (J. Osborn's observed D_{eff} in a porous membrane), and 2 x 10^{-9} m^2/s (approximately $D_{eff} = vR_p$ solved for our system: 0.3 mm/s * 5 µm). The resulting characteristic diffusion times are: 12.5 x 10^{-3} s, 0.125 s, and 1.25 s. At the relatively slow flow rate of 0.3 mm/s, even the slowest diffusion time occurs faster than the time for the solute to travel 0.5 mm downstream, which provides an intuitive understanding of why the solute diffusivity is not the primary parameter that governs the distribution of bound protein.

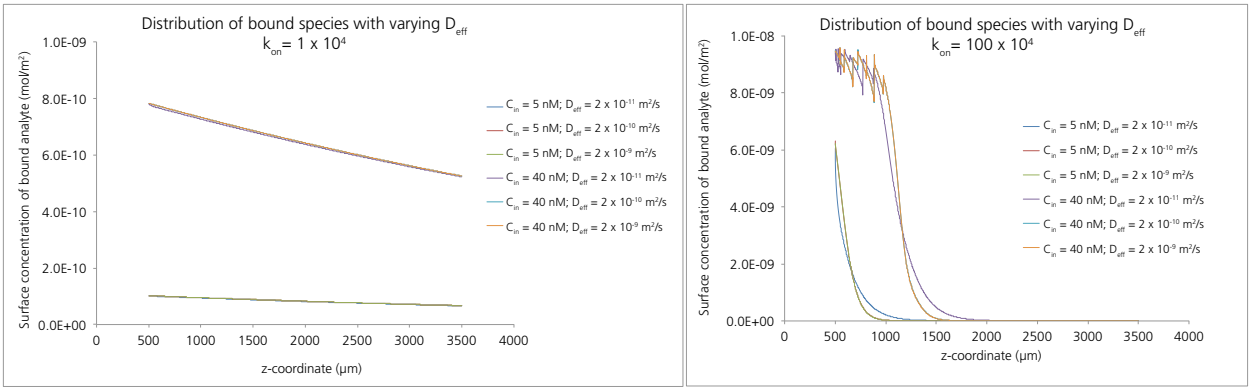

Figure 74: Plots showing the distribution of the bound species with respect to the z-coordinate of the model "pipe" when varying the effective diffusivity, D_{eff}, at two different inlet concentrations. The time point shown is at time= 400 seconds. At left is a simulation with k_{on} set to 1 x 10^4 [L/(mol*s)], at two different concentrations (upper set of lines versus lower set of lines) and three D_{eff} values (indistinguishable within each set). At right is an analogous simulation, with k_{on} set to 100 x 10^4 [L/(mol*s)], at two different concentrations (left set of lines versus right set of lines) and three D_{eff} values (close together, but not indistinguishable within each set). At both extremes of k_{on} values and concentrations, the variations due to the differences in D_{eff} values are small relative to the differences due to k_{on} values or concentrations, suggesting that within the relevant parameter ranges, this model is relatively insensitive to D_{eff}. Note: the jagged edges near the saturation point of 1 x 10^{-8} mol/m^2, on the high-concentration, high-k_{on} curves are model artifacts due to the relatively large time steps (5 sec.) and coarse mesh (1 µm) that were necessary to keep computation times reasonable. This assessment is supported by model simulations (not shown) that gradually decreased the time step from 100 sec. to 5 sec., and simulations that decreased the mesh size from 1.2 to 0.8 µm (smaller than 0.8 µm was not feasible with the extended aspect ratio), and these modifications dramatically improved the jagged edges without affecting the rest of the curve.

Off-rate: k_{off}

The off-rate included to describe the un-binding interaction has a more substantial effect than D_{eff}, but as with diffusivity, within the relevant range, the off-rate is less influential than on-rate or concentration in governing the final distribution of bound species (Figure 75). This can be rationalized with a quick approximation of the unbinding timescale: $1/k_{off}$. For $k_{off} = 1 \times 10^{-3}$ s^{-1}, this timescale is 1000 seconds, comparable to the duration of the simulation, which is why those curves are slightly apart from the lower k_{off} values—the off rate is just beginning to be relevant. For k_{off} values faster than 1×10^{-3} s^{-1}, k_{off} *will* have a profound effect on the distribution of bound analyte, whereas lower k_{off} values will just approach the curve at $k_{off} = 0$ s^{-1}. Faster off rates are not relevant to our model however, because $k_{off} > 1 \times 10^{-3}$ s^{-1} is a more rapid off-rate than typically observed in specific binding interactions.

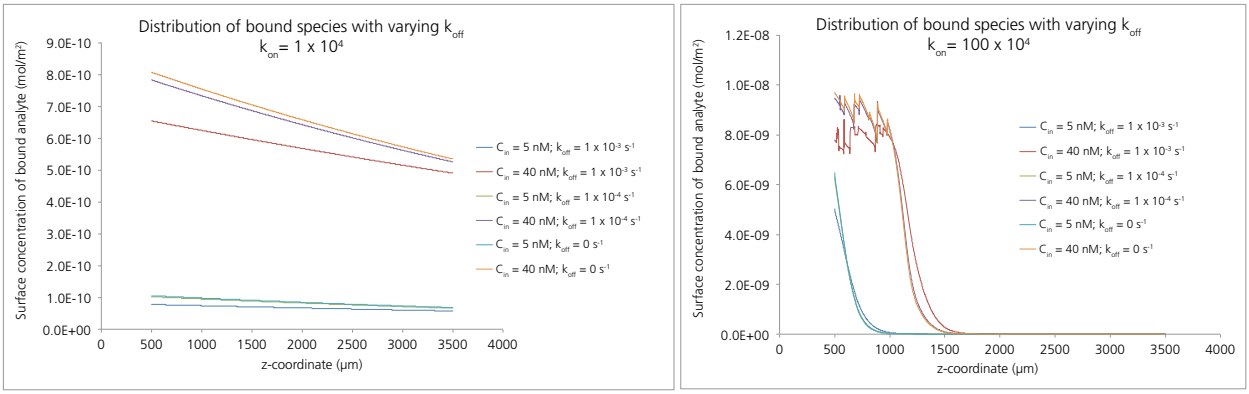

Figure 75: Plots showing the distribution of the bound species with respect to the z-coordinate of the model "pipe" when varying the off-rate, k_{off}. The time point shown is at time= 400 seconds. At left is a simulation with k_{on} set to 1×10^4 [L/(mol*s)], at two different concentrations (upper set of lines versus lower set of lines) and three k_{off} values (grouped together by concentration, but clearly distinguishable from one another). At right is an analogous simulation, with k_{on} set to 100×10^4 [L/(mol*s)], at two different concentrations (left set of lines versus right set of lines) and three k_{off} values (clustered even closer together than at low k_{on}). Based on these comparisons at both extremes of k_{on} values and concentrations, the variations due to the differences in k_{off} values are small relative to the differences due to k_{on} values or concentrations. As described in Figure 74, the jagged curve of the high-concentration simulations in the graph on the right is a model artifact caused by the large time steps and coarse mesh.

On-rate: k_{on}

The reaction on-rate is one of the most important parameters governing the distribution of bound analyte on the surface. When k_{on} is varied across the relevant range of values (1 x 10^4 – 100 x 10^4 [L/(mol*s)]), the distribution of surface-bound protein varied dramatically across the range of k_{on} values, at both extremes of the concentration range (Figure 76). This effect should not be surprising however, because the on-rate directly controls the rate at which new complexes are formed.

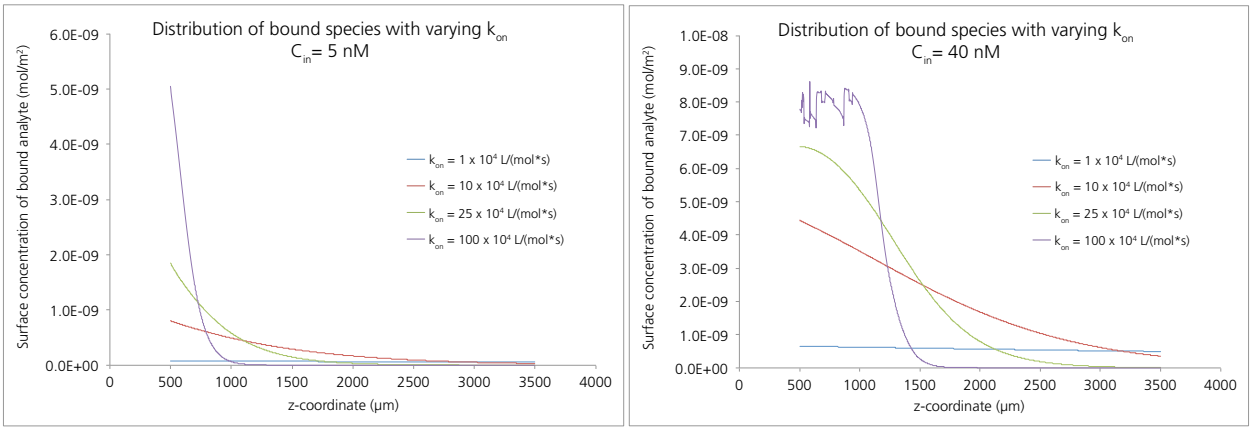

Figure 76: Plots showing the distribution of the bound species with respect to the z-coordinate of the model "pipe" when varying the on-rate, k_{on}. The time point shown is at time= 400 seconds. At left is a simulation with C_{in} set to 5 nM, at four k_{on} values. All four k_{on} values result in surface-bound analyte distribution profiles that are distinct from one another. At right is an analogous simulation, with C_{in} set to 40 nM at four k_{on} values, and again, the shape of each profile is distinct from the others. Based on these comparisons at both extremes of concentrations, the variations due to the differences in k_{on} values are a dominant parameter that governs the distribution of the surface bound species. As described in Figure 74, the jagged curve of the high-concentration simulation in the graph on the right is a model artifact caused by the large time steps and coarse mesh.

Surface site density

Surface site density also plays a major role in determining the distribution of bound analyte, because a higher concentration of available sites increases the surface saturation level, and therefore, for a rapid binding interaction, the analyte is depleted from solution in a shorter distance (Figure 77), which we also observed in Chapter 4. In the simulation here we varied the surface site density by 4x below and above the estimated value of 1 x 10^{-8}

mol/m², to include 0.25 x 10^{-8} mol/m² and 4 x 10^{-8} mol/m², the simulation results are shown in Figure 77.

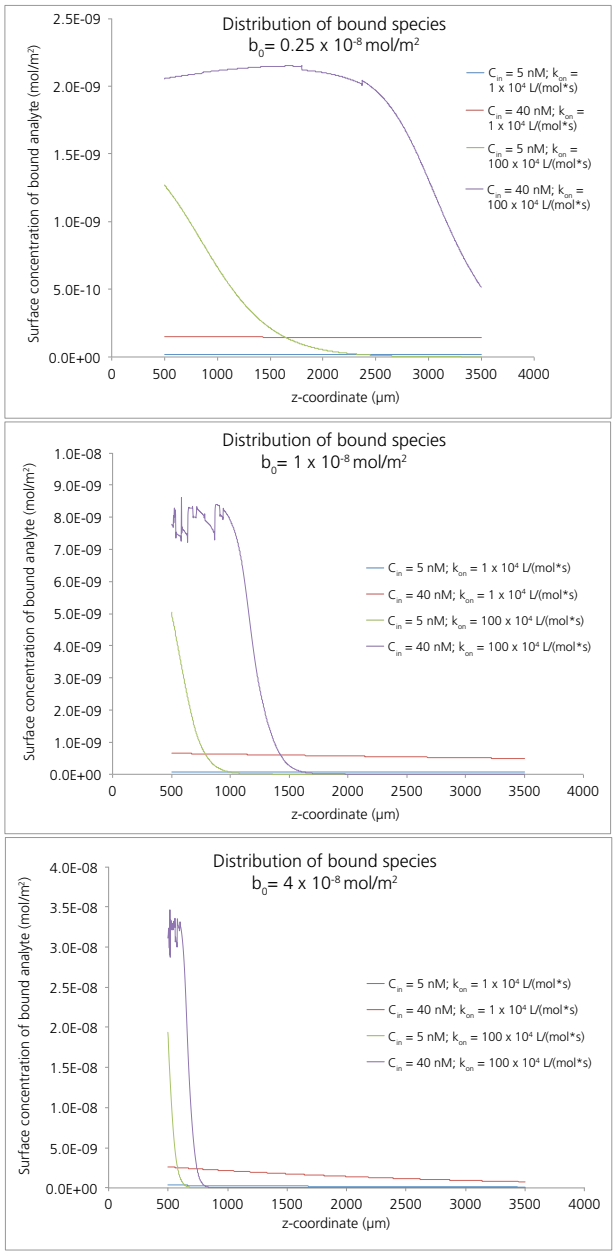

Figure 77: Plots comparing the distribution of bound analyte when the surface site density (b_0) is varied. Two concentrations (blue and green lines: 5 nM; red and purple lines: 40 nM) and two k_{on} values (purple and green: 100 x 10^4 L/(mol*s); red and blue: 1 x 10^4 L/(mol*s)) were compared for each b_0. At fast k_{on}, higher b_0 results in depletion of the analyte in a shorter distance along the binding zone (compare purple and green curves across all plots), whereas the difference in the shapes of low-k_{on} curves is less pronounced, though increasing b_0 does cause a steeper curve. Also, because more sites are available, high b_0 results in higher maximum surface bound concentration for all curves.

The methods we used to approximate the concentration of available sites were based on experimental data, and a simple, but reasonable calculation based on approximate protein dimensions. Additionally, the same approximation in Chapter 4 yielded experimentally consistent results, so it is unlikely that this approximation is inaccurate by orders of magnitude. However, the number of available binding sites is dependent on the orientation of the capture species, as well as the robustness of the adsorption of the capture species to the membrane, so it is useful to examine a range of values for this parameter.

7.2.4 Comparison between model and experiment

To validate the model, we used a well-characterized but simple binding interaction—Protein G to IgG. Initially we had tried to use the *Pf*HRP2 system described in Chapter 6, however the 2-step sandwich of that assay, plus the multivalency of all of the components, added significantly more variables to fit in the model, and correspondingly more opportunities for error. Capturing fluorescently-labeled IgG with Protein G molecules adsorbed to the surface, however, is ideal for this model comparison because we can directly detect the captured species, reducing the number of necessary parameters, and because the interaction has already been thoroughly characterized [169, 170].

Experimental methods

Nitrocellulose membranes were cut into 8-leg combs on a CO_2 laser (Universal Laser Systems, Scottsdale, AZ) as described previously [130]. Protein G at 1 mg/ml in 0.1 MCitrate buffer pH 4.5 mg/ml (Thermo Scientific) was printed in a 3 mm-wide patch on each leg of the 8-leg device, using the S3 Flexarrayer piezoelectric printer (Scienion AG, Berlin, Germany). The 3 mm wide patch spanned the 3-mm width of each strip, and was patterned by printing 10 lines spaced 250 μm apart (the lines spread roughly 250 μm, so the final width of the patch was 3 mm), with 12 dots per line also spaced 250 μm apart.

Patterned drop volumes were roughly 450 pL, and 30 drops were deposited per spot. In the 10-line patch, first lines 1, 2, 5, 6, 9, 10 were printed, and then immediately following, lines 3, 4, 7, 8 were printed. This staggered printing method was intended to prevent over-saturating the membrane with liquid, which can cause excess liquid to wick into the first-wetted region, leaving an uneven distribution of protein. However, as can be seen in the experimental results, it is clear that this was not successful: it appears that lines 3 and 4 blended together and lines 7 and 8 blended together, and contained a lower level of Protein G than the initial round of patterned lines (1, 2, 5, 6, 9, 10). Despite this shortcoming, the grouped printing method did ensure that each pair of lines in the first round of printing [(1,2) (5,6) (9,10)] contained equal amounts of Protein G, because the sets did not overlap during the first round of printing, preventing the liquid in those lines from oversaturating and wicking back toward line 1.

To run the experiment, 8-leg devices were taped to cellulose wicking pads. A 96-well plate was loaded with the first row containing 20 μL PBS to completely wet the strips and ensure a constant flow rate before adding the sample, the second row containing 20 μL sample, and the third row containing 20 μL PBS for a wash. The five sample conditions were: 0 nM, 5 nM, 10 nM, 20 nM, and 40 nM IgG in PBS +1% BSA as a real-time blocking agent to prevent non-specific adsorption of the IgG to the upstream region of the membrane. Each sample was run in quadruplicate.

Strips were imaged with a Nikon SMZ1500 stereomicroscopescope, at 2x magnification for 4 seconds each. Images were normalized by a fluorescent flood image taken of a piece of fluorescent green PMMA, averaged, and then re-normalized by the maximum intensity of the 40 nM IgG samples, so that the data could be presented on a zero to one scale.

Model parameters for comparison

Though the reported k_{on} and k_{off} values for this interaction vary somewhat depending on the specific IgG subclass [170], one study reported k_{on} ~$3.3x10^4$ $M^{-1}s^{-1}$ and k_{off} ~$3x10^{-4}$ s^{-1} in PBS [169], so we used those values for the model input when comparing to Protein G-IgG binding experiments.

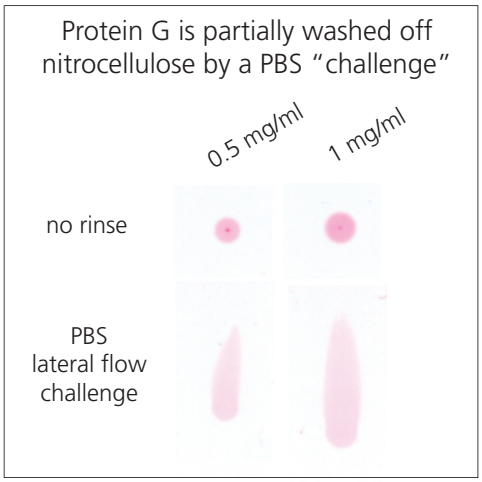

Figure 78: Lateral flow challenge of Protein G spots with PBS compared to non-challenged spots showing that PBS partially displaces some of the surface-adsorbed Protein G, leaving fewer than anticipated available binding sites to capture IgG

As described above, the inlet velocity and concentrations were measured, so those values were used in the simulation.

To determine an appropriate surface site density of Protein G after a PBS rinse, we performed a "lateral flow challenge" experiment and printed several Protein G spots (450 pL each) at both 0.5 mg/ml and 1 mg/ml on two sets of nitrocellulose strips. After drying the spots overnight, PBS was wicked through one set of the strips via lateral flow, and then those strips were dried and stained with Ponceau S (Figure 78). Based on this image, it is clear that some of the Protein G is displaced during wet-out with PBS, so we decreased the initial surface site concentration to 5 x 10^{-9} mol/m^2, but also ran simulations at 3 x 10^{-9} mol/m^2 and 1 x 10^{-8} mol/m^2 to compare with the experimental results.

The model-simulated results of surface-bound concentration profiles were all normalized by the highest value present in the 40 nM simulated plot, so that they would be on the same intensity scale as the normalized experimental plots and could be plotted on the same axes for comparison.

Comparison between experiment and simulation

Experimental plots of the IgG distribution resulting from capture by Protein-G immobilized on nitrocellulose were compared to the predictions generated from the single-pore model using the parameters described above. The overall shapes of the curves are very similar, as are the relative intensities of the surface concentration profiles resulting from different input concentrations (Figure 79). The uneven bumps in the experimental data, due to uneven deposition of Protein G during printing, present the most significant departure from the simulated profiles. Future experiments could improve the method used to deposit Protein G to achieve more even distribution of the capture species. Furthermore incorporating a wider range of input concentrations, intentionally varied b_0 levels (which could be achieved by mixing Protein G with a non-IgG-binding protein), and varied inlet flow velocities could all be used to generate more data points to compare to model simulations, which could be used in a non-linear fitting algorithm to find the highest-quality fit.

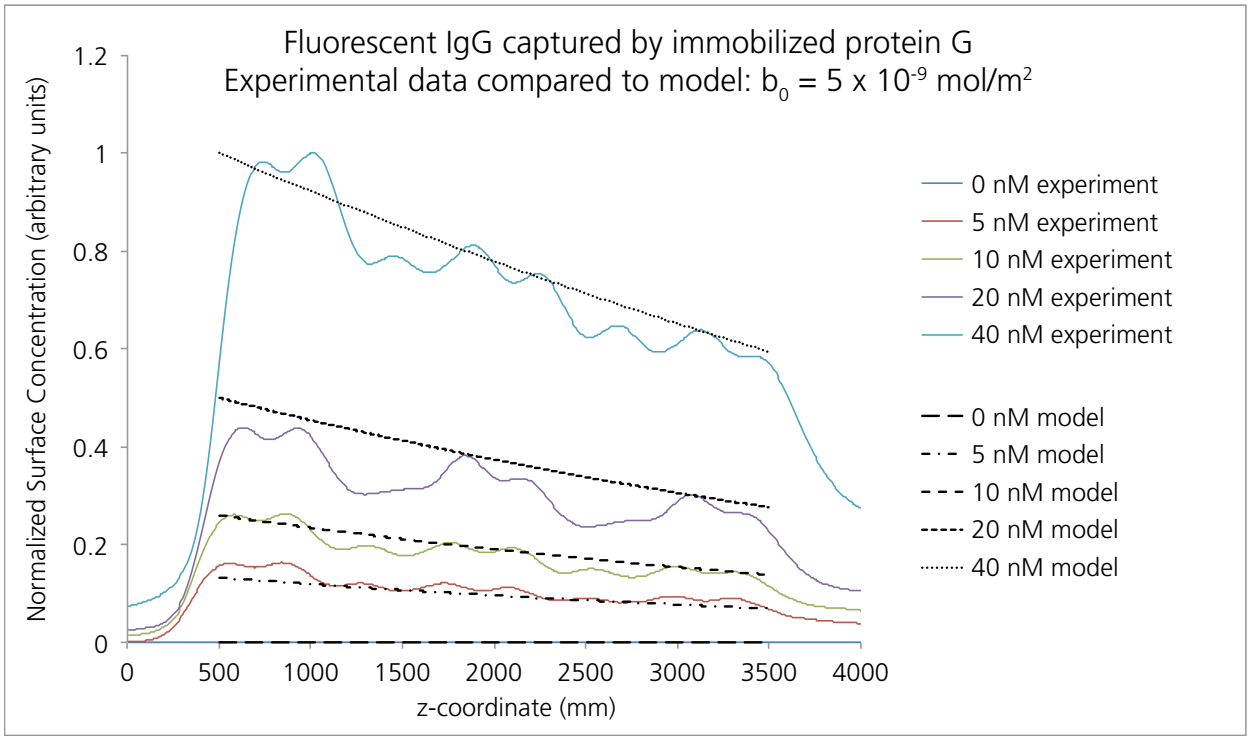

Figure 79: Experimental data from Protein-G capturing IgG on nitrocellulose (solid lines) compared to the predictions generated from the single-pore model (dotted lines). Overall, the shapes of the curves coincide well, aside from the uneven bumps present in the experimental data. This is especially apparent when the experimental plots are compared with simulated plots generated using slightly varied binding site density values (Figure 80). Though the match between the simulation and experiment is close, the fit is still not perfect, and future studies could improve the method used to deposit Protein G to achieve more even distribution of the capture species. Additionally, repeating these experiments with a wider range of input concentrations, intentionally varied b_0 levels, and varied inlet flow velocities could all be used to generate more data points to compare to model simulations. Our goal in developing this model however was to build a tool that could begin to explore the transport and binding parameters governing a 2DPN system, and this comparison between the simulation and experimental data supports that the model is a reasonable approximation of reality.

To confirm that our initial approximation of 5×10^{-9} mol/m^2 as the input value for the concentration of available surface sites (b_0) was a reasonable assumption, we ran the simulation with two other b_0 values: 3×10^{-9} mol/m^2 and 1×10^{-8} mol/m^2 to compare with the experimental results. The plots are shown in Figure 80 on page 193, and it is possible to tell by comparing the plots visually that the distribution of bound species is too steep in (B), indicating that the b_0 value is too high, while the distribution in (D) is too shallow, indicating that the b_0 value is too low. Overlaying the simulation from (C) with the

experimental data, as was shown in Figure 79, shows that the simulation-predicted surface concentration and the experimental data are comparable.

This demonstration that the simulation predicts a surface-bound concentration distribution that is consistent with experimental data supports that this single-pore model can be used as a reasonable approximation of the reality of a complex 2DPN, and therefore that by probing parameter space using this simplified model can provide a theoretical understanding of the effects of different transport and binding parameters on the behavior of 2DPN assays.

7.2.5 Conclusions from single-pore model

As discussed earlier in this chapter, we varied the input parameters across a range of values to explore the impact that different parameters had on the output signal of the simulated binding interaction. Future work could further refine the model by comparing with a range of experimental parameters and performing a more rigorous computational fit. We hope that this tool will be useful to others seeking to refine or better understand the components of a binding assay, and that simulated experiments will have the ability to guide more targeted experiments for the highest yield in assay performance.

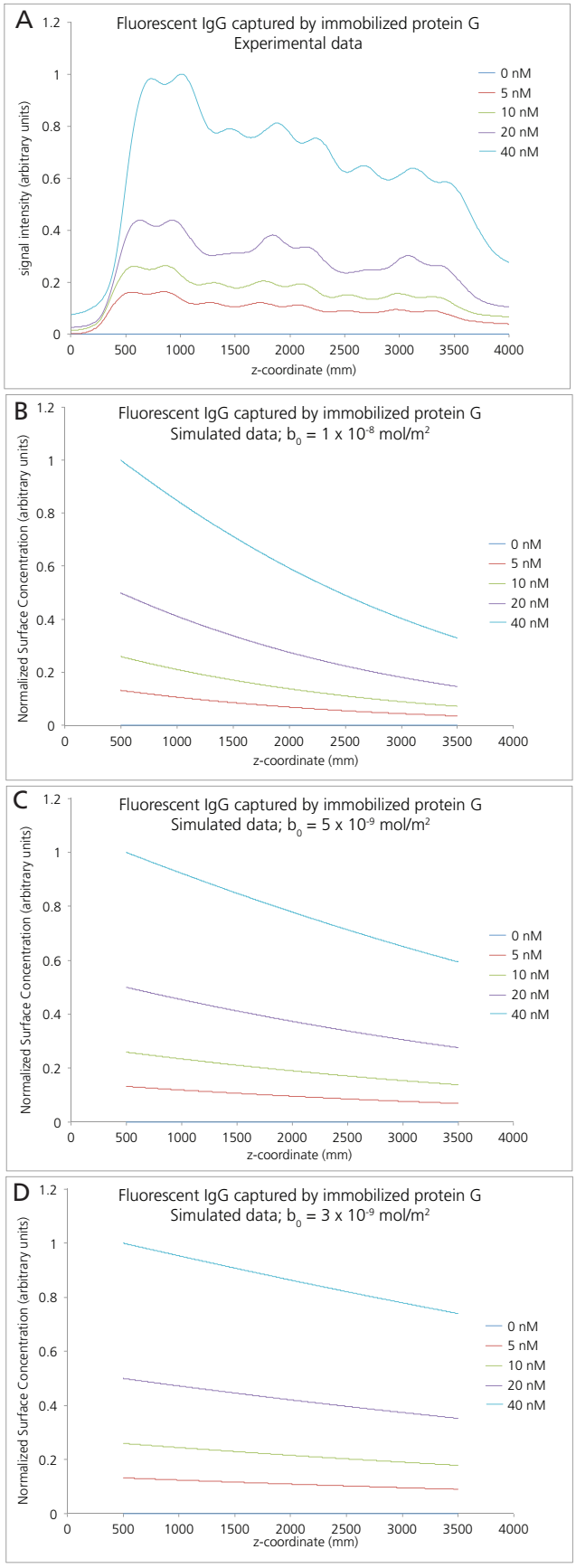

Figure 80: Experimental data (A) compared with three different simulations with varying b_0, initial surface site concentration: 1 x 10^{-8} mol/m^2 (B), 5 x 10^{-9} mol/m^2 (C), and 3 x 10^{-9} mol/m^2 (D). By visual comparison it is possible to tell that the distribution of bound species is too steep in (B), indicating that the b_0 value is too high. Similarly, the distribution in (D) is too shallow, indicating that the b_0 value is too low. Overlaying the simulation from (C) with the experimental data, as was shown in Figure 79, shows that the curvature of the simulation and the experimental data are comparable.

7.3 Develop a reaction model to study effect of premixing multivalent analyte with multivalent IgG-gold conjugate

The second Comsol Multiphysics model described in this chapter was designed to predict the relative frequency of different complexed species present when two multivalent species are mixed and allowed to bind. The specific case that we were interested in here is the premixing of the malaria antigen *Pf*HRP2 with a gold-IgG conjugate detection species. The *Pf*HRP2 antigen contains 18 epitopes recognized by the particular IgG that is used for detection [172], and a single gold nanoparticle contains roughly 12 IgG molecules immobilized on its surface [173].

Elain Fu and Tinny Liang showed experimentally that the signal distribution in a sandwich immunoassay detection region is significantly different if the antigen and conjugate are premixed before applying them to the assay strip, when compared the sequential delivery of first the antigen and then the detection conjugate (Figure 81).

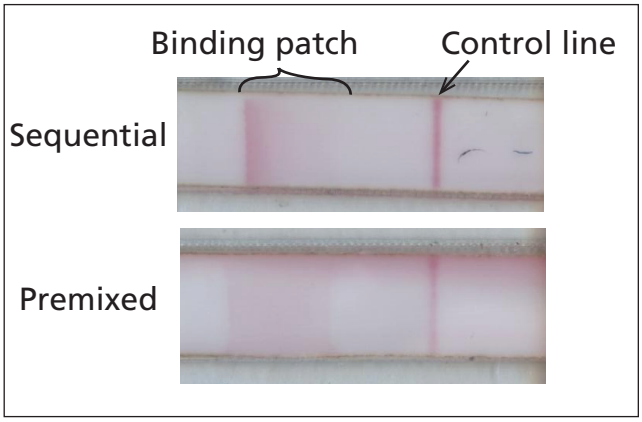

Figure 81: Sequential delivery of PfHRP2 then conjugate results in a dark leading edge, with signal falling off rapidly, whereas premixed antigen and conjugate results in a uniform but faint binding region. The concentration of PfHRP2 used here was 5 ng/ml: (Data from Tinny Liang and Elain Fu).

They hypothesized that the capture molecule used in this assay, a monoclonal IgM, has a lower affinity for the complexed species, with a *Pf*HRP2 molecule bound to a gold conjugate, versus the lone *Pf*HRP2 molecule. This theory makes logical sense: a single PfHRP2 has more rotational freedom than the large gold conjugate (a 40 nm gold nanoparticle, plus IgGs decorating the surface) to position favorably for capture by the surface IgM. Furthermore, there is the

added problem of differential coverage of gold conjugates by *Pf*HRP2—it will be much faster for a "fully-covered" conjugate to be captured by the surface IgM, whereas a conjugate that only has a single *Pf*HRP2 will be captured more slowly because it requires more precise rotation into a position where the surface can access the *Pf*HRP2. "Double-complexed" conjugates, where two gold nanoparticles are bridged by a single *Pf*HRP2, will have the lowest likelihood of capture by the IgM on the surface. The large nanoparticles likely hide the PfHRP2 completely from the surface IgM, making this species invisible to detection. Even double-complexes with multiple *Pf*HRP2 molecules on the surface are likely to have low on-rates of binding, because of their even-longer rotational diffusion times, and the possibility that available PfHRP2 molecules are sterically blocked by the second nanoparticle.

This model is designed to provide some clarity to the question of the different levels of conjugate-antigen binding, and suggest the likely distribution of complexes for premixed PfHRP2 and gold conjugate, depending on the input concentrations of conjugate and antigen.

7.3.1 Model components and parameters

Physics

This Comsol Multiphysics (Comsol, Inc., Burlington, MA) model is very simple; it is described as "zero-dimensional" because there is no spatial geometry, it consists only of a set of reactions occurring over time. The general reaction in this system is:

$$[\mathrm{Pf}HRP2] + [AuNP] \underset{k_{off}}{\overset{k_{on}}{\rightleftharpoons}} [complex]$$

However, because both the *Pf*HRP2 and the gold nanoparticle are highly multivalent, there are many possible complexes and reactions involving complexes, as illustrated in the schematic in Figure 82. The cartoon of *Pf*HRP2 is an attempt to represent the theoretical PfHRP2 structure published in the Protein Data Bank [174]; no crystal structure of PfHRP2 is available in the Protein Data Bank.

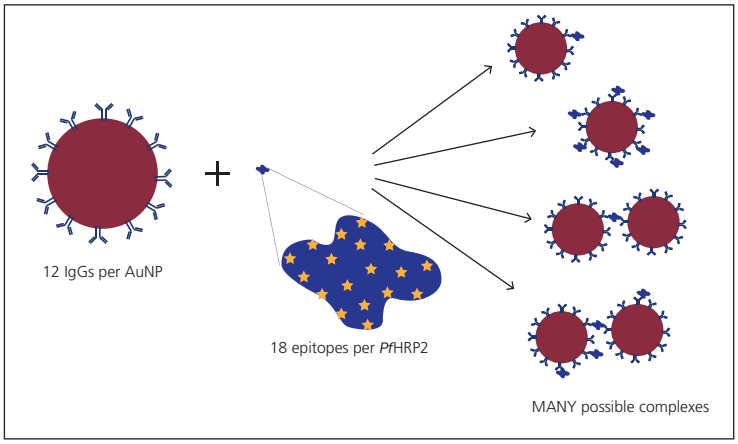

Figure 82: Schematic of the multitude of binding interactions that can occur with multivalent binding partners such as a gold conjugate (AuNP for gold nanoparticle) with *Pf*HRP2.

The reactions that we implemented in the model include single nanoparticle complexes bound from 1–24 PfHRP2 molecules, and we call those "complex 1" through "complex 24"; additionally, complexes where two nanoparticles are joined by a PfHRP2 are referred to as "double complexes", and are numbered by the number of PfHRP2 molecules associated with them—i.e. "double complex 1" is two nanoparticles sharing a single PfHRP2, and "double complex 4" is two nanoparticles sharing one PfHRP2, with an additional 3 PfHRP2 molecules bound to other IgGs. Theoretically a variety of "triple complexes" are possible—generated by either three nanoparticles sharing a single PfHRP2, which is unlikely due the high steric hindrance of that interaction, or by a string of three nanoparticles joined by 2PfHRP2 molecules—one at each junction (and similarly, a "quadruple complex" could exist as a string of four nanoparticles, connected by three PfHRP2s, and so on). We have chosen

to neglect all complexes involving more than two gold nanoparticles, to simplify the model somewhat.

Additionally, only double complexes up to “double complex 10” were included, to simplify the model. We compared a simulation that only included double complexes up to “double complex 9” to one that included up to “double complex 10”, and found that between the two simulations the amount of the “double complex 1” and the total amount of double complexes remained the same; the only difference between the two simulations was a slightly changed the distribution of species among the different types of similar species (i.e. a shift from “complex 7” to “complex 8” or from “double complex 6” to “double complex 7”). These minor differences are not essential to the broader question of the distribution of complex species among rapidly binding, slowly binding, and non-binding categories, because we hypothesized that the major difference between the capture rates of different species is due to three main causes—(1) complexes with few *Pf*HRP2 molecules must rotate into position for capture, and this rotation is even slower for double complexes, (2) “double complex 1” species are unable to be captured due to severe steric hindrance, and (3) complexes with many PfHRP2 molecules will bind much faster because little rotation is needed to orient appropriately for binding.

Parameters

Parameter	Value	Meaning	Justification
k_{on}	1 x 10^5 $M^{-1}s^{-1}$	On rate	Literature
k_{off}	1 x 10^{-5} s^{-1}	Off rate	Literature
[*Pf*HRP2]	Varies: 100 pM–200 nM	Concentration of antigen	Measured
[AuNP]	0.75 nM gold (OD 5)	Concentration of gold conjugate	Manufacturer-reported

The on- and off-rate parameters were approximated based on literature values for high-affinity IgG-antigen interactions [139, 140]—this on- and off- rate yields a K_d of 100 pM, which is on the order of reported high-affinity antibody-antigen interactions. Published studies of our particular detection antibody have not measured the on- and off-rates, but they have shown that this particular detection antibody has particularly high affinity due to the 18 epitopes present in a single *Pf*HRP2 [172]. The initial *Pf*HRP2 concentration is based on assay input concentrations typically used in the laboratory for this assay stack.

The initial gold conjugate (AuNP) concentration was set based on the manufacturer's reported relationship between the optical density (OD) of a gold nanoparticle solution and the number of nanoparticles it contains (see Appendix C).

7.3.2 Model predictions and discussion

This model is in an early stage, and the predicted distributions of species have not been experimentally verified; however, because antibody-antigen binding is known to follow very well characterized binding kinetics models, the general principle of the model is consistent with reality. Concentration input values are measured based on stock solutions, or reported

from the manufacturer, leaving only the on- and off-rates as the primary source of error. Even though the on- and off-rates are not exactly accurate, they are both within a reasonable range and can help to approximate some valid conclusions about this system over time.

First, the distributions of all species vary over time as the binding reaction progresses, and some species are limiting. For instance, at low initial *Pf*HRP2 levels, there is much more gold conjugate than *Pf*HRP2, leading to a high level of "complex 1", but rising numbers of "double complex1" as time progresses, because the "complex 1" binds to lone conjugate (Figure 83 and Figure 84 A). Conversely, at high initial *Pf*HRP2 levels, there is vastly more PfHRP2 than gold nanoparticles, leading to "complex 24" levels approximately equal to the input gold conjugate concentration (Figure 83 and Figure 84 E). At mid-range input levels of *Pf*HRP2 the distribution of "complex 1" rises and then drops again as it binds more *Pf*HRP2, and low-*Pf*HRP2 complexes shift toward higher-*Pf*HRP2 complexes, or double complexes—depending on which species are at highest concentration. When there is excess PfHRP2, complexes are driven toward higher-*Pf*HRP2 complexes (Figure 83 and Figure 84 D and E), however, when there is excess conjugate or other complexes, the levels of double complexes rise (Figure 83 and Figure 84 A and B). The 2 nM initial PfHRP2 concentration simulation (Figure 83 and Figure 84C) is a middle ground, where mid-range complexes and double complexes are both increasing. When examining the relative levels of species, recall that each "AuNP" is covered with 12 IgGs, or 24 binding sites, so this initial concentration of binding sites is 18 nM, and each complex contains some free IgGs (except "complex 24"), so even though it appears that *Pf*HRP2 is in excess in the 2 nM *Pf*HRP2 case, there are actually significantly more available binding sites. These distributions are not perfectly accurate—several more experiments are needed to develop a fully fitted model—however,

we can learn a lot about the system by trying to gain a sense of these relative distributions over time, and how they are driven by the initial parameters of the system. Prior to modeling the changing distribution over time, the simplification that we were left with was assuming that the only species are "complexed *Pf*HRP2", "free *Pf*HRP2" and "AuNP"—neglecting a significant portion of the complicated system that exists in the real premixed binding reaction. Despite the imperfections of the model, it has real value in demonstrating how dramatically different the available species are for each set of initial concentrations.

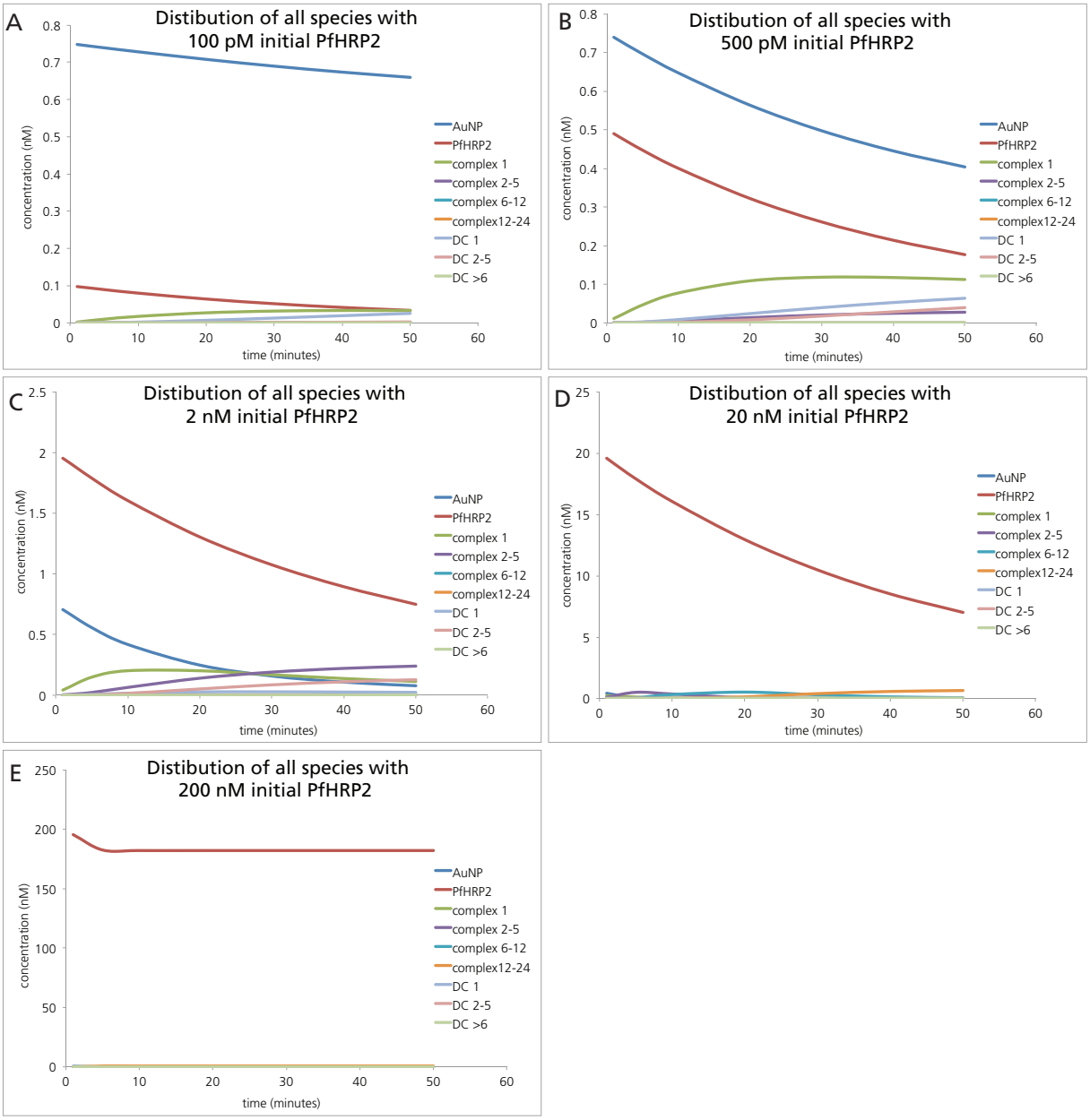

Figure 83: Comparison of species distribution over time for several input *Pf*HRP2 concentrations. (A and B) At low initial *Pf*HRP2 levels (100 pM or 500 pM) there is much, much more gold conjugate than *Pf*HRP2 or any of the complexes. (C) At 2 nM, the concentration of *Pf*HRP2 is greater than that of AuNPs, however, because each AuNP has 12 IgGs on the surface, there are still many more available binding sites on nanoparticles than there are PfHRP2 molecules, leading to a rinse of double complexes (pink line). (D and E) At high initial *Pf*HRP2 levels (20 nM and 200 nM) there is vastly more PfHRP2 than gold nanoparticles, and the excess PfHRP2 drives complexes toward higher-*Pf*HRP2 complexes. Figure 84 illustrates the distribution of complexes in greater resolution. For ease of interpretation, complexes have been group together: complex 1 alone, complexes 2–5 summed, complexes 6–12 summed, complexes 12–24 summed; double complex ("DC") 1 alone, double complexes 2–5 summed, and double complexes greater than 6 summed.

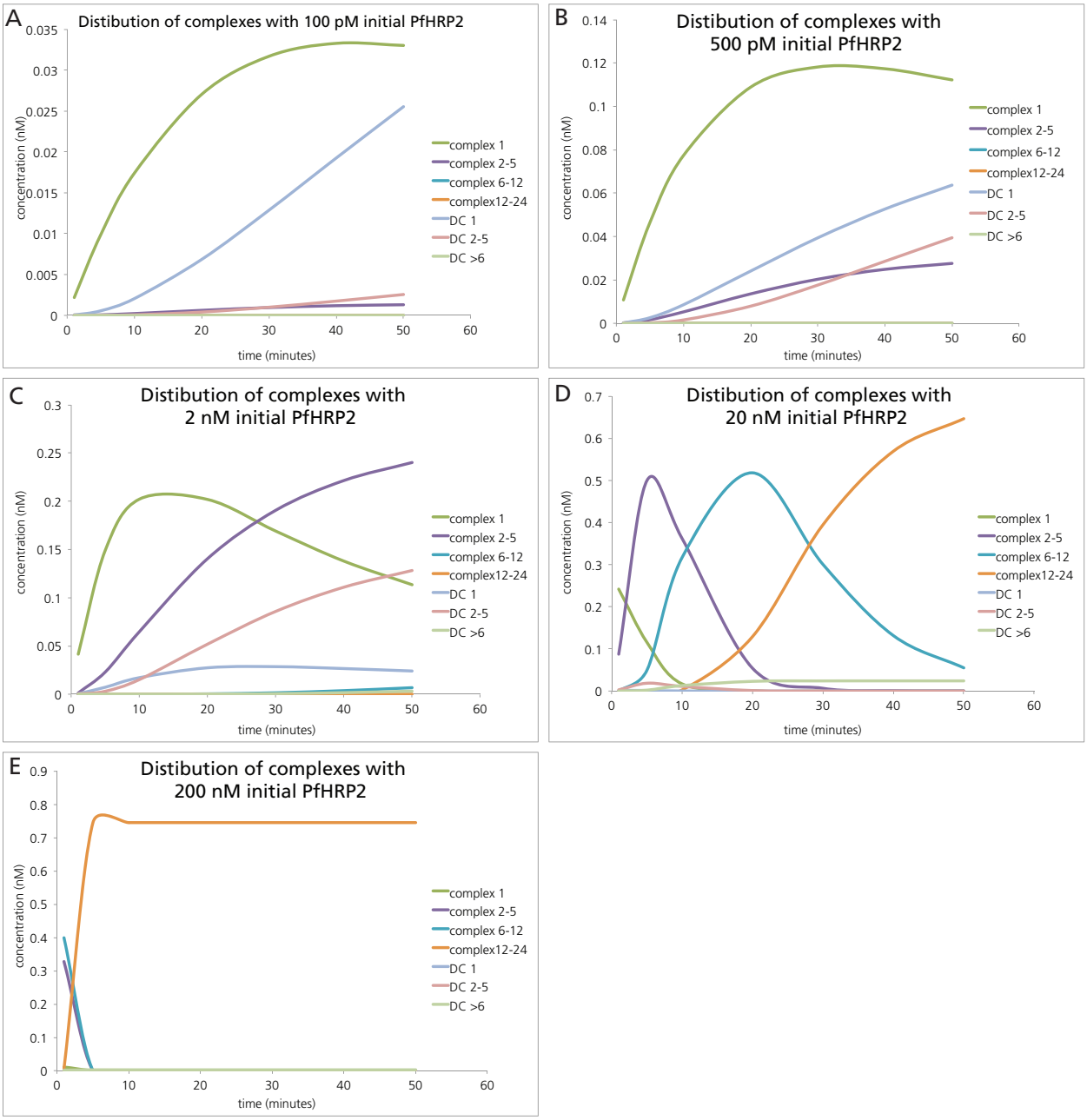

Figure 84: Comparison of bound complex distribution over time for several input *Pf*HRP2 concentrations. (A and B) At low initial *Pf*HRP2 levels, when gold conjugate is in excess, "complex 1" is the initial predominant species, but the level of "double complex1" increases as time progresses, because the "complex 1" binds to the available conjugate. (C) At mid-levels of PfHRP2, both mid-range complexes and double complexes are increasing, due to the comparable availability of PfHRP2 and binding sites on the conjugate. (D) At high initial *Pf*HRP2 levels, there is vastly more PfHRP2 than gold nanoparticles, leading to highly covered complexes. (E) At *very* high concentration of PfHRP2, all of the input conjugate quickly becomes saturated with PfHRP2 as "complex 24", at levels approximately equal to the input gold conjugate concentration. For ease of interpretation, complexes have been group together: complex 1 alone, complexes 2–5 summed, complexes 6–12 summed, complexes 12–24 summed; double complex 1 alone, double complexes 2–5 summed, and double complexes greater than 6 summed.

The second type of information we can gather from this model is the distribution of species for each concentration at a given time point. This type of measurement is essentially what is done in a premixed lateral flow immunoassay: the analyte and conjugate mix together and are allowed to bind for some period of time, and then they are bound by the capture species immobilized on the membrane for detection. With this model however, we can compare the relative levels of different species for each initial *Pf*HRP2 concentration (Figure 85 shows this simulation at the 10 minute time point). Given the hypothesis that different complex species have different binding constants with the capture IgM, due to their different sizes, shapes and the surface coverage with *Pf*HRP2, the information about the varying distribution of complexes could inform our understanding of the signal generated in a lateral flow immunoassay. This model allows us to recognize that at different times and with different initial concentrations, there are truly different mixtures of species binding at the capture zone.

Using the reaction model described here, Elain Fu added variable complex-distribution to the Comsol model she had built to simulate a lateral flow assay, comparing premixing *Pf*HRP2 with conjugate versus sequential reagent addition. The addition of variable complex distribution enabled simulation of variable binding interactions based on the different species present in the premixed condition, and improved the model's fit to the data gathered by her and Tinny Liang.

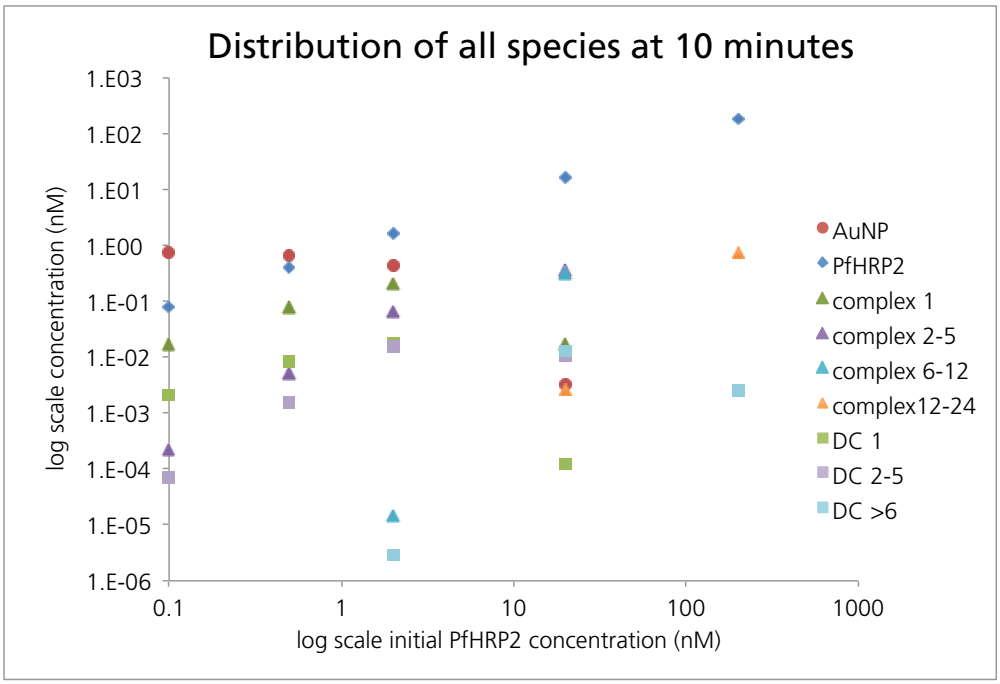

Figure 85: Comparison of the distribution of different species depending on the initial PfHRP2 concentration, at t= 10 minutes. The distribution of species at each initial PfHRP2 concentration can be examined, to evaluate the quantity of surface-bindable species, and to approximate the relative levels of species with varying binding rates. For example, at 200 nM initial PfHRP2, nearly all of the complexes are highly covered with PfHRP2, whereas at 100 pM initial PfHRP2, most of the antigen has not even been bound to conjugate yet. Because we hypothesize that different species have different binding rates to the surface-bound IgM in the lateral flow immunoassay, the range of species present at a given time could be used to more accurately model assay signal in a premixed lateral flow immunoassay. Note: several species were present at concentrations less than 1 fM, and these values were neglected for simplicity.

The next steps for this model will be to perform experimental validation of the predicted distribution of complexes at a wide range of initial *Pf*HRP2 and gold conjugate concentrations. Additionally, other students are working on traditional SPR measurements to determine the antibody-antigen kinetics, and these parameters can be used as model inputs, which should improve the model's performance. Then, using this model integrated with E. Fu's lateral flow model, a range of inputs and flow rates could be simulated to determine optimal assay conditions. Additionally, this model on its own is a useful tool to facilitate understanding how the distribution of complexes depends on several parameters, and it could be applied to premixing binding interactions.

7.4 Conclusions

In Chapter 7 we have designed and built two simplified theoretical computational models, both based on well-described physics, to explore how variations in a range of parameters the can be used to describe a 2DPN assay system affect the resulting binding interactions in the assay. Using these tools we were able examine and begin to understand the underlying physics involved in the complex system of flow, transport, and reactions in a porous medium.

The "single pore" model described first in this chapter allows us to probe the effects of transport and binding parameters on the *surface* interactions within a pore. Unlike typical bulk porous media binding models, this model explicitly defines the surface, but neglects the complex structure of the porous medium. This model allowed us to examine how parameters such as diffusivity, binding on- and off-rates, and surface site density would theoretically affect the surface-bound distribution of a captured analyte, and this gives us a better conceptual understanding of the roles of the many different processes occurring simultaneously in these devices.

The multivalent reaction model, described second in this chapter, allows us to simulate a gold conjugate binding a multivalent analyte, and demonstrates the many different complexed species that are present in solution. Different complexes likely have different avidities for the surface-bound capture species, which could lead to different signal profiles in 2DPNs, and therefore the variations in distribution must be considered when simulating a premixed lateral flow assay. In addition to improving simulations of premixing, this model also allows enhanced understanding of the complex binding interactions, and reminds us that at different times and with different initial concentrations, there are truly different mixtures of species binding at the capture zone.

Both of the models described here have the very interesting and important attribute that they can provide a *conceptual* understanding of the system by simulating how variations in different parameters affect the performance of the system. In some ways this attribute is perhaps even more important than the potential for simulating experiments before performing them on the bench—we truly hope that others can use these models to built their understanding of the complexities hidden within such an ostensibly simple system.

8 Overall Conclusions

8.1 Summary of work

In this project we developed a set of methods and models that are a valuable step toward the goal of fully controlled and "engineerable" assays. The reagent patterning, adsorption and rehydration techniques can be integrated into a wide range of 2DPN devices for a broad range of applications, and the wide variety of computational models will enhance the utility of the laboratory techniques.

First, the process of printing reagents onto nitrocellulose membranes has been characterized, examining and modeling the imbibition of liquids into membranes. Second, techniques were developed to study protein adsorption to surfaces, and a model was developed to evaluate and compare different rates of this adsorption process. Third, methods were developed to pattern and dry reagents for storage directly within the nitrocellulose membranes, and subsequently rehydrate them in a variety of controlled spatial and temporal distributions in a device. Fourth, a multi-step malaria assay was implemented using solely patterned and dried reagents. Fifth, a computational model of transport and binding of reagents within a single pore was developed to provide insight into the various parameters governing assay signal. Finally, another computational model was built to illustrate the multitude of binding interactions that occur when multivalent analytes and antibodies are used in an assay system.

Chapter 3 examined and characterized the technique of printing reagents onto nitrocellulose to more precisely control the distribution of liquids as they are a deposited onto the surface of, and wick into a nitrocellulose membrane. Furthermore, a computational model was developed to better understand the flow rates within the membrane as liquids

are imbibed into the material. The process of liquid deposition onto membrane is central to several aspects of 2DPN design, from capture molecule deposition, (which we studied in Chapter 4), through reagent patterning for rehydration (developed in Chapter 5).

Chapter 4 developed a set of techniques to study protein adsorption to porous membranes. Though the path to a simple and high-throughput assay was not straightforward, the final successful method was based on the predictable liquid deposition properties of precision printing on nitrocellulose, as described in Chapter 3. After comparing these protein adsorption experiments qualitatively, we built a model to simulate the surface adsorption process, using the underlying physics of the printing model from Chapter 3. With this model we were able to evaluate and compare different rates of this adsorption process, and simulate variations in concentration and kinetics to better understand the parameters that governed adsorption during printing.

Chapter 5 also takes advantage of our in depth understanding of printing reagents—several techniques were developed to pattern reagents for dry storage directly within the nitrocellulose membranes. These techniques enabled the subsequent rehydration of dried reagent depots in a variety of tightly controlled spatial and temporal distributions within a device. Again, to enhance the "engineerablity" of these techniques, a companion computational model was developed to simulate how different spatial and temporal distributions could be tuned.

Chapter 6 uses the reagent patterning and rehydration techniques developed in Chapter 5 to implement a multi-step high-sensitivity 2DPN immunoassay using solely patterned and dried reagents. These techniques are extensible to other assay reagents, illustrate the potential of patterning reagents directly onto assay devices; this demonstration is a first

step towards fully integrated 2DPN assays. Furthermore, these patterning methods also have the potential to simplify device fabrication by reducing the number of components, and reduce user steps by facilitating automated operation.

Chapter 7 is something of a departure from the preceding chapters in this document. Two different computational models were developed to enhance our understanding of the complex interactions of the many phenomena that occur simultaneously within a 2DPN assay. The first model simplifies the entire assay system to a single pore, to facilitate the incorporation of convective and diffusive transport, along with surface binding events. The second model discussed here was built to illustrate the multitude of binding interactions that occur when multivalent analytes and detection antibodies are used in an assay system. Depending on the relative concentrations of different species, very different complexes can be formed in the system, and the detectability of each type of complexes could be very different within a single 2DPN assay. Both of these models are in a very early stage, but have already proven their worth by enabling us to see directly how the system is likely to respond to variations in its key parameters.

8.2 Implications

Overall, one of the main benefits of the 2DPN technology is the availability of fluidic control and programming in inexpensive paper devices. The techniques described here enable precisely controlled printing, enhanced understanding of adsorption, and spatially and temporally controlled rehydration, and expand the capabilities of 2DPNs to enable even more sophisticated control mechanisms that will improve assay performance while maintaining the ease-of-use, low cost, and rapid time-to-result of existing rapid tests. Additionally, the computational models developed in this work can be used to predict experimental outcomes and minimize the number of benchtop experiments that need to be

performed by determining beforehand a set of interesting conditions for a particular purpose, while also enhancing our intuition and understanding of the complex interactions of the different aspects of that system.

Future work

The work presented in this dissertation has addressed several different aspects of 2DPN design and development, but through that process, several more interesting questions were revealed.

The work studying reagent printing in Chapters 3 revealed that our model of printing is sufficient for examining the imbibition of liquids into porous membranes, but we completely neglected the complex drying process as liquid is drawn outward by evaporation. This is particularly important when we turn toward the protein adsorption studies in Chapter 4— again we neglected evaporation, but the "coffee ring" effect visible in several of the protein spots suggests that a better understanding of evaporation could improve models of protein distribution after deposition.

The model described in Chapter 4 could also be improved by more extensive experiments with a variety of proteins and better estimates of surface capacity, to extend the relevance of the parameter fits— with more data points, this model could be linked with a curve-fitting algorithm to generate more rigorous parameter predictions for a wide range of protein-surface interactions. Another interesting direction for this technique could be to approximate the effective binding constants of specific binding interactions within the porous matrix by printing a labeled analyte onto a surface pre-coated with the corresponding binding partner. It is likely that SPR measurements do not always

accurately reflect the effective binding constants for interactions occurring within the complex system of a porous material.

The set of methods to control rehydration of patterned reagents, described in Chapter 5, form an interesting suite of complementary techniques to achieve a variety of rehydration profiles. New patterns or surprising combinations of the existing patterns could be created computationally using the model system, and then subsequent experiments could evaluate the agreement between predictions and reality, exploring the edges of the model utility while also examining limitations of the physical patterning techniques. One particular rehydration profile that has not yet been demonstrated, but could have real value is assays, is a delayed rehydration mechanism that does not *elongate* the duration of the delayed spot.

The example assay shown in Chapter 6 is an excellent first step towards using patterned reagents in 2DPN assays for simplified fabrication and improved integration, however that benchtop assay is still far from clinical utility. Long-term stability studies need to be performed to confirm that the shelf life of the incorporated patterned reagents at ambient and extreme temperatures is sufficient for clinical use. The performance of the assay using real clinical samples should be assessed to yield clinical sensitivity and specificity, in addition to the analytical limit of detection measurements. Finally, before this assay is able to be produced commercially, manufacturing processes need to be developed, to turn the concept of 2DPN manufacture via roll-to-roll printing and cutting in reality.

Finally, the models described in Chapter 7 are truly just the first steps into an area that has significant potential for improving the "engineerablity" of these paper diagnostic devices. Both models require more thorough validation across a range of known binding interactions and better approximations of input parameters to refine their capabilities,

however after that, these models could be used to evaluate the effects of different design parameters—such as conjugate concentration, flow velocity, or capture region length—on detection performance in any assay system, *prior* to running dozens of experimental conditions.

8.3 Final thoughts

In carrying out the work described here, I have put a great deal of thought into the meaning and implications of a truly engineerable 2DPN system. Other engineering disciplines have tried-and-true techniques to design and model their systems in advance; saving experimentation for the design that is most likely to work. Civil engineers don't build a dozen bridges looking for the one that will hold sufficient weight, yet often in designing our 2DPN devices we must iterate through several similar experiments to find the perfect conditions. Some of this is due to the variability of biology—who knows why Lot #27 of the antibody works better than Lot #32? We *do* think through problems logically, considering the implications of the particular set of conditions we hope to test, piecing together our understanding of transport phenomena, binding kinetics and optics, but we so rarely do the math to calculate whether an experiment *should* work, or quantitatively what the outcome is likely to be. A significant reason why we don't do that math is because the systems are messy and unclear, and the tools available to us for designing and fabricating 2DPN devices are still somewhat imprecise. The methods developed in this project were aimed at creating a set of well-characterized techniques to perform the necessary functions within paper diagnostic tests, so that the operation of these devices is predictable—and able to be modeled computationally. The models developed here were designed seeking to make a step towards the vision of future 2DPN engineers simulating experiments, comparing theoretical results, and conceptually understanding the inner working of the system. All of

the inner workings of immunoassays are invisible to us and we only see the output signal at the end, but there are so many pieces involved that are easy to lose sight of if we only run assay after assay at the bench and do not take the time to think about the complex physical processes that are interacting in every assay stack. I sincerely hope that the techniques and models that I have developed will serve as a first step toward the goal of fully engineerable 2DPNs.

Appendix A: Publications

Journal Articles

1. **Fridley GE***, Holstein CA*, Oza SB*, Yager P. "The Evolution of Nitrocellulose as a Material for Bioassays." MRS Bulletin, 2013 **38**(4): 326-330.

2. **GE Fridley**, HQ Le, E Fu, P Yager. "Spatial and Temporal Controls for the Rehydration of Patterned Reagents." Lab on a Chip, 2012. **12**(21): p. 4321-4327.

3. JT Kirk*, **GE Fridley***, JW Chamberlain, EJ Christiansen, M Hochberg, DM Ratner. "Multiplexed inkjet functionalization of silicon photonic biosensors" Lab on a Chip, 2010. **11**(7): 1372–1377.

4. **Fridley GE**, Le HQ, Yager P. "A highly sensitive immunoassay based on controlled rehydration of patterned reagents in a 2-dimensional paper network" Anal. Chem. 2014. DOI: 10.1021/ac500872j

5. CA Holstein*, **Fridley, GE***, Adcock CA, Yager P. "Methods and models to examine protein adsorption to nitrocellulose" *In preparation* 2014.

6. **Fridley GE**, P Yager. "Modeling transport and surface binding reactions in porous media as a single pore" *In preparation* 2014.

7. **Fridley GE**, P Yager. "Precision 2DPN design by modeling imbibition and surface adsorption of proteins during printing on nitrocellulose membranes" *In preparation* 2014.

8. Liang T, **Fridley GE**, P Yager, E Fu. "Modeling premixing and sequential delivery of detection reagents in paper microfluidic assays to improve limit of detection" *In preparation* 2014.

*these authors contributed equally

Conference Presentations and Posters

1. **GE Fridley**, HQ Le, E Fu, P Yager. "Spatial and Temporal Controls for Rehydration of Dried Reagents Stored in a Porous Device." In: Fifteenth International Conference on Miniaturized Systems for Chemistry and Life Sciences (MicroTAS 2011), 2011 October 3-6; Seattle, WA, USA.

2. **GE Fridley**, HQ Le, E Fu, P Yager. "A Multistep Immunoassay Using Dry, Patterned Reagents in a Two-Dimensional Paper Network" In: Sixteenth International Conference on Miniaturized Systems for Chemistry and Life Sciences (MicroTAS 2012), 2012. October 28-November 1; Okinawa, Japan

3. **GE Fridley**, J Buser, SA Byrnes, P Kauffman, P Yager. "Controlling Reagent Rehydration in Paper Networks to Improve Point-of-Care Diagnostics" Microfluidics 2.0 Workshop December 1-2, 2012; Boston, MA, USA.

4. CA Holstein, **GE Fridley**, E Fu, P Yager. "Understanding Protein Adsorption to Nitrocellulose: Lessons from IgG Binding." Gordon Research Seminar and Gordon Research Conference in Physics and Chemistry of Microfluidics, 2013.

5. **GE Fridley**, HQ Le, CA Holstein, SA Byrnes, P Yager. "Developments in Paper-Based Microfluidic Assays." Scienion North America Symposium, August 2, 2013; Houston, TX, USA.

6. Liang T, **Fridley GE**, Yager P, and E Fu. "Investigation of the format-dependent spatial distribution of binding in a malaria antigen assay; implications for higher-sensitivity detection." BMES 2014, October 22-25, 2014; San Antonio, TX, USA.

Appendix B: References

1. Yager, P., et al., *Microfluidic diagnostic technologies for global public health.* Nature, 2006. **442**(7101): p. 412-418.
2. Yager, P., G.J. Domingo, and J. Gerdes, *Point-of-care diagnostics for global health.* Annual Review of Biomedical Engineering, 2008. **10**: p. 107-144.
3. Squires, D.A. *Explaining High Health Care Spending in the United States: An International Comparison of Supply, Utilization, Prices, and Quality*. Issues in International Health Policy, 2012. **10**, 14.
4. *The Patient Protection and Affordable Care Act*, in *United States of America*. 2010.
5. *Beyond Borders: Matters of Evidence*, G.T. Giovannetti and G. Jaggi, Editors. 2013.
6. Poehling, K.A., et al., *Bedside diagnosis of influenzavirus infections in hospitalized children.* Pediatrics, 2002. **110**(1): p. 83-88.
7. Posthuma-Trumpie, G.A., J. Korf, and A. van Amerongen, *Lateral flow (immuno) assay: its strengths, weaknesses, opportunities and threats. A literature survey.* Analytical and Bioanalytical Chemistry, 2009. **393**(2): p. 569-582.
8. Cazacu, A.C., et al., *Comparison of lateral-flow immunoassay and enzyme immunoassay with viral culture for rapid detection of influenza virus in nasal wash specimens from children.* Journal of Clinical Microbiology, 2003. **41**(5): p. 2132-2134.
9. Shakely, D., et al., *The Usefulness of Rapid Diagnostic Tests in the New Context of Low Malaria Transmission in Zanzibar.* Plos One, 2013. **8**(9).
10. Frean, J., et al., *Case management of malaria: Diagnosis.* Samj South African Medical Journal, 2013. **103**(10): p. 789-793.
11. Wilson, M.L., *Laboratory Diagnosis of Malaria Conventional and Rapid Diagnostic Methods.* Archives of Pathology & Laboratory Medicine, 2013. **137**(6): p. 805-811.
12. Fu, E., et al., *Chemical signal amplification in two-dimensional paper networks.* Sensors and Actuators B-Chemical, 2010. **149**(1): p. 325-328.
13. Fu, E., et al., *Controlled reagent transport in disposable 2D paper networks.* Lab on a Chip, 2010. **10**(7): p. 918-920.
14. Fu, E., et al., *Enhanced Sensitivity of Lateral Flow Tests Using a Two-Dimensional Paper Network Format.* Analytical Chemistry, 2011. **83**(20): p. 7941-7946.
15. Osborn, J.L., et al., *Microfluidics without pumps: reinventing the T-sensor and H-filter in paper networks.* Lab on a Chip, 2010. **10**(20): p. 2659-2665.
16. Organization, W.H., *The global burden of disease: 2004 update*. 2004.
17. Peeling, R.W., et al., *Rapid tests for sexually transmitted infections (STIs): the way forward.* Sexually Transmitted Infections, 2006. **82**: p. V1-V6.
18. Mabey, D., et al., *Diagnostics for the developing world.* Nature Reviews Microbiology, 2004. **2**(3): p. 231-240.
19. *The Patient Protection and Affordable Care Act*, in *United States*. 2010.
20. *DxBox will diagnose diseases.* Trac-Trends in Analytical Chemistry, 2007. **26**(4): p. VII-VIII.
21. Arnaud, C.H., *Improving diagnosis of tropical diseases.* Chemical & Engineering News, 2007. **85**(12): p. 56-58.
22. Wong, R. and H. Tse, *Lateral Flow Immunoassay*. 2009, Humana Press: New York.
23. Quach, C., et al., *QuickVue influenza test for rapid detection of influenza A and B viruses in a pediatric population.* Clinical and Diagnostic Laboratory Immunology, 2002. **9**(4): p. 925-926.

24. Beadle, C., et al., *DIAGNOSIS OF MALARIA BY DETECTION OF PLASMODIUM-FALCIPARUM HRP-2 ANTIGEN WITH A RAPID DIPSTICK ANTIGEN-CAPTURE ASSAY.* Lancet, 1994. **343**(8897): p. 564-568.
25. Moody, A., *Rapid diagnostic tests for malaria parasites.* Clinical Microbiology Reviews, 2002. **15**(1): p. 66-+.
26. Wongsrichanalai, C., et al., *A review of malaria diagnostic tools: Microscopy and rapid diagnostic test (RDT).* American Journal of Tropical Medicine and Hygiene, 2007. **77**(6): p. 119-127.
27. Ketema, F., et al., *A 10-minute, US Food and Drug Administration-approved HIV test.* Expert Review of Molecular Diagnostics, 2005. **5**(2): p. 135-143.
28. Branson, B.M., *State of the art for diagnosis of HIV infection.* Clinical Infectious Diseases, 2007. **45**: p. S221-S225.
29. O'Connell, R.J., et al., *Performance of the OraQuick rapid antibody test for diagnosis of human immunodeficiency virus type 1 infection in patients with various levels of exposure to highly active antiretroviral therapy.* Journal of Clinical Microbiology, 2003. **41**(5): p. 2153-2155.
30. Carrilho, E., et al., *Paper Microzone Plates.* Analytical Chemistry, 2009. **81**(15): p. 5990-5998.
31. Carrilho, E., A.W. Martinez, and G.M. Whitesides, *Understanding Wax Printing: A Simple Micropatterning Process for Paper-Based Microfluidics.* Analytical Chemistry, 2009. **81**(16): p. 7091-7095.
32. Cheng, C.M., et al., *Paper-Based ELISA.* Angewandte Chemie-International Edition, 2010. **49**(28): p. 4771-4774.
33. Martinez, A.W., et al., *Patterned paper as a platform for inexpensive, low-volume, portable bioassays.* Angewandte Chemie-International Edition, 2007. **46**(8): p. 1318-1320.
34. Martinez, A.W., et al., *FLASH: A rapid method for prototyping paper-based microfluidic devices.* Lab on a Chip, 2008. **8**(12): p. 2146-2150.
35. Martinez, A.W., et al., *Simple telemedicine for developing regions: Camera phones and paper-based microfluidic devices for real-time, off-site diagnosis.* Analytical Chemistry, 2008. **80**(10): p. 3699-3707.
36. Martinez, A.W., S.T. Phillips, and G.M. Whitesides, *Three-dimensional microfluidic devices fabricated in layered paper and tape.* Proceedings of the National Academy of Sciences of the United States of America, 2008. **105**(50): p. 19606-19611.
37. Martinez, A.W., et al., *Diagnostics for the Developing World: Microfluidic Paper-Based Analytical Devices.* Analytical Chemistry, 2010. **82**(1): p. 3-10.
38. Martinez, A.W., et al., *Programmable diagnostic devices made from paper and tape.* Lab on a Chip, 2010. **10**(19): p. 2499-2504.
39. Fu, E.L., et al., *Transport in two-dimensional paper networks.* Microfluidics and Nanofluidics, 2011. **10**(1): p. 29-35.
40. Wang, J., et al., *A self-powered, one-step chip for rapid, quantitative and multiplexed detection of proteins from pinpricks of whole blood.* Lab on a Chip, 2010. **10**(22): p. 3157-3162.
41. Lutz, B.R., et al., *Two-dimensional paper networks: programmable fluidic disconnects for multi-step processes in shaped paper.* Lab on a Chip, 2011. **11**(24): p. 4274-4278.
42. Noh, H. and S.T. Phillips, *Fluidic Timers for Time-Dependent, Point-of-Care Assays on Paper.* Analytical Chemistry, 2010. **82**(19): p. 8071-8078.

43. Noh, N. and S.T. Phillips, *Metering the Capillary-Driven Flow of Fluids in Paper-Based Microfluidic Devices.* Analytical Chemistry, 2010. **82**(10): p. 4181-4187.
44. Fu, E., et al., *Two-Dimensional Paper Network Format That Enables Simple Multistep Assays for Use in Low-Resource Settings in the Context of Malaria Antigen Detection.* Analytical Chemistry, 2012. **84**(10): p. 4574-4579.
45. Wild, D., *The Immunoassay Handbook*, in *Theory and Applications of Ligand Binding, ELISA and Related Techniques*. 2013, Elsevier Ltd.
46. Cox KL, D.V., Kriauciunas A, et al., *Immunoassay Methods*, S. GS, G.-E. N, and A.M.e. al., Editors. 2012 May 1 [Updated 2012 Oct 1], Eli Lilly & Company and the National Center for Advancing Translational Sciences Assay Guidance Manual [Internet]. Bethesda (MD).
47. Nery, E.W. and L.T. Kubota, *Sensing approaches on paper-based devices: a review.* Analytical and Bioanalytical Chemistry, 2013. **405**(24): p. 7573-7595.
48. Liang, J., Y.Y. Wang, and B. Liu, *Paper-based fluoroimmunoassay for rapid and sensitive detection of antigen.* Rsc Advances, 2012. **2**(9): p. 3878-3884.
49. Ramachandran, S., et al., *Long-term dry storage of an enzyme-based reagent system for ELISA in point-of-care devices.* Analyst, 2014. **139**(6): p. 1456-1462.
50. Engvall, E., K. Jonsson, and P. Perlmann, *ENZYME-LINKED IMMUNOSORBENT ASSAY .2. QUANTITATIVE ASSAY OF PROTEIN ANTIGEN, IMMUNOGLOBULIN G, BY MEANS OF ENZYME-LABELLED ANTIGEN AND ANTIBODY-COATED TUBES.* Biochimica Et Biophysica Acta, 1971. **251**(3): p. 427-+.
51. Engvall, E. and P. Perlmann, *ENZYME-LINKED IMMUNOSORBENT ASSAY (ELISA) QUANTITATIVE ASSAY OF IMMUNOGLOBULIN-G.* Immunochemistry, 1971. **8**(9): p. 871-&.
52. Engvall, E. and P. Perlmann, *ENZYME-LINKED IMMUNOSORBENT ASSAY, ELISA .3. QUANTITATION OF SPECIFIC ANTIBODIES BY ENZYME-LABELED ANTI-IMMUNOGLOBULIN IN ANTIGEN-COATED TUBES.* Journal of Immunology, 1972. **109**(1): p. 129-&.
53. Holgate, C.S., et al., *IMMUNOGOLD SILVER STAINING - NEW METHOD OF IMMUNOSTAINING WITH ENHANCED SENSITIVITY.* Journal of Histochemistry & Cytochemistry, 1983. **31**(7): p. 938-944.
54. Weipoltshammer, K., et al., *Signal enhancement at the electron microscopic level using Nanogold and gold-based autometallography.* Histochemistry and Cell Biology, 2000. **114**(6): p. 489-495.
55. Lei, K.F. and Y.K.C. Butt, *Colorimetric immunoassay chip based on gold nanoparticles and gold enhancement.* Microfluidics and Nanofluidics, 2010. **8**(1): p. 131-137.
56. Yeh, C.-H., et al., *An immunoassay using antibody-gold nanoparticle conjugate, silver enhancement and flatbed scanner.* Microfluidics and Nanofluidics, 2009. **6**(1): p. 85-91.
57. Schuck, P., *Use of surface plasmon resonance to probe the equilibrium and dynamic aspects of interactions between biological macromolecules.* Annual Review of Biophysics and Biomolecular Structure, 1997. **26**: p. 541-566.
58. Green, N.M., *AVIDIN AND STREPTAVIDIN.* Methods in Enzymology, 1990. **184**: p. 51-67.
59. Lafleur, L., et al., *Progress toward multiplexed sample-to-result detection in low resource settings using microfluidic immunoassay cards.* Lab on a Chip, 2012. **12**(6): p. 1119-1127.

60. Cohen, I.M. and P.K. Kundu, *Fluid Mechanics*. Fourth Edition ed. 2008, Burlington, MA: Elsevier.
61. Bird, R.R., W.E. Stewart, and E.N. Lightfoot, *Transport Phenomena*. 2002, John Wiley & Sons, Inc. p. 148.
62. Purcell, E.M., *LIFE AT LOW REYNOLDS-NUMBER.* American Journal of Physics, 1977. **45**(1): p. 3-11.
63. Sutera, S.P. and R. Skalak, *THE HISTORY OF POISEUILLE LAW.* Annual Review of Fluid Mechanics, 1993. **25**: p. 1-19.
64. Kirby, B.J., *Micro- and Nanoscale Fluid Mechanics: Transport in Microfluidic Devices*. 2010, New York, NY: Cambridge University Press.
65. Taylor, G., *DISPERSION OF SOLUBLE MATTER IN SOLVENT FLOWING SLOWLY THROUGH A TUBE.* Proceedings of the Royal Society of London Series a-Mathematical and Physical Sciences, 1953. **219**(1137): p. 186-203.
66. Aris, R., *ON THE DISPERSION OF A SOLUTE IN A FLUID FLOWING THROUGH A TUBE.* Proceedings of the Royal Society of London Series a-Mathematical and Physical Sciences, 1956. **235**(1200): p. 67-77.
67. Darcy, H., *Les Fontaines Publiques de la Ville de Dijon*. 1856: Dalmont, Paris.
68. Bell, J.M. and F.K. Cameron, *The flow of liquids through capillary spaces.* Journal of Physical Chemistry, 1906. **10**(8): p. 658-674.
69. Washburn, E.W., *The dynamics of capillary flow.* Physical Review, 1921. **17**(3): p. 273-283.
70. Clennell, M.B., *Tortuosity: a guide through the maze.* Developments in Petrophysics, 1997. **122**: p. 299-344.
71. Gommes, C.J., et al., *Practical Methods for Measuring the Tortuosity of Porous Materials from Binary or Gray-Tone Tomographic Reconstructions.* Aiche Journal, 2009. **55**(8): p. 2000-2012.
72. Kim, I.C. and S. Torquato, *DIFFUSION OF FINITE-SIZED BROWNIAN PARTICLES IN POROUS-MEDIA.* Journal of Chemical Physics, 1992. **96**(2): p. 1498-1503.
73. Buser, J., *unpublished data*. 2014.
74. Corporation, M., *Rapid Lateral Flow Test Strips: Considerations for Product Development*. 2008: Billerica, MA.
75. Adler, P.M., *Porous Media: Geometry and Transports*. Butterworth-Heinemann Series in Chemical Engineering, ed. H. Brenner. 1992, Boston, MA.
76. Lucas, R., *The time law of the capillary rise of liquids.* Kolloid-Zeitschrift, 1918. **23**(1): p. 15-22.
77. *Modeling and Applications of Transport Phenomena in Porous Media*. Theory and Applications of Transport in Porous Media. 1991, Norwell, MA: Kluwer Academic Publishers.
78. *Recent advances in problems of flow and transport in porous media*. Theory and applications of transport in porous media. 1998, Boston, MA: Kluwer Academic Press.
79. Osborn, J.L., *Novel Paper Networks for Point-of-Care Sample Preparation and Indirect IgM Detection*, in *Bioengineering*. 2011, University of Washington: Seattle, WA.
80. Bijeljic, B. and M.J. Blunt, *Pore-scale modeling of transverse dispersion in porous media.* Water Resources Research, 2007. **43**(12).
81. Berkowitz, B., et al., *Modeling non-Fickian transport in geological formations as a continuous time random walk.* Reviews of Geophysics, 2006. **44**(2): p. 49.

82. Bijeljic, B., A.H. Muggeridge, and M.J. Blunt, *Pore-scale modeling of longitudinal dispersion.* Water Resources Research, 2004. **40**(11): p. 9.
83. Bijeljic, B. and M.J. Blunt, *Pore-scale modeling and continuous time random walk analysis of dispersion in porous media.* Water Resources Research, 2006. **42**(1).
84. Bijeljic, B., et al., *Predictions of non-Fickian solute transport in different classes of porous media using direct simulation on pore-scale images.* Physical Review E, 2013. **87**(1): p. 9.
85. Mostaghimi, P., B. Bijeljic, and M.J. Blunt, *Simulation of Flow and Dispersion on Pore-Space Images.* Spe Journal, 2012. **17**(4): p. 1131-1141.
86. Hilpert, M. and A. Ben-David, *Infiltration of liquid droplets into porous media: Effects of dynamic contact angle and contact angle hysteresis.* International Journal of Multiphase Flow, 2009. **35**(3): p. 205-218.
87. Holman, R.K., et al., *Spreading and infiltration of inkjet-printed polymer solution droplets on a porous substrate.* Journal of Colloid and Interface Science, 2002. **249**(2): p. 432-440.
88. Clarke, A., et al., *Spreading and imbibition of liquid droplets on porous surfaces.* Langmuir, 2002. **18**(8): p. 2980-2984.
89. Denesuk, M., et al., *CAPILLARY PENETRATION OF LIQUID DROPLETS INTO POROUS MATERIALS.* Journal of Colloid and Interface Science, 1993. **158**(1): p. 114-120.
90. Israelachvili, J.N., *Intermolecular and Surface Forces*. Third Edition ed. 2011, Waltham, MA: Elsevier.
91. Weisbrod, N., et al., *Effective Darcy-scale contact angles in porous media imbibing solutions of various surface tensions.* Water Resources Research, 2009. **45**.
92. Clayton J . Radke , M.G.V., and Victor M . Starov, *Wetting and Spreading Dynamics*. 2007: CRC Press. 501-506.
93. Bacri, L. and F. Brochard-Wyart, *Droplet suction on porous media.* European Physical Journal E, 2000. **3**(1): p. 87-97.
94. de Gennes, P.-G., F. Brochard-Wyart, and D. Quéré, *Capillarity and Wetting Phenomena: drops, bubbles, pearls, waves*. 2004, New York, NY: Springer.
95. Wang, J., et al., *Dye deposition patterns obtained in line printing on macroporous membranes: Improvement of line sharpness by liquid redistribution.* Journal of Membrane Science, 2008. **318**(1-2): p. 280-287.
96. Xiao, J.F., H.A. Stone, and D. Attinger, *Source-like Solution for Radial Imbibition into a Homogeneous Semi-infinite Porous Medium.* Langmuir, 2012. **28**(9): p. 4208-4212.
97. Frank, X. and P. Perre, *Droplet spreading on a porous surface: A lattice Boltzmann study.* Physics of Fluids, 2012. **24**(4): p. 11.
98. Marmur, A., *DROP PENETRATION INTO A THIN POROUS-MEDIUM.* Journal of Colloid and Interface Science, 1988. **123**(1): p. 161-169.
99. Marmur, A., *THE RADIAL CAPILLARY.* Journal of Colloid and Interface Science, 1988. **124**(1): p. 301-308.
100. Stevens, D.Y., et al., *Enabling a microfluidic immunoassay for the developing world by integration of on-card dry reagent storage.* Lab on a Chip, 2008. **8**(12): p. 2038-2045.
101. Crowe, J.H., J.F. Carpenter, and L.M. Crowe, *The role of vitrification in anhydrobiosis*. Annual Review of Physiology, 1998. **60**: p. 73-103.
102. Garcia, E., et al., *Controlled microfluidic reconstitution of functional protein from an anhydrous storage depot.* Lab on a Chip, 2004. **4**(1): p. 78-82.

103. Draber, P., E. Draberova, and M. Novakova, *STABILITY OF MONOCLONAL IGM ANTIBODIES FREEZE-DRIED IN THE PRESENCE OF TREHALOSE.* Journal of Immunological Methods, 1995. **181**(1): p. 37-43.
104. Chang, B.S., et al., *Physical factors affecting the storage stability of freeze-dried interleukin-1 receptor antagonist: Glass transition and protein conformation.* Archives of Biochemistry and Biophysics, 1996. **331**(2): p. 249-258.
105. Mazzobre, M.F., M.D. Buera, and J. Chirife, *Protective role of trehalose on thermal stability of lactase in relation to its glass and crystal forming properties and effect of delaying crystallization.* Food Science and Technology-Lebensmittel-Wissenschaft & Technologie, 1997. **30**(3): p. 324-329.
106. Elias, M.E. and A.M. Elias, *Trehalose plus water fragile system: properties and glass transition.* Journal of Molecular Liquids, 1999. **83**(1-3): p. 303-310.
107. Miller, D.P., R.E. Anderson, and J.J. de Pablo, *Stabilization of lactate dehydrogenase following freeze-thawing and vacuum-drying in the presence of trehalose and borate.* Pharmaceutical Research, 1998. **15**(8): p. 1215-1221.
108. Dungchai, W., O. Chailapakul, and C.S. Henry, *Use of multiple colorimetric indicators for paper-based microfluidic devices.* Analytica Chimica Acta, 2010. **674**(2): p. 227-233.
109. Abe, K., K. Suzuki, and D. Citterio, *Inkjet-printed microfluidic multianalyte chemical sensing paper.* Analytical Chemistry, 2008. **80**(18): p. 6928-6934.
110. Abe, K., et al., *Inkjet-printed paperfluidic immuno-chemical sensing device.* Analytical and Bioanalytical Chemistry, 2010. **398**(2): p. 885-893.
111. Gonzalez-Macia, L., et al., *Advanced printing and deposition methodologies for the fabrication of biosensors and biodevices.* Analyst, 2010. **135**(5): p. 845-867.
112. Newman, J.D., A.P.F. Turner, and G. Marrazza, *INK-JET PRINTING FOR THE FABRICATION OF AMPEROMETRIC GLUCOSE BIOSENSORS.* Analytica Chimica Acta, 1992. **262**(1): p. 13-17.
113. Hasenbank, M.S., et al., *Demonstration of multi-analyte patterning using piezoelectric inkjet printing of multiple layers.* Analytica Chimica Acta, 2008. **611**(1): p. 80-88.
114. Nishioka, G.M., A.A. Markey, and C.K. Holloway, *Protein damage in drop-on-demand printers.* Journal of the American Chemical Society, 2004. **126**(50): p. 16320-16321.
115. Lonini, L., et al., *Dispensing an enzyme-conjugated solution into an ELISA plate by adapting ink-jet printers.* Journal of Biochemical and Biophysical Methods, 2008. **70**(6): p. 1180-1184.
116. Mendez, S., et al., *Imbibition in Porous Membranes of Complex Shape: Quasi-stationary Flow in Thin Rectangular Segments.* Langmuir, 2010. **26**(2): p. 1380-1385.
117. GE Life Sciences, April 17, 2014; Available from: http://www.gelifesciences.com/webapp/wcs/stores/servlet/catalog/en/GELifeSciences/products/AlternativeProductStructure_23135/29017319.
118. Rasband, W.S., *ImageJ*. 1997-2014, U.S. National Institutes of Health: Bethesda, MD, USA.
119. Clayton J . Radke , M.G.V., and Victor M . Starov, *Kinetics of Wetting*. Wetting and Spreading Dynamics. 2007: CRC Press. 165-314.
120. Holterman, H.J., *Kinetics and evaporation of water drops in air*. 2003, Wageningen, The Netherlands: Instituut Voor Milieu- en Agritechniek, Wageningen University.

121. Tonkinson, J.L. and B.A. Stillman, *Nitrocellulose: A tried and true polymer finds utility as a post-genomic substrate.* Frontiers in Bioscience, 2002. **7**: p. C1-C12.
122. Towbin, H., T. Staehelin, and J. Gordon, *ELECTROPHORETIC TRANSFER OF PROTEINS FROM POLYACRYLAMIDE GELS TO NITROCELLULOSE SHEETS - PROCEDURE AND SOME APPLICATIONS.* Proceedings of the National Academy of Sciences of the United States of America, 1979. **76**(9): p. 4350-4354.
123. Burnette, W.N., *WESTERN BLOTTING - ELECTROPHORETIC TRANSFER OF PROTEINS FROM SODIUM DODECYL SULFATE-POLYACRYLAMIDE GELS TO UNMODIFIED NITROCELLULOSE AND RADIOGRAPHIC DETECTION WITH ANTIBODY AND RADIOIODINATED PROTEIN-A.* Analytical Biochemistry, 1981. **112**(2): p. 195-203.
124. Liedberg, B., C. Nylander, and I. Lundstrom, *SURFACE-PLASMON RESONANCE FOR GAS-DETECTION AND BIOSENSING.* Sensors and Actuators, 1983. **4**(2): p. 299-304.
125. Homola, J., S.S. Yee, and G. Gauglitz, *Surface plasmon resonance sensors: review.* Sensors and Actuators B-Chemical, 1999. **54**(1-2): p. 3-15.
126. Rich, R.L. and D.G. Myszka, *Advances in surface plasmon resonance biosensor analysis.* Current Opinion in Biotechnology, 2000. **11**(1): p. 54-61.
127. Rich, R.L. and D.G. Myszka, *Higher-throughput, label-free, real-time molecular interaction analysis.* Analytical Biochemistry, 2007. **361**(1): p. 1-6.
128. Hou, W.C., et al., *Distribution of Fullerene Nanomaterials between Water and Model Biological Membranes.* Langmuir, 2011. **27**(19): p. 11899-11905.
129. Hou, W.C., et al., *Distribution of Functionalized Gold Nanoparticles between Water and Lipid Bilayers as Model Cell Membranes.* Environmental Science & Technology, 2012. **46**(3): p. 1869-1876.
130. Spicar-Mihalic, P., et al., *CO2 laser cutting and ablative etching for the fabrication of paper-based devices.* Journal of Micromechanics and Microengineering, 2013. **23**(6).
131. Dharmaraja, S., et al. *Programming paper networks for point of care diagnostics*. 2013.
132. Schmid, M., *StackProfileData*. 2010.
133. *Ponceau S Staining Solution Product Information*, S. Aldrich, Editor. 1998: Saint Louis, MO.
134. Sanchez, J.C., et al., *IMPROVING THE DETECTION OF PROTEINS AFTER TRANSFER TO POLYVINYLIDENE DIFLUORIDE MEMBRANES.* Electrophoresis, 1992. **13**(9-10): p. 715-717.
135. Klein, D., R.M. Kern, and R.Z. Sokol, *A METHOD FOR QUANTIFICATION AND CORRECTION OF PROTEINS AFTER TRANSFER TO IMMOBILIZATION MEMBRANES.* Biochemistry and Molecular Biology International, 1995. **36**(1): p. 59-66.
136. Langmuir, I., *THE ADSORPTION OF GASES ON PLANE SURFACES OF GLASS, MICA AND PLATINUM.* Journal of the American Chemical Society, 1918. **40**: p. 1361-1403.
137. Nelson, D.L. and M.M. Cox, *Lehninger Principles of Biochemistry*. 2005, W.H. Freeman and Company: New York, NY.
138. Christian, G.D., *Analytical Chemistry*. 1994, John Wiley & Sons: United States of America.

139. Welschof, M., et al., *The antigen-binding domain of a human IgG-anti-F(ab')(2) autoantibody.* Proceedings of the National Academy of Sciences of the United States of America, 1997. **94**(5): p. 1902-1907.
140. Steckbeck, J.D., et al., *Kinetic rates of antibody binding correlate with neutralization sensitivity of variant simian immunodeficiency virus strains.* Journal of Virology, 2005. **79**(19): p. 12311-12320.
141. Wright, A.K. and M.R. Thompson, *HYDRODYNAMIC STRUCTURE OF BOVINE SERUM-ALBUMIN DETERMINED BY TRANSIENT ELECTRIC BIREFRINGENCE.* Biophysical Journal, 1975. **15**(2): p. 137-141.
142. Pagana, K.D. and T.J. Pagana, *Mosby's Diagnostic and Laboratory Test Reference*. Eighth edition ed. 2007, Philadelphia, PA: Elsevier.
143. Rosenson, R.S., A. McCormick, and E.F. Uretz, *Distribution of blood viscosity values and biochemical correlates in healthy adults.* Clinical Chemistry, 1996. **42**(8): p. 1189-1195.
144. Tanford, C. and J.G. Buzzell, *THE VISCOSITY OF AQUEOUS SOLUTIONS OF BOVINE SERUM ALBUMIN BETWEEN PH 4.3 AND 10.5.* Journal of Physical Chemistry, 1956. **60**(2): p. 225-231.
145. Kestin, J., M. Sokolov, and W.A. Wakeham, *VISCOSITY OF LIQUID WATER IN RANGE -8-DEGREES-C TO 150-DEGREES-C.* Journal of Physical and Chemical Reference Data, 1978. **7**(3): p. 941-948.
146. Segur, J.B. and H.E. Oberstar, *VISCOSITY OF GLYCEROL AND ITS AQUEOUS SOLUTIONS*. Industrial and Engineering Chemistry, 1951. **43**(9): p. 2117-2120.
147. Fridley, G.E., et al., *Controlled release of dry reagents in porous media for tunable temporal and spatial distribution upon rehydration.* Lab on a Chip, 2012. **12**(21): p. 4321-4327.
148. Buchan, J.L. and R.I. Savage, *PAPER CHROMATOGRAPHY OF SOME STARCH CONVERSION PRODUCTS.* Analyst, 1952. **77**(917): p. 401-&.
149. Kocourek, J., M. Ticha, and J. Kostir, *USE OF DIPHENYLAMINE-ANILINE-PHOSPHORIC ACID REAGENT IN DETECTION AND DIFFERENTIATION OF MONOSACCHARDIES AND THEIR DERIVATIVES ON PAPER CHROMATOGRAMS*. Journal of Chromatography, 1966. **24**(1): p. 117-&.
150. Partridge, S.M. and R.G. Westall, *FILTER-PAPER PARTITION CHROMATOGRAPHY OF SUGARS .1. GENERAL DESCRIPTION AND APPLICATION TO THE QUALITATIVE ANALYSIS OF SUGARS IN APPLE JUICE, EGG WHITE AND FOETAL BLOOD OF SHEEP.* Biochemical Journal, 1948. **42**(2): p. 238-&.
151. Dewhalley, H.C.S., N. Albon, and D. Gross, *APPLICATIONS OF PAPER CHROMATOGRAPHIC METHODS IN THE SUGAR AND ALLIED INDUSTRIES.* Analyst, 1951. **76**(902): p. 287-&.
152. Garcia, E., in *Bioengineering*. 2006, University of Washington.
153. Isco, *Iscotables : a handbook of data for biological and physical scientists*. 1982, Lincoln, Neb.: Isco.
154. Buser, J., *unpublished data*. 2012.
155. Govindarajan, A.V., et al., *A low cost point-of-care viscous sample preparation device for molecular diagnosis in the developing world; an example of microfluidic origami.* Lab on a Chip, 2012. **12**(1): p. 174-181.
156. Fu, E., et al., *Two-Dimensional Paper Network Format That Enables Simple Multistep Assays for Use in Low-Resource Settings in the Context of Malaria Antigen Detection.* Anal Chem, 2012.

157. Hitzbleck, M., L. Gervais, and E. Delamarche, *Controlled release of reagents in capillary-driven microfluidics using reagent integrators.* Lab on a Chip, 2011. **11**(16): p. 2680-2685.
158. Kifude, C.M., et al., *Enzyme-linked immunosorbent assay for detection of Plasmodium falciparum histidine-rich protein 2 in blood, plasma, and serum.* Clinical and Vaccine Immunology, 2008. **15**(6): p. 1012-1018.
159. UNITAID, *Malaria Diagnostic Technology Landscape Report*. 2011, World Health Organization: Geneva.
160. Uyeki, T.M., et al., *Low Sensitivity of Rapid Diagnostic Test for Influenza.* Clinical Infectious Diseases, 2009. **48**(9): p. E89-E92.
161. Vasoo, S., J. Stevens, and K. Singh, *Rapid Antigen Tests for Diagnosis of Pandemic (Swine) Influenza A/H1N1.* Clinical Infectious Diseases, 2009. **49**(7): p. 1090-1093.
162. Fridley, G.E., et al., *Controlled release of dry reagents in porous media for tunable temporal and spatial distribution upon rehydration.* Lab Chip, 2012.
163. Armbruster, D.A. and T. Pry, *Limit of blank, limit of detection and limit of quantitation.* Clin Biochem Rev, 2008. **29 Suppl 1**: p. S49-52.
164. Guerin, P.J., et al., *Malaria: current status of control, diagnosis, treatment, and a proposed agenda for research and development.* Lancet Infectious Diseases, 2002. **2**(9): p. 564-573.
165. Butterworth, A.S., et al., *An improved method for undertaking limiting dilution assays for in vitro cloning of Plasmodium falciparum parasites.* Malaria Journal, 2011. **10**.
166. Dondorp, A.M., et al., *Estimation of the total parasite biomass in acute falciparum malaria from plasma PfHRP2.* Plos Medicine, 2005. **2**(8): p. 788-797.
167. Marquart, L., et al., *Modelling the dynamics of Plasmodium falciparum histidine-rich protein 2 in human malaria to better understand malaria rapid diagnostic test performance.* Malaria Journal, 2012. **11**: p. 9.
168. Hendriksen, I.C.E., et al., *Evaluation of a PfHRP(2) and a pLDH-based Rapid Diagnostic Test for the Diagnosis of Severe Malaria in 2 Populations of African Children.* Clinical Infectious Diseases, 2011. **52**(9): p. 1100-1107.
169. Saha, K., F. Bender, and E. Gizeli, *Comparative study of IgG binding to proteins G and A: Nonequilibrium kinetic and binding constant determination with the acoustic waveguide device.* Analytical Chemistry, 2003. **75**(4): p. 835-842.
170. Bronner, V., M. Tabul, and T. Bravman, *Rapid Screening and Selection of Optimal Antibody Capturing Agents Using the ProteOnTM XPR36 Protein Interaction Array System*. 2009, Bio-Rad Laboratories.
171. Carta, G. and A. Jungbauer, *Protein Chromatography: Process Development and Scale-up*. 2010, John Wiley & Sons. p. 36.
172. Lee, N., et al., *Identification of Optimal Epitopes for Plasmodium falciparum Rapid Diagnostic Tests That Target Histidine-Rich Proteins 2 and 3.* Journal of Clinical Microbiology, 2012. **50**(4): p. 1397-1405.
173. Jones, R. and BBInternational, *Question about Custom Conjugates*, G. Fridley, Editor.: (email).
174. Sharan, R. and J. Sharma, *Theoretical Model of Histidine Rich Protein II of the P. falciparum*, in *PDB ID: 1L8M*. 2002: Protein Data Bank.

Appendix C: Supporting documents

Particle Diameter	OD @ 520nm	No. Particles per ml	No. Moles Particle per ml	Molar Particle Concentration (No. moles per L)	Mass of Gold per ml (g)	Moles of Gold per litre
20	1	7.00E+11	1.1624E-12	1.1624E-09	5.66E-05	2.87E-04
20	5	3.50E+12	5.81202E-12	5.81202E-09	2.83E-04	1.44E-03
20	10	7.00E+12	1.1624E-11	1.1624E-08	5.66E-04	2.87E-03
20	15	1.05E+13	1.74361E-11	1.74361E-07	8.49E-04	4.31E-03
20	50	3.50E+13	5.81202E-11	5.81202E-07	2.83E-03	1.44E-02
20	100	7.00E+13	1.1624E-10	5.81202E-05	5.66E-03	2.87E-02
40	1	9.00E+10	1.49452E-13	1.49452E-10	5.82E-05	2.96E-04
40	5	4.50E+11	7.4726E-13	7.4726E-10	2.91E-04	1.48E-03
40	10	9.00E+11	1.49452E-12	1.49452E-09	5.82E-04	2.96E-03
40	15	1.35E+12	2.24178E-12	2.24178E-09	8.73E-04	4.43E-03
40	50	4.50E+12	7.4726E-12	7.4726E-09	2.91E-03	1.48E-02
40	100	9.00E+12	1.49452E-11	1.49452E-08	5.82E-03	2.96E-02
60	1	2.60E+10	4.3175E-14	4.3175E-11	5.68E-05	2.88E-04
60	5	1.30E+11	2.15875E-13	2.15875E-10	2.84E-04	1.44E-03
60	10	2.60E+11	4.3175E-13	4.3175E-10	5.68E-04	2.88E-03
60	15	3.90E+11	6.47625E-13	6.47625E-10	8.51E-04	4.32E-03
60	50	1.30E+12	2.15875E-12	2.15875E-09	2.84E-03	1.44E-02
60	100	2.60E+12	4.3175E-12	4.3175E-09	5.68E-03	2.88E-02
80	1	1.10E+10	1.82664E-14	1.82664E-11	5.69E-05	2.89E-04
80	5	5.50E+10	9.13318E-14	9.13318E-11	2.85E-04	1.44E-03
80	10	1.10E+11	1.82664E-13	1.82664E-10	5.69E-04	2.89E-03
80	15	1.65E+11	2.73995E-13	2.73995E-10	8.54E-04	4.33E-03
80	50	5.50E+11	9.13318E-13	9.13318E-10	2.85E-03	1.44E-02
80	100	1.10E+12	1.82664E-12	1.82664E-09	5.69E-03	2.89E-02

Figure 86: Manufacturer reported information about number of gold nanoparticles per mL at varying OD values. Information from BBInternational, Cardiff, UK.